

**Project Report  
STK-255**

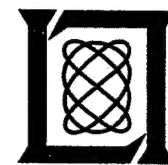
**Proceedings of the 2000  
Space Control Conference**

**S.E. Andrews  
Editor**

**11–13 April 2000**

---

**Lincoln Laboratory**  
MASSACHUSETTS INSTITUTE OF TECHNOLOGY  
LEXINGTON, MASSACHUSETTS



Prepared with partial support of the Department of the Air Force  
under Contract F19628-95-C-0002.

Approved for public release; distribution is unlimited.

DTIC QUALITY INSPECTED 2

20000512 003

This report is based on studies performed at Lincoln Laboratory, a center for research operated by Massachusetts Institute of Technology. The work was sponsored by the Department of the Air Force, AFSPC/DOY, under Contract F19628-95-C-0002.

This report may be reproduced to satisfy needs of U.S. Government agencies.

The ESC Public Affairs Office has reviewed this report, and it is releasable to the National Technical Information Service, where it will be available to the general public, including foreign nationals.

This technical report has been reviewed and is approved for publication.

**FOR THE COMMANDER**

  
Gary Tutungian  
Administrative Contracting Officer  
Plans and Programs Directorate  
Contracted Support Management

Non-Lincoln Recipients

PLEASE DO NOT RETURN

Permission is given to destroy this document  
when it is no longer needed.

MASSACHUSETTS INSTITUTE OF TECHNOLOGY  
LINCOLN LABORATORY

**PROCEEDINGS OF THE 2000  
SPACE CONTROL CONFERENCE**

**PROJECT REPORT STK-255**

**11-13 APRIL 2000**

**Approved for public release; distribution is unlimited.**

**LEXINGTON**

**MASSACHUSETTS**

LEXINGTON

MASSACHUSETTS

## PREFACE

The eighteenth Annual Space Control Conference was held on 11, 12 and 13 April 2000. ESC acts as administrative sponsor of the event which is held at the Lincoln Laboratory facility on Hanscom AFB, and the program is coordinated with Air Force Space Command and the Air Force Research Laboratory. The purpose of this series of conferences is to provide a forum for the presentation and discussion of space control issues.

This *Proceedings* documents those presentations from this conference that were received in time for pre-conference publication. The papers contained were reproduced directly from copies supplied by their authors (with minor mechanical changes where necessary). It is hoped that this publication will enhance the utility of the conference.

Dr. Susan E. Andrews  
Editor

## TABLE OF CONTENTS

Space Catalogue Growth Model for Simulation <i>M.D. Hejduk – SenCom Corporation</i> <i>R.S. Daw – AFSPC/SWC/AESS</i>	1
Contributions of the GEODSS System to Catalog Maintenance <i>J.G. Miller – The MITRE Corporation</i> <i>W.G. Schick – ITT Industries, Systems Division</i>	13
Geosynchronous Satellite Orbit Pattern: Improvements to SBV Geosynchronous Belt <i>K.S. Capelle and J. Sharma – MIT Lincoln Laboratory</i>	29
Small Aperture Telescope Augmentation (SATA) Concept <i>P. Kervin – Det 15 AFRL</i> <i>Maj M. Nutter – AFSPC/DRCS</i> <i>Capt C. Baker – ESC/NDWG</i> <i>P. Sydney, V. Soo Hoo and K. Hamada – Boeing Rocketdyne Technical Services</i> <i>D. Nishimoto – Oceanit Laboratories</i> <i>L. Crawford – Schafer Corporation</i>	43
Orbital Debris and the Environmental Restoration of Space: A Report to the Congressional Defense Committees <i>D.B. Spencer – The Pennsylvania State University</i> <i>C.B. Hogge – Air Force Research Laboratory</i> <i>W.S. Campbell, M.E. Sorge and S.R. McWaters – The Aerospace Corporation</i>	57
Predictions and Control of Space Environments <i>W.J. Burke – Air Force Research Laboratory, Space Vehicles Directorate</i>	65
First GEO Survey Test Observations with the ESA 1 m Telescope in Tenerife <i>T. Schildknecht, U. Hugentobler and M. Ploner – Astronomical Institute, University of Berne</i>	73
A GEO Debris Survey Using NASA's CCD Debris Telescope (CDT) <i>J.L. Africano, J.V. Lambert and P.F. Sydney – Boeing North American</i> <i>E.G. Stansbery – NASA/Johnson Space Center</i> <i>K.S. Jarvis – Lockheed Martin Space Operations</i>	81

Probability of Collision in the Geostationary Orbit <i>R.A. LeClair – MIT Lincoln Laboratory</i>	85
Orbital Debris Size Estimation from Radar Cross Section Measurements R. Lambour, T. Morgan and N. Rajan – <i>MIT Lincoln Laboratory</i>	93
Progress Report for the Canadian Automated Small Telescope for Orbital Research (CASTOR) Satellite Tracking Facility <i>M.A. Earl and T.J. Racey – The Space Surveillance Research and Analysis Laboratory, Dept. of Physics, Royal Military College of Canada</i>	107
Space Surveillance with the Space-Based Visible Sensor <i>J. Sharma – MIT Lincoln Laboratory</i>	115
Determination of Photometric Filters for Satellite Observations Using SILC Data <i>T. Payne, D. Payne and D. Sanchez – Schafer Corporation</i> <i>S. Gregory – University of New Mexico/AFRL</i> <i>L. Kann and D. Werling – Air Force Research Laboratory</i> <i>C. Davis and L. Finkner – Boeing</i>	125
Space Object Identification (SOI) Using the Raven Telescopes <i>J.V. Lambert, P. Sydney, V. Soo Hoo, J. Africano – Boeing</i> <i>P.W. Kervin – Air Force Research Laboratory</i>	135
High Precision Real Time Metric Processing for the MOSS and LINEAR Systems <i>E.C. Pearce, F. Shelly and J.A. Johnson – MIT Lincoln Laboratory</i>	145
COBRA DANE Space Surveillance Capabilities <i>P. Chorman – Riverside Research Institute</i>	159
Operations at the Lincoln Space Surveillance Complex <i>F.D. Rosenberg – MIT Lincoln Laboratory</i>	169
Lincoln Space Surveillance Complex (LSSC) Modernization <i>T.L. Sangiolo – MIT Lincoln Laboratory</i>	175
Configuration Trades for a Space Object Surveillance Fence <i>J.K. Beard – Raytheon Electronic Systems</i>	183
Distributed Tracking <i>A. Collinson – Collinson Systems Limited</i> <i>M.A. Bailey – UK Ministry of Defence</i> <i>S.J. Goodenough – Defence Evaluation and Research Agency</i> <i>E. Goodchild - ASA</i>	193

## Space Catalogue Growth Model for Simulations

M.D. Hejduk, SenCom Corporation<sup>1</sup>

R.S. Daw, AFSPC/SWC/AESS<sup>2</sup>

The Space Surveillance Network Analysis Model (SSNAM) is a SSN simulation tool under development for AFSPC/DOY that will be used as a force structure decision aid, providing details of the effects of adding and deleting sensors, altering tracking requirements, and modifying event processing, among other applications. One of the tasks to which it is expected to be put frequently is to assess the performance of both an unmodified and an altered SSN at some point in the future, and to this end a durable space catalogue growth model needs to be available to the tool in order to create representative space catalogues for these future points. SenCom and the SWC were tasked by DOY to develop such a model for use by SSNAM.

In years past, catalogue growth projections were usually executed by applying curve-fitting techniques (almost always linear regression) to historical population data for the catalogue considered in aggregate or at only the highest levels of division (*e.g.*, near-Earth vs. deep-space). This approach had the advantages of simplicity of execution and reliability in terms of meeting the general quality-of-fit criteria applied to linear regression, but it also introduced disadvantages. Mixing orbit regimes that are volatile from a catalogue growth perspective with those that are well behaved placed an upper limit on the model's fidelity. Even more disappointing was the approach's inability to predict the future proportionality among different orbit types. While it might furnish a total NE object count for a future time, it could not predict, for example, what proportion of these NE objects would occupy a high-drag orbit regime. As the SSNAM tool will simulate observations and differential corrections, it is essential that the model be told which satellites in a constructed future catalogue occupy which orbit types, especially difficult-to-maintain ones, so that processing workload and element set accuracies may be modeled correctly.

In a re-contextualization of the “short-arc” assumption, some previous catalogue growth studies have presumed that because the growth projections are usually for only a short period into the future, it is adequate to use the proportions observed at the last time-point of the fit interval for the entire prediction interval. For very short predictions this is perhaps true, but for those that are at all extended it is not acceptable. Figure 1 shows how the relative proportions of inclination

---

<sup>1</sup> 4575 Galley Road, # 300; Colorado Springs, CO 80975. E-mail: mhejduk@earthlink.net

<sup>2</sup> Put a mailing address here. E-mail: dawrs@swc.schriever.af.mil

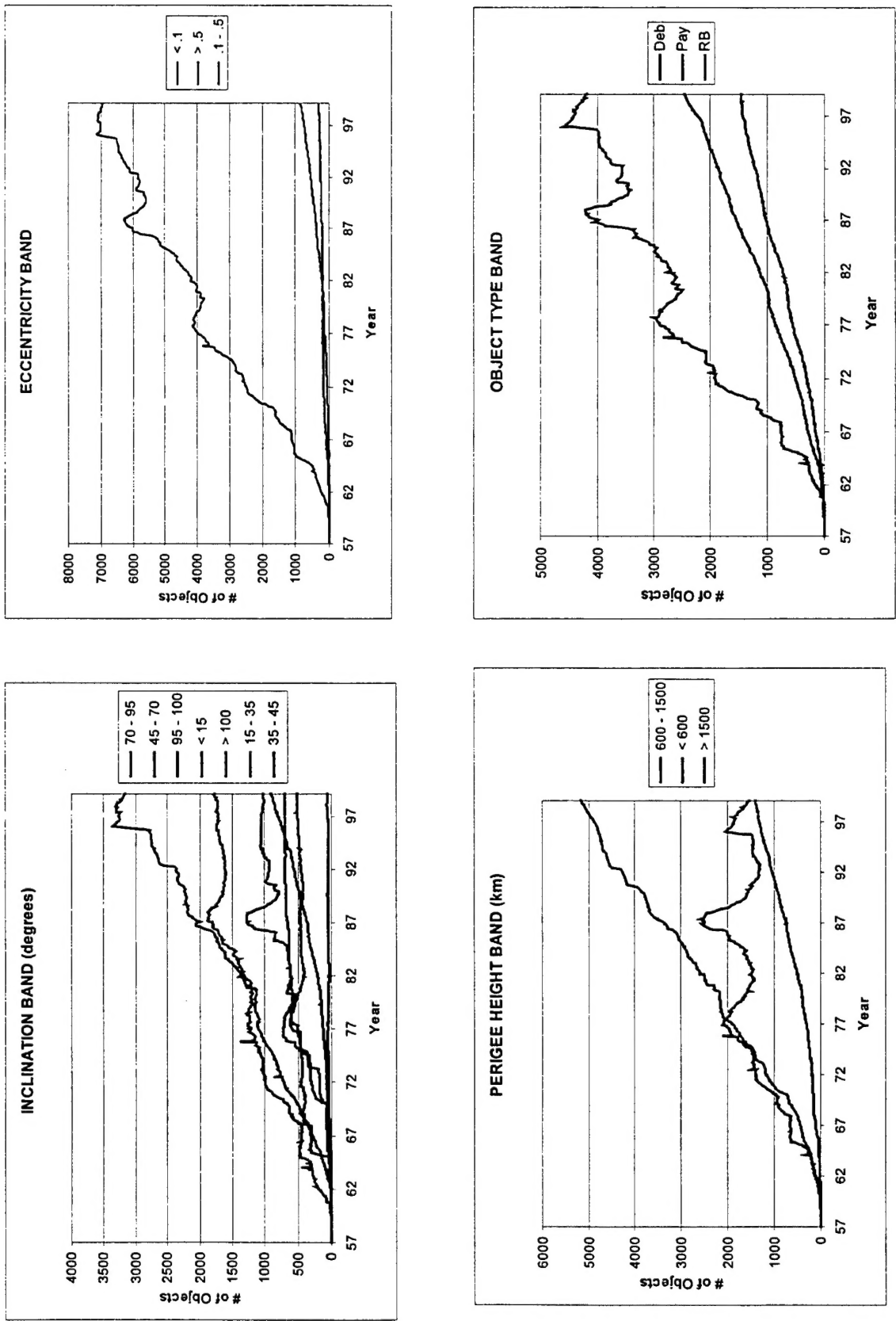


Figure 1: Space catalogue growth by orbit and object category. Figures are derived from SATCAT data. The order of series in each graph's legend corresponds to the order of the series at the last time point. Even though only raw count numbers are plotted (rather than proportions of catalogue), it is clear that the growth rates among different bands of an orbital parameter or object type are quite different, resulting in that parameter's comprising a

band, eccentricity band, perigee height band, and object type band have changed over time. For some of these categories there is rather little change, but for the majority it is considerable. A growth model to be used in simulations that will model SSN performance a decade or more into the future must model the changing proportions of certain critical divisions among orbit and satellite types.

The critical divisions that were selected for the growth model are inclination, eccentricity, perigee height, and object type bands. Inclination bands were selected because they can be mapped credibly to country/region of origin, and launch rates comprise a significant input to the growth of objects in all object types. The bands selected are equatorial-based launches and geosynchronous launches ( $i < 15^\circ$ ); geosynchronous transfer orbit offscourings, Eastern Test Range, NASA, international, civilian, and scientific launches ( $15^\circ < i < 35^\circ$ ); low-latitude launches ( $35^\circ < i < 45^\circ$ ); high-latitude coverage regions ( $45^\circ < i < 70^\circ$ ); transitional region ( $70^\circ < i < 95^\circ$ ); sun-synchronous launches ( $95^\circ < i < 100^\circ$ ); and other launches ( $i < 100^\circ$ ). Eccentricity bands were chosen because they relate to the general ease of element set maintenance. The three bands selected are circular ( $e < .1$ ), moderately eccentric ( $.1 < e < .5$ ), and highly eccentric ( $e > .5$ ). Perigee height bands were chosen because they govern the amount of atmospheric drag to which a satellite will be subjected. The three bands selected are dense atmosphere ( $p < 600\text{km}$ ), tenuous atmosphere ( $600 < p < 1500$ ), and little to no atmosphere ( $p > 1500$ ). Finally, object type bands were chosen because of their relationship to object behavior and indirect relationship to RCS. The three bands selected are payloads, rocket bodies, and debris. A fourth band, unknown (meaning analyst satellites), was also selected and used in the analysis. However, the extreme difficulty in distinguishing between analyst satellites that may relate to a legitimate but not-yet-catalogued object and those that are the chaff of analysis or UCT processing, and the extreme schizophrenia of the population data (and therefore also of the associated curve fits) for such objects, has made it difficult to determine what to do with data for this object type; results for unknown objects are thus omitted from this presentation.

These four divisions are arranged in nested fashion, much like a Porphyrian Tree. The most basic division is into the seven inclination bands, because they are (at least somewhat) causally linked to launch rates. Each of these inclination bands is then subdivided for orbital type into three eccentricity bands, with these three bands' being further subdivided into the three perigee height bands. Having executed divisions for launch rate and orbital type, the final nested division is into the three object type bands. This successive division results in 189 independent bins of satellites, independent because each object is placed in only one bin. Figure 2 provides an "organizational chart" view of this nested arrangement.

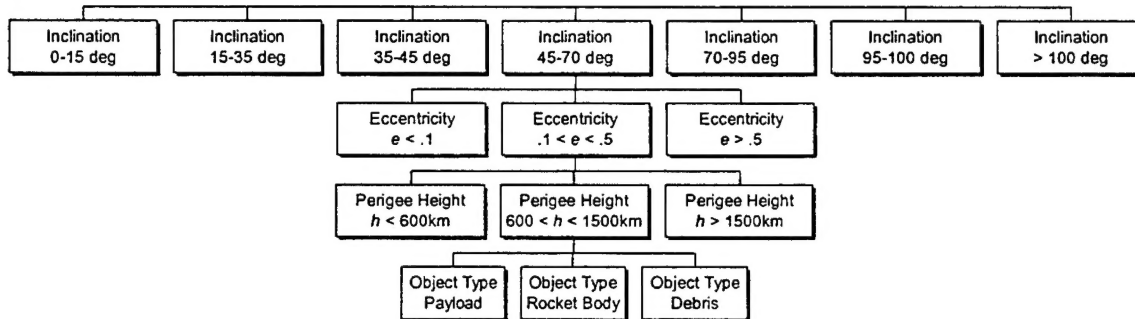


Figure 2: Nested arrangement of orbital type and object bins

Having thus established the bin definitions and nesting arrangement, the next step is to determine whether it is preferable to use the historical SATCAT or collected SATF files as the source for the historical population data for each bin. A SATCAT file provides both a full time-range of data (as population data can be extracted from it all the way back to 1957) and the simplicity of containing all the needed information in a virtually error-free single file. Its chief disadvantages are that for objects still in orbit it provides only the most recent elset and for decayed objects only the original cataloguing elset; as objects do move about during their life in orbit, the SATCAT, by failing to account for this dynamic, provides a monolithic presentation of the catalogue heavily influenced by the particular SATCAT's creation date. Furthermore, new objects generated from satellite break-ups are assigned the same cataloguing date as their parent object, moving these objects' creation improperly further back in time and thus skewing the temporal unfolding of the catalogue's growth, unless some stratagem be implemented to try to correct for this.<sup>3</sup>

Collecting SATF files (the daily ops elset files used in Cheyenne Mountain) at some regular interval and tabulating population data from them will deliver the analysis from the stasis imposed by the SATCAT and thus produce a more accurate data set, but it introduces its own disadvantages. SATF files are cumbersome to collect and filter (an issue because it is intended that the catalogue growth model be re-run periodically in order to incorporate the latest observed

<sup>3</sup> The correction approach used in the present study is to assign to each debris object the catalogue date of the next piece in the SATCAT with an A-suffix on its international designator. When new objects are discovered that are determined to be linked to some other object (e.g., created by a satellite break-up), they are assigned the same international designator as their parent but with an incremented alphanumeric suffix. Pieces with only an "A" as their suffix are known to be a result of fresh cataloguing events and not derived from some other object, so their cataloguing date as reported in the SATCAT must correspond very closely to the day that that object actually appeared in space as a discrete object. Using the cataloguing date of the next "A-suffixed" piece as the cataloguing date for debris objects approximates the actual day of cataloguing of the debris object to within a month in most cases, whereas the officially-assigned cataloguing date, derived from the object's parent, can easily be off by a decade or more.

population data), contain more frequent occurrences of data corruption, and have been reliably retained historically only since 1987. The question to be asked is whether the differences in population data gleaned from the SATCAT versus the SATF are significant enough that the additional logistical overhead required to use SATF data be justified. Figure 3 examines three cases of convergence and/or difference between SATCAT and SATF data, concluding that there are enough cases of sufficiently significant difference that the SATF approach is necessary.

Next to be decided is the curve-fitting approach and fit interval to be used for each bin. A high-fidelity fit is of course the primary objective, but of competing importance is simplicity of approach. The growth model is intended to be run automatically by trained but not necessarily schooled operators, at perhaps frequent intervals. Fit methods that can produce high quality-of-fit results but that require manual massaging of the selected fit interval or fit parameters, or that in some circumstances produce perturbed results that must be screened for manually, are not acceptable. In short, presumption lies with the ease and stability of linear regression: a large number of bins must respond sufficiently poorly to linear regression in order to displace its primacy and force the introduction of some other method that would require more care and feeding.

Because the SATF, rather than SATCAT, was selected as the data source, data availability was limited to 1987 forward; this circumstance obviously affects the selection of the fit span. It seems proper to select fit spans that are multiples of the eleven-year solar cycle so that any periodicity introduced thereby can be evenly represented. The total amount of data presently available is nearly such a multiple, exceeding it by somewhat more than a year. For the present trials, all the available data were used; but for future applications of the model it is probably best to use a sliding eleven-year period back from the most recent data point. Once twenty-two years of data are available, it may be desirable to double the fit span. Of course, it is poor practice to use linear regression to predict into the future for a period longer than the fit span; so the prediction interval is limited to eleven years also.

An initial run of regression analysis was conducted on all 189 bins, using the usual  $t$ - and  $F$ -test evaluation criteria, to obtain an initial view of the bins' response to linear regression. A determinate fit was presumed if the  $F$ -test result was less than .05 and the slope and intercept  $t$ -test results were greater than 2. Fits for 78 of the 189 bins, or 41%, failed to meet these criteria, hardly an encouraging result. On further examination, it was discovered that most of the failing bins contained either very few objects or no objects at all. Sparsely-populated bins frequently produce indeterminate fits; and although empty bins should in principle produce the highly-reliable fit of  $y = 0$ , the quality-of-fit indices are not actually calculable for such a case, allowing it to be registered as a failure. Additionally, many of the lightly-populated bins that did pass the quality-of-fit checks produced questionable

**Figure 3a: convergence case.** The SATCAT and SATF population information for this bin are nearly identical, as can be seen by the amount of overlap. Because the bin is not for debris, there is no cataloguing date issue to address.

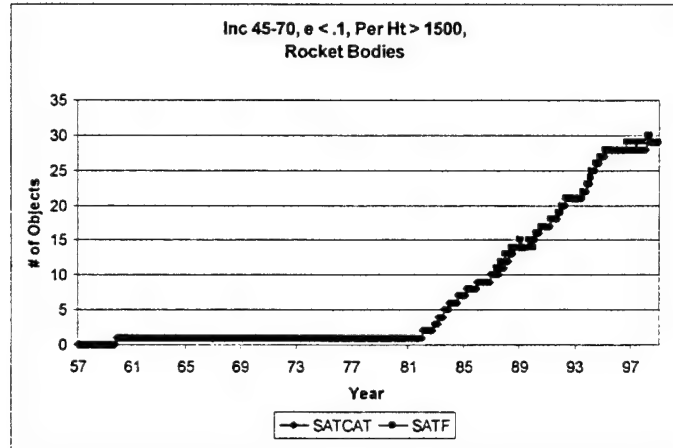


**Figure 3b: divergence case, direction preserved.** Significant space events (here a small and large break-up) throw into relief the differences between using for debris objects their cataloguing date as presented (w/o A) and correcting it by using that of the next A-suffixed piece (w/A). There are considerable differences between even this corrected version and that given by the more reliable SATF, due to many pieces' vacillating in and out of the bin's boundaries (but that lay within them at cataloguing). Linear fits of both the SATCAT and SATF data, while differing in slope, will at least produce the same growth direction.

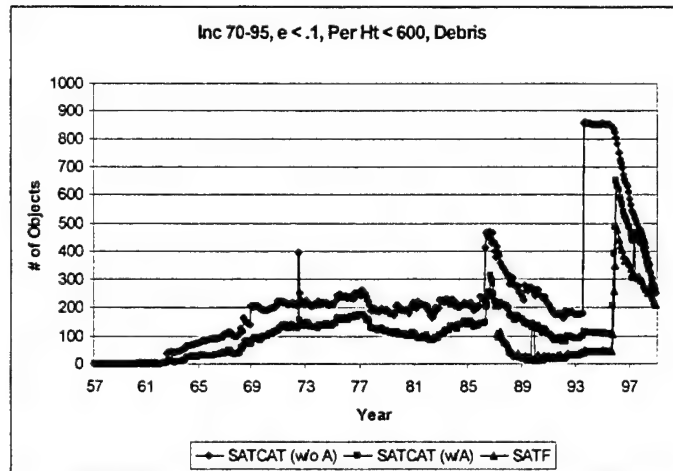
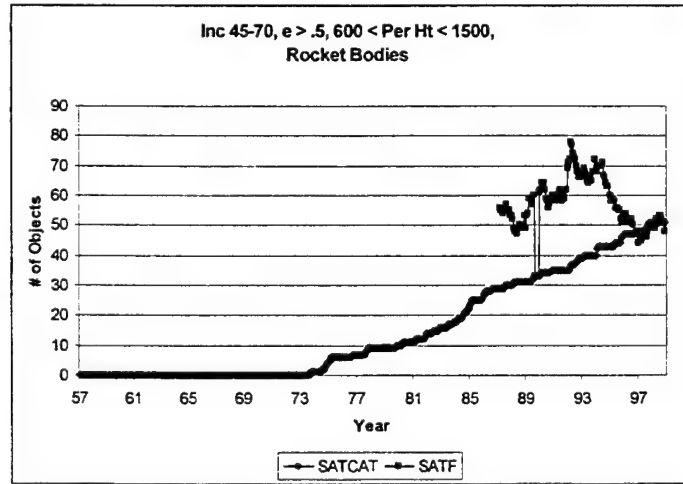


**Figure 3c: divergence case, direction not preserved.** Notable differences exist between the SATCAT and SATF, due to the same type of boundary vacillation noted above. However, the situation is somewhat worse here because linear fits of the SATCAT and SATF data will differ not just in value but also in sign—a SATCAT fit will yield a projection of increase, whereas a SATF fit will yield one of decrease. There are enough cases of this and the above (3b) type that prudence counsels use of the SATF data as the population data source.



fit results, with the calculated fit line differing in direction (*i.e.*, sign of slope) from the obvious trend of the most recent data. In light of all this, it was decided to prescind from attempting a fit for sparsely-populated bins, using the mean size of the bin (taken over what would have been the fit span) as an invariant projection value for that bin's future size. The transition from usually questionable to usually acceptable fits, as assessed subjectively by the authors, seemed to be at a bin size of about thirty satellites (using most recently observed size, rather than historical high); this was the threshold chosen for enabling fitting rather than using a static projection of the mean over the fit span. Implementation of this exclusion produces the following bin disposition:

Bin Disposition	# of Bins	# of Objects	% of Objects
Excluded for insufficient data (< 30 obj)	147	641	7.9%
Excluded for fit-quality failure	7	998	12.3%
Bins with successful fits	35	6453	79.7%

While the number of bins excluded for insufficient data seems at first extraordinarily high, it actually represents relatively few objects. Adequately-populated bins excluded for quality-of-fit reasons (for which the mean-based projection, which constitutes a reasonable prediction for indeterminate cases, is used) represent a somewhat higher number of objects; but it is encouraging that 80% of the total objects occur in bins that are actively fitted. If the quality of these fits is judged to be adequate, the 20% exclusion rate is not high enough to stymie linear regression, especially when more than half of the excluded objects occur in data-clumped bins for which a projected mean is the desired prediction approach.

Once a fit passes the determinacy test, fit quality is usually assessed by the  $r^2$  value, which represents the percentage of the variance held in common by the actual data and the regression. Higher values represent better correlation and thus better fit quality. The following table divides the possible  $r^2$  values into deciles to determine how the  $r^2$  values for the 35 actively-fit bins are distributed:

$r^2$ Decile	# of Bins	% of Bins	Inverted Cumulative %	# of Objects	% of Objects	Inverted Cumulative %
.9 - 1	9	25.7%	25.7%	2565	39.7%	39.7%
.8 - .9	7	20.0%	45.7%	1520	23.6%	63.3%
.7 - .8	3	8.6%	54.3%	125	1.9%	65.2%
.6 - .7	2	5.7%	60.0%	118	1.8%	67.1%
.5 - .6	3	8.6%	68.6%	799	12.4%	79.5%
.4 - .5	4	11.4%	80.0%	968	15.0%	94.5%
.3 - .4	3	8.6%	88.6%	104	1.6%	96.1%
.2 - .3	2	5.7%	94.3%	120	1.9%	97.9%
.1 - .2	2	5.7%	100.0%	134	2.1%	100.0%
0 - .1	0	0.0%	100.0%	0	0.0%	100.0%

It is interesting that *ca.* 68% of the total objects (the usual  $1-\sigma$  cut-off, even though the use of standard deviation terminology is misleading here) are in bins with an  $r^2$  value better than .60 and *ca.* 95% of the total objects (the usual  $2-\sigma$  cut-off) are in bins with an  $r^2$  better than .40. An assessment of whether this performance is good enough to declare the linear regression approach to be adequate is naturally subjective, but a more consistent set of criteria has been established for the Pearson correlation coefficient (the square root of  $r^2$ ).<sup>4</sup> Guilford<sup>5</sup> suggests the following mapping of heuristic quality-of-fit descriptions to Pearson values:

Heuristic Description	Pearson Value	$r^2$ Equivalent
Slight, almost negligible relationship	< .20	< .04
Low correlation; definite but small relationship	.20 - .40	.04 - .16
Moderate correlation; substantial relationship	.40 - .70	.16 - .49
High correlation; marked relationship	.70 - .90	.49 - .81
Very high correlation; very dependable relationship	> .90	> .81

63% of the objects for which fits were run fall into the “very dependable” category, and something on the order of 85-90% fall into the “marked” category. In the social sciences, such results would be considered excellent. While one may still wish for a better outcome in an engineering framework, considering that the bins that were fit include perturbing space events, such as break-ups and quasi-periodic “object cleansing” due to the solar cycle, it would probably be necessary to pursue a more elaborate fitting approach to achieve superior correlation indices. Because simplicity and ease-of-use were also goals of the present catalogue growth model, and because the linear regression results are considered excellent by social science standards, it was judged adequate to deploy only linear regression for bin-fitting.

With fit coefficients available for the actively-fit bins and projected means available for the remainder, it is easy to produce growth projections for each bin. Growth data for indices that are composites of different bins are obtained by adding the bins’ projected growth data at each predicted time point. Growth projections for the principal orbit type and object divisions used in this analysis are presented in Figure 4; corresponding information for the proportion of the catalogue that each division comprises is provided in Figure 5. Finally, the table

---

<sup>4</sup> Actually, it is more precise, as the etymology would indicate, to define  $r^2$  as the square of the Pearson correlation coefficient. In addition to being a numerical value, the Pearson index is signed, with the sign indicating whether the correlation is direct or inverted.

<sup>5</sup> J.P. Guilford, *Fundamental Statistics in Psychology and Education* (New York: McGraw-Hill, 1956), p. 145. Some claim that the correlation standards used in the social sciences are too permissive, but there seems to be no widely-embraced corresponding standard for engineering applications.

below provides growth data for catalogue divisions commonly encountered in space surveillance analyses.<sup>6</sup>

Date	NE	DS	GEO	High-e	Manned Flight	Debris
1/2001	6416	1836	759	846	1413	4311
1/2002	6510	1904	794	869	1431	4366
1/2003	6604	1972	830	891	1449	4421
1/2004	6697	2039	866	914	1468	4476
1/2005	6791	2107	902	936	1486	4531
1/2006	6888	2175	938	959	1507	4589
1/2007	6990	2242	974	981	1533	4652
1/2008	7093	2310	1010	1004	1560	4715
1/2009	7197	2378	1045	1026	1587	4779
1/2010	7301	2446	1081	1049	1614	4844

---

<sup>6</sup> The following definitions of terms and calculation approaches are used to produce this table. NE orbits have an orbital period < 225 minutes; DS  $\geq$  225 minutes. This distinction is not directly derivable from the binning approach used in the analysis. However, as most bins consist of entirely NE or entirely DS objects, a bin assignment scheme was created that, for the 12/1/99 SATF, was within five satellites of the count derived from examining the orbital period. A variety of definitions of the geostationary orbit type are in use; the contents of the  $i < 15^\circ$ ,  $e < .1$ , Per Ht  $< 600\text{km}$  match the 11/99 geosynchronous catalogued object count to within thirty satellites. High-eccentricity is here defined as  $e > 0.5$ . Manned-flight objects are defined as those with a perigee height  $< 600\text{km}$ . Debris objects are those catalogued objects that are not payloads, rocket bodies, or space platforms.

From this, it can be observed that in the table the counts for geostationary satellites are also included in the DS column; and the high-e, manned-flight, and debris counts are included in both the NE and DS columns, as appropriate.

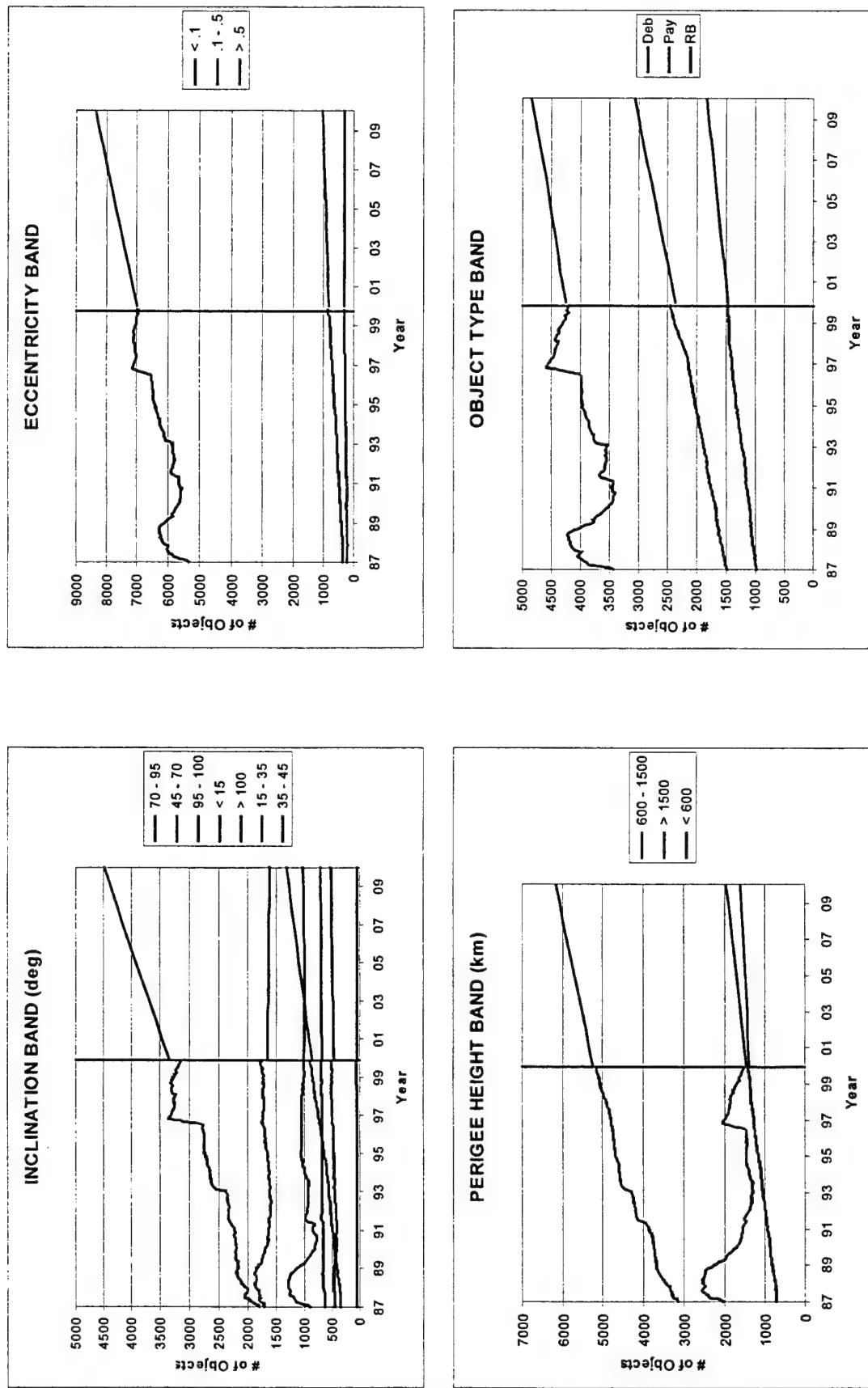
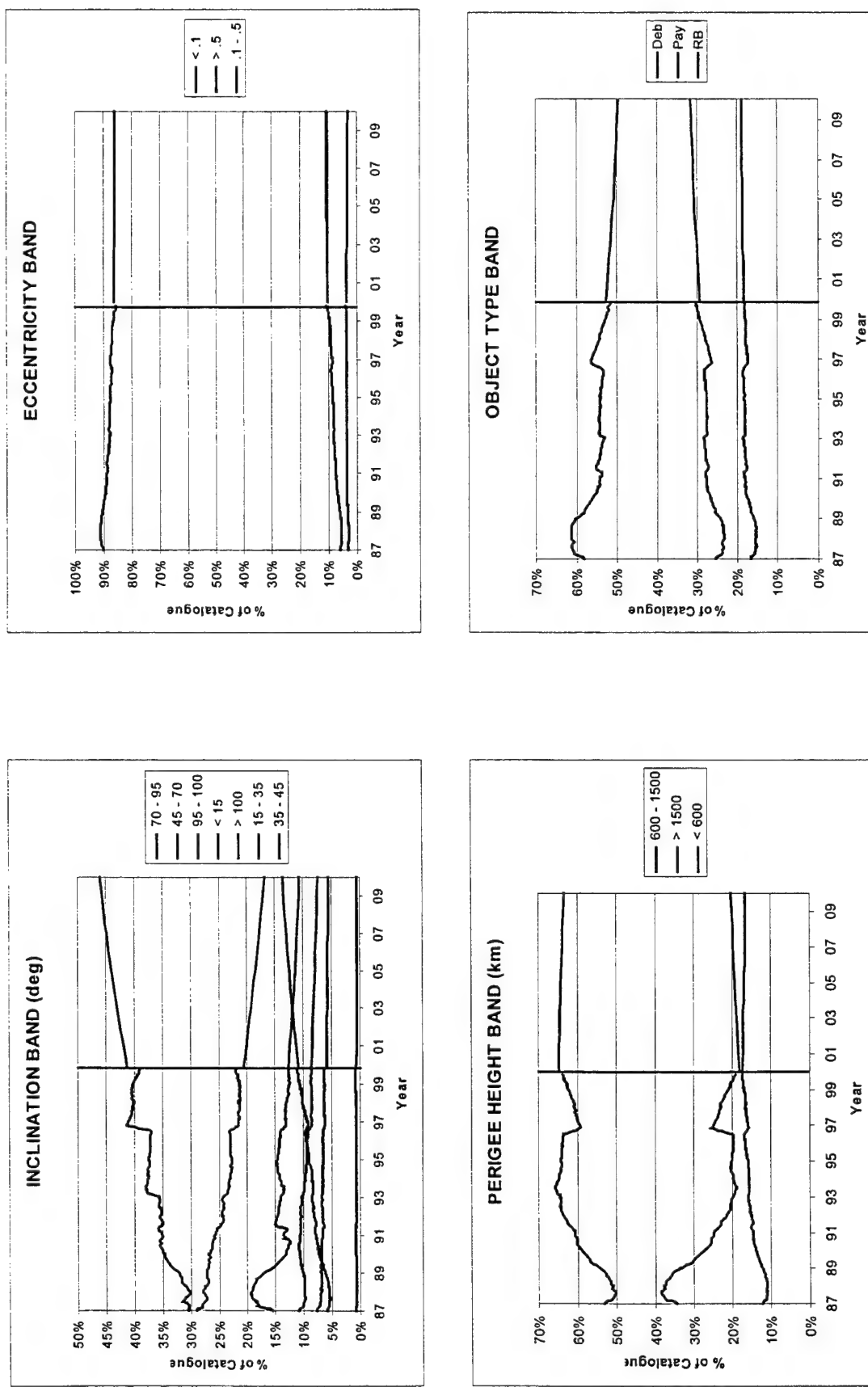


Figure 4: Space catalogue historical and projected growth by orbit and object category. Values to the left of each vertical line are SATF population data; those to the right are model projections. The order of series in each graph's legend corresponds to the order of the various series at the last time point.



**Figure 5:** Space catalogue historical and projected growth by orbit and object category, as percentage of total catalogue. Values to the left of each vertical line are SATF population data, those to the right are model projections, each of which is given as a percentage of total catalogue. The order of series in each graph's legend corresponds to the order of the various series at the last time point.

## Contributions of the GEODSS System to Catalog Maintenance

J. G. Miller (The MITRE Corporation), W. G. Schick (ITT Industries, Systems Division)

The Electronic Systems Center completed the Ground-based Electro-Optical Deep-Space Surveillance (GEODSS) Modification Program (GMP) in 1999 with new mission critical computer resources, including sensor controllers at the GEODSS sensor sites and an Optical Command, Control, and Communications Facility (OC3F) at Edwards AFB. The GEODSS system with the GMP configuration became operational on 3 August 1999, with the OC3F dynamically scheduling the three GEODSS sites in response to tasking from the Space Defense Operations Center (SPADOC). SPADOC still tasks the individual GEODSS sites, Socorro, Maui, and Diego Garcia, based on site visibility and capacity, but the site tasking messages are transmitted to the OC3F instead of the individual sites. The OC3F combines the individual site tasking messages into a single database and dynamically schedules the individual sites in near real-time, independent of which site SPADOC tasked. For example, a high-priority satellite may be tasked by SPADOC to Socorro and not Maui, even though it has visibility, but the dynamic scheduler may schedule Maui to track the satellite because Socorro is clouded over during the satellite pass. SPADOC tasks the optical sites hours before their shooting periods begin, assuming clear skies, because it cannot predict the weather in advance.

The OC3F also converts track requests from SPADOC into several tracklets of three obs each, separated in time by at least ten minutes, to achieve better orbit distribution of the observations. This benefits catalog maintenance by producing more accurate element sets. In accordance with U. S. Space Command Instruction UI 10-40, SPADOC tasks satellites to sensors at a category 1 through 5 (category 1 has the highest priority) and a suffix A through Z, indicating the number of tasked tracks and the number of observations per track. As a hypothetical example, consider a semi-synchronous satellite that is visible to all three GEODSS sites. Suppose SPADOC determines that the satellite only needs to be tasked to two sensors, which could be any combination of radar and optical sensors with visibility. Suppose SPADOC tasks Socorro at 2K and Diego Garcia at 2K, i.e. category 2 and suffix K, indicating one track of five observations. K is the most frequently used suffix by SPADOC for ground-based optical sensors. When the OC3F receives Socorro's tasking message from SPADOC, it converts the suffix for each satellite into the number of 3-ob tracklets necessary to provide at least as many observations in SPADOC's track request. For the K suffix, this would be two tracklets, providing SPADOC one more observation than requested but in two tracks or tracklets. When the OC3F receives Diego Garcia's tasking message, it does the same conversion to tracklets. So the hypothetical satellite would have a requirement of four tracklets in the dynamic scheduler's database. The OC3F would attempt to obtain the four tracklets for this satellite from any site that has visibility, based on the real-time optimization and prioritization of all other requests. It is possible that Socorro could be scheduled to provide one of the tracklets, Maui two of the tracklets, and Diego Garcia one of the tracklets to satisfy SPADOC's tasking request. This would result in a total of 12 observations in four tracklets, two more observations than SPADOC requested.

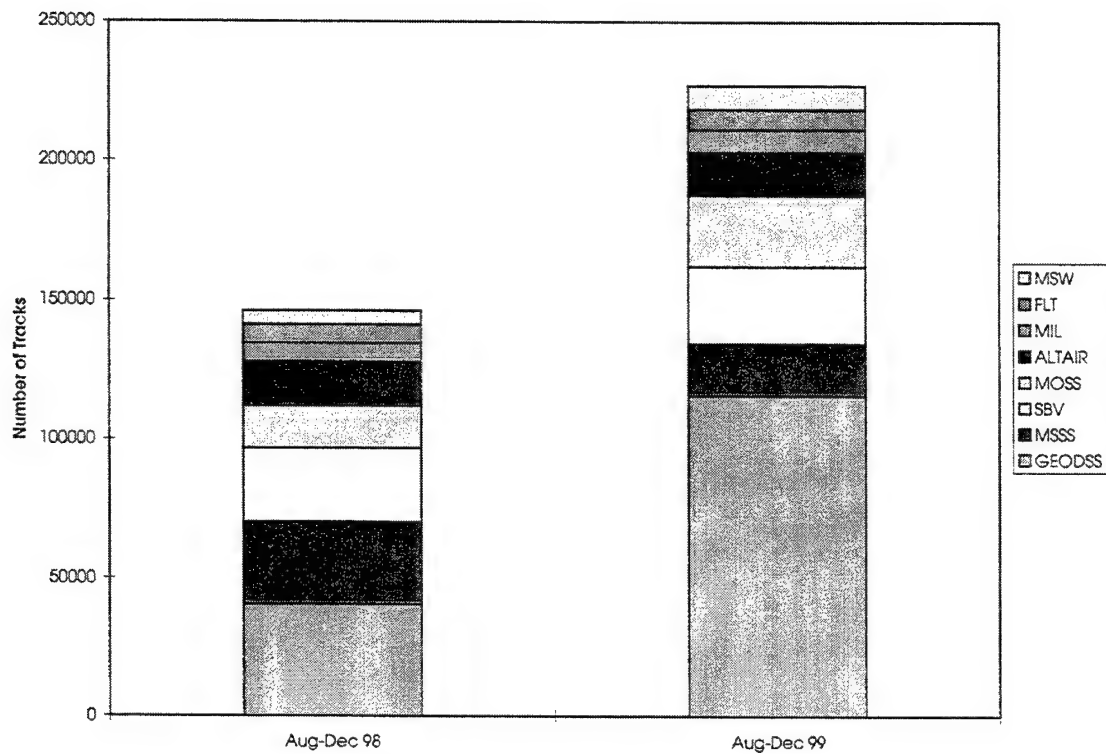
GEODSS with the GMP configuration now produces more tracks, on more objects, and provides more observations per day, on average, than the legacy GEODSS system. The purpose of this paper is to show the effect of this increased throughput on catalog maintenance.

The throughput of GEODSS under GMP from August 1999 through December 1999 is compared with the throughput of the GEODSS legacy system from August 1998 through December 1998, so that the time intervals cover the same months of the year. Figure 1 shows the track response for these two time intervals from all deep-space sensors. The other deep-space sensors include the Maui Space Surveillance System (MSSS), the Space Based Visible (SBV) sensor on board the MSX satellite, the Moron Optical Space Surveillance (MOSS) system, the ALTAIR and Millstone (MIL) radars, and the passive RF sites, Feltwell (FLT) and Misawa (MSW). The post-processing software that reconstructs tracks from SPADOC observation files defines a track to be a contiguous collection of observations on a satellite from a sensor over a short time interval. Thus, GEODSS tracklets are counted as tracks by this software.

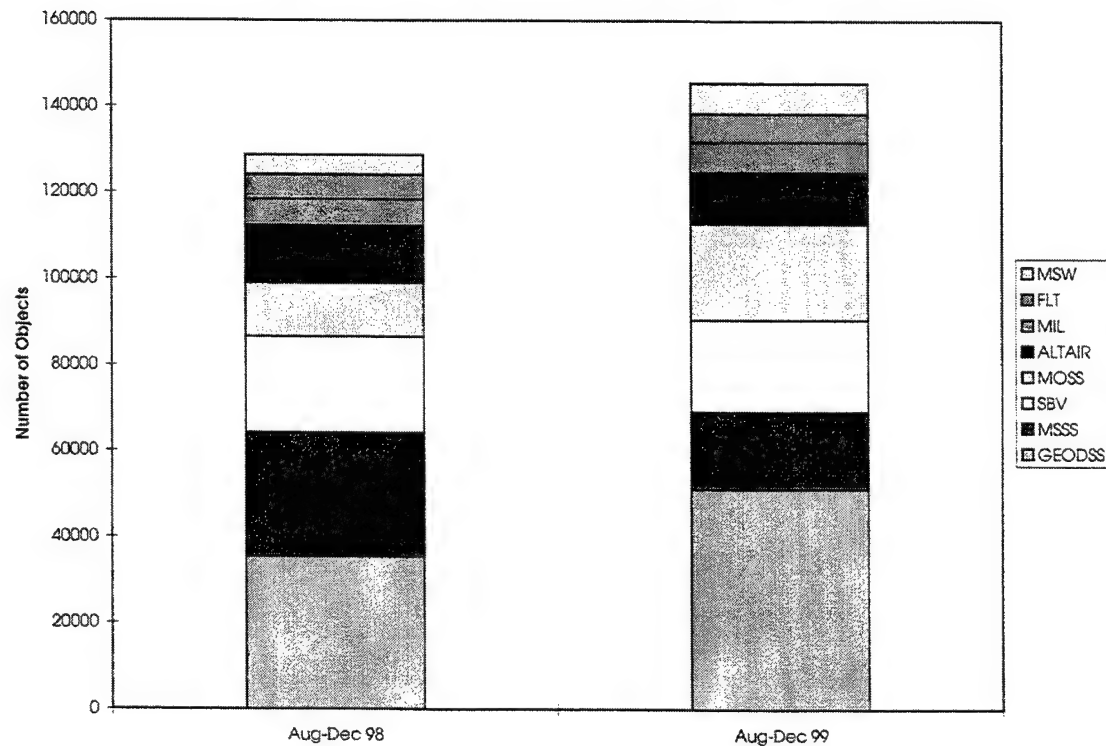
Given that the OC3F converts SPADOC 5-ob track requests into two 3-ob tracklets, one would expect GEODSS under GMP to produce twice as many tracks as legacy GEODSS, based on this post-processing software. It is evident from Figure 1 that the GEODSS track throughput has more than doubled (legacy GEODSS provided 40,658 tracks and GMP provided 116,052 tracks for a 185 percent increase). The legacy GEODSS system did have red time from August through December 1998 due to GMP testing. However, the third cameras, both on auxiliary telescopes at Socorro and Maui, were available for spacetrack under the legacy GEODSS system, but are not available under GMP. These auxiliary telescopes will be replaced with main telescopes in the future and scheduled by the OC3F. This will further increase the GEODSS throughput under GMP. The SBV track throughput essentially remained the same for these two time intervals, 26519 and 27563, respectively. It is also evident from Figure 1 that the MSSS track throughput has decreased (from 29577 to 18534 for a 37 percent decrease), and the MOSS track throughput has increased (from 15376 to 25532 for a 66 percent increase). The decrease from MSSS is due to the refurbishment of the 1.2 meter telescope to support Near Earth Asteroid Tracking (NEAT) during the latter part of 1999. In 2000, the 1.2 meter telescope will be used three weeks per month supporting NEAT and only available one week per month for spacetrack. The spacetrack throughput from MSSS will only decrease further in 2000. The increase from MOSS is due to two factors. The site was exhausting its tasking list before the end of its shooting period and just revisiting previously attempted satellites with no success. On 7 February 1999, the daily number of tracks tasked by SPADOC was increased from 250 to 400 at the site's request. On 13 April 1999, operational changes were made at the site to improve the scheduling efficiency by adjusting the miss weight so that satellites would not continue to be scheduled after several missed acquisitions.

Figure 2 shows the object response from the deep-space sensors. The GEODSS object throughput went from 35454 to 51289 for a 45 percent increase. The SBV object throughput essentially remained the same for these two time intervals, 22372 and 21363, respectively. The MSSS object throughput went from 28738 to 17866 for a 38 percent decrease. The MOSS object throughput went from 12445 to 22237 for a 79 percent increase.

Figure 3 shows the observation response from the deep-space sensors. The GEODSS observation throughput went from 202545 to 385753 for a 90 percent increase. The SBV observation throughput essentially remained the same, 81734 and 83454, respectively. The MSSS observation throughput went from 157221 to 97994 for a 38 percent decrease. The MOSS observation throughput went from 80668 to 126669 for a 57 percent increase.



**Figure 1. Track Response from the Deep-Space Sensors**



**Figure 2. Object Response from the Deep-Space Sensors**

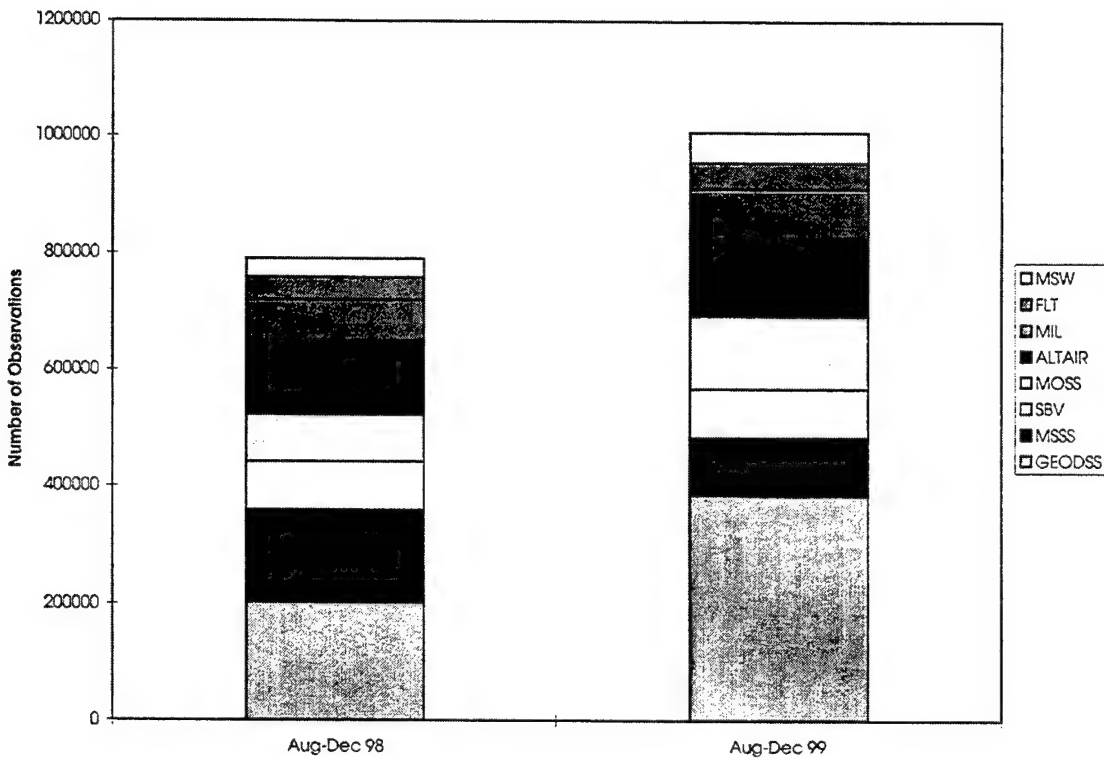


**Figure 3. Observation Response from the Deep-Space Sensors**

From August 1998 through December 1998, the average number of observations per track from the legacy GEODSS system was 5.0. From August 1999 through December 1999, the average number of observations per track from GEODSS under GMP was 3.3, agreeing with the 3-ob tracklet scheduling by the OC3F for most of the objects. For SBV, the average number of observations per track was 3.0 for both time intervals. The most frequently used tasking suffix for SBV by SPADOC is C, which specifies one track of four observations. The frame processing from SBV's signal processor produces two observations from the endpoints of a streak on the focal plane array. It takes two streaks on the same satellite to produce the four observations requested by SPADOC. For half of the satellites tracked by SBV, a second streak is not obtained, thus explaining the average 3.0 observations per track. For MSSS, the average number of observations per track for these two time intervals was 5.3 and 5.0, respectively.

The GEODSS track response over time is shown in Figure 4. An operational assessment of GMP was done in May 1999. The OC3F's conversion of SPADOC tasked tracks to 3-ob tracklets is clearly seen in the increased track throughput. The increased track throughput is seen again in the beginning of August 1999 when GMP became operational. The GEODSS object response over time is shown in Figure 5. The upper curve in Figure 5 is the number of unique objects tasked to the GEODSS system, which has remained fairly constant except for the fall of 1998. The same object may be tasked by SPADOC to multiple GEODSS sites on a given day, and these objects are counted only once. The bottom curve is the number of unique objects tracked by the GEODSS system. If more than one GEODSS site tracks the same object or the same site tracks an object multiple times on a given day, the object is counted only once. The

increase in May 1999 and again in August 1999 is evident in Figure 5, but it is not as significant as the increase in track throughput. Many of the additional tracks (or tracklets) are on the same object in order to satisfy SPADOC's total observation request. The GEODSS observation response over time is shown in Figure 6 with increased throughput under GMP.

The MOSS track response over time is shown in Figure 7. The increase from 250 to 400 tasked tracks by SPADOC on 7 February 1999 is clearly seen in the upper curve with a corresponding increase in track throughput. Since the sensor tasking function in SPADOC uses a maximum track limit as a measure of a site's capacity, the upper curve is a step function that changes when the track limit for a site is updated in the SPADOC database. The site requested an increase from 400 to 600 tasked tracks per day on 23 April 1999. There seems to be no immediate change in the MOSS track response after 23 April 1999. The only effect is to reduce MOSS' percentage track response (number of tracks acquired divided by the number of tasked tracks times 100). A site's percentage response can be very misleading without looking at the absolute response numbers. There is an increase in track throughput beginning in August 1999, which cannot be explained. It appears that MOSS is over tasked at 600 tracks per day and that 500 tracks per day would be more appropriate. There needs to be a balance between providing an optical site with enough tasking so that it does not run out of objects to schedule during its shooting period and not over tasking the site, in which case the percentage response will decrease. In the latter case, objects will not get tracked that could have been tasked by SPADOC to other sites.

The MOSS object response over time is shown in Figure 8. An increase in object throughput is noticeable beginning in February 1999, with a further increase beginning in August 1999. The number of tasked objects per day by SPADOC is not constant because some objects are tasked to a site for multiple tracks. The number of tasked objects will always be less than or equal to the number of tasked tracks.

The MOSS observation response over time is shown in Figure 9. An increase in observation throughput is noticeable beginning in February 1999, with a further increase beginning in August 1999.

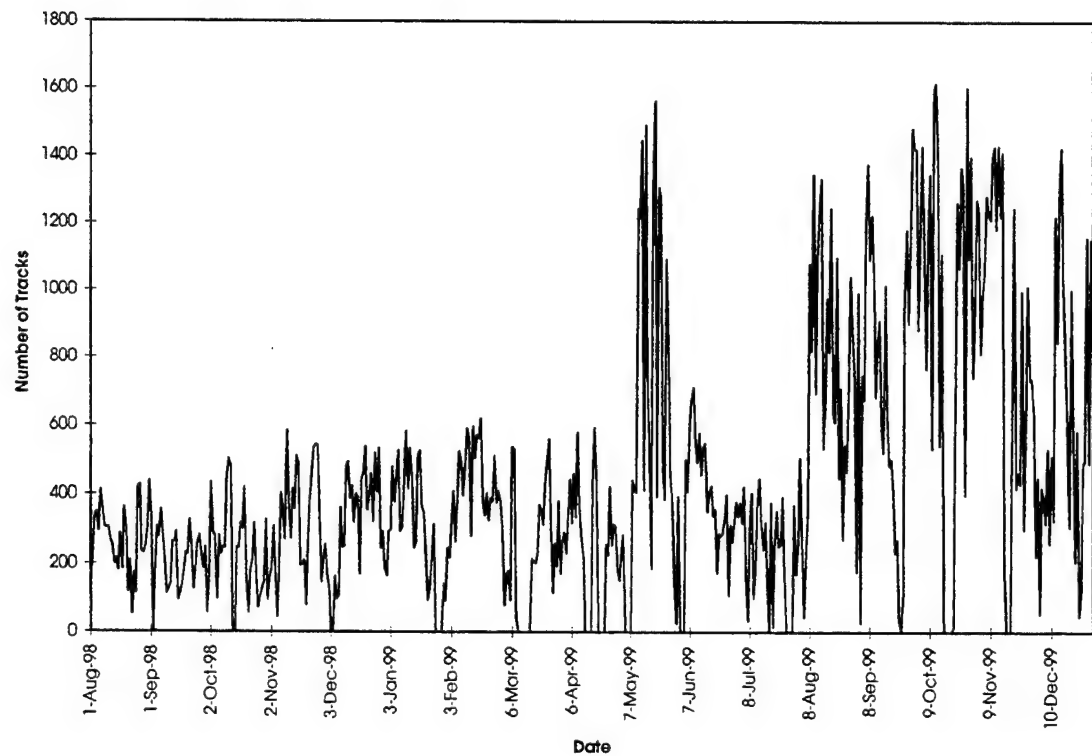


**Figure 4. GEODSS Track Response**

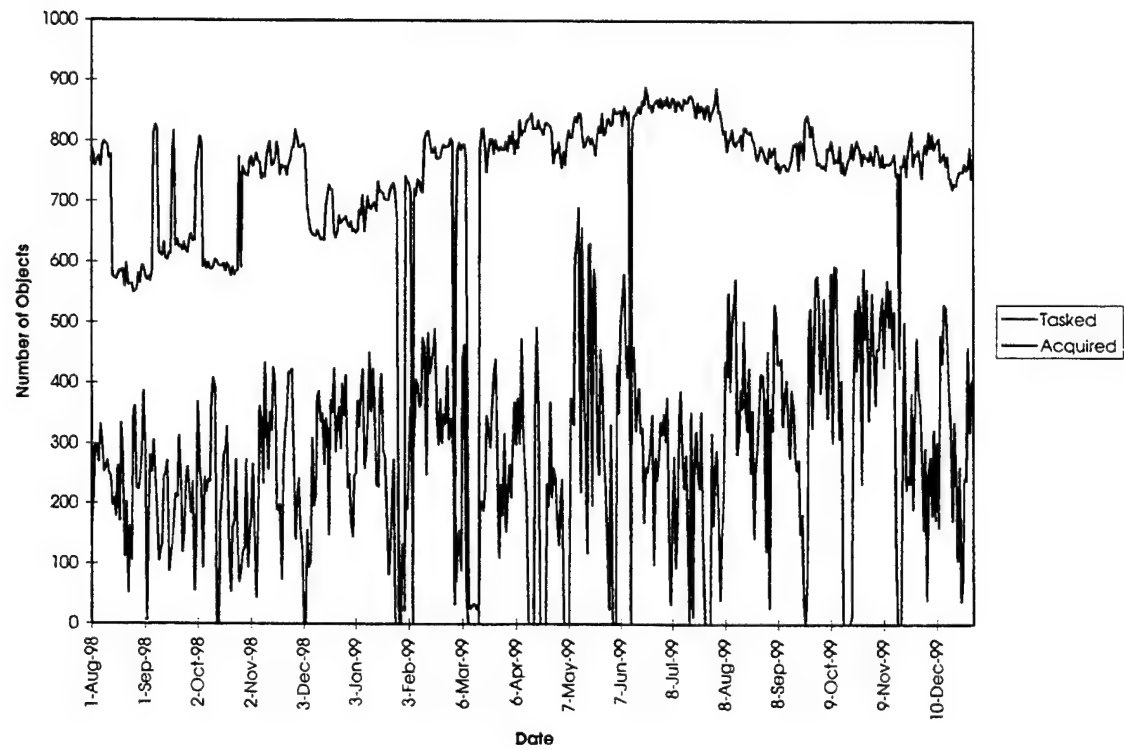


**Figure 5. GEODSS Object Response**

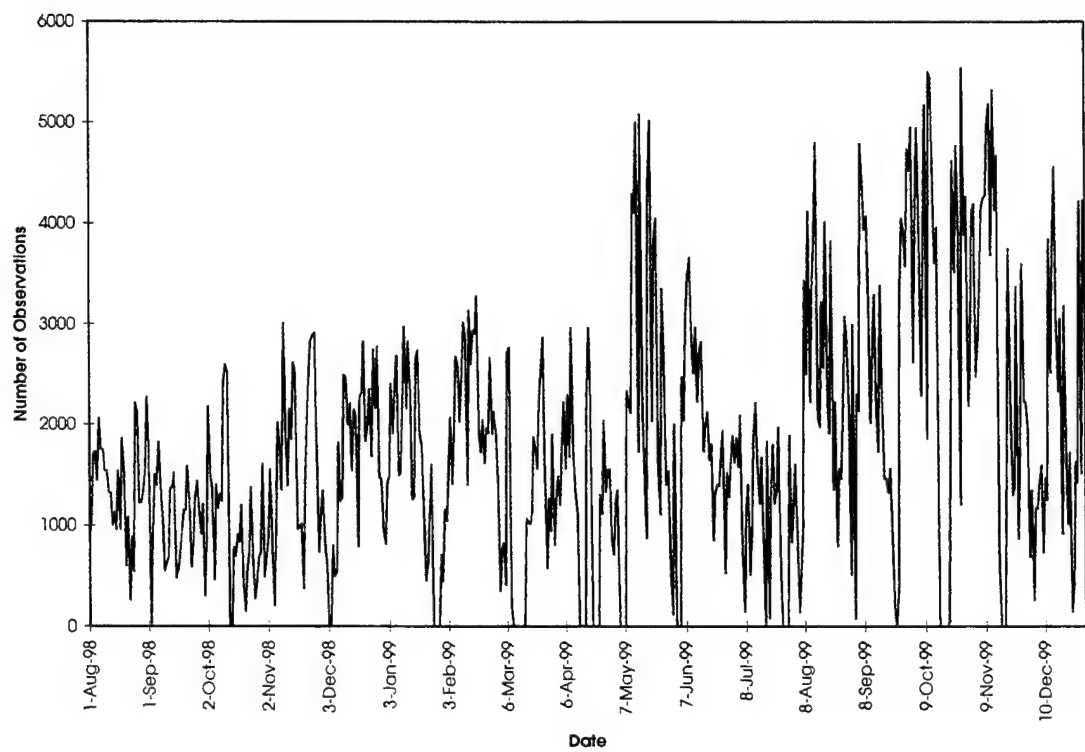


**Figure 6. GEODSS Observation Response**

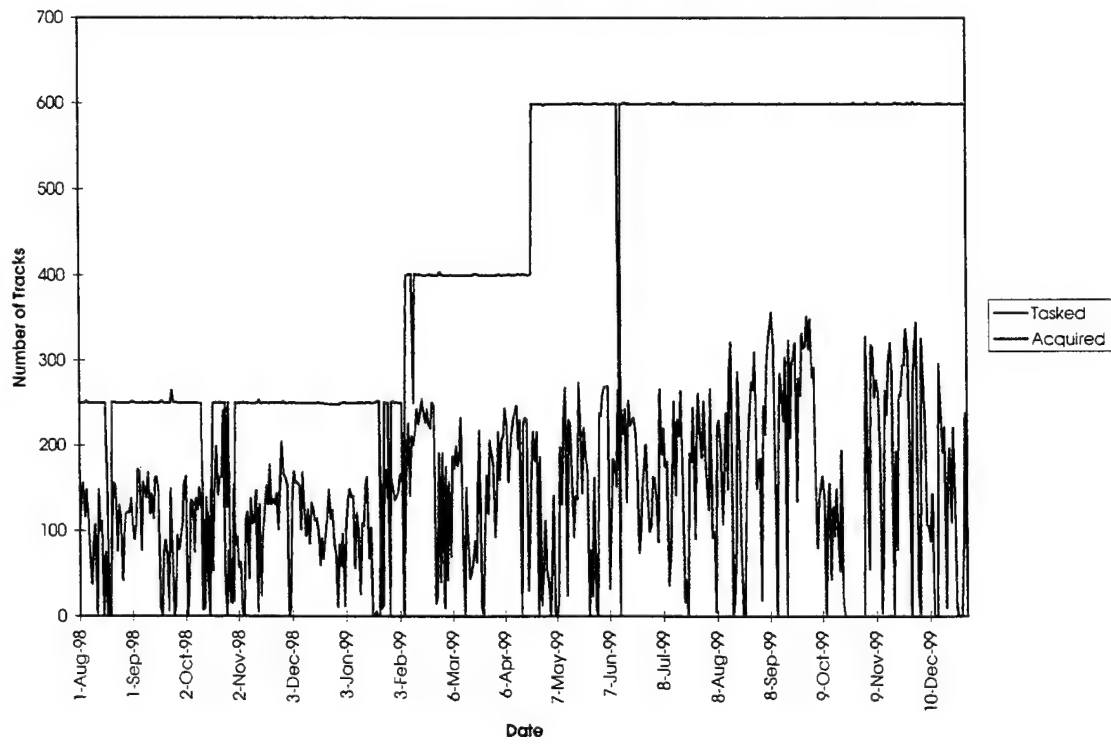


**Figure 7. MOSS Track Response**

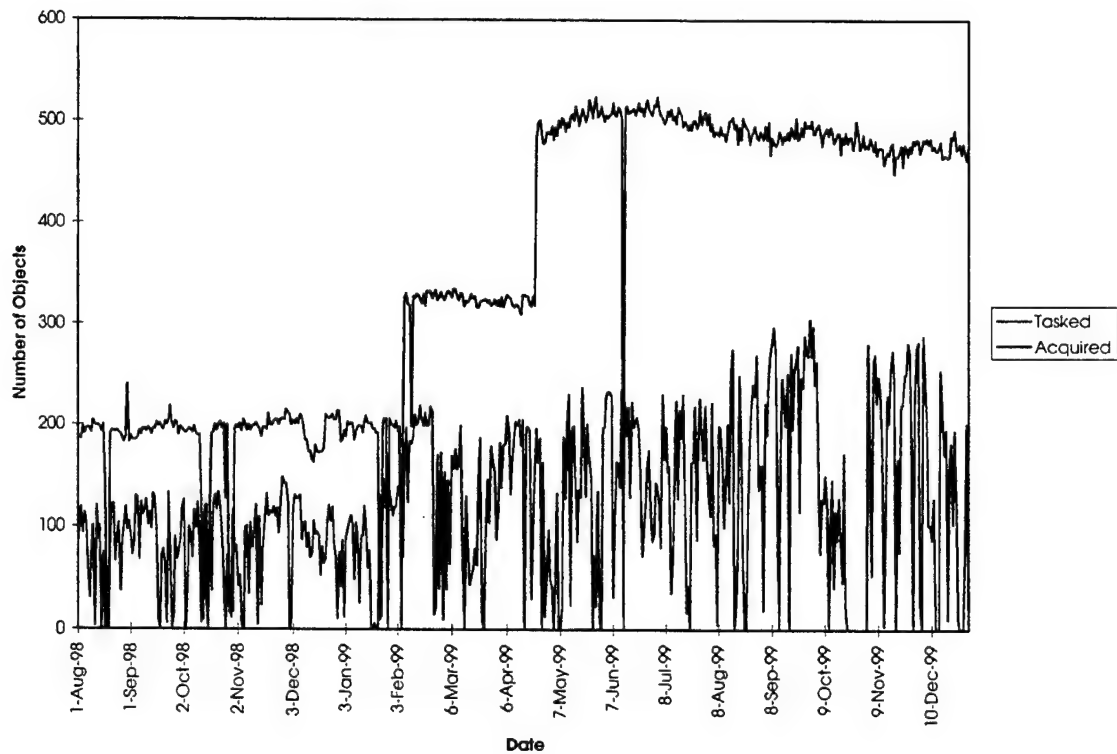


**Figure 8. MOSS Object Response**

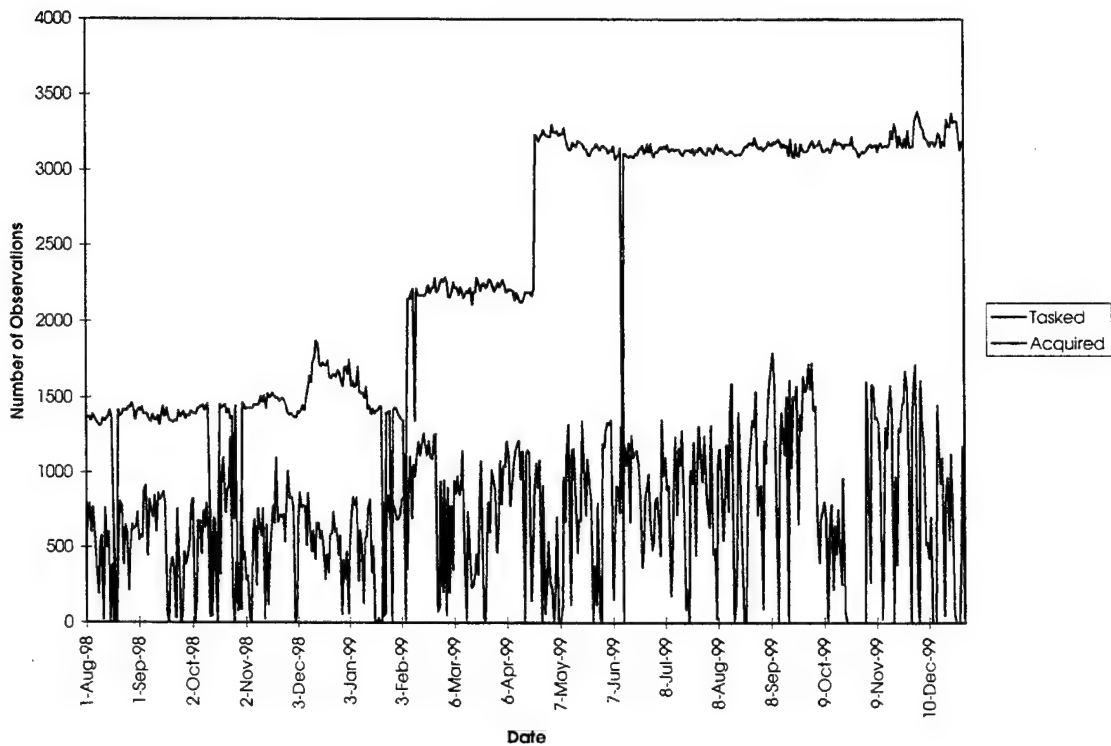


**Figure 9. MOSS Observation Response**

The impact of the increased throughput from GEODSS under GMP and from MOSS on the deep-space satellite catalog is now investigated. Table 1 shows the number of deep-space satellites (period greater than 225 minutes) on 31 December 1999, broken down by cataloged and analyst satellites and by orbit type. The Naval Space Command Fence and the Eglin radar contribute by far the most tracks on deep-space satellites, even though they are near-earth sensors. Most of these "deep-space" tracks from the Fence and Eglin are on satellites in highly eccentric orbits and are obtained near perigee. The impact of GMP and MOSS on the subset of the catalog consisting of all deep-space satellites will be minimal because their tracking data constitutes such a small percentage of the total data.

**Table 1. Number of Deep-Space Satellites on 31 December 1999**

	Deep-Space	Geosynchronous	Deep-Space Other
Cataloged Satellites	1812	736	1076
Analyst Satellites	674	98	576
Total	2486	834	1652

GEODSS provides the most tracking data on geosynchronous satellites. It might be expected that a significant improvement in the GEODSS throughput by GMP would be reflected in the statistics of the geosynchronous satellites. The number of analyst satellites fluctuates daily due to uncorrelated track (UCT) processing. Statistics on the geosynchronous cataloged satellites

will be shown because this subset of the catalog represents known objects and is rather stable over time.

The long-term average epoch age of the geosynchronous cataloged satellites dropped from 5.0 days to 4.2 days after SBV became operational in April 1998 as a contributing sensor to the Space Surveillance Network. Figure 10 shows the daily average epoch age of geosynchronous cataloged satellites, which is around 4.0 days in August 1998. However, the daily average epoch age increased the latter part of 1998 even with the observations from SBV. This increase in average epoch age is strongly correlated with the increase in the geosynchronous work list. The work list consists of satellites whose element set has failed an automatic differential correction (DC) on SPADOC. The epoch age of these satellites is not current, yet there are recent observations in the database that have not been used to update the element set. If human resources are not applied to manually update the element sets of satellites on the work list, the age of the element sets continue to grow older and the work list increases from new failures from the automatic DC process on SPADOC.

The daily average epoch age did drop in early 1999, which is correlated with the drop in the number of satellites on the work list. The increased MOSS throughput beginning in February 1999 may have also contributed to the decrease in average epoch age. The decrease in average epoch age in May 1999 correlates with the operation assessment of GMP. However, there is no decrease in average epoch age beginning in August 1999 when GMP became operational. In fact, there is an increase in average epoch age in November and December 1999, but this appears to be correlated with an increase in the number of satellites on the work list. The impact of the increased throughput of GEODSS under GMP and from MOSS appears to be minimal and can be offset by increases in the work list.

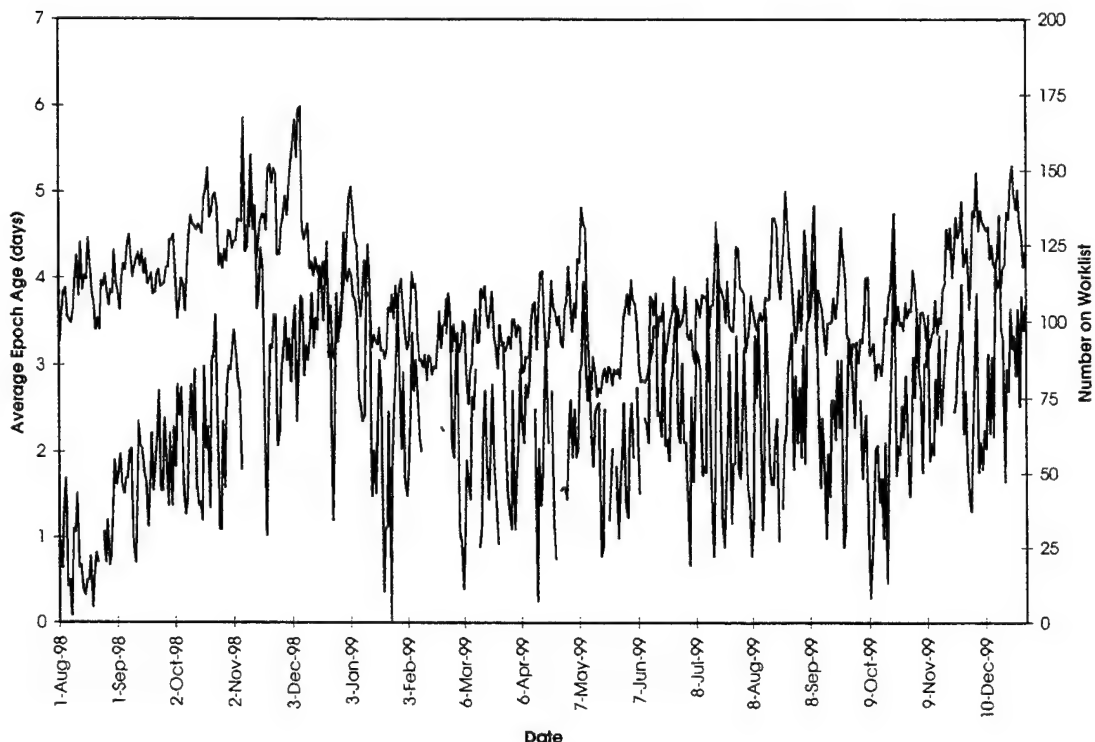


**Figure 10. Average Epoch Age of Geosynchronous Cataloged Satellites**

The increase in object throughput of GEODSS under GMP is not as nearly as large as the increase in the track and observation throughput. An increase in object throughput will have a greater impact on the average epoch age than an increase in track or observation throughput because more satellites will be updated with a current epoch. If all the GEODSS 3-ob tracklets were taken on different satellites, the average epoch age would probably decrease but the SPADOC observation request would not be satisfied as well. More satellites can always be tracked at the expense of providing fewer observations per satellite. SBV has taken the approach of maximizing the object throughput at the expense of not always getting a second streak on the same satellite. GMP maximizes observation throughput by scheduling enough tracklets for each satellite to satisfy SPADOC's request.

The long-term average error growth rate of the geosynchronous cataloged element sets dropped from 10.6 km/day to 9.6 km/day after SBV became operational in April 1998. Figure 11 shows the daily average error growth rate and long-term average of the geosynchronous cataloged satellites. The long-term average dropped from 9.6 km/day to 8.9 km/day after GEODSS with the GMP configuration became operational in August 1999.

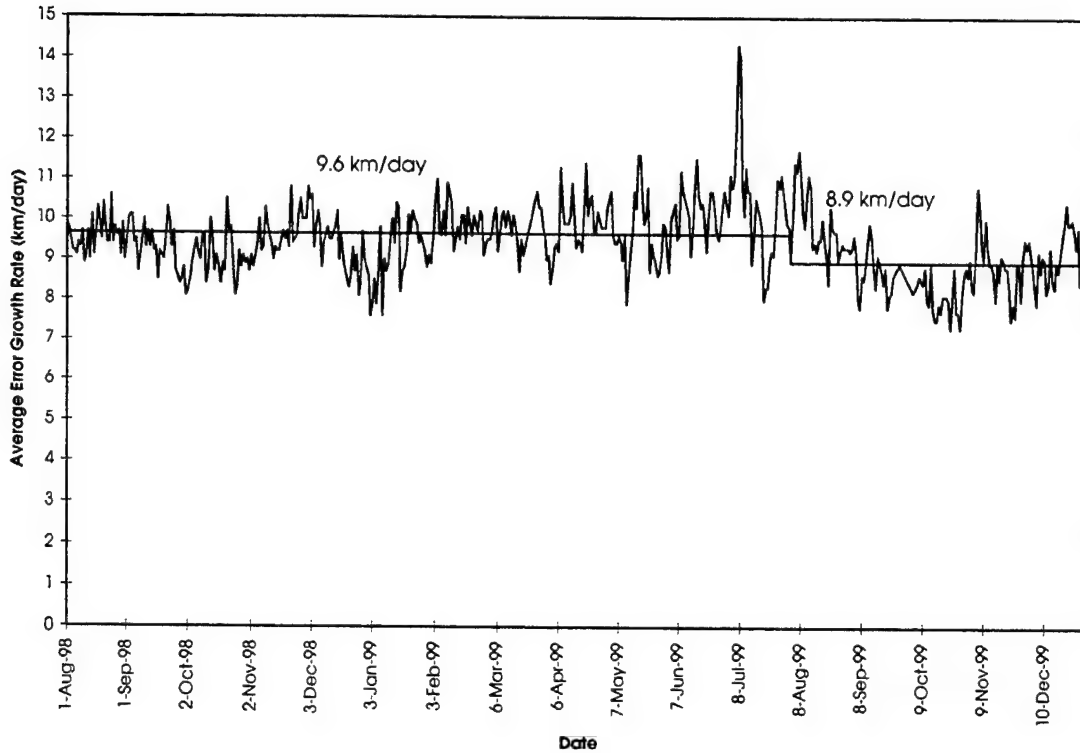


**Figure 11. Average Error Growth Rate of Geosynchronous Cataloged Satellites**

Two reasons may account for this drop in error growth rate. Two 3-ob tracklets spread over time provide better orbit distribution of the observations and should provide a more accurate element set than a 5-ob track taken at one point in the orbit. Also, an observational coordinate system mismatch between GEODSS and SPADOC was corrected in GMP. SPADOC was expecting right ascension and declination to be in topocentric coordinates, and legacy GEODSS was using a heliocentric coordinate system. The computation of aberration is coordinate system dependent, and this coordinate system mismatch for the observational data caused SPADOC to compute a significant bias in right ascension, which was not really present in the site data but an artifact of the coordinate system. Average biases and sigmas for right ascension and declination for each sensor before and after GMP are displayed in Figures 12 and 13, respectively. Note that MOSS and MSX were not changed by GMP, but their biases before and after GMP (3 August 1999) have been included for comparison sake.

Reference orbits for the calibration of the optical deep-space sensors are generated using laser-ranging observations obtained from NASA's Crustal Dynamics Data Information System. Reference orbit fits of centimeter-level root mean square (RMS) are generated for Lageos 1 (SATNO 08820), Lageos 2 (SATNO 22195), Etalon 1 (SATNO 19751), and Etalon 2 (SATNO 20026). Additionally, declassified GPS precise ephemeris files are obtained from the National Imagery and Mapping Agency (NIMA) for GPS satellites 34, 35, and 36 (SATNOs 22779, 22877, and 23027). The deep-space sensors are routinely tasked to track these satellites, and then those observations are compared against the reference orbits. Calibrations are performed using two weeks of sensor observations and calculating the residuals against the reference orbits.

The mean, one sigma standard deviation, and RMS of all the individual observables are computed from the residuals. Where sufficient observational data are available, the results (biases and sigmas) were very consistent.

Note that prior to GMP, the three GEODSS sites display a noticeable bias in right ascension. After GMP the bias has become negligible. Even more significant is the improvement in the right ascension and declination sigmas after GMP. In some cases there is a 400 percent improvement. The third cameras, both on auxiliary GEODSS telescopes at Socorro and Maui, have yet to be replaced by main telescopes and therefore have yet to produce post-GMP data. MOSS has not yet corrected the reference frame in which it provides its data to SPADOC, and thus has not shown the improvement that the post-GMP GEODSS sensors have. A software release at MOSS in the spring of 2000 will correct this problem. MSX has always provided its data in the correct reference frame and thus does not show any biases. Its average sigmas appear to be higher than that of the GEODSS sensors, but this could be due to its low response to calibration tasking. MSX only provides about 10 to 12 observations on the calibration satellites in any two-week period.

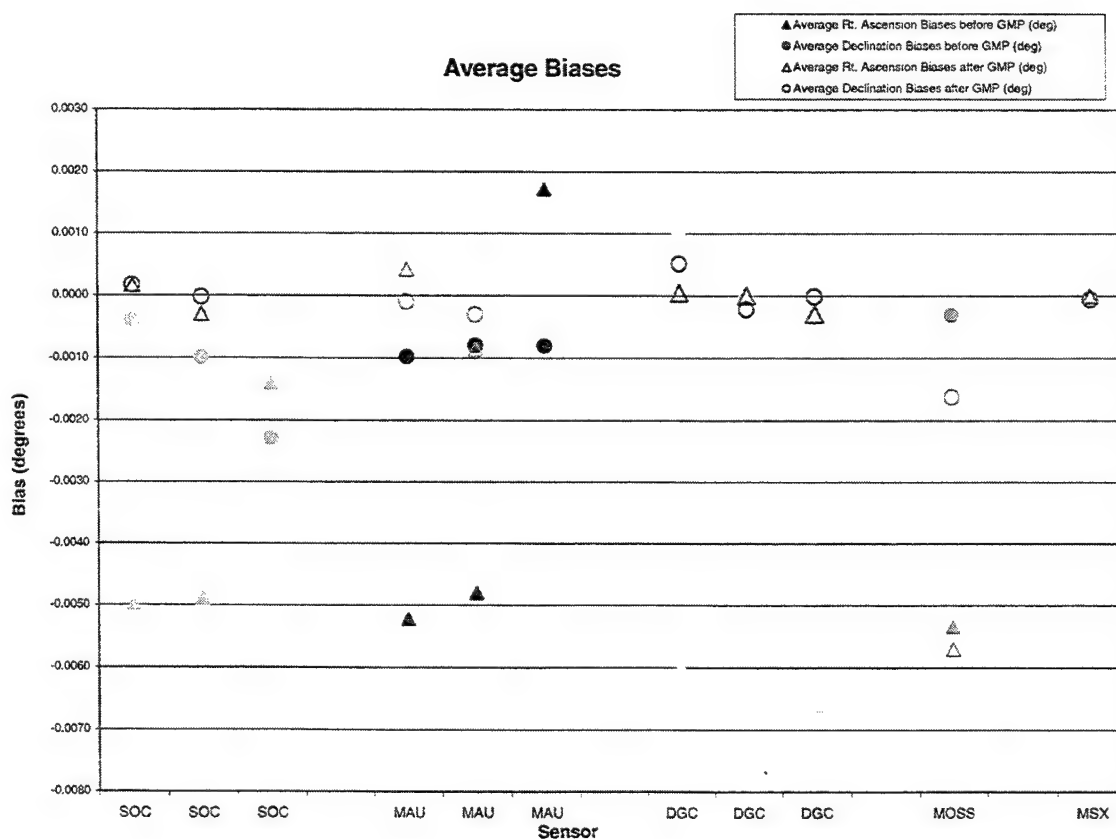


**Figure 12. Average Biases of Optical Sensors**

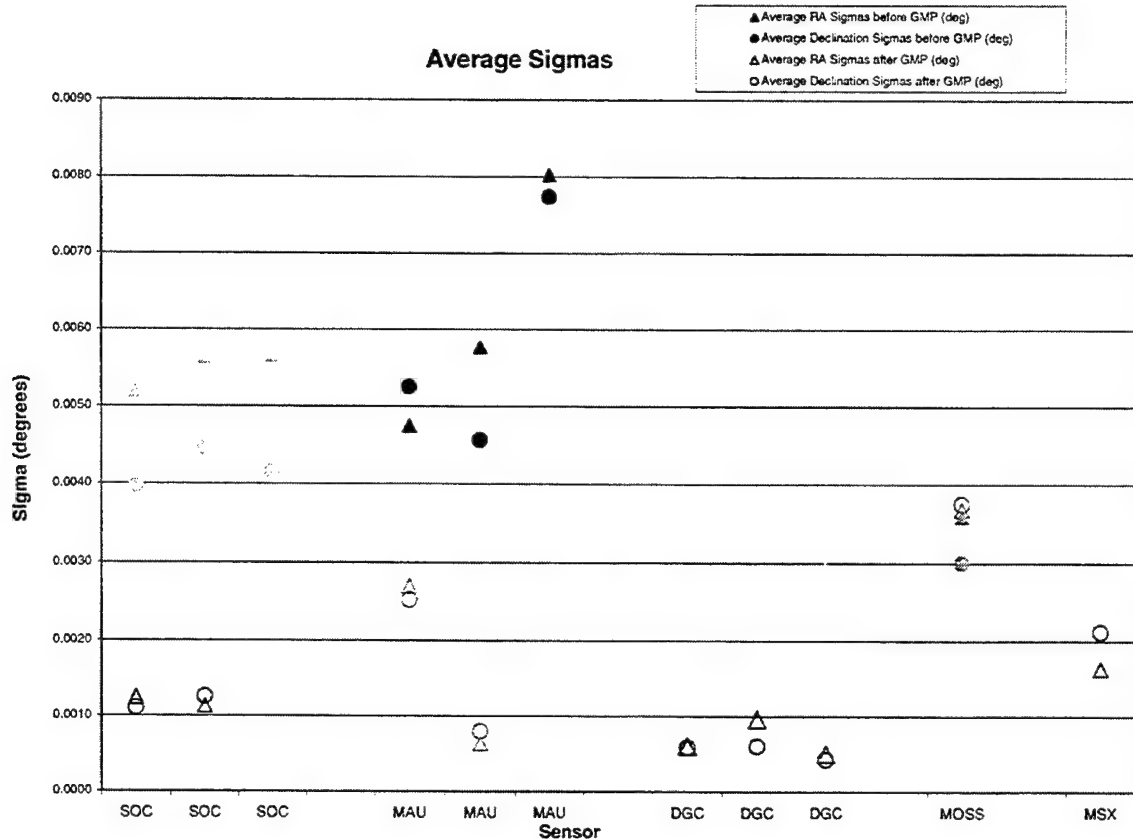


**Figure 13. Average Sigmas of Optical Sensors**

Figure 14 shows the first pass residuals for Camera 1 at Socorro. This is typical of a standard calibration run except that the time scale has been greatly extended beyond the usual 14 days of observations. Notice the drastic improvement in the right ascension and declination residuals after the post-GMP changes beginning 3 August 1999 (day 215).

Although sensor bias can be corrected in satellite orbit determinations, the larger sigmas generally result in a less accurate orbit fit. Thus, the smaller right ascension and declination sigmas of the post-GMP GEODSS are also contributing to a more accurate deep-space satellite catalog.

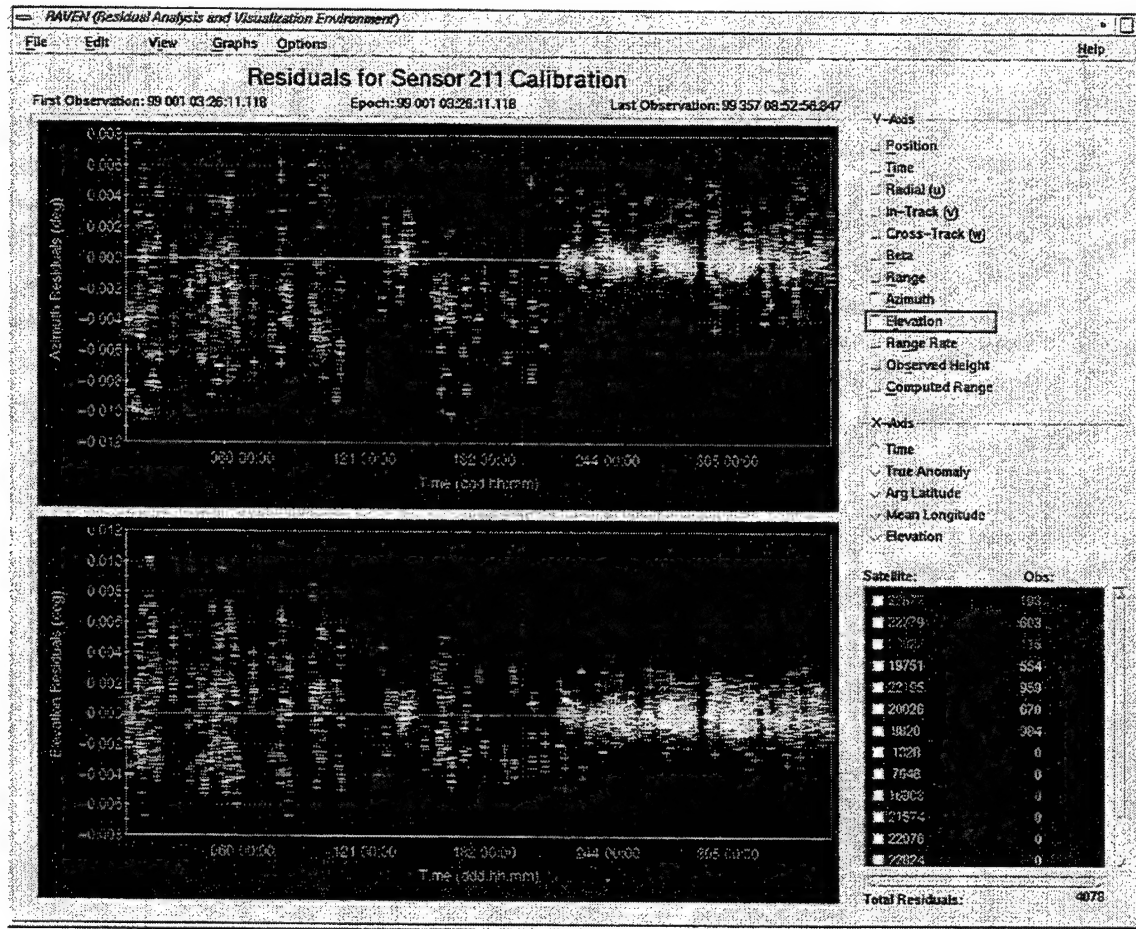


Figure 14. First Pass Residuals for Camera 1 at Socorro

## Geosynchronous Satellite Orbit Pattern: Improvements to SBV Geosynchronous Search

K. S. Capelle, J. Sharma (MIT Lincoln Laboratory)

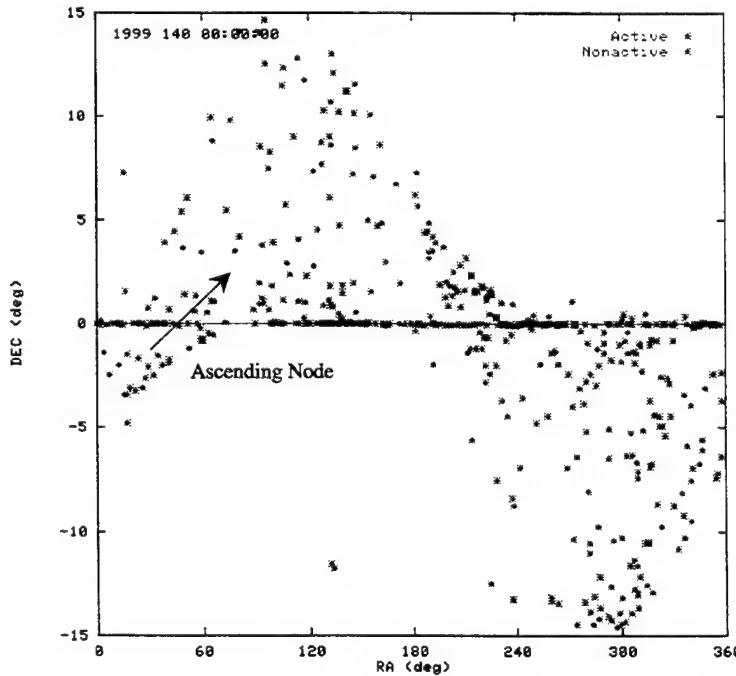
### **Abstract**

Utilizing the wide field-of-view and global coverage of the Space-Based Visible (SBV) space surveillance sensor on the Midcourse Space Experiment (MSX) satellite, an improved approach to space surveillance of the geosynchronous satellite population has been explored. The geosynchronous satellites occupy a narrow region of inclinations and ascending nodes resulting from the exploitation of the natural orbital perturbations by the geosynchronous satellite station-keeping strategies currently employed. By augmenting the current search scheme to take advantage of this structure, SBV's geosynchronous (GEO) search technique can be improved. An understanding of the behavior of this pattern is not only applicable to improving SBV search techniques, but can increase the geosynchronous satellite surveillance efficiency of any space-based or ground-based optical sensor.

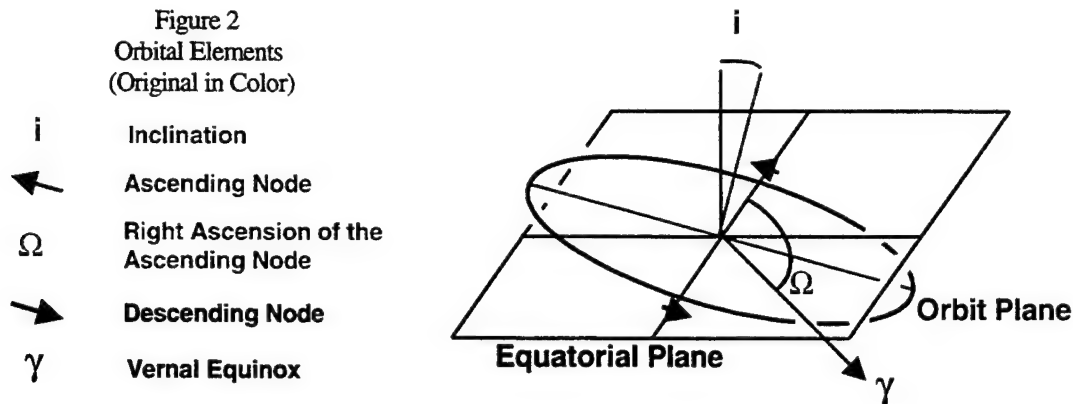
### **1. Introduction**

The general philosophy of geosynchronous orbit station-keeping to maintain small orbit inclinations exploits the luni-solar and geopotential perturbation trends. This practice has introduced a clustering in the ascending nodes of the geosynchronous satellite orbits. The narrow distribution of inclinations and ascending nodes has resulted in the population pattern observed in Figure 1, which portrays the instantaneous location of the approximate 650 geosynchronous objects in orbit around the Earth, with inclinations less than 15° and periods of approximately 24 hours.

Figure 1  
Geosynchronous Object Population in Declination versus Right Ascension  
20 May 1999, 0 UT  
(Original in Color)



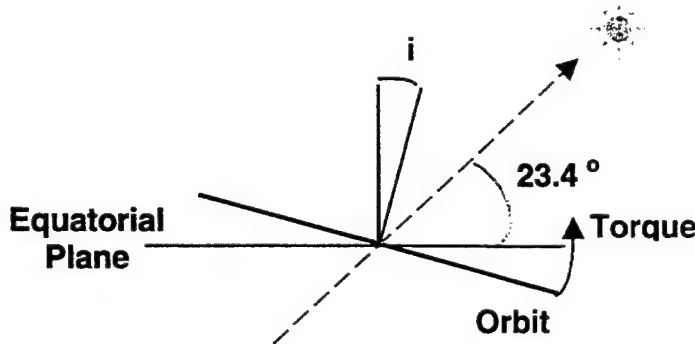
Discussion of the causes of this geosynchronous pattern involve the main orbital elements depicted in Figure 2. In particular, inclination and right ascension of the ascending node are important in this discussion, in which right ascension is measured from the vernal equinox,  $\gamma$ .



### 1.1 Luni-Solar and Geopotential Perturbations

The main factor causing the unique patterned behavior of the geosynchronous satellites is the operational exploitation of the perturbation forces from the sun, the moon, and the oblateness of the Earth. These luni-solar and  $J_2$  geopotential perturbations produce a torque on the orbit plane of a satellite resulting from the net out-of-plane force component acting on the orbiting object. This torque results in the correlated periodic progression of the inclination and ascending node of each geosynchronous object. A diagram of the effect of the sun and moon on an orbit is provided as Figure 3, in which the maximum inclination of the sun during the year is  $23.4^\circ$  and the moon is about  $5^\circ$ . The result is satellite orbital evolution similar to gyroscopic motion with secular precession of the orbital angular momentum vector about the ecliptic pole.<sup>4</sup> The effects are observed as an approximately 53-year periodic correlated variation in the inclination and the ascending node.

Figure 3  
Example of the Luni-Solar Perturbational Torque



## 2. Relationship Between Ascending Node and Inclination

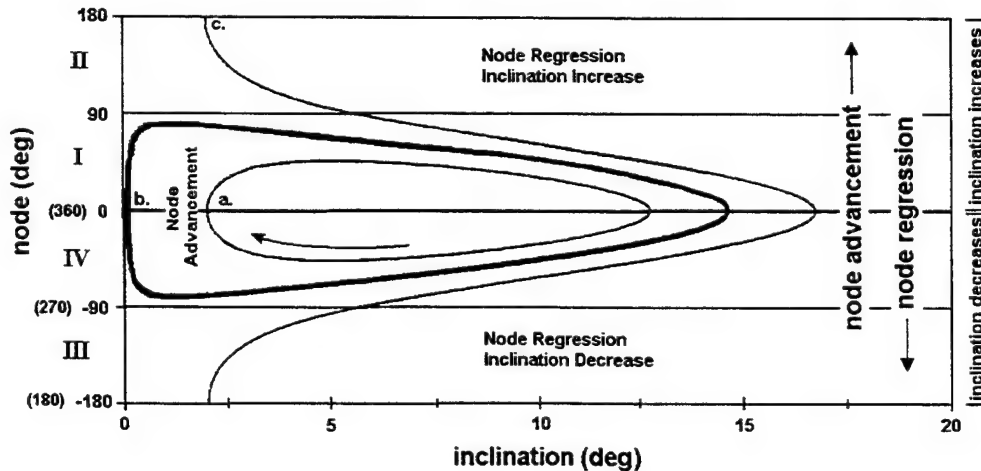
### 2.1 Theoretical Relationship

The equations of orbital motion, which are illustrated in reference 4, reveal the general characteristics of the orbital progression of perturbed geosynchronous objects. In particular, there exists a significant relationship between the inclination and the right ascension of the ascending node, resulting from the perturbational effects on the orbit.

In the upcoming sections, reference is made to quadrants of ascending-node space. These quadrants are clearly labeled in Figure 4 and correspond to degree space as follows: Quadrant I ( $0^\circ$  to  $90^\circ$ ), Quadrant II ( $90^\circ$  to  $180^\circ$ ), Quadrant III ( $180^\circ$  to  $270^\circ$  or  $-180^\circ$  to  $-90^\circ$ ), and Quadrant IV ( $270^\circ$  to  $360^\circ$  or  $-90^\circ$  to  $0^\circ$ ).

The significant relationship between the inclination and right ascension of the ascending node, resulting from perturbational effects on the orbit, can be observed by plotting the right ascension of the ascending node versus inclination, as shown in Figure 4. This results in a distinct clockwise pattern with a 53-year cycle, which has a varying shape depending on the initial conditions and the subsequent trends of the inclination and ascending node. As shown, for an orbit beginning with low inclination in either Quadrants I or IV, an egg or triangular-shaped pattern is created (Figure 4, Curve a or b). In contrast, for an orbit beginning in Quadrants II or III, the pattern is bell-shaped (Figure 4, Curve c).

Figure 4  
Theory Depicting the Progression of the  
Right Ascension of the Ascending Node versus Inclination<sup>4</sup>  
(Patterns dependent on initial conditions of the inclination and ascending node)



Curve a: egg-shaped progression for an orbit with low inclination in nodal Quadrant I or IV  
Curve b: triangular-shaped progression, intermediate situation between case a and c  
Curve c: bell-shaped progression for an orbit in nodal Quadrant II or III

For the egg and triangular-shaped patterns (Figure 4, Curve a or b), it is apparent that the node is advancing between  $270^\circ$  and  $90^\circ$  for the low inclinations in which the minimum inclination occurs at a node of  $0^\circ$ . Regression of the node occurs for the higher inclinations in which a maximum inclination occurs at a node of  $0^\circ$ . In contrast, there is no nodal advancement for the bell-shaped curve (Figure 4, Curve c); the node continually regresses. The maximum inclination achieved is dependent on the minimum inclination and the initial conditions. Another apparent trend is that the inclination increases for ascending nodes in Quadrants I and II, but decreases for ascending nodes in Quadrants III or IV, as shown in Figure 4.

## 2.2 Experimental Support of Theory

### 2.2a History of Inclination and Ascending Node

The graphs of the inclination and the right ascension of the ascending node can be analyzed over time to glean further clarification of their relationship. For the orbit beginning with a low inclination in Quadrants I or IV, the pattern is egg or triangular-shaped (Figure 4, Curve a and b) and the following structure to the histories of the inclination and right ascension of the ascending node is observed. For a typical case without station-keeping, the Soviet Cosmos 1894 SCC# 18443, the histories of inclination and right ascension of the ascending node, as obtained from a database of element sets maintained at MIT Lincoln Laboratory, are portrayed in Figures 5a and 5b. Detailed analysis of the relationship between the inclination and ascending node shows that this experimental data supports the theory depicted in Figure 4, Curves a and b.

Figure 5  
Inclination (a) and Ascending Node (b) Historical Data (SCC# 18443)

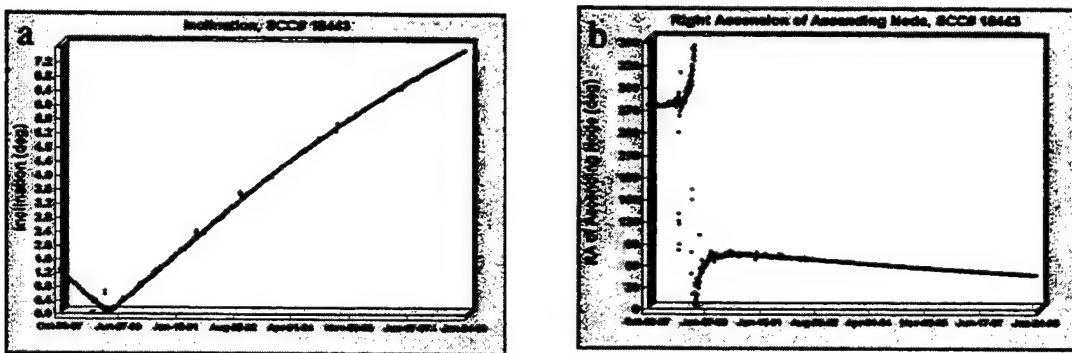
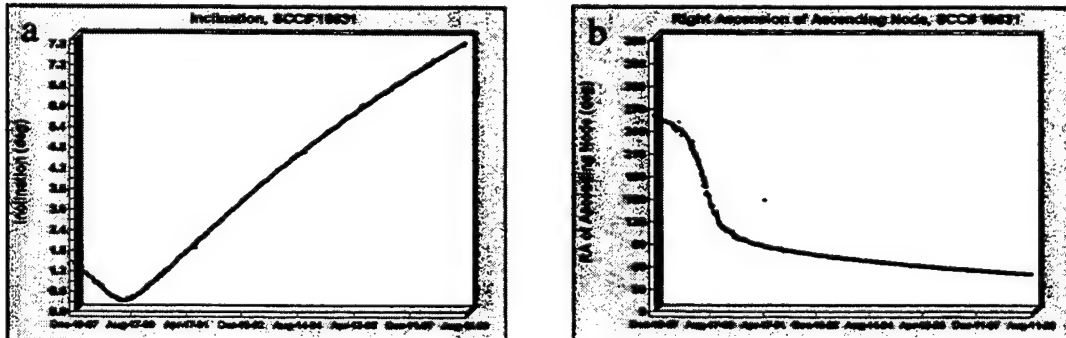


Figure 5a and 5b portray the inclination and ascending node of a geosynchronous satellite with an orbit beginning with a low, decreasing inclination and a node greater than  $270^\circ$  in Quadrant IV. In this situation, the ascending node will advance while the inclination continues to decrease; this agrees with the trend previously encountered in Figure 4 in which the inclination is shown to decrease for nodes in both Quadrants III and IV. For very small inclinations, there is a rapid advancement of the node, as shown in Figure 5b. After the node passes  $0^\circ$ , it continues to advance, but the inclination now increases, agreeing with the theory that the inclination increases for nodes in both Quadrants I and II. Then, as the node approaches  $90^\circ$ , the advancement of the node diminishes and the regression of the node dominates. At this point below  $90^\circ$ , the right ascension of the ascending node of this object's orbit begins and continues to regress about  $3^\circ$  per year.

The case in which the ascending node versus inclination curve is egg or triangular-shaped agrees with the theory. Another aspect of the phenomena to explore is the other extreme in which the graph of the ascending node versus inclination is bell-shaped (Figure 4, Curve c). By initiating the orbit's ascending node in Quadrants II or III, the bell-shaped pattern of the ascending node versus inclination arises. In this situation, the regression of the node dominates; again, the inclination increases in Quadrants I and II and decreases in III and IV, in agreement with the theory. The reader is referred to Figures 6a and 6b, in which the histories of the inclination and right ascension of the ascending node for Soviet Raduga 21, SCC# 18631, are portrayed.

Figure 6  
Inclination (a) and Ascending Node (b) Historical Data (SCC# 18631)



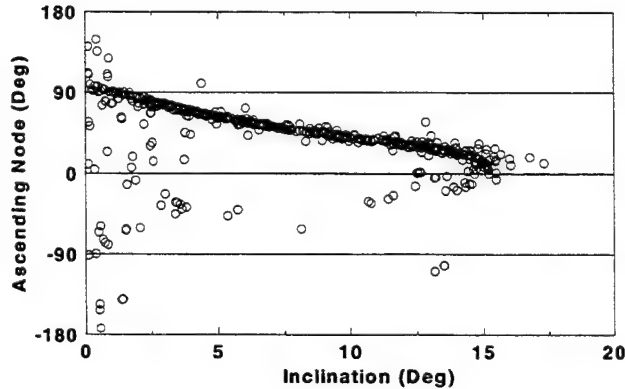
In Figures 5 and 6, no station-keeping maneuvers are performed; the satellites were launched at a few degrees inclination to take advantage of the decreasing inclination trend. The inclination, while continuing to follow the perturbational cycle, remained low enough during the satellite's operational lifetime without the need for station-keeping. For certain satellite applications, more precise orbits are required involving station-keeping as frequent as every couple weeks to maintain inclination under a couple tenths of a degree.

By examining Figure 4 and the previously discussed inclination plots, it becomes apparent that the inclination decreases lowest in the triangular pattern. In order to maintain near-zero inclinations, satellites are therefore launched and undergo station-keeping maneuvers to force the satellite's orbit into the triangular-shaped situation, as seen in the base of the pattern shown in Figure 4. This is accomplished, as depicted in Figures 5a and 5b, by initializing the orbit with the right ascension of the ascending node in the fourth quadrant, operationally, at about 280°. This practice takes advantage of the maximum effects of the perturbations, driving the inclination down, resulting in the progression of the ascending node and inclination following the triangular-shaped pattern. To maintain low inclinations, station-keeping maneuvers are performed to reinitiate this portion of the cycle whenever the inclination enters the increasing inclination cycle and begins to exceed the acceptable limits.

## 2.2b Relationship between Ascending Node and Inclination

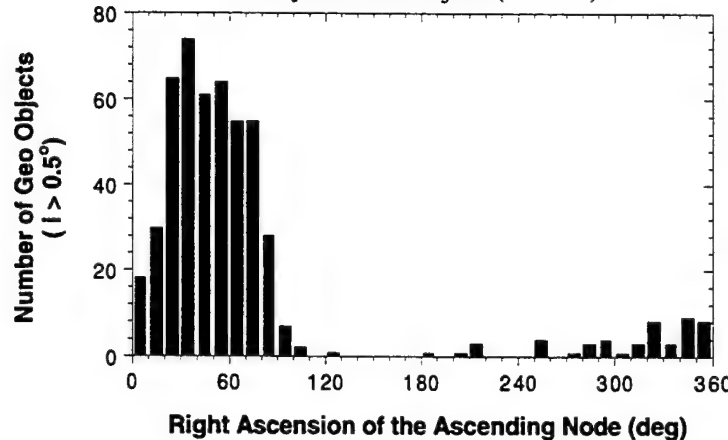
Over thirty years have elapsed since the first satellites were launched into geosynchronous orbit. There are approximately 650 geosynchronous objects currently in near-circular orbits. As seen in Figure 7, we can begin to see the structure of the geosynchronous population following the trend portrayed in Figure 4. Over time, each satellite will continue clockwise, following the pattern depicted in Figure 4, returning to the start in approximately 53 years. Because geosynchronous satellites have only been launched into Earth's orbit for about thirty years, the satellites have evolved, at most, a little greater than about half-way through the perturbational cycle; half of the pattern of Figure 4 can be observed in Figure 7. It is apparent that the experimental data supports the theoretical predictions for the progression of the ascending node and the inclination.

Figure 7  
Experimental Data of the Ascending Node vs. Inclination for  
Geosynchronous Objects where  $i > 0.5^\circ$



Of particular interest, the main-belt objects are following the trend of ascending node versus inclination observed in Figure 4, Curve c, and result in a clustering of the ascending nodes of the geosynchronous objects between 0° and 90° right ascension. This observation is further supported by the results shown in Figure 8 which depicts a histogram of right ascension of the ascending nodes for geosynchronous objects with inclinations greater than 0.5°. Geosynchronous objects with inclinations less than 0.5° are removed from the histogram because they are predominantly station-kept satellites which are maneuvered frequently. Furthermore, the right ascension of the ascending node becomes ill-defined as the inclination becomes near-zero and proves difficult to accurately estimate using Space Surveillance Network data.

**Figure 8**  
**Histogram of the Right Ascension of the Ascending Nodes for  
 Geosynchronous Objects ( $i > 0.5^\circ$ )**



Currently, this clustering of ascending nodes between  $0^\circ$  and  $90^\circ$  right ascension is static producing the pattern of the geosynchronous objects in right ascension and declination, as seen in Figure 1. Because of the relationship between right ascension and longitude in time, this pattern translates to the similar structure in latitude versus longitude. However, in this case the equatorial crossings progress in time with an approximate 24-hour period; details of this structure will be discussed in detail, later.

As the cycle of ascending node versus inclination continues to progress, more and more objects will enter the second half of the cycle, shown in Figure 4, augmenting the structure of the geosynchronous population pattern over time. Assuming geosynchronous objects are predominantly in orbits following the triangular-shaped pattern as shown in Figure 4, then eventually these objects will populate the orbit space with ascending nodes from  $270^\circ$  to  $90^\circ$  and will result in a blurring of the population pattern.

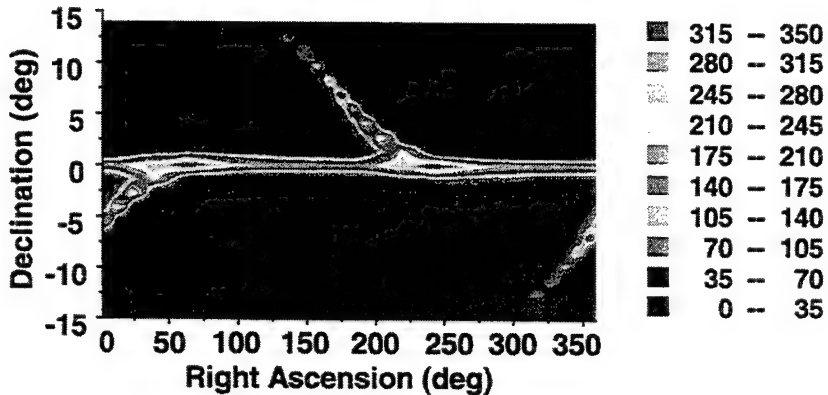
In addition, the oldest drifting geosynchronous objects currently have relatively large inclinations with respect to the operational geostationary satellites, but analysis indicates that in 20-30 years some of the older drifting geosynchronous objects near the end of the 53-year perturbational cycle will begin reaching near-zero inclination orbits again. Currently, the higher inclination drifting objects pass through the geosynchronous belt twice per orbit, at the ascending and descending nodes. Once the drifters return to low inclination and reenter the equatorial belt, they will become a greater hazard to operational satellites due to the increase in the statistically low collision probability.

### 3. Geosynchronous Satellite Population Pattern

#### 3.1 Declination versus Right Ascension

In the right ascension and declination inertial space coordinates, the geosynchronous satellite nodal regions are essentially fixed in time as shown in Figure 9, which is essentially a 2D histogram portraying the distinct-object density over a 24-hour period. The contours indicate the number of distinct objects passing through a  $1.4^\circ \times 1.4^\circ$  region of inertial space over a 24 hour period. The relevance of  $1.4^\circ$  relates to the dimension of the SBV CCD focal plane. The highest density regions are centered at  $0^\circ$  declination at approximately  $65^\circ$  and  $245^\circ$ , the clustering of the ascending and descending nodes of the geosynchronous orbits, respectively. In addition, there are distinct high-density regions extending above and below the belt, from which the population extends in a confined sinusoidal region. While the structure of the population remains wholly unchanged, each geosynchronous object progresses left to right along a sinusoidal trajectory through the prominent population region as shown in Figure 10. The main reason for this distribution is the cluster of geosynchronous orbit ascending nodes between  $0^\circ$  and  $90^\circ$  right ascension, as shown in Figure 8.

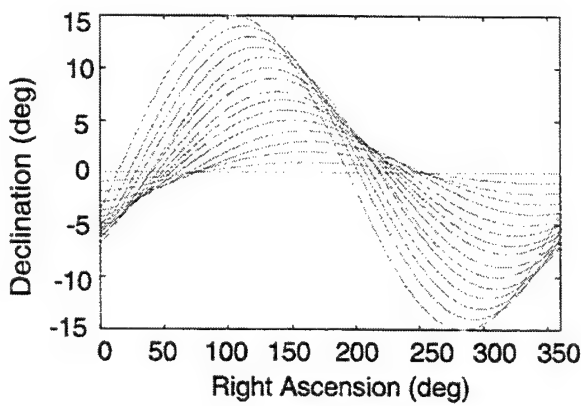
Figure 9  
Distinct Satellite Object Density: May 20, 1999  
(Original in Color)



As can be observed in Figure 9, there exists a relatively high-density population of objects along 0° declination. This consists of approximately 200, out of the approximate 650 represented geosynchronous object population, that are station-kept, active geosynchronous satellites maintained at 0° declination. As previously mentioned, there exists higher density nodal regions centered at approximately 65° and 245° right ascension and 0° declination. These are a result of higher inclination objects passing through the population of active geostationary satellites.

Away from the near-zero inclination population, an additional clustering of objects is observed above and below the belt. In particular, to the left of the nodal regions, there are observable increases in density extending from the equatorial plane. This structure can easily be explained by comparing Figure 9 with Figure 10, which depicts the sinusoidal orbit tracks of fifteen geosynchronous objects where each object moves along the orbit trajectory from left to right. These higher inclination objects have periods of approximately 24 hours, but are slightly offset at their nodal crossings. This slight dispersion of the sinusoidal waves results in the higher densities, shown in Figure 10, extending above and below the belt.

Figure 10  
Orbit Traces of 15 Geosynchronous Objects with Varying Inclinations

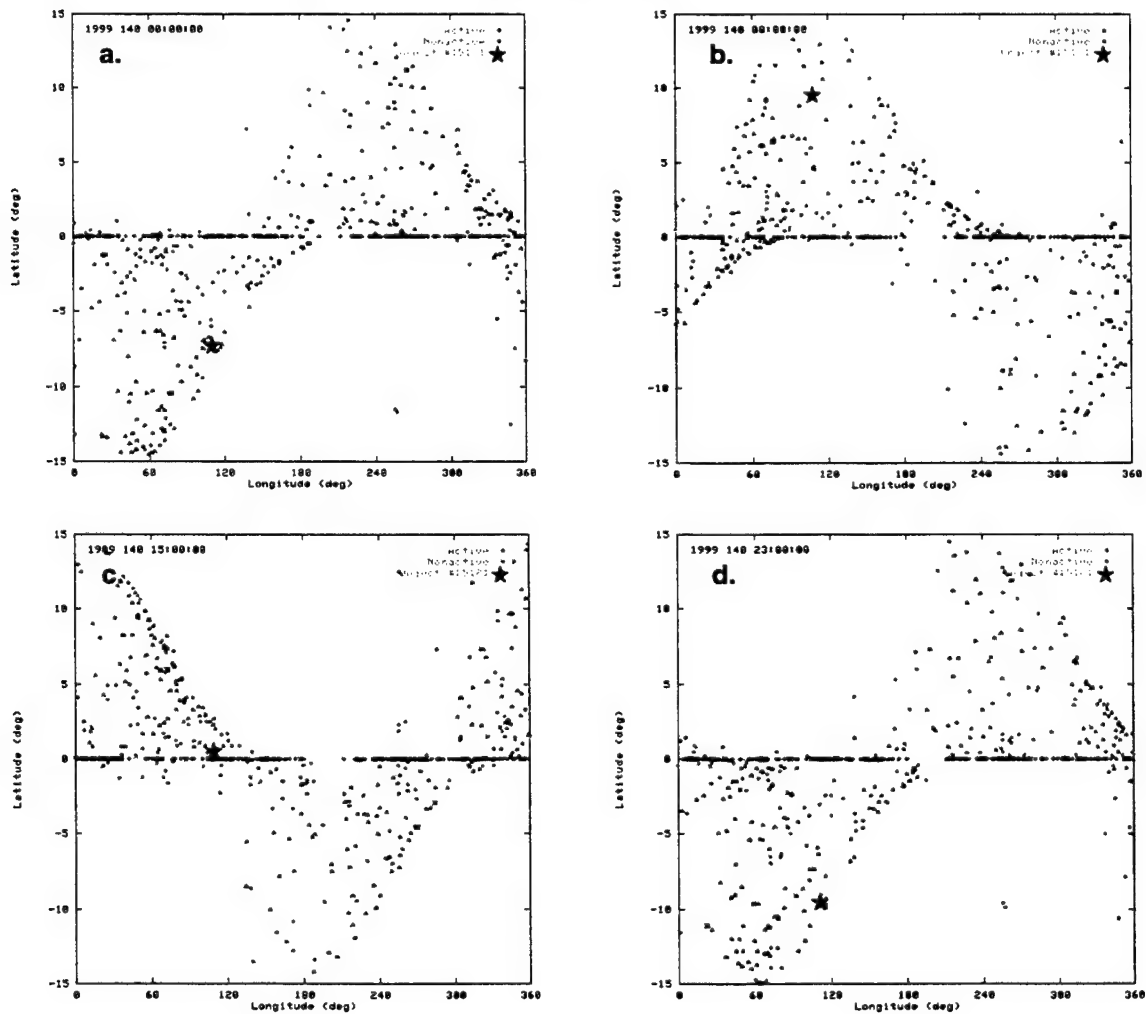


At each nodal crossing, approximately 315 to 350 objects cross over a given 24 hours. Given that the geosynchronous catalog has approximately 650 objects, this is about half of the geosynchronous population. Thus, in a given 1.4° x 1.4° CCD field located at the center of the nodal crossing, about half of the geosynchronous catalog could be observed daily where 1.4° relates to the dimension of the SBV CCD focal plane. Of course, this is extremely inefficient, but offers a limit to what can be accomplished.

### 3.2 Latitude versus Longitude

In contrast to the sinusoidal object motion in declination versus right ascension space, geosynchronous objects move vertically with respect to latitude versus longitude, mapping out a narrow figure-eight pattern due to orbit perturbations. Because of the scale in the Figures below, the drift motion in longitude is not noticeable, resulting in only apparent vertical motion as shown by the highlighted satellite SCC# 15181, Gorizont 10. As opposed to the static nodal regions in declination versus right ascension space which occur at approximately 65° and 245° right ascension and 0° declination, the location of the equatorial crossing of the geosynchronous orbits in latitude versus longitude space is dynamic. The structure of the population in geographic coordinates moves in time due to the relationship between longitude and right ascension resulting from the rotation of the Earth. This is shown in Figure 11, depicting the progression of the geosynchronous satellite population in latitude versus longitude. Each plot is labeled by the year, day of year, and the Universal Time (UT) hour:minute:second. The population pattern and the equatorial plane crossings move in longitude with a period of approximately 24 hours; the motion of the pattern is right to left over time as shown in Figure 11.

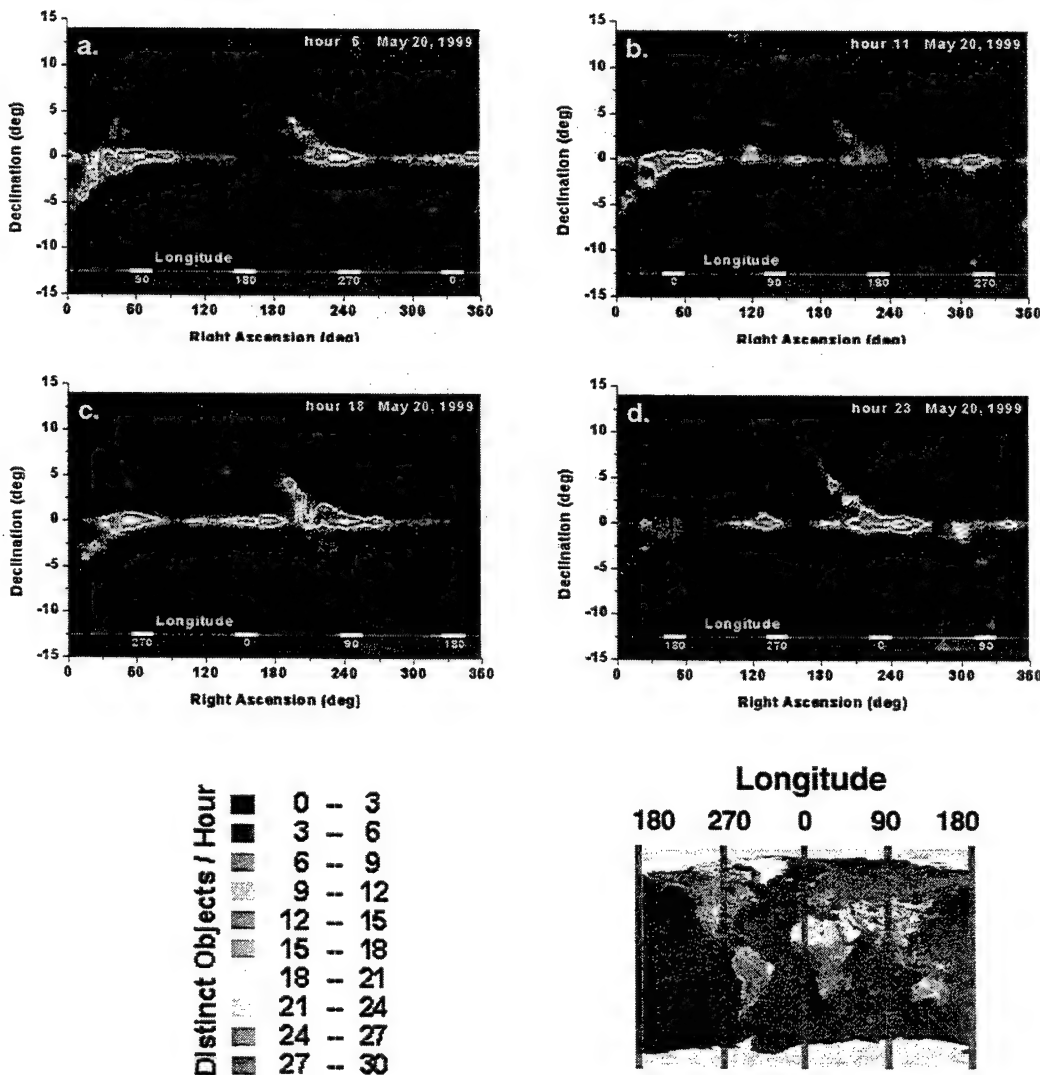
Figure 11  
Progression of the Geosynchronous Satellite Population in Latitude versus Longitude  
(Original in Color)



#### 4. Space-Based Visible (SBV) Space Surveillance Applications

The goal of the investigation into the geosynchronous population was to propose possible changes in the way the SBV geosynchronous search is conducted. To investigate the benefit of taking advantage of the geosynchronous satellite population pattern, a movie of the populations' progression was created and studied. Four frames of the 24-hour movie, each an hour long integration of the geosynchronous population on 20 May 1999, are portrayed as Figure 12. Also included is a legend depicting the density, in distinct objects per hour, and a map depicting the longitude coordinates of the Earth. In particular, the longitudinal location of the following regions of interest are  $0^{\circ}$  -  $90^{\circ}$  Europe,  $180^{\circ}$  Pacific,  $270^{\circ}$  North America.

Figure 12  
Geosynchronous Hourly Population Density  
(Original in Color)



As can be observed in Figure 12, a maximum of about 30 distinct objects per hour pass by the most densely populated areas of the geosynchronous belt at approximately  $65^{\circ}$  and  $245^{\circ}$  right ascension and  $0^{\circ}$  declination. This is a result of the intersection of the high inclination geosynchronous belt objects and the large population of active satellites near North America and Europe. These contour plots indicate that centering the  $1.4^{\circ} \times 1.4^{\circ}$  CCD and collecting data at the highly dense nodal regions could result in a maximum of this many distinct correlations per hour. Additional unexpected observations could be made because it is also possible that conjunctions with low altitude or deep space objects could further increase the number of objects detected. Currently, SBV performs search operations by centering the four  $1.4^{\circ} \times 1.4^{\circ}$  CCDs along the geosynchronous belt and taking data in sequence at a rate of about  $50^{\circ}$  longitude per hour; primarily, SBV search concentrates on  $0^{\circ}$  to  $90^{\circ}$  longitude with no weight currently given to the nodal regions.

#### 4.1 SBV Event Timing

Firstly, the timing of the SBV events was explored to determine how well the events coincide with the natural variations in the geosynchronous population. The current SBV events are both 4 hours each. The first begins at approximately 0:30 hours UT, and the second begins at approximately 16 hours UT. From the comparison of the movie of the progression of the geosynchronous population density, it is apparent that the SBV event timing does not take advantage of natural population density maxima.

The first aspect of the geosynchronous population to be explored was the large fluctuations in density along  $0^{\circ}$  declination. At approximately  $270^{\circ}$  east longitude there exists a large satellite population serving the United States, Canada, and South America. As observed in Figure 12, this region coincides with the first node, approximately  $65^{\circ}$  right ascension, at 18 UT and the second, approximately  $245^{\circ}$ , at 6 UT as shown in the frames provided as Figure 12. In addition, in the region just above  $0^{\circ}$  east longitude there exists the large European satellite population; this is not only a highly dense satellite population, but also frequently involves maneuvered satellites for which it is important to maintain accurate observations. This region of satellites coincides with the first node near 11 UT and the second node at around 23 UT.

Next, the SBV event times and the associated geosynchronous population density were explored to ascertain whether the current event times were taking advantage of the natural population fluctuations. During the first SBV event from hour 0:30 to 4:30 UT on May 20, 1999, the following regions coincide with the higher density nodal crossings. The first node at approximately  $65^{\circ}$  occurs when the longitude corresponds to Russia, China, and the Western Pacific. The second node, at approximately  $245^{\circ}$ , coincides with the Atlantic Ocean; the high-density region above  $0^{\circ}$  east longitude has just passed and the American cluster has not reached it yet. From hour 16 to 20 UT, the first node does have a modest coincidence with the American satellite clusters during this event, but more desirable would be to search during the conjunction of the European satellite cluster with the nodal crossings. In addition, the second node occurs when the longitude corresponds with Russia, but the event ends just before the highest density region over mid and western Europe crosses the node.

The conclusion is that, currently, the event timings are poor, we are not directly exploiting the natural fluctuations of the geosynchronous satellite population in our current search program. One approach that increases the effectiveness of SBV during search is by searching the most dense nodal crossing regions when either the satellite cluster over Europe or the North America passes through the nodal regions. In particular, the times when sparse regions such as when the population over the Pacific coincides with the nodal crossings, should be avoided.

It would seem that the event times could easily be manipulated to concentrate on the times when the nodal regions coincide with  $0^{\circ}$ - $90^{\circ}$  or  $270^{\circ}$  east longitude, thus solving the geosynchronous search problems. However, moving the event windows to overlay the peak density of the nodal crossing is far more involved due to additional factors that need to be considered. These include the time dependence of this pattern over the year and the specifics about the distribution of the highly dense population regions as well as their effect on the current search scheme.

## 4.2 Time-Dependent Accessibility

As a space-based sensor, the observations made by SBV are strongly dependent on the position of the SBV sensor, the sun, and the object to be viewed. Optimally, the phase angle, which is the angle between the sun, the object, and the SBV sensor, should be less than  $60^\circ$  so that the objects are well illuminated by the sun. If the moon is assumed to be the target object,  $0^\circ$  phase angle corresponds to the full moon, while  $180^\circ$  phase angle corresponds to the new moon. To avoid damaging the SBV sensor and the MSX spacecraft, high phase angles are not allowed; the spacecraft cannot point to within  $40^\circ$  of the sun.

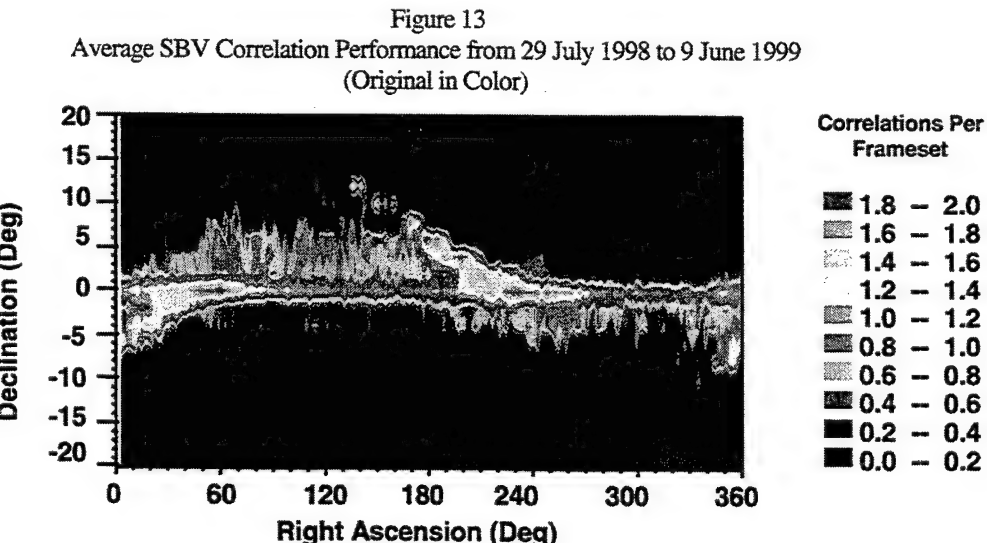
The orbit of the Earth about the sun causes the right ascension of the sun to change slowly, less than a degree per day, while the declination fluctuates between approximately plus or minus  $23.4^\circ$ , depending on the time of year. Because of the phase angle requirement, it follows that only the portion of the right ascension and declination sky opposite the sun can be optimally viewed for certain times of the year. Fortunately, the geosynchronous objects stream through right ascension once a day, but in contrast, viewing the nodes is limited because they are essentially constant in right ascension and time. Thus, one node is observable for one half of the year, and the other node is observable for the other half of the year; observing at either nodal region is poor every 6 months during the sun's transition halfway between the nodal regions corresponding to  $90^\circ$  phase angles.

## 4.3 Distribution in the Ascending Node

Another issue related to searching the nodal regions is that the ascending nodes are dependent on inclination as shown in Figure 10. This poses problems with creating a leak-proof fence for all inclinations because the range of nodal crossings is actually quite broad, spanning almost  $90^\circ$ . Thus, the search of the geosynchronous objects cannot just be focused at one specific small region in space along the equatorial plane because the entire population cannot be accommodated. In order to more successfully accommodate the search of the high inclination objects, as well as the low inclination objects, the search scheme will have to involve a substantial search region.

## 4.4 Motivation

Despite occasional limitations, concentrating on the high-density regions can help to improve the geosynchronous search algorithm. This is supported by the results in Figure 13, which portray the average performance of SBV; the correlations per discrete frameset were averaged over inertial space coordinates, declination and right ascension, over the time period from 29 July 1998 to 9 June 1999. More correlations are observed in the regions coinciding with the higher density of geosynchronous objects. Thus, the structure of the geosynchronous pattern is operationally observed despite the fact that this plot is obtained from both search and tasking data which did not involve optimization of the geosynchronous population structure. Therefore, by implementing a new search strategy to take advantage of the geometry of the geosynchronous population, it is expected that further improvement to search productivity and efficiency can be obtained.



#### 4.5 Search Options

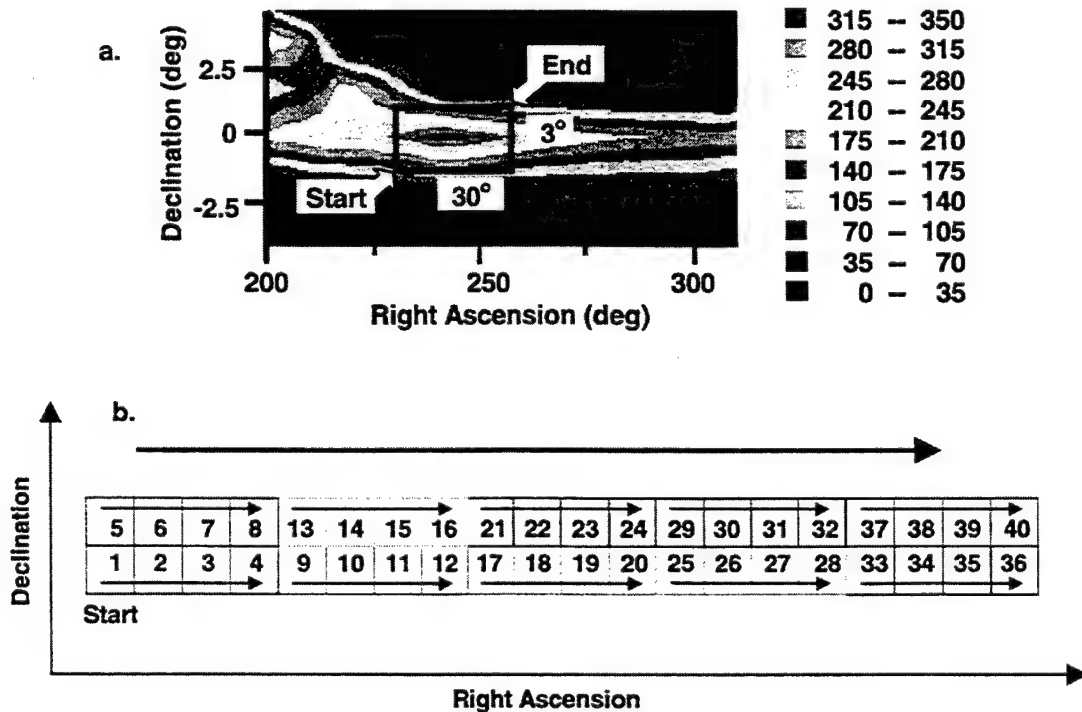
By analyzing the timing of the high satellite density coincidence with the nodes, a scheme for structuring the search and the choice of CCD placement can be made to vastly improve the search capability or even provide a leak-proof geosynchronous object fence. The goal is to explore and choose the best option for the Space-Based Visible (SBV) sensor, as well as the optical sensors within the Space Surveillance Network.

Because of the time-dependent accessibility due to the sun, density variation with longitude, variation of the ascending node with inclination, and varying density maxima over time, the two current four-hour event times do not allow for maximum productivity. One optimization for the search capability involves choosing the events to coincide with the times of day when the nodal crossings are most dense; when the European and American geosynchronous satellites cross the nodal regions. Unfortunately, the time of day when a certain region in longitude coincides with a particular value of right ascension varies with time over a year. This vastly changing coincidence of right ascension and longitude over time makes the scheduling of events much more problematic, because it is not possible to optimize the criteria without constantly changing the event times.

Because of the difficulty in maximizing the productivity with the two current four-hour event windows, one option currently being investigated involves spreading the 8 hours of data collection over 24 hours, to make a nearly leak-proof fence of the entire geosynchronous belt. This would allow flexibility to more easily accommodate the high-density nodal crossing times and would involve more search time, approximately 6 out of 8 hours, introducing a paradigm in current space surveillance techniques. The remaining time, approximately two hours, will involve tasking.

After detailed analysis, the proposed search scheme to create a fence of the geosynchronous objects at the nodal regions is shown in Figure 14. SBV has four  $1.4^\circ \times 1.4^\circ$  CCDs which can be aligned horizontally along the equatorial plane; the squares in Figure 14b depict each CCD field-of-view. After the four CCD observations have been made, a maneuver is performed to slightly overlap the previously viewed region. Data is taken in the order portrayed in Figure 14, in which a maneuver is performed between each set of four. This search covers approximately  $30^\circ$  of right ascension by  $3^\circ$  of declination at one nodal region.

Figure 14  
24-Hour Geosynchronous Fence Strategy  
(Original in Color)



Because the SBV sensor is only currently funded to gather data for 8 hours per day, the spacecraft will have to be put in park-mode attitude for approximately 70 minutes of each 105 minute orbit. Out of the 35 minutes of data collection per orbit, the current search scheme entails search for 25 minutes per 105 minute orbit and tasking for the rest. There are approximately 14 orbits per day for SBV, therefore the search region can be revisited 14 total times per day. This results in 6 hours of search and about two hours of tasking, equaling the current 8 hours per day. The definition of the event windows could be defined as two equal events or the data collection sets for each orbit could be separated or grouped resulting in a maximum of 14 events.

This new search scheme could have the capability of producing a nearly leak-proof fence of the active geosynchronous satellites over the 24-hour period, by observing a nodal region once per revolution of the MSX satellite, approximately 14 times per day. The formation of the CCDs is designed to maximize efficiency and fence capability to view objects exactly once per day. A simulation of the geosynchronous leak-proof performance resulted in 92% of the active satellites and 71% of all geosynchronous objects detected once per day, assuming 100% detection rate for any object in the CCD field-of-view. Again, the fence is performed in about 5.8 hours of tracking over 24 hours with the only possible holes due to the download of the data from the spacecraft.

#### 4.6 Future

The second on-board signal processor on the SBV has been activated to support this new search technique. This capability increases the productivity of the SBV by 20-30%. This has been of highest priority because productivity would be improved for both search and tasking. In addition, this will enable technology demonstrations of the greater limits available to space-based space surveillance sensors.

Currently, experiments are being conducted to test this new search scheme and the implementation of the second on-board signal processor. Technology demonstrations of this new search scheme are being conducted once a week on maintenance days to try to ascertain the full impact of the planned changes. This test phase will provide time to validate the new plan and enable time for Conjunction-Optimized Look-Ahead (COLA) to be changed to accommodate the nodal region geosynchronous search fence. Results are promising, but refinements to the experiments are still being made in order to fully investigate this phenomenon and its impact on SBV operations.

### 5. Conclusion

Geosynchronous objects occupy a well-defined region due to perturbations and station-keeping which constrain the inclination and location of the ascending node. This pattern observed in the geosynchronous object population is of importance because current operations indicate that the SBV is more efficient in collecting observations in the pattern's densest regions. Detailed knowledge about this population pattern has resulted in the exploration to further exploit the clustering of the geosynchronous objects and improve the productivity and efficiency of the wide field-of-view, global coverage SBV geosynchronous search efforts. Initial results show potential improvement in our detection rates. In addition, a new paradigm in space surveillance could result from exploiting the details of this population geometry, improving geosynchronous satellite surveillance efficiency for any space-based or ground-based optical sensor.

### 6. References

1. Chao, C. C. "Geosynchronous Disposal Orbit Stability." AIAA-98-4186, Pp. 20-33.
2. Friesen, L. J., Jackson IV, A. A., Zook, H. A., Kessler, D. J. "Analysis of Orbital Perturbations Acting on Objects in Orbits Near Geosynchronous Earth Orbit." Journal of Geophysical Research, Vol. 97, No. E3, Pp. 3845-3863, Mar. 25, 1992
3. Soop, E. M. Handbook of Geostationary Orbits. Kluwer Academic Publishers, Dordrecht, The Netherlands and Micrcosm, Inc, Torrance, CA. European Space Agency, 1994.
4. Vaughan, S. H., T. L. Mullikin. "Long Term Behavior of Inactive Satellites and Debris Near Geosynchronous Orbits". AAS 95-200. Pp. 1571-1585.

## **Small Aperture Telescope Augmentation (SATA) Concept**

Linda Crawford (Schafer Corporation)  
Paul Kervin (Det 15 AFRL)  
Maj Michael Nutter (AFSPC/DRCS)  
Capt Charlie Baker (ESC/NDWG)  
Paul Sydney, Vicki Soo Hoo, Kris Hamada (Boeing Rocketdyne Technical Services)  
Daron Nishimoto (Oceanit Laboratories)

The concept of using small aperture telescope systems was evaluated in a 1999 joint effort by Air Force Space Command (AFSPC) and two Air Force Materiel Command organizations, Electronic Systems Center (ESC) and Air Force Research Laboratory (AFRL). This test was a follow-on activity to a 1998 Space Warfare Center (SWC)/Space Battlelab (SB) project, where a telescope developed by Detachment (Det) 15 AFRL and Boeing RTS, coupled with a MIT/LL weather protection system and system scheduler, was demonstrated at the 18<sup>th</sup> Space Surveillance Squadron (18 SPSS), Edwards Air Force Base, CA.

This SATA test used a longer test period (August-December 1999) to evaluate the effectiveness and suitability of a SATA system that integrated low-cost commercial technology. The performance effectiveness evaluation consisted of three data collection phases; the first two used two SATA systems with different capabilities but with tasking derived from two of the operational Ground-based Electro-Optical Deep Space Surveillance (GEOSS) sites. The third phase used tasking for all potential deep space satellites in the coverage with the upgraded SATA system. The reliability and maintainability of this system was planned to be documented through the collection of a long-term maintenance and logistics data set and through a Continuous Process Improvement to upgrade the system components, while the system was deployed.

This paper describes the test approach, the SATA specifications of the two systems used, data collection from the remote site at Edwards Air Force Base, the methods and technology used in the system operation, and the automated data analysis. This paper will also summarize the performance statistics results, conclusions, and future plans, to include AFRL installing such a system at the Maui Space Surveillance System (MSSS) site.

### **TEST OBJECTIVES**

The SATA concept includes small aperture, relatively inexpensive custom telescope systems with commercial components. To demonstrate the utility of the SATA concept, this test addressed whether a SATA system could be deployed, operated, and maintained.

However, certain testing, programmatic, manning, and funding constraints prevented the comprehensive evaluation of all the objectives. For example, the SATA observational data could not be included with the data from the other operational SSN sensors (not ITW/AA certified) and the on-site support and maintenance logs were provided on a non-interference basis which did not yield sufficient data to evaluate fully the reliability, maintainability, and availability (RMA) of the system. However, this test did provide a long-term data set to establish the role of a SATA system and its ability to successfully track deep space satellites.

### **APPROACH**

AFSPC/DRCS and AFSPC/DOYO provided oversight and performance data analysis with support from Schafer Corporation and SenCom Corporation. SWC/AES provided correlation software and sensor data calibration assessments. 18SPSS provided on-site facilities and operations support. AFRL Det 15, with Boeing RTS and Oceanit Laboratories, developed, deployed, and operated the SATA system. ESC/NDWG wrote the test plan.

The initial system used for the testing of the SATA concept from mid-August through September 1999 was the telescope system previously installed and operated at Edwards AFB, CA from September 1997 to August 1998 for the SWC/SB project. This system was upgraded during the test period with new and more capable commercial components that were used for the second part of the formal test conducted between October-December 1999. This system was operated remotely from Maui (Det 15 AFRL) with site support (power,

communications, limited test monitoring, operational support and on-site facilities maintenance by 18 SPSS personnel). The system was in a ready state 24 hours per day during the entire test period. This means that, theoretically, at any moment during the test period, a remote operator could call upon the system to attempt observations. The system was operational, meaning that it was attempting the tracking of satellites and the collection of data between dusk and dawn. To address the suitability or logistic-related objectives, maintenance and logistics logs were to be maintained by AFRL/Det 15, Boeing, and 18SPSS, and forwarded for evaluation. The SATA performance and logistics data were to be statistically compiled and analyzed and will be an input to the final report. Figure 1 illustrates the test concept.

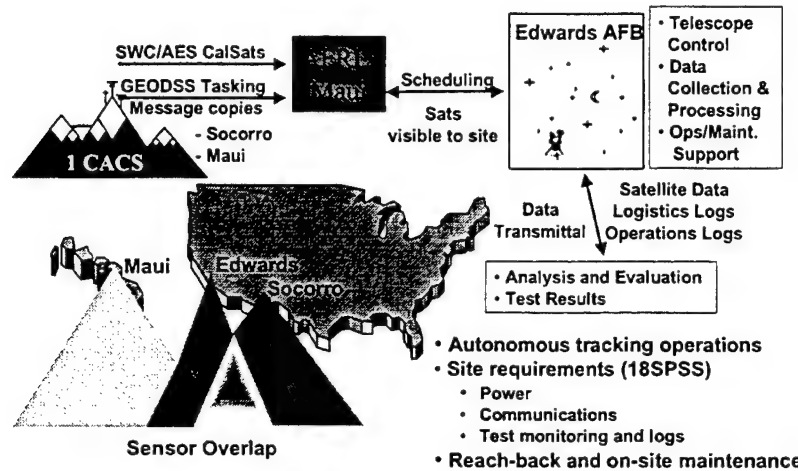


**Figure 1: SATA Test Concept**

There were three phases of the SATA test in which the data collection capabilities were assessed. In Phase 1, conducted mid-August to October 1999, the SATA system was the one from the 1998 SWC/SB project, except that the MIT/LL scheduler was replaced with a new scheduler as part of the *RavenManager* software. This system derived its daily tasking from the GEODSS Sites 1 (Socorro, NM) and 3 (Maui, HI) tasking messages sent by the 21 Space Wing organizations. The scheduler determined those satellites that were geographically visible to the SATA location and developed a schedule for collecting observations. In addition, the scheduler applied certain filters to eliminate satellite-viewing opportunities with excessive angular rate, proximity to the moon, wrong meridian, insufficient viewing overlap, poor phase angle, and minimum elevation. The SATA system provided the metric data on deep space satellites, satisfying the tasking categories and suffixes, and transmitted that observational data in the standard B3 observation format to AFRL Det 15 and Boeing. In the event that the SATA system satisfied all scheduled derived tasking from the GEODSS sites during that daily observing period, it was scheduled with additional taskings to ensure the equipment was kept working.

Phase 2, conducted October-mid-November 1999, again used the derived GEODSS taskings to evaluate how well an upgraded SATA system in that location could track deep space satellites. The same procedures as for Phase 1 were used. In addition, SWC/AES provided tasking for calibration satellites which could be used to later assess the quality of the observations by comparing the errors in observed position as reported by SATA compared to the known orbit position.

Phase 3, conducted mid-November through 31 December 1999, developed its tasking from all cataloged deep space satellites with element sets observable from Edwards AFB. Derived GEODSS tasking and calibration satellite tasking were not used in Phase 3. The same SATA system as for Phase 2 was used. This phase tested the ability of SATA to detect and track a variety of objects with all orbit types, element set ages, viewing angular rates, and brightness levels, as shown in Table 1. The purpose of establishing these bins was to determine what was the most appropriate niche for a SATA system.

**Table 1: SATA Utility Determination Bins**

ORBIT TYPE	INCLINATION (deg)	ECCENTRICITY	REVS/DAY
Geosynchronous (GEO1)	< = 5	Circular < = .2	> .9, < = 1.1
Geosynchronous (GEO2)	> 5, < = 15	Circular < = .2	> .9, < = 1.1
Geosynchronous (GEO3)	> 15	Circular < = .2	> .9, < = 1.1
Half-Synchronous	< = 5	Circular < = .2	> 1.1, < = 2.6
Semi-Sync Elliptical Earth Orbit (EEO1)	< = 12	Elliptical > .2	> .9, < = 2.6
Semi-Sync (EEO2)	> 12, < = 20	Elliptical > .2	> .9, < = 2.6
Semi-Synch (EEO3)	> 20, < = 60	Elliptical > .2	> .9, < = 2.6
Molniya-Type	> 60	Elliptical > .2	> .9, < = 2.6
Multi-Day/ High Earth Orbit (HEO)			< = .9
Less-than-Half-Sync (GPS)	> 5	Circular < = .2	> 1.1, < = 2.6
Other Deep Space (ODS)			> 2.6, < 6.4

BRIGHTNESS/APARENT VISUAL MAGNITUDE	ELSET AGE (days)	PHASE ANGLE (deg)	ANGULAR RATE (arcsec/sec)
< = 11	< = 2	< = 10	< = 10
> 11, < = 12	> 2, < = 5	> 10, <= 20	> 10, <= 20
> 12, < = 13	> 5, < = 10	> 20, <= 30	> 20, <= 30
> 13, < = 14	> 10, < = 30	> 30, <= 40	> 30, <= 40
> 15, < = 16	> 30	> 40, <= 50	>40
> 16, < = 17		> 50	
> 17			

#### SATA SYSTEM DESCRIPTION

The SATA system was derived from the Raven telescope concept that was developed by AFRL Det 15 and its support contractors at Maui, HI for the SWC/SB demonstration. The SATA design was based on commercial components with custom interfaces with the intent to achieve a system that would be easy to operate, maintain, repair, and upgrade. The operational elements of the system include:

- 1) a computer-controlled telescope to autonomously track objects of interest without direct intervention by an operator;
- 2) an imaging sensor;
- 3) Global Positioning System (GPS) system;
- 4) a dome to house the telescope;
- 5) a telescope control computer;
- 6) a data processing computer with a 'scheduler' (*RavenManager*) to autonomously select suitable objects for observation, and a satellite correlator (provided by SWC/AES) which minimizes object mistagging by associating a satellite with a series of metric measurements using SSN orbital element sets;
- 7) an automated weather station that measures wind speed, temperature, relative humidity and precipitation to protect the sensitive equipment from inclement weather conditions; and
- 8) communications.

**Telescope.** The telescope used initially in the SATA project was the same telescope used in the SWC/SB program. During the course of the SATA test, an upgraded system was deployed with increased field of view (FOV) and higher angular rate capabilities. Table 2 lists the specifications. Three technicians achieved the replacement and alignment of the telescope in less than two days, with a total system downtime of about 1.5 nights. The Torus Optics telescope is shown in Figure 2.

**Table 2: SATA System Specifications**

	Original System used in SATA Phase 1	Upgraded SATA System for Phases 2 and 3
<b>Aperture</b>	40 cm (16 in)	36.25 cm (14.5 in)
<b>Focal length</b>	150 cm (60 in)	108.75 cm (43.5 in)
<b>f-number</b>	3.75	3
<b>Telescope/Mount</b>	Paramount telescope with open-framed truss and German equatorial mount	Newtonian telescope with open-framed truss and shroud
<b>FOV</b>	28 arcmin square	38 arcmin square
<b>Angular rate</b>	30 arcsec/sec	45 arcsec/sec
<b>Manufacturer</b>	Star Telescope (Software Bisque, CO)	Torus Optics, IA

**Imaging Sensor.** The imaging sensor was a commercial 512 by 512 pixel thinned back-illuminated Apogee AP-7 Charge Coupled Device (CCD) provided by Apogee Instruments, Inc. The AP-7 CCD was placed at prime focus for the Paramount Telescope, and was side-mounted at the secondary focus for the Newtonian Torus Optics telescope. The AP-7 camera uses the SITe SIA502AB CCD chip with 24  $\mu\text{m}$  pixels, 16 bit A/D at 30 kHz,  $\sim$ 14 photoelectrons noise with a gain of 5.5 photoelectrons / ADU, a responsivity from 300 - 1000 nm, with a peak responsivity of  $\sim$ 85% between 600 - 800 nm. The CCD camera is complemented with a two stage thermoelectric cooler running at a nominal  $-25^\circ\text{C}$ .

**GPS System.** Datum GPS Receiver and Timing interface card are triggered by the camera shutter and provided accurate timing for the metric data.

**Dome.** Ash Manufacturing, the manufacturer of the GEODSS domes, provided the 3.2 meter (10.5 foot) dome shown in Figure 3. Merlin Controls provided the automation for the dome. The dome control system uses a Marine battery and recharging solar cell mounted on the dome itself to power the dome shutter and windscreens. This system provides an alternative to cable connections or slip rings between the upper and lower portions of the dome, which are potentially problematic. Initially, a Light Emitting Diode (LED) and photodiode on the ring motor was to provide the home position information, as well as a single communication connection point for initiating dome opening and closing. However, because of erratic operation, it became necessary to replace the LED system with a Radio Frequency (RF) transmitter/receiver package, which enabled the handoff of dome open and close commands regardless of the position of the dome. A magnetically activated ‘single-pull-double-throw’ switch was installed to indicate the home position for the dome, and the dome controllers were upgraded to provide feedback on the current status (open or closed) of the dome shutter and windscreens. The upgrades to the dome control system were, in large measure, designed to improve the consistency of automated operation of the dome shutter. It should be pointed out that this dome control mechanism was not initially designed to communicate with the specific software and hardware components of this particular system. It was the only system component not pre-tested at the Maui site, and so it represents normal ‘growing-pains’ for such a prototype dome control mechanism.

The high desert climate at Edwards AFB was a major concern with temperatures ranging from 120  $^{\circ}\text{F}$  to 50  $^{\circ}\text{F}$  since the control electronics were to be run continuously. In addition, high dome interior temperatures at the start of the night could also reduce the effectiveness of the CCD thermoelectric cooler. As a result, a timer-activated air conditioner was installed in the dome to keep the interior temperature in the 70 – 80  $^{\circ}\text{F}$  range during the day, while turning off before sunset to minimize temperature gradients. This has been highly successful in preventing failure of electronics in the dome, and increasing the efficiency of the CCD thermoelectric cooler. An added issue was that the large temperature fluctuations manifested focus changes in the optics during the late evening / early morning hours, when the temperatures have been the coldest. The extent of the defocusing effect, as well as its affect on the system performance is still being assessed.

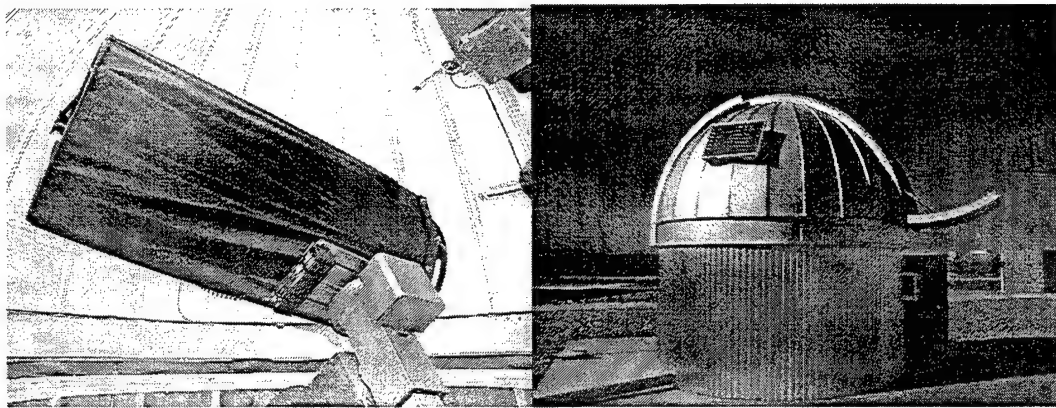


**Figure 2: Torus Optics Telescope**

**Figure 3: Ash Dome**

Telescope Control Computer. This computer is a commercial Pentium-based PC running Windows NT 4.0. The telescope and camera control software is a commercial package called TheSky developed by Software Bisque. TheSky package consists of several inter-communicating modules that allows the telescope to track autonomously, and which include:

- 1) TheSky application itself, which monitors the telescope and dome positions;
- 2) CCDSof, providing CCD camera control, including thermoelectric cooling and CCD exposure time;
- 3) Automadome, which provides interfacing to the dome control system;
- 4) GPStfp, which provides interfacing to the Datum GPS receiver;
- 5) Tpoint, which provides telescope mount modeling for accurate pointing; and
- 6) Orchestrat, which enables scripting of telescope pointing, satellite tracking, camera acquisition, and data transfer.

Data Processing Workstation. The data processing workstation (called *Odin*) is a Silicon Graphics Octane UNIX workstation running IRIX 6.4. Resident is the *RavenManager* software, developed by AFRL and Boeing RTS, which is the overall customized system manager that provides the commercial software interfaces, diagnostics, data handling, scheduling, and data logging to adapt this system to tracking satellites. *RavenManager* also handles the determination and scheduling of the object to be observed based on several selection considerations. These selection criteria (filters) include:

- 1) minimal (10 deg) Sun-satellite-observer phase angle to increase observing at peak brightness;
- 2) minimal times that the telescope is required to cross the meridian, as repeated crossings significantly decrease the throughput for the system. This is accomplished by confining the telescope to one side of the meridian (azimuth less than 180 degrees) for the first half of the night then switching to objects on the other side of the meridian (azimuth greater than 180 degrees) for the second half of the night;
- 3) no element sets older than 45 days;
- 4) minimum of 20 degrees elevation (consistent with operational sensors);
- 5) limiting angular rates to 30 arcsec/sec or less for the Star Instruments telescope, and 45 arcsec/sec or less for the new Torus Optics telescope (otherwise satellite image moves across the FOV too quickly to obtain sufficient data);
- 6) proximity to the moon no less than 30 degrees; and
- 7) insufficient time for adequate viewing conditions (insufficient overlap).

Weather Station. As a part of the SATA program, an autonomous weather monitoring system was developed to provide protection against equipment damaging weather conditions. The weather sensor included an optical precipitation sensor, wind speed and direction monitor, and a temperature and relative humidity (RH) sensor.

Scientific Technology, Inc. manufactured the optical precipitation sensor while the R.M. Young Company provided the wind speed monitor, temperature and RH sensor, and the programmable translator. The wind speed/direction, precipitation, and temperature and RH sensors were all mounted on a tower ~2.5 m. (~8 ft.) high, located ~3 m. (~10 ft.) from the Ash dome and provided weather updates once each 30-second increment. The weather station is shown in Figure 4.

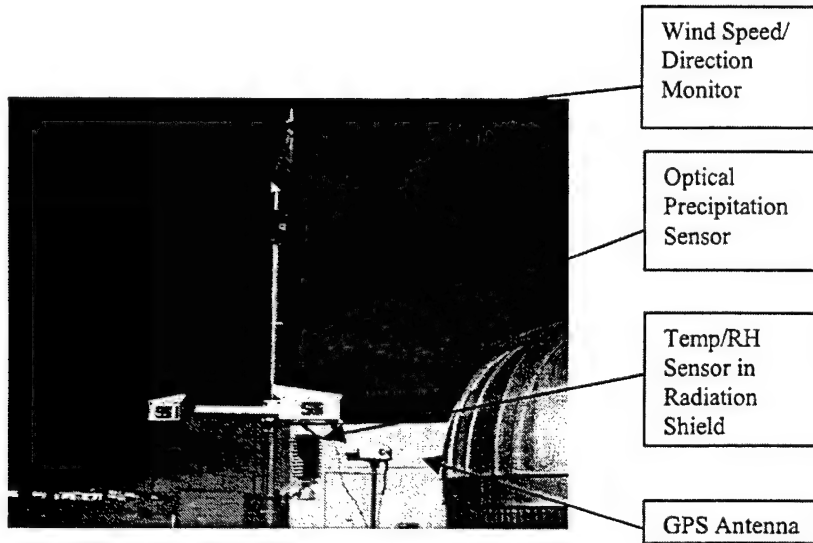


Figure 4: Weather Station

Communications. Remote monitoring and software updates to the system were possible using low bandwidth communications links between the *Odin* Data Processing Workstation at Edwards AFB, and the AFRL facilities in Maui.

#### OPERATIONS AND DATA ANALYSIS

In operation, the SATA systems have two tracking modes, sidereal and stare. In sidereal tracking mode, the telescope moves to compensate for the rotation of the Earth, so stars appear as point sources whereas satellites generally appear as streaks. In stare tracking mode, the telescope position is fixed, causing the stars to appear as streaks moving at sidereal rate and along the equatorial axis, while geostationary satellites appear as point sources and other deep space objects appear as streaks at arbitrary angles and rates. Both tracking modes have their advantages and disadvantages. For dim or flashing near-geostationary objects, stare tracking mode allows the satellite irradiance to dwell and accumulate on just a few pixels, providing a higher signal to noise ratio and improving the probability for detection. The disadvantage of stare tracking is that the streaking stars tend to clutter the image background, increasing the opportunity for bright star streaks to overlap onto dim objects, and may often require multiple images to achieve the stated test requirement of 5 metric marks. Sidereal tracking assures that satellites will appear as distinct streaks against a background of point-like stellar objects. In sidereal mode, the CCD shutter was operated in the following manner, it was opened for 20 seconds, closed for 10 seconds, and opened again for 10 seconds before the images were downloaded from the CCD. By observing the relative locations of the 20-second streak and the 10-second streak, the velocity vector for the satellite is uniquely determined. In addition, the endpoints of each streak along with the center of the 20-second streak provided 5 metric marks separated by 10 seconds each. The sidereal tracking disadvantage is the corollary to stare mode's advantage. In sidereal mode, satellite irradiance is smeared along a range of pixels at sidereal rates or higher decreasing the probability of detecting faint objects.

Once tasking for an object is determined, *RavenManager* generates an observation script, which is sent to the Telescope Control Computer. *Odin* then monitors weather and communication status until an image data file in Flexible Image Transport System (FITS) format is transferred using File Transfer Protocol (FTP) from the

Telescope Control Computer. The FITS image file is then analyzed to detect all stars in the field as well as locate any satellites present in the image. The detected stars are matched against the nominal positions of catalog stars from the Hubble Guide Star Catalog and from this correlation, the equatorial position, orientation, and scale of the image is determined in mean equator and mean equinox of J2000 for the topocentric location of Edwards AFB, CA. Using this computed transformation, the pixel positions of any detected satellites at shutter open and close are converted to equatorial coordinates. Annual (stellar) aberration is applied to the satellite's coordinates to account for light time travel variations due to the Earth's motion around the Sun. These corrected coordinates are then converted to B3 format and correlated against an online database of deep space satellite element sets using correlation software provided by SWC/AES. After correlation, the tagged metric observations are stored along with brightness magnitude estimates.

## RESULTS

SATA testing occurred from 15 August 1999 through 31 December 1999. The Phase 1 system that was not tasked with as many satellites to track was used during August and September. Through 5 December, both SATA systems accumulated over 932 hours of operation, and over 19,000 acquisitions with an average acquisition rate of 55% after filtering the satellites visible to the site. The operational hours include red and yellow weather that decreased the acquisition rate. Peak system performance could achieve acquisition rates of over 70%. A weekly summary is shown in Table 3.

**Table 3: Weekly Summary of SATA Performance (Original and Upgraded System)**

System	Week Of	Operational Hours/week (hh:mm)	# Objects Attempted	Attempts/hour	# Objects Acquired	Acquired/hour	# Acquired/# Attempted Rate (%)
<b>Original System</b>	8/15	17:55	668	28.2	388	21.6	58.1
	8/22	46:02	1229	37.8	623	13.5	50.7
	8/29	55:51	1837	38.1	1254	22.4	68.3
	9/5	55:34	1702	30.9	1022	18.4	60.0
	9/12	32:31	1263	37.1	700	21.7	55.4
	9/19	64:29	2472	38.3	1113	17.3	45.0
	9/26	26:05	821	34.3	445	17.2	54.2
<b>TOTAL</b>		<b>298:45</b>	<b>9992</b>		<b>5545</b>		
<b>Upgraded SATA</b>	10/3	53:12	2291	42.5	1453	27.3	63.4
	10/10	74:03	2872	38.2	1718	23.2	59.8
	10/17	54:03	2393	44.3	1692	31.3	70.7
	10/24	72:42	3084	43.7	979	13.5	31.7
	10/31	75:51	3309	43.7	1982	26.1	59.9
	11/7	74:02	2981	40.3	1634	22.1	54.8
	11/14	56:23	2149	36.5	1305	23.2	60.7
	11/21	77:19	2897	37.4	1449	18.8	50.0
	11/28	76:34	2455	38.1	1019	13.3	41.5
	12/5	20:30	964	44.3	549	26.8	57.0
<b>TOTALS</b>		<b>634:21</b>	<b>25395</b>		<b>13780</b>		

The system and its components were in a ready state 24 hours/day fairly continuously for the entire test period. The Phase 1 system operated an average of 6 hours per day and the upgraded SATA system (Phases 2 and 3) operated an average of 9 hrs/day, with down time being a combination of red weather, corrective and preventive maintenance, and length of observing period. Corrective maintenance were caused by three events: rats chewing through cables, electronics hit by lightning, and a dome/telescope control computer interface problem that frequently did not open the dome at the beginning of the observing period. Interface problems were discovered during the testing period and required several modifications of the *RavenManager* software to provide

diagnostics and solutions to the problems as they occurred. The dome problem was due to the implementation of a prototype system that had not been completely tested prior to installation, which was a constraint of the test.

The system could not be monitored continuously during its periods of operations since the 18SPSS personnel could only monitor the system on a non-interference basis, given their primary duties. Thus the Maui staff monitored the test primarily remotely. Additionally, the test was conducted for a finite time period that limited the amount of data collected. This precluded a rigorous evaluation of the objectives associated with RMA and logistics. However, the limited amount of RMA data recorded showed that this prototype system cannot be deployed in a remote location without operational and maintenance support capabilities. If deployed in a remote location, downtime may occur until the problem is detected and fixed.

This SATA system was designed to track autonomously, but could not necessarily operate totally autonomously during the testing period since it required periodic checking by on-site staff to ensure the equipment was operating correctly. Preventive maintenance (such as optics alignment, gear lubrication, and optics cleaning) was done several times and took 1-2 hours to complete. A benefit gained from the testing process was the discovery that this type of system in its harsh desert environment needs periodic preventive maintenance to ensure maximum performance. For example, immediately prior to one of the maintenance periods, the acquisition rate was 60%, and immediately after the maintenance it was 70-73%. However, the acquisition rates averaged over a longer time period were lower as shown in the tables below. Also, the current system is geared for R&D so the components can be easily modified. For an operational system, some components should be permanently set to minimize any movement/misalignment.

The scheduler *RavenManager* took the satellites scheduled for data collection, applied the filters to determine the site's visibility opportunities to "see" the satellite and forwarded the tasking to the system. Table 4 shows the statistics of the scheduled versus tasked objects, separated by the Phase 2 and Phase 3 portions of the test. The insufficient overlap category were those passes with insufficient time for adequate viewing conditions.

**Table 4: SATA Tasked versus Scheduled Statistics**

**SATA VISIBILITY/SCHEDULER PHASE 2 - DERIVED GEODSS TASKING (1 Oct- 7 Nov 99, 9-12 Nov 99), Upgraded SATA**

	total	below	moon	poor phase	High angle	wrong	Insuff.	total	total	% sched
	tasked	min elev	proximity	angle	rate	meridian	overlap	invalid	sched	vs tasked
Totals	18887	3763	5	0	245	2106	2564	8683	10204	54.02%
Avg	460.7	91.8	0.1	0.0	6.0	51.4	62.5	233.5	246.4	53.5%
min	292	65	0	0	1	31	39	74	152	36.0%
max	515	112	1	0	9	65	91	297	284	63.0%
%of invalid		43.43%	0.00%	0.00%	2.81%	24.24%	29.52%			
total days		41								

**SATA VISIBILITY/SCHEDULER PHASE 3 - TRACK ALL DEEP SPACE SATELLITES WITH ELEMENT SETS  
WITHIN COVERAGE (8, 13 Nov - 31 Dec 99), Upgraded SATA**

	total	below	moon	poor phase	High angle	wrong	Insuf.	total	total	% sched
	tasked	min elev	proximity	angle	rate	meridian	overlap	invalid	sched	vs tasked
Totals	53494	20285	20	0	538	5499	7040	33382	20112	37.60%
Avg	2139.8	811.4	0.8	0.0	21.5	220.0	281.6	1335.3	804.5	37.6%
Min	1800	777	0	0	18	196	236	1270	463	25.7%
Max	2205	847	2	0	25	247	326	1370	861	40.0%
% of invalid		60.77%	0.01%	0.00%	1.61%	16.47%	21.09%			
total days		25								

min elevation - 20 deg

min phase angle/shadow - 10 deg

min moon separation-30deg

max angular rate - 45 arcsecs/sec

For Phase 2, statistics were determined on the number of satellites tasked to the GEODSS Socorro and Maui sites that the SATA system at its current Edwards AFB location could see (Table 5) and acquired. An examination of the tasking and scheduling logs recorded by *RavenManager* showed that the satellites tasked to those GEODSS sites and not seen by SATA were primarily geosynchronous and below the minimum elevation criteria. During Phase 2, the average number of satellites tasked daily for Socorro was 412 and for Maui 413.

To give an indication of how much tasking from the two GEODSS was derived by SATA, the following percentages were computed: tasked satellites that were visible to SATA (averaged over Phase 2) were 17% for Socorro and 32% for Maui tasking. Note that the SATA site location was based on an existing system at Edwards AFB, CA, and may not be an optimal location for a small telescope system.

Tables 5-9 summarize the detection and tracking capabilities of the original system during Phase 1 (derived GEODSS tasking). Tables 10-14 summarize the upgraded SATA system performance in Phase 2 (derived GEODSS tasking). Tables 15-19 summarize the upgraded SATA system performance in Phase 3 (track all deep space satellites with element sets in the coverage area) of the test period, as binned by the orbit types and viewing parameters listed in Table 1. For the brightness/apparent magnitude statistics there is only one table, that for acquired satellites versus total number acquired. If the system did not track the satellite, it could not make an estimate of the brightness.

**Table 5: Scheduled versus Acquired Statistics (Phase 1)**

Bins	%Scheduled/ Total Orbit	# Scheduled	# Acquired	%Acq/ Scheduled
GEO1	15.99%	43	28	65.12%
GEO2	29.74%	80	45	56.25%
GEO3	1.49%	4	4	100.00%
Half-Sync	0.00%	0	0	
EEO1	7.81%	21	12	57.14%
EEO2	1.86%	5	4	80.00%
EEO3	3.72%	10	4	40.00%
Molniya	12.64%	34	20	58.82%
HEO	2.23%	6	3	50.00%
GPS	7.43%	20	7	35.00%
ODS	17.10%	46	20	43.48%
TOTALS	100.00%	269	147	54.65%

**Table 6: Angular Rate Statistics (Phase 1)**

Bin (arcsec/sec)	# Scheduled	# Acquired	% Acq/ Scheduled
< 10	43	21	48.84%
10-20	171	97	56.73%
20-30	55	29	52.73%
30-40	0	0	
40+	0	0	
TOTALS	269	147	54.65%

**Table 7: Phase Angle Statistics (Phase 1)**

Bin (deg)	# Scheduled	# Acquired	% Acq/ Scheduled
< 10	2	2	100.00%
10-20	90	53	58.89%
20-30	63	36	57.14%
30-40	58	34	58.62%
40-50	26	10	38.46%
50+	30	12	40.00%
TOTALS	269	147	54.65%

**Table 8: Element Set Age Statistics (Phase 1)**

Bin (days)	# Scheduled	# Acquired	% Acq/ Scheduled
< 2	19	16	84.21%
2-5	142	85	59.86%
5-10	82	38	46.34%
10-30	23	8	34.78%
30+	3	0	0.00%
TOTALS	269	147	54.65%

**Table 9: Magnitude Statistics (Phase 1)**

Bin (magnitude)	# Acquired	% Acq/ Total # Acquired
<11	98	66.67%
11-12	17	11.56%
12-13	21	14.29%
13-14	7	4.76%
14-15	2	1.36%
15-16	2	1.36%
16-17	0	0.00%
17+	0	0.00%
TOTALS	147	100.00%

**Table 10: Scheduled versus Acquired Statistics (Phase 2)**

Bins	%Scheduled/ Total Orbit	# Scheduled	# Acquired	%Acq/ Scheduled
GEO1	15.73%	81	52	64.20%
GEO2	16.50%	85	34	40.00%
GEO3	1.55%	8	7	87.50%
Half-Sync	0.00%	0	0	
EEO1	4.08%	21	10	47.62%
EEO2	1.17%	6	6	100.00%
EEO3	4.85%	25	20	80.00%
Molniya	29.13%	150	107	71.33%
HEO	2.33%	12	8	66.67%
GPS	8.93%	46	17	36.96%
ODS	15.73%	81	31	38.27%
TOTALS	100.00%	515	292	56.70%

**Table 11: Angular Rate Statistics (Phase 2)**

Bin (arcsec/sec)	# Scheduled	# Acquired	% Acq/ Scheduled
< 10	61	49	80.33%
10-20	300	180	60.00%
20-30	50	25	50.00%
30-40	102	38	37.25%
40+	2	0	0.00%
TOTALS	515	292	56.70%

**Table 12: Phase Angle Statistics (Phase 2)**

Bin (deg)	# Scheduled	# Acquired	% Acq/ Scheduled
< 10	1	1	100.00%
10-20	179	79	44.13%
20-30	172	109	63.37%
30-40	85	55	64.71%
40-50	68	30	44.12%
50+	10	8	80.00%
TOTALS	515	292	56.70%

**Table 13: Element Set Age Statistics (Phase 2)**

Bin (days)	# Scheduled	# Acquired	% Acq/ Scheduled
< 2	30	21	70.00%
2-5	221	133	60.18%
5-10	182	95	52.20%
10-30	73	37	50.68%
30+	9	6	66.67%
TOTALS	515	292	56.70%

**Table 14: Magnitude Statistics (Phase 2)**

Bin (magnitude)	# Acquired	% Acq/ Total # Acquired
<11	160	54.78%
11-12	71	24.42%
12-13	43	14.73%
13-14	13	4.45%
14-15	4	1.37%
15-16	1	0.34%
16-17	0	0.00%
17+	0	0.00%
TOTALS	292	100.00%

**Table 15: Scheduled versus Acquired Statistics (Phase 3)**

Bins	%Scheduled/ Total Orbit	# Scheduled	# Acquired	%Acq/ Scheduled
GEO1	15.50%	73	45	61.64%
GEO2	26.33%	124	78	62.90%
GEO3	3.18%	15	11	73.33%
Half-Sync	0.00%	0	0	
EEO1	1.70%	8	5	62.50%
EEO2	0.42%	2	2	100.00%
EEO3	2.76%	13	8	61.54%
Molniya	29.09%	137	91	66.42%
HEO	0.42%	2	2	100.00%
GPS	8.28%	39	15	38.46%
ODS	12.31%	58	18	31.03%
TOTALS	100.00%	471	275	58.39%

**Table 16: Angular Rate Statistics (Phase 3)**

Bin (arcsec/sec)	# Scheduled	# Acquired	% Acq/ Scheduled
< 10	41	29	70.73%
10-20	309	192	62.14%
20-30	47	28	59.57%
30-40	72	26	36.11%
40+	2	0	0.00%
TOTALS	471	275	58.39%

**Table 17: Phase Angle Statistics (Phase 3)**

Bin (deg)	# Scheduled	# Acquired	% Acq/ Scheduled
< 10	6	6	100.00%
10-20	164	78	47.56%
20-30	236	140	59.32%
30-40	29	21	72.41%
40-50	29	24	82.76%
50+	7	6	85.71%
TOTALS	471	275	58.39%

**Table 18: Element Set Age Statistics (Phase 3)**

Bin (days)	# Scheduled	# Acquired	% Acq/ Scheduled
< 2	5	5	100.00%
2-5	6	6	100.00%
5-10	298	187	62.75%
10-30	149	74	49.66%
30+	13	3	23.08%
<b>TOTALS</b>	<b>471</b>	<b>275</b>	<b>58.39%</b>

**Table 19: Magnitude Statistics (Phase 3)**

Bin (magnitude)	# Acquired	% Acq/ Total # Acquired
<11	92	33.45%
11-12	73	26.55%
12-13	84	30.55%
13-14	19	6.91%
14-15	6	2.18%
15-16	1	0.36%
16-17	0	0.00%
17+	0	0.00%
<b>TOTALS</b>	<b>275</b>	<b>100.00%</b>

The upgraded SATA system (Phases 2 and 3) attempted and acquired approximately 20% more objects/hour than the system used in Phase 1, but the acquisition rate was approximately the same. This indicates that the increased slew rate provided by the smaller size of the new equipment was successful in increasing the number of attempts made in a given night. (See Tables 5 and 10) However, the increased field of view did not improve the odds of observing a particular scheduled object, or the acquisition rate. The stable acquisition rate provided evidence for the theory that the satellite element set age might be the primary factor in determining whether an acquisition will be made successfully. (See Tables 8, 13, and 18) There was not much different in performance results between the two modes of data collection (derived GEODSS tasking and all satellite catalog developed tracking). In analyzing the GEODSS tasking, they are tasked for all of the orbit types, so the taskings for both modes were similar, and therefore, yielded similar results.

The niche of the small telescope system may be inferred from the observation statistics, which show that the small telescope performance was acceptable over a wide range of object attributes. For example, Tables 5, 10 and 15 indicate an acceptable level of performance on a wide range of satellite types with the exception of the GPS and ODS orbits. Other tables show the expected dependence on attributes such as apparent magnitude, i.e., the system acquires brighter objects more frequently than dimmer objects, and so on. The system thus seems limited mainly by objects that are visible to its location. The niche then would be to position such a system in a location suitable for viewing all deep space objects which are not visible or are inadequately covered by other active sensors. A number of such systems would enhance the ability to be insensitive to localized weather conditions.

During the test conduct, SWC/AES provided the measurement accuracy of the SATA data, using approximately 150 observations from an Etalon calibration satellite. The results were sigma of .0015 deg for right ascension (RA) and sigma of .0120 deg for declination (DEC). The biases were .0004 deg for RA and .0018 deg for DEC. The difference in quality of the measurements caused a review of how the SATA software determined the position of the satellite from the star reference catalog. For these polar orbits, the software was jumping in declination position to a nearby bright star. The calibration results were re-run after the conclusion of the test using observations listing the correct satellite declination values. The calibration results were then sigma of .0009 deg for RA and .0020 deg for DEC, with corresponding biases of .0003 deg for RA and .0029 deg for DEC. There appears to still be a bias in the declination measurement that warrants further analysis. However, these measurement accuracy sigmas are comparable to those of the operational electro-optical systems, which are in the .001 to .005 deg range.

## TEST CONCLUSIONS

The SATA test successfully collected a substantial amount of data to help determine if a small aperture telescope system could successfully track deep space satellites with varying orbits and apparent visual magnitudes. The results of this test will be documented in a comprehensive technical report for AFSPC.

Many components, primarily hardware, of this system successfully used commercial products. This provides an enhanced ability to obtain replacement parts inexpensively, and upgrade system components when more modern

technology becomes available. A pre-planned upgrade of small telescope equipment can be executed with a very minimal downtime. For example, the replacement of the telescope itself, by three technicians in 1.5 nights emphasizes this aspect of the system.

It was not possible to construct the entire system from commercial components. Certain items of software, for example, the satellite scheduler, have no viable commercial market with its specialized requirements and functions, and as such are better designed as custom components for the system. The dome controller issue illustrates the complexity involved in troubleshooting an intermittent problem with a new system component at a remote location. Many vendors who had quality commercial components applicable to the system, were small companies without large support staff. This had the effect of delaying the troubleshooting of problems with vendor equipment, as manpower constraints limited the support time that vendors could offer.

Remote monitoring and software updates to the system using low bandwidth communications links were very successful during the testing period. This indicates that such a system could successfully and easily be monitored, and its custom software maintained remotely via a communications interface. Significant logging of system actions proved invaluable to remotely troubleshooting the system. For instance, it was possible to determine when the dome control issue had affected system performance, by referring to the automatically generated logs of the *RavenManager* scheduler.

An autonomous system operating in a harsh environment will need routine maintenance from on-site personnel. During the SATA test it was discovered that maintenance actions such as applying grease to the telescope mount gears improved system operation.

The limited logistics and maintenance data indicated that customized commercial small astronomical telescope systems are not presently well suited for an unattended environment with more stringent operational space surveillance requirements. Future development and testing of both hardware and software components and their interfaces will be required to complete these types of test objectives.

## FUTURE PLANS

Following the completion of the SATA project, AFRL will deploy a new Raven telescope at the MSSS facility on the summit of Haleakala, Maui, HI. This location will provide enhanced viewing conditions for the assessment of the system performance, and will allow the MSSS Raven to participate as a contributing astrometry sensor for the operational and R&D telescopes located at the MSSS facility. In addition, this MSSS Raven project will continue the investigation towards an autonomous small telescope system.

## Orbital Debris and the Environmental Restoration of Space: A Report to the Congressional Defense Committees

D.B. Spencer (The Pennsylvania State University), C.B. Hogge (Air Force Research Laboratory), W.S. Campbell, M.E. Sorge, S.R. McWaters (The Aerospace Corporation)

### Abstract

Congressional language from the 1998 Senate Armed Services Committee (SASC) authorization bill "...directs the Secretary of the Air Force to undertake a design study of a system that could catalogue and track debris down to 1 cm in size out to 1,000 kilometers in altitude". The "design study is to be coordinated among these laboratories" (Air Force Research Laboratory, Los Alamos and Lawrence Livermore National Laboratories) and is "to include a detailed cost estimate." Several other organizations within the U.S. Government that have current programs that address the potentially serious problem posed by debris fragments participated in this study, and expertise from these organizations were tapped, as well.

While the SASC language indicates that "modern optical detectors, aided with laser radar, could undertake to catalogue this small debris", this study found that maintaining a catalogue of 1 cm size objects will require a space surveillance network of both optical and radar sensors.

Designing an optical system to catalogue 1-cm objects would require hundreds of sensors around the world to deal with the limitations of optical sensors. Development of a complete system to detect, track, and catalogue space objects down to 1 cm in size should include both radar and optical surveillance systems, and would not be feasible for "...less than a few million dollars", as the SASC was led to believe.

### Introduction

The Department of Defense (DOD) and National Aeronautics and Space Administration (NASA) have jointly developed an orbital debris work plan in response to recommendations in the U.S. Government *Interagency Report on Orbital Debris – 1995*<sup>1</sup>. It also lays out the technical objectives necessary for the U.S. Government to demonstrate its leadership role in minimizing the creation of orbital debris consistent with mission requirements and cost effectiveness. Consistent with the Interagency report recommendations, this work plan emphasizes continued U.S. Government activities in the following three areas:

- Improving our understanding and monitoring of the debris environment through an appropriate mix of measurements and simulations;
- Working with other government agencies and with industry on voluntary design guidelines to minimize the future creation of orbital debris; and
- Working with other spacefaring nations and international organizations to adopt common debris minimization practices.

Both NASA and DOD have ongoing activities regarding orbital debris monitoring, research, and mitigation. The joint work plan both directs the work to be conducted and is the means to coordinate agency activities. As in the past, each party shall bear the cost of fulfilling its respective responsibilities dependent upon the availability of appropriated funds.

The 1989 *Interagency Report on Orbital Debris*<sup>2</sup> noted the ambiguities of measurements on the debris environment. Since that time NASA, with the assistance of DOD, has continued to conduct measurements of the Low Earth Orbit (LEO) debris environment. Although uncertainty remains, there has now emerged a better assessment of the orbital debris environment in LEO. Recent measurements and extrapolations indicate populations a factor of two lower than predicted in 1989 at Space Station altitudes and a factor of two higher at the 1,000 km altitude. In Geosynchronous Earth Orbit (GEO), however, NASA has only conducted an exploratory campaign to measure the debris environment. Efforts should continue in order to refine our understanding of the current environment, as well as, to monitor changes in the environment with time. Contributions to the current debris environment continue to be essentially proportional to the level of space activity by a given spacefaring nation.

The orbital debris environment in LEO is more of a concern for space operations that involve large spacecraft in orbit for long periods of time. For example, one would expect a typical DOD satellite ( $40 \text{ m}^2$  in 950 km polar orbit) to be hit by an object one cm or larger once every 500 years. In contrast, Space Station ( $5,000 \text{ m}^2$  at 400 km altitude, 51.6 degree inclination orbit) would expect to have one such collision on average every 71 years. Taking note of all that has been learned since 1989, the International Space Station Program has taken steps to maximize protection from debris penetration by implementing state-of-the-art shielding; utilizing existing ground radars to track and avoid larger debris; and actively developing operational and design options that will minimize the risk to the crew and the Station.

Over the last several years, there have been a series of proposals to develop large LEO satellite constellations. These constellations could present a new concern for the orbital debris environment. For those constellations that have a large aggregate area, the collision probabilities are sufficiently high that additional abatement measures may need to be considered. This is particularly true for high inclination orbits, which leads to higher spatial density over the poles.

NASA and DOD have expended considerable effort to monitor the orbital environment. For example, the modification of the DOD Space Surveillance Network's (SSN) Haystack radar for orbital debris measurements has greatly enhanced our ability to sample the LEO debris environment. The Haystack radar is essential for sampling and estimating the very hard to observe one to ten cm debris population in LEO. Today the SSN is primarily focused on meeting operational national security requirements that limits the time spent using the network for debris research. Also, the SSN was not designed to globally detect and track small debris objects. Consequently, statistical models must be used to characterize the current debris population at LEO and GEO.

The development and utilization of statistically based predictive models has improved. For example, NASA has continued the development of an engineering model first used in 1990. The

Air Force borrowed the framework of a NASA research model and made several modifications, including an upgrade to the imbedded empirical breakup model. These improvements to our predictive capability when combined with our increased knowledge of the debris environment, have led to the postulate that failure to take any mitigation action could lead to an increase in orbital debris in the coming years. The outcomes of these simulations vary greatly depending on the assumptions used and the space traffic model used. Assuming a continuation of launch activity at the same average rate as over the last ten years, average future solar cycles, and future operational practices that will minimize but not eliminate the possibility of explosions in orbit, most models predict an increase in orbital debris. Similarly, most models indicate that the use of operational practices to limit the orbital lifetime of spent upper stages and payloads, and the emptying of possible energy vessels, has the potential to mitigate the growth of orbital debris.

The 1996 U.S. Government space policy<sup>3</sup> requires all space sectors to seek to minimize the creation of orbital debris consistent with mission requirements and cost effectiveness. NASA has issued a comprehensive agency policy concerning orbital debris. The DOD (in particular the Air Force and the U.S. Space Command) has, since 1987, practiced orbital debris minimization. Both DOD and NASA are consistent with the current national orbital debris policy.

The 1996 U.S. Government space policy directs that the U.S. Government take a leadership role in the appropriate international fora to encourage other nations to adopt policies and practices similar to those of the U.S. Government. The United States and other spacefaring nations have initiated voluntary design measures (i.e., tethering of operational debris such as lens caps and the use of debris free devices for separation and release), as well as, operational procedures to minimize the generation of orbital debris consistent with mission requirements and cost effectiveness. The United States considers the development of technical cooperation and consensus to be an important step toward any potential measures relating to orbital debris.

### Study Methodology

The Deputy Assistant Secretary for Science, Technology and Engineering, Office of the Secretary of the Air Force (Acquisition), SAF/AQR, tasked the Air Force Research Laboratory (AFRL/CC) to perform this study. A team was assembled with representatives from the Air Force Research Laboratory (AFRL), Air Force Space Command (AFSPC), Jet Propulsion Laboratory (JPL), Lawrence Livermore National Laboratory (LLNL), Los Alamos National Laboratory (LANL), Massachusetts Institute of Technology Lincoln Laboratory (MIT/LL), NASA Johnson Space Center (JSC) and Navy Space Command (NAVSPACECOM). The team met in a series of workshops and discussed the current level of understanding of the risk posed to space operations by the space debris environment, the requirements for tracking and cataloguing debris objects, and the optical and radar concepts and capabilities for accomplishing the cataloguing task.

The team evaluated current capabilities and considered a variety of issues related to the effects of space debris on U.S. space assets. Collision risks posed by small debris are well quantified through Air Force and NASA multiyear statistical sampling of the debris. Determining "how

much risk is posed by this growing debris field” is a complex process involving highly accurate knowledge of position and velocity plus realistic models for predicting future events.

The team then placed its focus on the requirements for a system that could track and catalogue debris down to one cm in size out to 1,000 km in altitude. Due to the differing characteristics of small debris, a fully capable tracking system should include both optical and radar systems. Current U. S. Space Command phased array radars detect, track and catalogue resident space objects that include operational satellites and debris larger than 30 centimeters. These radars have tracked and catalogued objects smaller than 30 centimeters, but the set of smaller objects is incomplete and their cataloguing is not part of routine operations. Furthermore, radar sensitivity drops quickly with range due to loss associated with transmission of an acquisition signal. Since optical detection uses reflected sunlight, both active and passive optical detectors are utilized to support cataloguing of objects in high altitude or high eccentricity orbits. Also, debris as small as one centimeter does not have a very predictable orbit, and therefore could require a significant amount of monitoring.

The SSN uses cataloguing to identify and differentiate among resident space objects (RSOs). Each RSO is assigned a sequential identifying number. The current processing software limits cataloguing to 16,000 RSOs, but with some hardware and memory upgrades, this catalogue can be extended to 40,000 objects. Further increases to the catalogue size would require major redesigns of the software and databases. Cataloguing debris as small as one cm out to a distance of 1,000 km could result in a collection of well over 100,000 objects. Requirements issues which need to be defined include whether to use a statistical approach versus discrete counting of debris objects, what revisit times are necessary to maintain catalogue entries at acceptable sensor tasking levels, what processing speeds should be used for sensor data correlation, and how should data dissemination be handled.

### Findings

Extending the current operational capabilities of the SSN to detect and catalogue debris down to five cm in size is being addressed as an element of the DOD-NASA work plan on orbital debris. It is, however, premature to state that the network will be modified and operated to do so. Presently, the DOD does not have a requirement to track small debris on the order of five cm. Similarly, it is not clear that should NASA have a requirement to track five cm debris that they would have the funds necessary to pay for the upgrades, operations, and maintenance.

Modeling provides an understanding of the scope of the undetected debris population. It is the most effective near-term approach for space system design and development of debris mitigation techniques. Tools and methodology for this statistical risk assessment have been developed by DOD and NASA and are being exercised for a limited number of space missions. Continued statistical sampling of the small debris population will continue in order to improve our understanding of the orbital debris environment.

Attempting to catalogue all debris down to one cm in size over altitudes up to 1,000 km would require sensor and processing upgrades costing hundreds of millions of dollars as well as

significant changes to current operations manning and tasking procedures. Development of capabilities for detecting and cataloguing small debris appears feasible; however, there are no requirements to do so and the need for doing this is not clear should such requirements materialize, they would significantly drive any potential system design. The technology is available, but costs of implementing the technology are expected to be significant.

Finally, study findings show that effective small particle collision warning requires model enhancements, application of high accuracy orbit determination techniques, and improvements in understanding atmospheric drag and other non-gravitational effects. Further information on this study can be found in reference 4.

### Cost Estimates

The team concluded that a system having the capability for comprehensive debris tracking and cataloguing down to one cm out to 1,000 km would cost far more than a few million dollars. The study includes preliminary estimates of three candidate systems.

The first system is an active optical system based on a ladar in combination with a telescope and acquiring radar. The High Performance Carbon Dioxide Ladar Surveillance Sensor (HI-CLASS) system serves as the cost model for the ladar. Each HI-CLASS unit's acquisition cost is about \$100M. Implementing this system would require an increased aperture from 0.6 meter (m) to a four m class telescope to achieve the required sensitivity. A four m class telescope similar to AEOS would run about \$100M for the telescope. Site preparation and infrastructure is estimated to cost about \$50M. Due to the extremely small field of view, the ladar system would also require an acquisition capability such as the radar equivalent to Haystack in sensitivity for another \$100M and \$1,500/hour of operation. It is possible that the large aperture telescope could be augmented at additional cost to perform the acquisition function. To build a comprehensive network would require at least four to seven of these sites spread out globally. Thus, a single site would run \$350M plus annual operations and maintenance costs of several million; the network is estimated to cost from \$1.4B to \$2.5B.

A second system is a passive optical system. Operational restrictions from weather and only twilight observing require a multiplicity of sites spread globally. Passive telescopes are not suited for collision warning support due to the vagaries of both debris object orbits and weather and thus adjunct radar systems would also be needed for comprehensive coverage of small debris threats to on-orbit assets. The portion of this study for passive optical systems looked at a combination of search systems (one search telescope with a two to three m mirror and four chase telescopes of one m class) and catalogue maintenance systems (one m class). Global number of sites was estimated to be a minimum of seven search sites and a minimum of 25 maintenance sites. The system design also assumes the use of commercial off-the-shelf optical components and autonomy for remote sites. Cost estimates increase when redundancy at the sites is added. Acquisition costs were estimated to be on the order of \$400M. Autonomous operations of the smaller telescopes (or at least minimal hands-on operations) should be planned for, although in the initial operating configuration, crewed sites would most likely be needed. Before this cost estimate is considered realistic, substantially more technical analysis is required. Technologies

and optical concepts suggested here have not been demonstrated and validated and require additional review. With the Advanced Electro-Optical System (AEOS) obtaining first light later this year, an excellent tool appropriate for conducting relevant experiments to validate and refine a passive optical system concept for debris detection and tracking will become available. The smallness of our cost estimate may reflect our lack of understanding of the requirements and capabilities of this kind of a system. We, therefore, recommend that these costs be considered with care.

The third system under consideration would be a radar system. Preliminary cost estimates for expanding radar coverage for small debris tracking were based on the 1992 study by NASA and AFSPC for Space Station collision avoidance<sup>5</sup> which produced an estimate of \$500M for SSN enhancements and additional time on collateral radar assets. Review of that study found that the objectives are still valid; however, since that study's time, some SSN facilities have been closed or are marked for closure; Naval Space Command has established plans for upgrade of the surveillance fence (\$20 to \$50M depending on the radio frequency to which radars are to be upgraded); and AFSPC is developing modernization requirements and operational procedure changes to address International Space Station collision avoidance support. Another factor that could impact DOD surveillance and space control assets is international coordination risk object tracking and impact prediction. Our preliminary cost estimate for upgrading the current radar systems and procuring new sites for more complete global coverage adds \$200M to the 1992 estimate for a total of \$700M.

### Conclusion

The DOD, with the Air Force in the lead, and NASA have a comprehensive joint work plan on orbital debris. This joint plan carries out the recommendations and direction from the 1995 White House Office of Science and Technology Policy (OSTP) Interagency Report on Orbital Debris and the President's 1996 National Space Policy. The objectives of the joint work plan are primarily threefold. First, improve our understanding and monitoring of the debris environment through an appropriate mix of measurements and simulations. Second, work with other government agencies and with industry on voluntary design guidelines to minimize the future creation of space debris. Third, work with other spacefaring nations and international organizations to adopt common debris minimization practices. With regard to monitoring and cataloguing one centimeter size particles at 1,000 kilometers in altitude, should it become necessary, the cost would be significantly higher than a few million dollars.

### References

1. "Interagency Report on Orbital Debris", Office of Science and Technology Policy, November 1995.
2. "Report on Orbital Debris", Interagency Group (Space), February 1989, National Security Council, Washington D.C.
3. U.S. National Space Policy, 14 September 1996.

4. Spencer, D.B. (Editor), "Orbital Debris and the Environmental Restoration of Space: A Report to the Congressional Defense Committees", AFRL-VS-PS-TR-1998-1024, February 1998.
5. "Debris Collision/Maneuver Avoidance." Presentation made to the Associate Administrator for Space Flight and the Associate Administrator for Space Station, NASA HQ. Dec. 4, 1992

## Prediction and Control of Space Environments

**W. J. Burke (AFRL, Space Vehicles Directorate)**

The October 1957 launch of Sputnik was initially regarded as a national disaster. However, the unhindered overflight of U. S. territory by a Soviet satellite set the international precedent needed to implement Eisenhower's Open Skies policy that had previously been rejected by Secretary General Khrushchev. Satellite-borne cameras became forces for stability in the Cold War since images from space could reveal to both sides the true disposition of military forces and thus, minimize the risk of an accidental outbreak of war.. The strategic benefits of space assets were recognized through ratification of four treaties negotiated by the Kennedy, Johnson, Nixon, and Carter administrations:

- (1) The Nuclear Weapons Test Ban Treaty (1963),
- (2) The Treaty on Principles Governing the Activities of States in the Exploration and Use of Outer Space (1967),
- (3) The Convention on International Liability for Damage Caused by Space Objects (1972), and
- (4) The Convention on the Prohibition of Military or Any Other Hostile Use of Environment Modification Techniques (1979) [1].

These treaties reflect the perceptions of four different administrations that assuring the integrity of everyone's "national means of verification" is in our highest national interest.

With the demise of the Cold War, the wisdom underlying restrictions imposed by these treaties may seem obsolete. During the Gulf War, our monopoly on intelligence from space allowed the undetected flanking maneuver that abruptly ended the conflict. The concept of "space control" entered our working vocabularies. In light of our national treaty obligations, what might this mean? Certainly, it implies improving technologies to enhance our national defense operational capabilities in space and to assure that our systems perform reliably. Wishing, however, cannot make it so. Critical spacecraft components degrade and die or may fail catastrophically from interactions with hazardous environments or from hostile human forces. For the foreseeable future, natural processes pose significantly greater dangers to the reliable operation of our space assets than enemy action. Air Force investments in research to understand environmental hazards to space systems and to mitigate their worst effects are, therefore, in the strategic national interest.

Air Force satellites orbiting the Earth are about 150 M km (8 light minutes) from the Sun. In thinking about the Sun, most take the Aristotelian view, regarding it as a uniformly luminous body that appears much the same from one day to the next. Galileo's sunspots are easily dismissed as inconsequential surface blemishes. At least two things are wrong with this perception: (1) The Sun

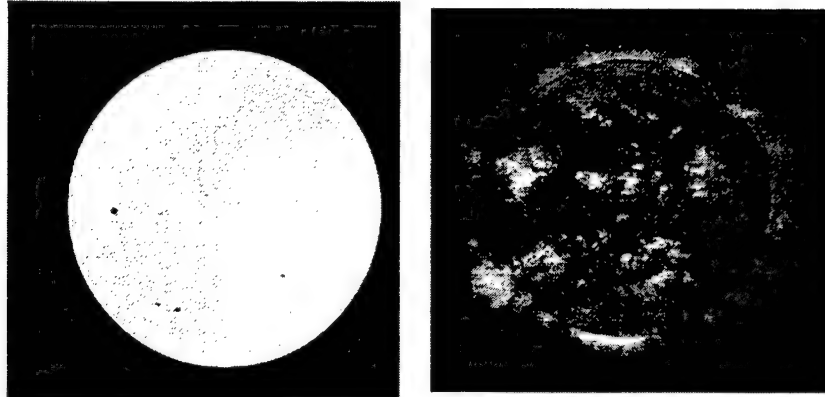


Figure 1. Simultaneous views of the Sun from the Yohkoh satellite at visible (left) and x-ray (right) wavelengths.

appears placid at visible wavelengths from the photosphere, but convulsive at ultraviolet and X-ray wavelengths. Figure 1 shows two simultaneous images from the Yohkoh satellite, one at visible wavelengths and the other at X-ray wavelengths. Sequences of such images reveal constant variability in X-ray emissions from the Sun. (2) The solar luminosity is  $4 \times 10^{26}$  J/s. Of this, about  $10^{17}$  J/s strikes the Earth. It is useful to consider these numbers in military terms;  $10^{13}$  Joules is the energy released during the detonation of a 1 megaton (MT) thermonuclear device. The Sun releases 40 trillion MT/s, of which  $10^4$  MT/s reaches the Earth. Small changes in solar electromagnetic or corpuscular emissions are very large by human standards and can significantly impact the operations of strategic space assets.

Of particular concern are geomagnetic storms that first manifest themselves as large, episodic variations in the Earth's magnetic field. Early satellites revealed that the Earth's magnetic field is confined by a solar wind that carries a weak magnetic flux. The most dangerous storms occur when large chunks of plasma and magnetic fields are violently ejected from the solar corona toward the Earth. These are aptly called coronal mass ejections (CMEs). The four sequential images in Figure 2 acquired by the SOHO satellite show the birth and initial expansion of a CME that caused a magnetic storm on Earth. The energy impacting the Earth's magnetic field can reach  $\sim 10^{14}$  J/s. Only 10 MT/s may seem small in comparison with the normal solar flux. However, visible photons only interact with the Earth's atmosphere and surface. The charged particles and electromagnetic fields of a CME act directly on the Earth's magnetic field and the plasma it contains. Present technologies allow continuous tracking of CME trajectories away from the Sun [2].

When a CME makes contact with the Earth's magnetic field the magnetosphere contracts. To achieve pressure balance with the new interplanetary environment, large amplitude magnetohydrodynamic (MHD) waves are launched inward. Energy is partitioned between compressional and transverse MHD waves. Until March 24, 1991, we thought that the compressional wave simply traveled toward Earth and produced positive magnetic spikes called storm sudden commencements.

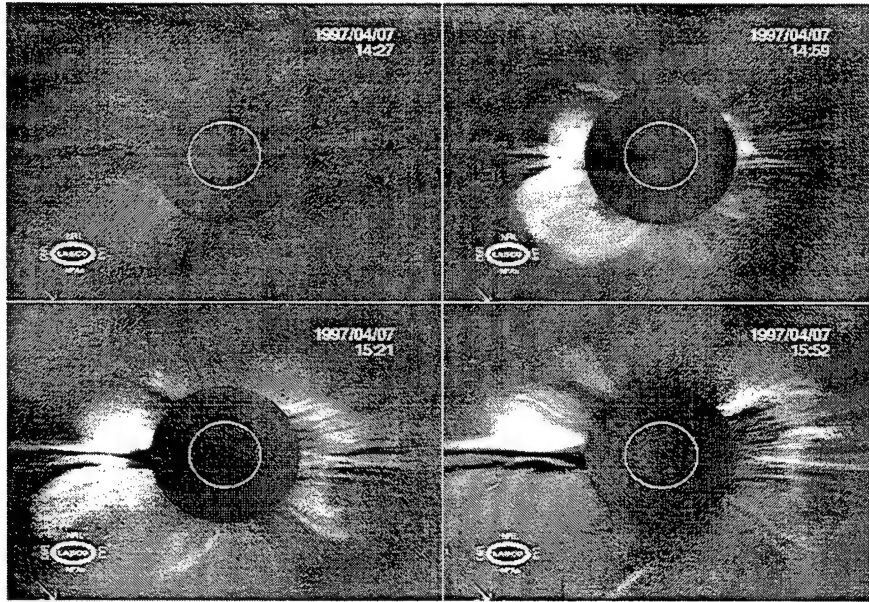


Figure 2. Development of a coronal mass ejection observed by the white light coronograph on the SOHO satellite.

Measurements from the Combined Release and Radiation Effects Satellite (CRRES) changed that perception. As an electromagnetic pulse passed CRRES, it was instantly bathed in multi-MeV electrons and ions. Figure 3 displays the fluence of 10.7 MeV protons observed by CRRES as a new radiation belt formed in minutes, not over days as normally occurs. The parent population for the high-energy ions and electrons of the new radiation belt was injected into the outer magnetosphere from the Sun by a solar flare observed at the birth of the CME [3]. The accelerated particles surfed the compressional wave into the inner magnetosphere, gaining energy all the way [4, 5]. The new radiation belt was still alive and well when CRRES died six months. After the launch of SAMPEX in July 1992, remnants of the injected electron population were identified and tracked, allowing estimates of radial and pitch-angle diffusion rates [6]. The March storm was unusual, but not unique. Another radiation belt creation event has been identified in the DMSP F7 database.

Why should the Air Force care about such events? Microprocessors and memory devices onboard satellites control the flow of information between sensors and spacecraft components. Typically chips are smaller than a penny. To paraphrase Churchill: never has so much depended on something so small. On the ground and in quiet space environments, processors and memory chips are highly reliable. However, in the radiation belts ionization trails created as corpuscular radiation passes through a memory chip can cause bit flips. Space charge can accumulate in wire insulation then migrate into computer components as a current burst [7]. Canadian and Japanese spacecraft were lost during magnetic storms when false commands were issued in this way. When operating for a long time in radiation environments chips decay simply from the accumulated effects of dose.

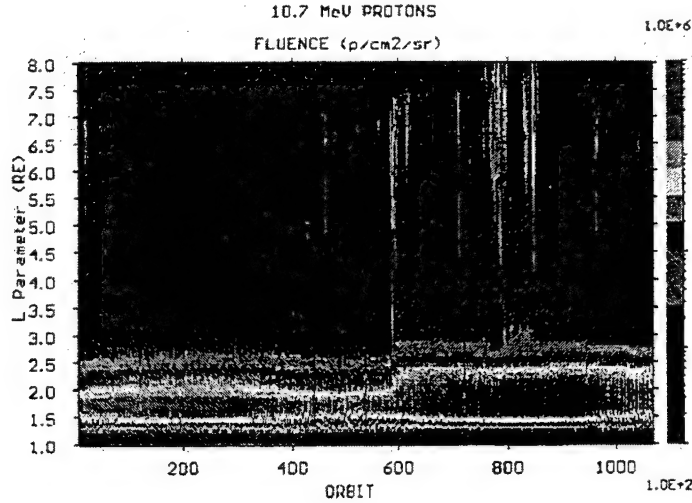


Figure 3. The fluence of 10.7 MeV protons observed during the lifetime of the CRRES satellite. The March storm occurred near the time of CRRES orbit #600. Energetic protons first appeared in the outer magnetosphere between  $L = 5$  and  $7$ . The shock caused by the CME impact carried them in to  $L = 2.5$ .

The transverse MHD waves launched by CME impacts carry magnetically field-aligned currents that couple the ionosphere to the energized interplanetary medium. Associated electric fields cause the ionospheric plasma to circulate in two large convection cells. Looking down from above the North Pole, one would see a clockwise rotating cell in the afternoon-evening sector and a counterclockwise rotating cell in the morning sector [8]. Satellite-borne sensors have measured total potential drops of  $>200$  kV and field aligned currents of  $\sim 10$  MA coupling the magnetosphere to the high-latitude ionosphere. Three things happen immediately after impact: (1) The high latitude ionosphere brightens with auroral light obscuring our ability to monitor strategic missile attack corridors on CONUS [9]. (2) The neutral atmosphere above 90 km heats up at a rate of  $2 \times 10^{12}$  J/s, or 12 MT/min. During the March 1989 magnetic storm, Joule heating of the upper atmosphere caused the temporary loss of about 3000 space catalog objects. (3) Electric fields permeate the magnetosphere energizing local ions and electrons. As a storm progresses, bright auroral forms appear at much lower latitudes than normal. The optical clutter in the night sky increases immensely and the mid-latitude ionosphere becomes turbulent disrupting long distance communications in areas where they are normally quite stable [10]. Energized electrons and ions migrate earthward to replenish the inner and outer radiation belts. Satellites at geostationary altitude charge to several tens of kilovolts [11].

In the initial and main phases of magnetic storms, electric fields at mid- to low-latitudes drive turbulence in the nightside ionosphere degrading the propagation of communications and navigation signals. Ionospheric turbulence significantly degraded both during the Gulf War and directly led to development of the Communications/Navigation Outage Forecast System (C/NOFS) satellite that is scheduled for launch in 2003. The goal of C/NOFS is to develop the tools needed to predict ionospheric disturbances and allow the Air Force to avoid potentially harmful disruptions of service.

Since we are now in a solar maximum phase the severe impact of solar storms may sound like grim news for the nation with the largest defense investment in space. But the last solar maximum taught us valuable lessons. The solar-terrestrial physics community is learning to exploit new technologies to mitigate the effects of storm-time disturbances.

The first step is to ensure that satellite operators have adequate warning of major storms. In January 1997 the SOHO and Yohkoh satellites observed the birth of a CME and optically tracked it to the Earth. The ACE satellite, now orbiting about a million miles upstream of the Earth, regularly monitors the solar wind density and speed and the interplanetary magnetic field. From these measurements we can predict ~45 minutes ahead of time the degree of magnetosphere compression and the electric potential that will be imposed on the magnetosphere-ionosphere system. Together with information from the DMSP and TIROS satellites we have the initial and external conditions to drive the Magnetospheric Specification and Forecast Model and the Ionospheric Specification Model developed for the 55th Space Weather Squadron.

A second practical step is to raise situational awareness so that the controllers of space systems know the radiation levels in which satellites are operating. Figure 4 shows a Compact Environment Anomaly Sensor (CEASE) developed by AFRL [12]. With 1 kg of mass and 2 W of power CEASE can specify the radiation in which a satellite is flying. When anomalies occur, engineers can take effective protective steps. For example, satellites flying at geostationary altitudes should carry small plasma thrusters which would activate automatically to discharge spacecraft surfaces as soon as onboard computers recognize that the host vehicle is in a charging environment [13].

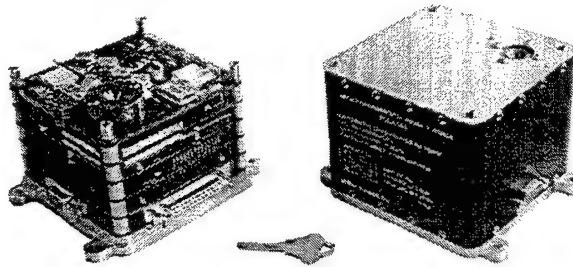


Figure 4. The CEASE sensor to monitor satellite radiation environments.

A third practical step is to develop technologies to clear the radiation belts of energetic particles within a day after magnetic storms occur. Dose rates to microelectronic components would be greatly reduced and operational lifetimes prolonged. Two facts should be recognized. (1) The radiation belts are not dangerous because they contain a large number of energetic particles. Their total content of  $10^{20}$  particles is roughly the same as the number of molecules in a thimble of air. Rather, the danger comes from trapped particles with enough energy to penetrate shielding and damage microelectronic devices. Outside the radiation belts the Earth's magnetic field is simply too

weak to trap these particles. If the average energy of the trapped particles is 6 MeV, then the total energy of the radiation belts is only  $\sim 10^5$  MT. We should be able to deal with this. (2) The radiation belts are generally cleared of energetic particles within a few weeks of a storm [14] by naturally occurring, low frequency radio waves. These waves interact strongly with trapped electrons and protons diffuse them out of the radiation belts into the upper atmosphere. A few strategically placed satellites with antennae emitting very low frequency waves at a few watts of power could accelerate these natural diffusive processes.

The U. S. currently enjoys unchallenged dominance in the use of space for national defense. No other nation relies so heavily on space for defense, and few nations are in a position to challenge that dominance. The primary hazards to which our space assets are exposed, therefore, arise simply because of the dynamics of solar activity.

We have been in space for a few decades, and must proceed with caution as we venture out onto this treacherous high ground, which is intermittently swept by violent storms. Only in the past decade have we introduced microelectronics to the space environment, and we do not yet know if they can survive the solar storm of the century. As stewards of our national space assets, the Air Force bears the significant responsibility to understand the environments in which our space systems operate. This responsibility is of vital national concern. In the last 20 years we have developed techniques to study the Sun that far transcend our normal sensing abilities. Through our analyses of measurements and simulations of the coupled magnetosphere-ionosphere system we now understand much about local responses and their impact on space systems.

Storm warnings reduce risk and allow time to implement procedures to mitigate catastrophic events. Satellite survivability improves when controllers power down instruments or take active measures to defend spacecraft in hazardous environments. Viewed from this perspective, a significant investment in forecasting space weather is in the highest national interest. By adapting what we have already learned about solar-terrestrial interactions, we have such capabilities within reach. Today space weather forecasting is far more a challenge to our wills than to our intellects.

Acknowledgement: Research presented in this report was supported by the Air Force Office of Scientific Research Task 2311G5.

#### References:

- [1] E. J. Osmanczyk, *The Encyclopedia of the United Nations and International Agreements*, Taylor and Francis, Philadelphia, 517-518, 1985.
- [2] N. J. Fox, M. Peredo, and B. J. Thompson, "Cradle to grave tracking of the January 6 - 11, 1997 Sun-Earth connection event", *Geophys. Res. Lett.*, 25, 2461-2464, 1998.
- [3] M. S. Gussenhoven, E. G. Mullen, and M. D. Violet, "Solar particle events as seen on CRRES", *Adv. Sp. Res.*, 14, 619-629, 1994.

- [4] X. -L. Li, I. Roth, M. Temerin, J. R. Wygant, M. K. Hudson, and J. B. Blake, "Simulation of the prompt energization and transport of radiation belt particles during the March 24, 1991 SSC", *Geophys. Res. Lett.*, 20, 2423-2426, 1993.
- [5] M. K. Hudson, A. D. Kotelnikov, X. -L. Li, I. Roth, M. Temerin, J. Wygant, J. B. Blake, and M. S. Gussenhoven, "Simulation of radiation belt formation during the March 24, 1991 SSC", *Geophys. Res. Lett.*, 22, 291-294, 1995.
- [6] M. D. Looper, J. B. Blake, R. A. Mewaldt, J. R. Cummings, and D. N. Baker, "Observations of remnants of the ultra relativistic electrons injected by the strong SSC of March 24, 1991", *Geophys. Res. Lett.*, 21, 2079-2082, 1994.
- [7] M. D. Violet and A. R. Fredrickson, "Spacecraft anomalies on the CRRES satellite correlated with the environment and insulator samples", *IEEE Trans Nucl. Sci.*, 40, 1512-1520, 1993.
- [8] J. P. Heppner and N. C. Maynard, "Empirical high-latitude electric field models", *J. Geophys. Res.*, 92, 4467-4489, 1987.
- [9] J. D. Craven, L. A. Frank, C. T. Russell, E. J. Smith, and R. P. Lepping, "Global auroral response to magnetospheric compressions by shocks in the solar wind: two case studies", in *Solar Wind-Magnetosphere Coupling*, ed. by Y. Kamide and J. A. Slavin, Terra Publ. Co., Tokyo, 367-380, 1986.
- [10] W. J. Burke, A. G. Rubin, N. C. Maynard, L. C. Gentile, P. J. Sultan, F. J. Rich, O. de La Beaujardiere, C. Y. Huang, and G. R. Wilson, "Ionospheric disturbances observed by DMSP at mid to low latitudes during the magnetic storm of June 4 - 6, 1991", *J. Geophys. Res.*, 105, in press, 2000.
- [11] H. B. Garrett, "The charging of spacecraft surfaces", *Rev. Geophys. Space Phys.*, 19, 577-616, 1981.
- [12] B. K. Dichter, J. O. McGarity, V. T. Jardonov, D. J. Sperry, A. C. Huber, J. A. Pantazis, E. G. Mullen, and M. S. Gussenhoven, "Compact Environmental Anomaly Sensor (CEASE): A novel spacecraft instrument for *in situ* measurements of environmental conditions", *IEEE Trans Nucl. Sci.*, 45, 2758-2764, 1998.
- [13] S. T. Lai, "An overview of electron and ion beam effects in charging and discharging of spacecraft", *IEEE Trans Nucl. Sci.*, 36, 2027-2032, 1989.
- [14] L. R. Lyons, and D. J. Williams, *Quantitative Aspects of Magnetospheric Physics*, D. Reidel Publ. Co., 133-206, 1984.

# First GEO Survey Test Observations with the ESA 1 m Telescope in Tenerife

*T. Schildknecht, U. Hugentobler, M. Ploner  
Astronomical Institute  
University of Bern  
Sidlerstrasse 5  
CH – 3012 Bern, Switzerland*

ESA has installed a 1 m telescope in Tenerife (on Canary Islands) which is partly dedicated to optical space debris surveys. The instrument is equipped with a 4k by 4k CCD mosaic, automatic tracking, data acquisition, and image processing software. First tests have been carried out from July to September 1999. The observation scenario consisted of survey series interrupted by follow-up observations for uncorrelated objects. The latter were scheduled using orbit information from the on-line processing. The analysis of 6473 CCD frames from 13 nights, covering 895 square degrees, yielded 56 catalogued and 150 uncatalogued objects. Objects as small as magnitude +20 were detected. This limited test survey confirms the existence of a previously suspected large population of small uncatalogued debris objects in the geostationary ring.

## Introduction

The growing population of space debris increases the treat to operational spacecraft and manned spaceflight. This fact has been recognized by the space agencies. Efforts to characterize the current debris population and its evolution have been intensified during previous years. The majority of the investigations focused on the low Earth orbit (LEO) region where the spatial density of objects is highest. The LEO region is furthermore of special interest, because it is the region of manned spaceflight, and in particular the location where the international space station (ISS) is operating.

On the other, hand there is the geostationary ring (GEO) region constituting a unique environment for science and for commercial applications. Spatial densities of debris objects in this region are currently – as far as we know – much lower than in certain LEO altitudes. In contrast to the situation in LEO at altitudes below 1000 km where atmospheric drag limits the lifetime of objects there is, however, no natural removal mechanism in GEO. All objects will stay there ‘forever’, the population of debris objects will grow only!

Currently, the GEO population of debris objects smaller than  $1 \text{ m}^2$  is mostly unknown. Mission related objects and several observed explosions must have produced a substantial amount of small objects, on the other hand.

In view of this situation, several space agencies started to perform optical observations of the GEO ring. NASA conducts optical surveys with a 0.32 m Schmidt telescope equipped with a CCD detector (from 1992 to 1994 at Mt. Haleakala, Maui, Hawaii, and from 1998 onwards in Cloudcroft, NM, (Africano et al., 2000)). The European Space Agency (ESA) has also

initiated its own program for optical observations of space debris using a 1 m Ritchey Chrétien telescope on Tenerife (Canary Islands).

## The Space Debris Observation System on Tenerife

ESA has installed a 1-meter Zeiss telescope at the Teide Observatory on Tenerife. This instrument will primarily serve as ground check-out terminal for the optical link between ARTEMIS and SPOT-4 (SILEX experiment). As the general characteristics of the telescope are suited for the detection and tracking of space debris, the main part of the remaining observation time is dedicated to debris related investigations. The instrument shall be used for detection, identification and tracking of space debris objects in LEO, GTO, and GEO, with priority given to the high altitude orbit regions. ESA has performed the necessary upgrades of the instrument (telescope and camera) and the software (instrument control and image acquisition as well as data processing and management) in order to achieve a highly automated survey system.

The optical system dedicated to space debris observations comprises a focal reducer system with a spherical secondary mirror and a 4096 x 4096 pixel CCD mosaic camera as detector. The observation system is able to image a field of 0.7 degrees several times per minute.

Given the high data rate of up to 64 MB per second it was necessary to equip the system with efficient software tools. Observation schedules are generated off-line and automatically executed by the instrument and data acquisition process. A crucial part of the system is the on-line data processing component performing the on-line search and near real time detection of moving objects. This component is also performing first orbit determination and correlation with catalogues.

## Detection and Observation Technique

The detection technique is based on an algorithm comparing several consecutive frames of the same field in the sky. Fixed background stars are identified on a series of frames and the remaining part of the frames scanned for any additional objects. The process includes filters to reject cosmic radiation events and other image 'defects'. In the next step the remaining 'moving' objects detected on the single frames are correlated over the series. A candidate object must appear on several frames and exhibit an apparent motion within ranges given by the types of orbits looked for (GEO, or LEO). After the astrometric reduction circular orbits for all detected objects are determined. As a last step the resulting elements and positions are correlated with the catalogue.

At this point the operator may decide to interrupt the scheduled survey sequence and execute some follow-up observations of newly detected objects. The decision depends on the type and objective of the survey. Follow-up observations are necessary in all cases where the build-up or maintenance of a catalogue (even of a temporary one) of debris is required.

Typically an observation series of a particular field in the sky takes about 30 minutes. The individual frames are exposed for 1 to 5 seconds and then read out at a rate of two frames per minute. The rather poor duty cycle is given by the time needed to read out the CCD and to process the data on-line. In order to improve the S/N for the moving objects we do not track sidereostatically during the exposures but with the expected motion of the objects (i.e., we

stare in a Earth fixed direction for GEO objects). The resulting area surveyed by one series is a single 0.7 X 0.7 degree field in an inertial system or a 7.5 x 0.7 degree field in an Earth fixed coordinate system.

## The Test Campaign

A first very limited test campaign has been conducted in the context of system tests of the ESA 1 m telescope from July to September 1999. The campaign consisted of 13 nights with a total observation time of 49 hours (Table 1). The observation directions were chosen in a such way that GEO objects were optimally illuminated by the sun. This implies a direction near the Earth shadow cone. All frames were exposed for two seconds and the series arranged in a way that a GEO object would appear on average on three consecutive frames.

	Surveys	Follow-ups
Number of series	100	102
Number of frames	5439	1034
Scanned Area	895 deg <sup>2</sup>	
Total Observation Time	49 hours	
Total Image Data	52 GB	

Table 1: Observation statistics for the autumn 1999 test campaign.

Figure 1 shows the distribution of the searched fields as seen in the horizon system from Tenerife. The survey was not homogeneous, neither in terms of sampled longitude/latitude space, nor in the orbital element space (we were most interested in objects on ‘high inclination’ orbits). A small section of a typical search frame containing two faint uncorrelated objects may be found in Figure 2.

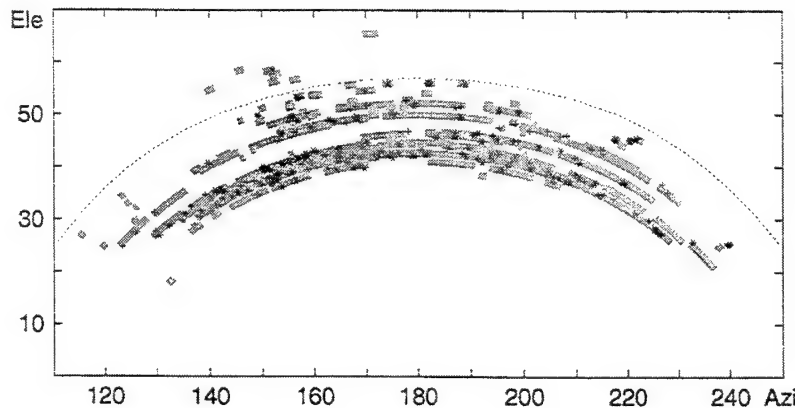


Figure 1: Search fields of the autumn 1999 test campaign. The dashed line indicates the location of the GEO ring as seen from Tenerife. Crosses indicate detections of correlated objects, and asterisks indicate detections of uncorrelated objects.

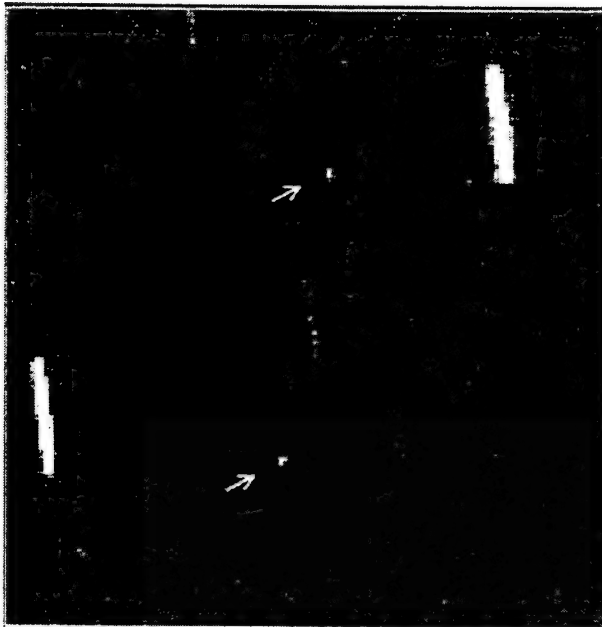


Figure 2: Section of a typical search frame containing two faint, uncorrelated objects (arrows). The background stars produced trailed images on the 2 second exposure.

## Results

All observation series were analyzed on-line. The process identified 360 single detections of correlated and 696 detections of uncorrelated objects (see Table 2). An off-line correlation over all series of all nights using orbit determination revealed 56 correlated and 150 uncorrelated objects. The number of detections per object and the number of nights per object is smaller for the uncorrelated objects. This is because the faint objects have a greater probability not to be detected at all, and because some uncorrelated objects may in fact be identical. Finally, for a given survey scheme the correlated objects have on average a greater probability to be re-observed in different nights due to their orbital characteristics.

	Correlated Objects	<i>Uncorrelated Objects</i>
Detections (multiple sights)	360	696
Objects	<b>56</b>	<b>150</b>
Number of Detections per Object	6.4	4.6
Number of Nights per Object	1.77	1.11

Table 2: Number of detections and objects. The first line gives the sum of detections on all single frames. The second line contains the number of objects after correlating orbits within single nights and among all nights of the campaign.

The visual magnitude distribution of the detected correlated and uncorrelated objects is given in Figure 3. The distribution is bimodal with the correlated objects clustered around

magnitude 12.5, and a large population of uncorrelated objects in the range from magnitude 15 to 21. There are a few bright objects which did not correlate with the available catalogue, most likely due to poor quality of the corresponding elements in the catalogue (e.g., objects which were recently maneuvered). In addition some classified objects were not contained in the reference catalogue.

It is important to note that the decrease in number of objects fainter than magnitude 18 is entirely due to the limiting magnitude of the observation system. The luminosity function beyond magnitude 18 could therefore still increase!

The space debris modeling community is, naturally, interested in physical properties of the population. From broad band magnitudes, however, we can only derive rough size estimates by assuming an average albedo for the objects. The relation between GEO object size and magnitude assuming an albedo of 0.08 (see Henize et al., 1992) is given in Table 3.

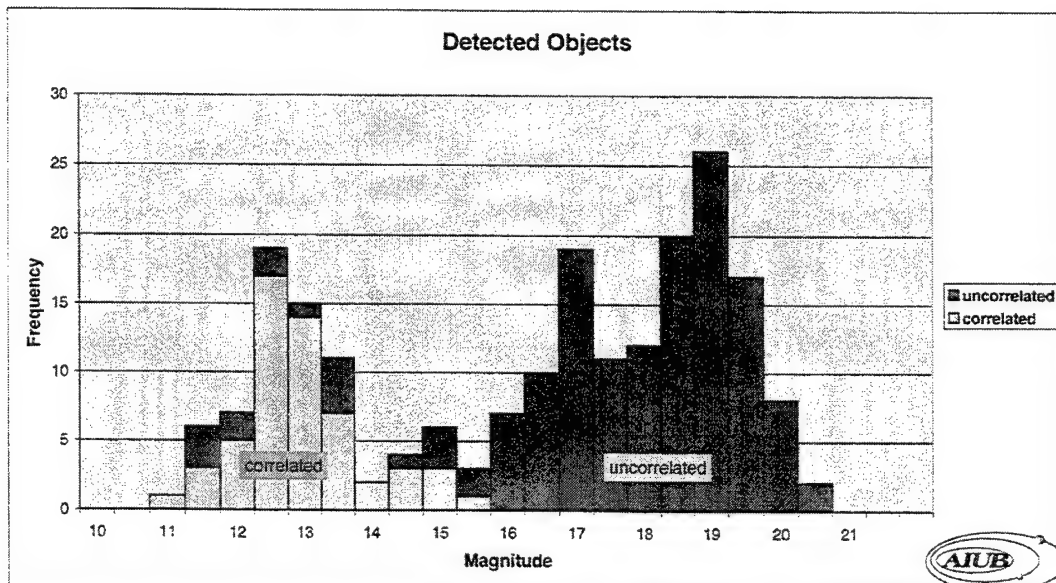


Figure 3: Visual magnitude distribution of correlated and uncorrelated objects.

$m_{vis}$	12	14	16	18	20
area [ $m^2$ ]	34	5.3	0.85	0.13	0.021
lin. size [m]	5.8	2.3	0.92	0.37	0.15

Table 3: GEO object area and linear size for given magnitude  $m_{vis}$  assuming an albedo of 0.08.

The distribution of the orbital elements, in particular that of the inclination versus the right ascension of the ascending node (see Figure 4) may give some indications concerning the potential sources of debris objects. The main structure observed in Figure 4 is well known. It

is caused by the precession of the orbital planes, due to the Earth's oblateness and luni-solar perturbations. There are, however, uncorrelated objects in unexpected regions, e.g., at high inclinations for ascending nodes between 100 and 150 degrees. A more detailed interpretation of the Figure 4 is difficult because of the very inhomogeneous sampling of the orbital element space by the observations. Apparent 'clumping' (e.g. at 30 degree ascending node, and 16 degree inclination) may be a pure observational selection effect.

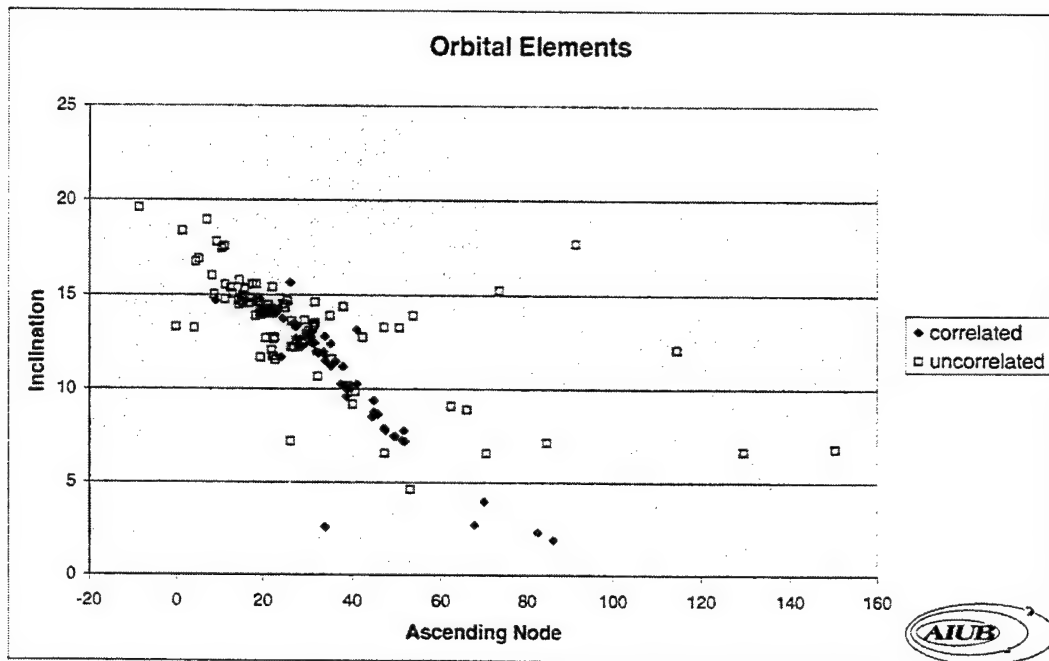


Figure 4: Distribution of orbital elements. Diamonds indicate correlated objects, and open squares uncorrelated objects, respectively.

## Conclusions

The first GEO survey test campaign with the ESA 1 m telescope at Tenerife was very successful. The system has proven its capability to detect space debris as faint as magnitude 20.5, corresponding to a physical size of about 20 centimeters.

The observed luminosity function is bimodal. About 75% of the objects in the observed magnitude range did not correlate with the available catalogue. The population of correlated objects is centered around magnitude 12.5 with the faintest members located at magnitude 15.5 corresponding to an object size of about 1 meter. The population of uncorrelated objects is steadily increasing towards fainter magnitudes. There is no cutoff seen at the low size end down to the limiting magnitude of the observation system.

This very limited survey confirms the existence of a previously suspected large population of small uncatalogued debris objects in GEO.

## **References**

Henize, K. G., J. Stanley, Optical Observations of Space Debris, *Orbital Debris: Technical Issues and Future Directions*, A. E. Potter (Ed.), NASA Conference Publication 10077, pp. 241--244 (1992)

Africano, J.L., P.F. Sydney, K.S. Jarvis, E.G. Stansbery, and M.K. Mulrooney, CCD Debris Telescope Observations of the Geosynchronous Orbital Debris Environment, NASA JSC Publication JSC-28884 (2000).

Schildknecht, T., U. Hugentobler, A. Verdun, Algorithms for Ground Based Optical Detection of Space Debris, *Advances in Space Research*, Vol. 16, Nr. 16, edited by W. Flury, pp. 47--50 (1995).

## **A GEO Debris Survey using NASA's CCD Debris Telescope (CDT)**

J. L. Africano, J. V. Lambert, P. F. Sydney (Boeing North American),  
E. G. Stansbery (NASA/Johnson Space Center), and K. S. Jarvis (Lockheed Martin Space Operations)

The National Aeronautics and Space Administration (NASA) has been using the Charged Coupled Device (CCD) Debris Telescope (CDT), a transportable 32-cm Schmidt telescope located near Cloudcroft, NM, to help characterize the debris environment in Geosynchronous Earth Orbit (GEO). The CDT is equipped with a SITe 512 X 512 CCD camera. The pixels are 24 microns square (12.5 arcseconds) resulting in a 1.7 by 1.7 degree field-of-view. The CDT system is capable of detecting 17<sup>th</sup> magnitude objects in a 20 second integration which corresponds to a ~0.6-meter diameter, 0.20 albedo object at 36,000 km. The telescope pointing and CCD operation are computer controlled to automatically collect data for an entire night. The CDT has collected more than 775 hrs of data since November, 1997. This report describes the collection and analysis of 68 hours of data collected over 10 nights.

The CDT used a search strategy optimized to collect data at low solar phase angle (where satellites, including debris, should be brightest). The strategy also utilized the fact that all objects must pass over the Earth's equator. By observing near the GEO belt, all uncontrolled objects will sooner or later pass through the field-of-view. Specifically, the search strategy used by the CDT was to observe a strip of GEO space eight degrees tall, centered at minus five degrees declination (the GEO belt as viewed from Cloudcroft). This strip either leads or follows the Earth's shadow by about ten degrees. The actual length of the strip depends upon the length of the night and the elevation of the Earth's shadow. The search pattern starts in the east at the beginning of the night and gradually moves to the west during the remainder of the night, tracking the Earth's shadow.

Studies have shown that the orbits of uncontrolled GEO objects oscillate around the stable Laplacian plane, which has an inclination of 7.5 degrees with respect to the equatorial plane. This oscillation is dominated by the combined effects of the Earth's oblateness (J2 term), and solar and lunar perturbations. The inclination oscillation period is about 50 years. Plots of the daily motion for cataloged GEO objects in Right Ascension vs. Declination as viewed from Cloudcroft show that most objects are grouped on one side or the other of the GEO belt at any given time. Using this knowledge, the search strategy can be altered to provide higher piece counts per observation.

The telescope is pointed to a position in the sky (a search field) and parked during each exposure. Due to the Earth's rotation, the stars leave streaks in the east-west direction. Objects orbiting the Earth will appear as streaks or points depending on their altitude and inclination. The actual observing sequence consists of a series of four exposures taken of approximately the same field. Each exposure is 20 seconds in duration with a 15 second "dead time" between exposures used to read out the CCD and to reposition the telescope. On average, 200 fields are collected per night, or 800 individual images.

Data from the CDT is processed using a software package originally developed for the “Raven” class telescope by the Air Force Research Laboratory (AFRL). The software has been extensively modified in order to account for instrumental differences between Raven and the CDT. The software package performs the following steps:

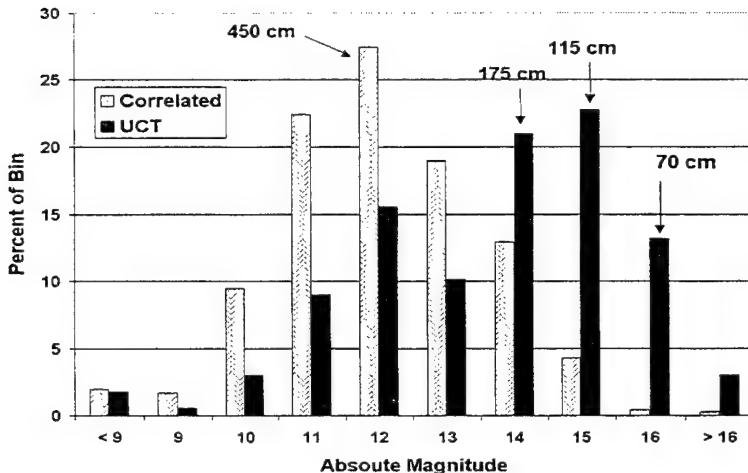
- 1) Image is calibrated for dark, bias and flat field effects
- 2) Sky background is determined and subtracted
- 3) x, y pixel positions for the center of each star streak is determined
- 4) Magnitude of each star streak is determined
- 5) x, y of the centroid of each satellite is determined
- 6) Table of Hubble Guide Star Catalog stars is created based on “commanded” pointing
- 7) Gauss’ triangles method for field matching
  - a) Determine true pointing (as opposed to “commanded”)
  - b) Map x, y pixel locations to RA, DEC using 6<sup>th</sup> order plate solution
- 8) Determine location and magnitude of each satellite

Serious pointing errors were detected during the initial data reduction runs. These errors were both large jumps from night to night and smaller systematic trends throughout a night. The large jumps were as much as three fovs. Manual procedures were developed to determine where the telescope was actually pointing at the beginning of each night based upon the star background. Procedures were also developed to automatically track the pointing error trends throughout the night. Upon investigation into the cause of these problems both software and hardware problems were found and fixed. Data collected since November, 1999 should be much better behaved.

Subsequent processing steps performed are:

- 1) identify objects as either known, cataloged objects (correlated) or uncorrelated targets (UCTs)
- 2) estimate orbital elements
- 3) associate identified UCTs which appear in multiple fields (within a night, no attempt has been made to correlate UCTs from night to night)
- 4) estimate the size of detected objects.

The following figure shows the size distribution of objects detected in the data processed to date (68 hours over 10 nights). The peak of the absolute magnitude distribution for the correlated targets corresponds to objects having average diameters of 4.5 meters. This result is in general agreement with the known sizes of intact satellites. The peak of the absolute magnitude distribution for the UCTs corresponds to objects having 1.1 meter diameters and then starts to roll off. Almost 40% of the UCTs have diameters 1.1 meters or smaller. The roll off in the distribution reflects detection capability of the CDT and does not reflect the true nature of the population.



Absolute magnitude and derived size distribution.

In summary, the CDT technology, like other small telescope programs has proven itself to be a cost effective way of providing large amounts of data on objects as small as 70 cm in diameter in GEO. Data collection is automated and very efficient. Data processing on the other hand, is time consuming at this point. However, the time to process data is improving and has been dramatically reduced, by more than 60% since February, 1999. Steady improvements are being made to the reduction code to increase the detection sensitivity, reduce the number of false detections and to increase the speed of the processing.

# Probability of Collision In the Geostationary Orbit

Raymond A. LeClair

The advent of geostationary satellite communication 37 years ago, and the resulting continued launch activity, has created a population of active and inactive geosynchronous satellites which will interact, with genuine possibility of collision, for the foreseeable future. As a result of the failure of Telstar 401 three years ago, MIT Lincoln Laboratory, in cooperation with commercial partners, began an investigation into this situation. Under the agreement, Lincoln worked to ensure a collision did not occur between Telstar 401 and partner satellites and to understand the scope and nature of the problem. The results of this cooperative activity and recent results to carefully characterize the actual probability of collision in the geostationary orbit are described.

**O**n 11 January 1997 Telstar 401 failed on orbit in the geostationary belt. It will now oscillate indefinitely near the geopotential well at 105 degrees West longitude, next year passing within ten to thirty kilometers of twenty-two active satellites stationed between 97 and 113 degrees West longitude. The behavior of Telstar 401, typical of inactive geosynchronous satellites, led six commercial satellite operators (AMSC, DirecTV, GE Americom, PanAmSat, SATMEX and Telesat Canada) to enter into a Cooperative Research and Development Agreement (CRDA) with MIT Lincoln Laboratory. The resulting cooperative activities sought to assess and respond to the threat posed by Telstar 401. With over 40 years of space surveillance technology development and sensor operations, MIT Lincoln Laboratory was recognized to be uniquely positioned to properly address this geosynchronous encounter threat. The longitude oscillation of Telstar 401 and resulting encounters with active satellites are shown in Figure 1.

The initial Geosynchronous Encounter Analysis (GEA) CRDA spanned two years beginning in mid 1997. During this period, Lincoln Laboratory provided timely warning of encounters between Telstar 401 and partner satellites and precision orbits for these objects for use in avoidance

maneuver planning. In all, 32 encounters between Telstar 401 and a partner satellite were supported in 24 months leading to nine avoidance maneuvers incorporated into routine station keeping and six dedicated avoidance maneuvers. Abbot, Thornton and Whited [1] describe the details of the support provided for many of these encounters, a process which has led to a validated concept of operations for encounter support at Lincoln.

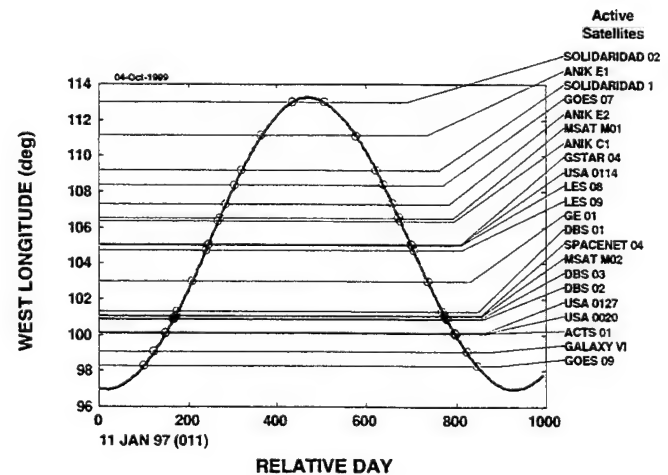
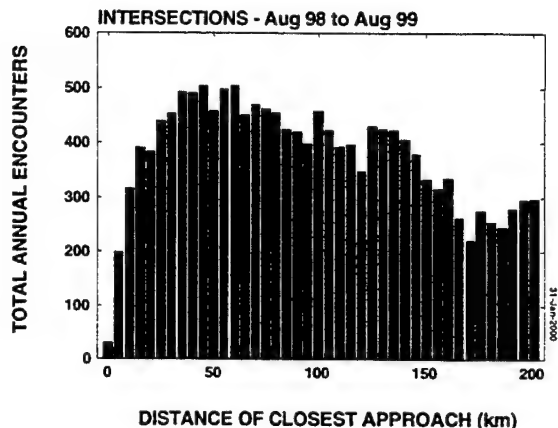


Figure 1. Telstar 401 Encounter Situation



**Figure 2.** Distribution of Encounter Distance of Closest Approach

In addition, as part of the cooperative agreement, a number of important research objectives were accomplished. Abbot and Thornton [2] undertook calibration of partner satellite ranging data to establish procedures for routine receipt, calibration and processing of partner ranging data for use in precision orbit determination. Abbot and Sharma [3] investigated the optimum mix of sensor data needed to meet orbit accuracy requirements for encounter support, finding that a combination of radar and optical data synergistically produces precision orbits with relatively few observations.

In order to determine the magnitude of the geosynchronous encounter threat, LeClair [4] determined the number of encounters between all active and inactive geosynchronous objects. An encounter was defined as a difference in geocentric radius less than 200 km and in longitude less than 0.2 degrees at the locations of the orbital plane intersections. Active satellites were considered to reside at the center of their station keeping box given by the semi-major axis and longitude of the ascending node of their orbit. Inactive satellites which could approach the geostationary radius (6.61 earth radii (er) or 42,200 km) within 200 km were propagated from August 1998 to August 1999 using DYNAMO, a precision numerical propagator developed at MIT Lincoln Laboratory and discussed more fully below. The resulting distribution of encounters as a function of the distance of closest approach is shown in Figure 2. Considering only those encounters with a distance of closest approach not more than 50 km, the results indicate 4152 encounters, between an active,

geostationary satellite and an inactive, geosynchronous object, will occur annually.

Although it was the failure of Telstar 401 and the resulting activity at Lincoln Laboratory which led to the recognition of this geosynchronous encounter problem, the situation arises as an unavoidable consequence of the recent launch history of geostationary communication satellites. The first successful geostationary communication satellite, Syncom II, launched in 1963 inaugurated a flurry of geostationary launch activity which gave rise to the initially rapid but continuing increase in the geostationary satellite population shown in Figure 3, using data from the Lincoln Space Surveillance Center (LSSC) databases. Initially this launch activity was dominated by military launch activity but during the mid 1980s to mid 1990s commercial launch activity began to dominate.

As a result of the encounter support concept of operations developed and validated at MIT Lincoln Laboratory and the accompanying investigation into the scope and nature of the problem, the initial two year CRDA has been extended for an additional two years. As part of the continued CRDA activity, Lincoln Laboratory will develop a system to monitor encounters between all cataloged threatening resident space objects and GEA CRDA partner satellites. Objectives of the system include automation of encounter support to produce the highest quality orbits and fewest false alarms while minimizing sensor time and analyst involvement. A conceptual block diagram of the Geosynchronous Monitoring and Warning System (GMWS) is shown in Figure 4.

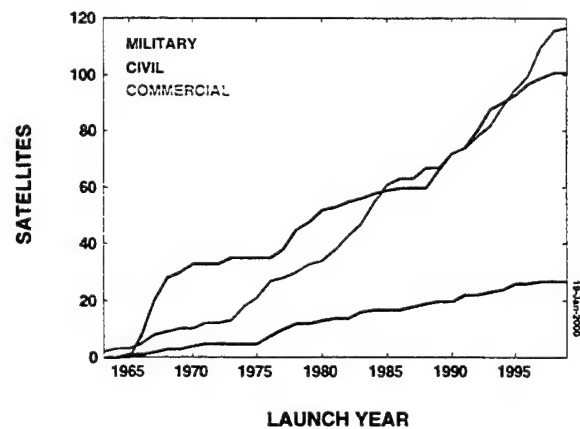


**Figure 3.** Thirty Years of Cumulative Launch Activity

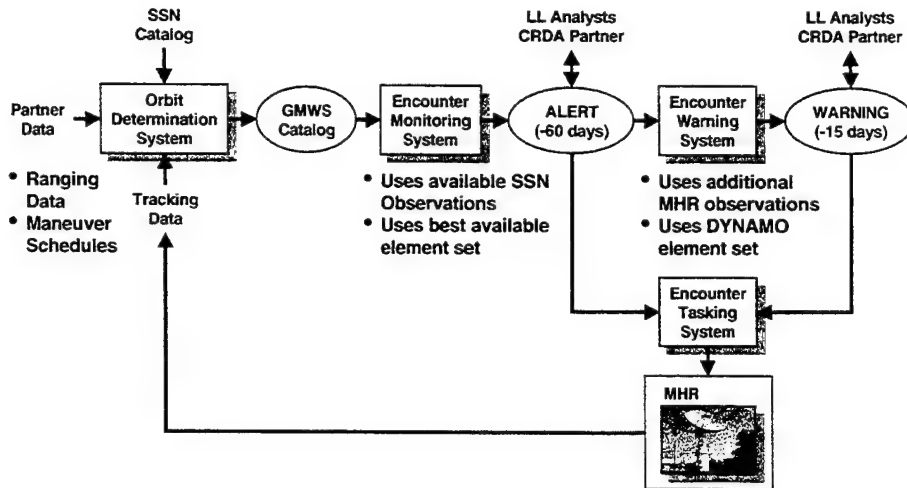


**Figure 4.** Geosynchronous Encounter Monitoring and Warning System Concept

In addition to the development of the GMWS, Lincoln has taken a careful look at the probability of collision in the geostationary orbit, the description of which forms the purpose of this document.

### Probability of Collision

Several authors have considered the problem of on-orbit collisions. For geostationary satellites, Hechler and Van der Ha [5] consider the probability of collision for the population of geostationary satellites on-orbit in 1981 and determine an annual collision rate of  $6 \times 10^{-6}$ . In the same year, Kessler [6] presents a straightforward approach which may be used to estimate the collision probability between orbiting objects in general. Kessler's approach is adapted and discussed below. Much more recently, a number of authors, including Alfriend [7] (and others) and Chan [8], have considered the probability of an on-orbit collision using the orbital covariances. The work by Chan, funded as part of the Iridium program by Motorola, is representative of this approach and discussed below.

#### Probability of Collision based on Orbital Covariances

By noting that the covariance matrices for the two orbits under consideration may be transformed to a common coordinate system, and noting that the random variables for the two orbits are independ-

ent, Chan shows that the covariances may be combined as a sum. Then by establishing an encounter coordinate system with  $xz$  plane and origin defined by the expected relative velocity and separation at the point of closest approach and aligning the  $x$  axis with the two objects, Chan arrives at a bivariate normal distribution for the separation at the point of closest approach with joint probability density function

$$f_2(x, z) = \frac{1}{2\pi\sigma_x\sigma_z\sqrt{1-\rho_{xz}^2}} \times e^{-\left[\left(\frac{x}{\sigma_x}\right)^2 - 2\rho_{xz}\left(\frac{x}{\sigma_x}\right)\left(\frac{z}{\sigma_z}\right) + \left(\frac{z}{\sigma_z}\right)^2\right]\left[\frac{1}{2(1-\rho_{xz}^2)}\right]} \quad (1)$$

where  $\sigma_x$ ,  $\sigma_z$  and  $\rho_{xz}$  are the separation standard deviations and correlation coefficient. For the case in which the collision radius,  $r_a$ , is much less than  $\sigma_x$  and  $\sigma_z$ ,  $f_2(x, z)$  may be integrated over the collision area, to obtain the collision probability  $P = \iint_A f_2(x, z) dx dz$ , by using the constant value  $f_2(x_c, 0)$ , where  $x_c$  denotes the expected value of the separation at closest approach, to obtain

$$P = \frac{r_a^2}{2\sigma_x\sigma_z\sqrt{1-\rho_{xz}^2}} e^{-\left[\frac{x_c^2}{2\sigma_x^2(1-\rho_{xz}^2)}\right]} \quad (2)$$

Although not noted by Chan, for the case in which  $x_e$  is small relative to  $\sigma_x$ , the probability of collision may be approximated by

$$P = \frac{r_a^2}{2\sigma_x \sigma_z \sqrt{1 - \rho_{xz}^2}} \quad (3)$$

which may be interpreted as the ratio of the collision area to the area over which the satellites are uniformly distributed at the point of closest approach. Chan continues, as does Alfriend, by noting the probability of collision may be placed in the following form

$$\begin{aligned} P = & \frac{1}{\sqrt{2\pi}\sigma_x} \int_{x_e - r_a}^{x_e + r_a} e^{-\left(\frac{x^2}{2\sigma_x^2}\right)} x \\ & \frac{1}{2} \left[ \operatorname{erf}\left(\frac{\lambda + m}{\sqrt{2}\sigma'}\right) + \operatorname{erf}\left(\frac{\lambda - m}{\sqrt{2}\sigma'}\right) \right] dx \end{aligned} \quad (4)$$

by completing the square in the  $z$  term, rearranging to make use of the error function and noting that the error function is an odd function, where

$$\begin{aligned} \lambda &= \sqrt{r_a^2 - (x - x_e)^2} \\ m &= \frac{\rho_{xz}\sigma_z}{\sigma_x} x \\ \sigma' &= \sigma_z \sqrt{1 - \rho_{xz}^2} \end{aligned} \quad (5)$$

and the error function is defined by

$$\operatorname{erf}(\xi) = \sqrt{\frac{2}{\pi}} \int_0^{\xi} e^{-t^2/2} dt \quad (6)$$

Equation (4) may be integrated numerically to gain physical insight into the form of the collision probability as a function of the separation standard deviation,  $\sigma_x$ , relative to the expected separation at the point of closest approach,  $x_e$ , by assuming  $\rho_{xz} = 0$  to obtain the result shown, in blue, in Figure 5. Note that the functional form remains the same for the three ratios of  $x_e$  relative to the collision radius,  $r_a$ , shown and exhibits a maximum near  $\sigma_x/x_e = 1/\sqrt{2}$ . Also shown in Figure 5, in magenta, is the corresponding result from equation (2). Note that except for the case in which  $x_e$  is only slightly larger than  $r_a$  is there any appreciable difference in the result.

More significantly, the probability of collision, which results using equation (3), shown in cyan, differs very little from these results provided  $\sigma_x > x_e$ . Therefore, for values of  $\sigma_x$  increasingly greater than  $x_e$ , the difference in probability of collision obtained by assuming a uniform rather than a bivariate normal distribution is increasingly negligible.

The interpretation of the probability of collision resulting using equation (4) in the region in which  $\sigma_x$  is smaller than  $x_e$  must be handled carefully. In this region the value of the probability of collision is increasingly determined by the tails of the separation probability density function which increasingly implies that the position of the satellites actually depart from the estimate by many standard deviations. In other words, were one to consider the satellite observations residuals one would find meaningful observations many standard deviations from the expected value. In fact, of course, such observations are routinely discarded as unphysical in the orbit determination process. Equation (4) is not physically meaningful in the region where  $\sigma_x$  is much less than  $x_e$ , since all that can be said is that the probability of collision is small; little may be meaningfully said about the order of that smallness. Furthermore, where equation (4) is perhaps applicable it is not needed since the probability of collision may be determined as a ratio of areas using equation (3).

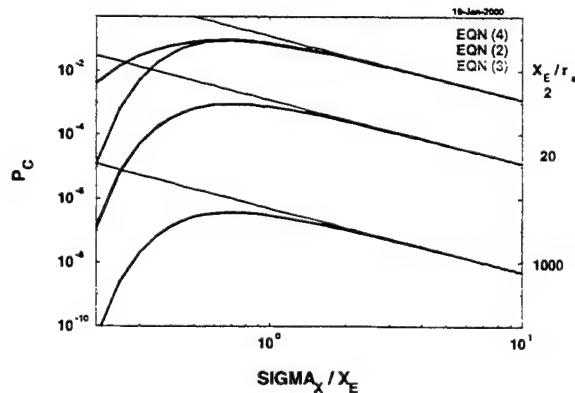


**Figure 5. Probability of Collision**

Another facet of this interpretation involves the realization that the orbit standard deviation describes the estimated rather than actual, physical trajectory of the satellite. That is, the trajectory of the orbiting objects is very well behaved and does not exhibit a significant random character, although our estimate of its position does.

#### *Probability of Collision based on Volume Density*

Consider now the probability of collision estimate which can be obtained following Kessler. Suppose  $N_A$  objects are actively maintained in a circular orbit of radius  $R \pm \varepsilon_r$ , and inclination  $\varepsilon_\theta$ , where  $\varepsilon_r$  and  $\varepsilon_\theta$  are constants representing the uncertainty in the orbital position. Then the volume density of these objects is

$$\frac{N_A}{2\varepsilon_r(2\varepsilon_\theta R)(2\pi R)} \quad (7)$$

Suppose an object is inactive in a circular orbit of radius  $R$  and inclination  $i$ . Denote the velocity of this object by  $V$ . This object spends

$$\frac{2\varepsilon_\theta R / (V \sin i)}{2\pi R / V} \quad (8)$$

of its orbital period in the volume occupied by the active objects, provided  $\varepsilon_\theta < i$ . Note that under the current circular orbit assumption, the inactive object spends twice as much time in the volume occupied by the active objects as indicated by equation (8). However, the eccentricity of most inactive geosynchronous objects typically limits the close approach to only one point on the intersection of the orbital planes. This reality is accounted for in equation (8). Suppose all of the objects are spherical and have a radius denoted by  $r$ . Denote the collision cross-sectional area by  $\sigma$  and assume, as an approximation, that  $\sigma = 2\pi r^2$ . The collision velocity is given by

$$V[(\cos i - 1)^2 + \sin^2 i]^{1/2} = V[2(1 - \cos i)]^{1/2} \quad (9)$$

Therefore the inactive object encounters volume potentially occupied by an active object at the rate

$$V[2(1 - \cos i)]^{1/2} \sigma \quad (10)$$

As a result the collision rate is given by combining equations (7), (8) and (10) to obtain

$$\frac{N_A V \sigma}{8\pi^2 \varepsilon_r^2 R^2} \left[ \frac{2(1 - \cos i)}{\sin^2 i} \right]^{1/2} \quad (11)$$

For  $\varepsilon_\theta < i < 15$  degrees the factor involving inclination differs from unity by no more than 0.0086. Since the inclination of the inactive population of geosynchronous satellites typically does not exceed fifteen degrees [9], this factor may be taken equal to unity to obtain the collision rate as

$$\frac{N_A V \sigma}{8\pi^2 \varepsilon_r^2 R^2} \quad (12)$$

which is independent of inclination. Therefore, for  $N_I$  inactive objects with arbitrary inclination, but  $\varepsilon_\theta < i < 15$  individually, the collision rate is

$$\frac{N_I N_A V \sigma}{8\pi^2 \varepsilon_r^2 R^2} \quad (13)$$

The historical LSSC database can be used to determine the number of active and inactive satellites,  $N_A$  and  $N_I$ , deployed to geostationary orbit. However, although the database contains the launch year of an object, it does not contain the year the satellite went out of service. However, by assuming an equivalent, average satellite life and verifying that the estimate of the current population, which results using this equivalent, average life agrees with the actual current population, an estimate can be made of the active and inactive satellite population over time. Then, assuming  $\varepsilon_r = 130$  km so that the simplified result derived here agree with Hechler and Van der Ha, this approach gives an annual collision rate of  $2.0 \times 10^{-4}$  for the present population. Furthermore, this estimate indicates that the probability of collision has increased by an order of magnitude in about eleven years, although the rate of increase is slowing slightly, as shown in Figure 6.

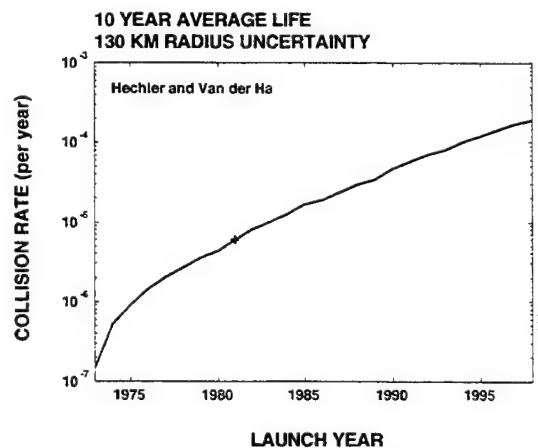
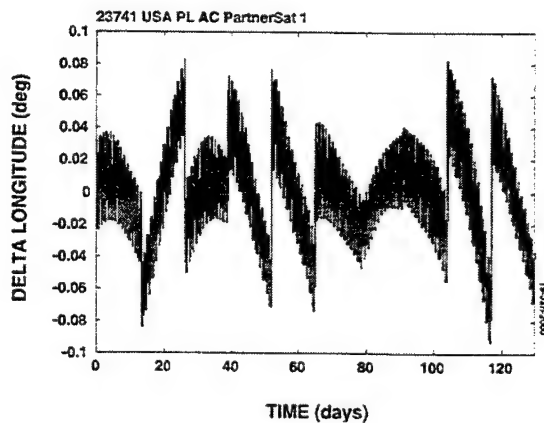


Figure 6. Historical Collision Rate Growth

### *Probability of Collision based on Station Keeping Behavior*

Active satellites in the geostationary orbit occupy a well-defined location by regulation and operational procedure. The International Telecommunication Union, publisher of the Radio Regulations (in effect, an international treaty), coordinates frequency and longitude assignments for geostationary communication satellites. Satellite operators typically control the longitude and inclination within  $\pm 0.05$  degrees in order to comply with this regulation. Operators perform longitude control maneuvers, termed east-west station keeping maneuvers, every two weeks, typically. Such maneuvers are required due to the geopotential of the earth, which tends to accelerate the satellite toward a geopotential well.

Since inactive satellites typically orbit appreciably inclined to the equator, they encounter the active, station-kept satellites with a relative velocity approximately perpendicular to the equatorial plane. Therefore, it is instructive to consider the position of the active satellites in an earth centered, fixed coordinate system *XYZ* where *Z* aligns with the earth's axis of rotation and *X* passes through the Greenwich meridian. Consider, for example, a typical partner satellite which will be termed PartnerSat 1. A recent element set may be propagated for two weeks in order to represent the motion of the satellite over an east-west station keeping cycle. By collecting the same result for, say, nine additional recent but different element sets, a statistically representative sample for the PartnerSat 1 east-west station-keeping performance is obtained.



**Figure 7.** Longitude Behavior for Ten Representative Station Keeping Periods

Such a process is illustrated in Figures 7 and 8. Figure 7 shows the longitude over ten 14-day segments, which result from the selected element sets. Figure 8 shows, in red, the orbit of PartnerSat 1 over one day for one particular element set, in yellow, the orbit for the same element set over the remaining 13 days and, in cyan, the orbit over 14 days of the remaining element sets. Note that although some of the element sets exhibit the expected station-keeping behavior expected, others exhibit an elevated drift rate. Nevertheless, the following results will demonstrate that the distribution of position is very adequately represented for the purpose of calculating the probability of collision.

During an encounter in which an inactive object occupies some region of the *XY* plane at the same time in which PartnerSat 1 occupies the same region, a collision is possible. The probability of a collision is given by the fraction of time PartnerSat 1 spends in this portion of the *XY* plane multiplied by the ratio of the collision area to the resolution cell area, as discussed above. Note that the size of the resolution cell must be chosen such that the maximum velocity of PartnerSat 1, relative to the center of its station-keeping box, does not cause the position of the satellite to step over a resolution cell during one propagation step. The resulting probability of collision distribution for PartnerSat 1 is shown in Figure 9. Note that the size of the station-keeping box was taken to be 100 km on a side, which accounts for 96.9% of the propagated positions and that a collision radius of 50 m was assumed.

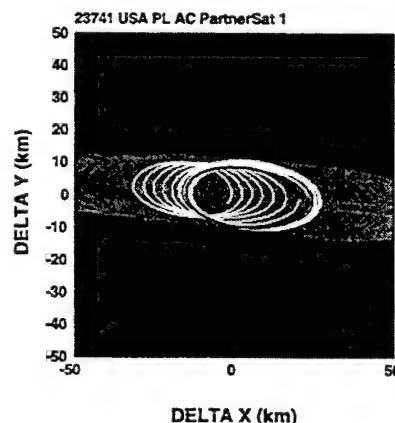


**Figure 8.** Relative Position During Ten Representative Station Keeping Periods

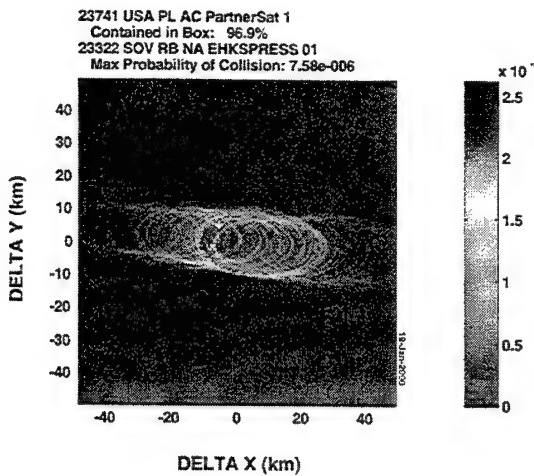


**Figure 9.** Typical Probability of Collision Distribution

As mentioned above, the set of threat objects may be reliably propagated with DYNAMO over even long spans. DYNAMO is a general-purpose orbit determination and ephemeris generation program based on strictly numerical methods to solve the equations of motion. DYNAMO uses the JGM3 gravity field model, includes direct lunar and solar effects, models body tides, solar radiation pressure, earth-reflected radiation and atmospheric drag, and simulates thrust forces and is capable of generating one-meter orbits given suitable observations. For the result presented here, the inactive objects are propagated over a one-year time period spanning approximately October 1999 to October 2000. The positions are compared to the position of each active object to determine the occurrences of an encounter, defined as a difference in position in the XY plane of no more than 50 km and in the Z direction of no more than 125 km. Note that an interpolation is done of the propagated position to times separated by no more than the time required for an inactive, geosynchronous object to travel 250 km in the Z direction by noting again that the maximum inclination of an inactive, geosynchronous satellite is fifteen degrees. The point of closest approach is then determined and the corresponding relative velocity used to transform the XY plane into one normal to this relative velocity. Unique encounters are determined as before, although in the transformed coordinates. An encounter is considered unique if it occurs no more frequently than a quarter orbital period. The white plus in Figure 9 shows the position at which a Russian

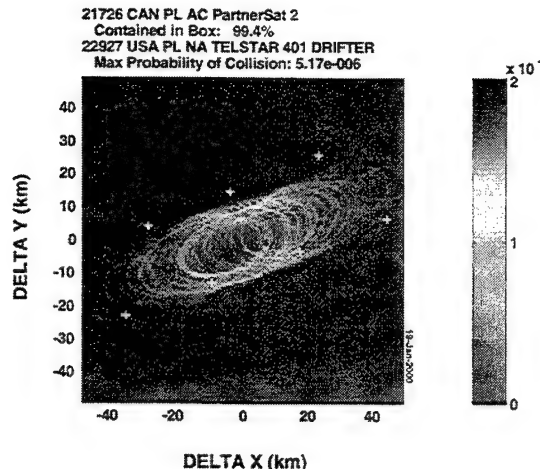


**Figure 10.** Typical Encounter with Telstar 401

rocket body for Ehkspress I encounters PartnerSat 1 and the corresponding probability of collision. Note that assuming a uniform distribution of the active satellite over a 100 km square and a 50 m collision radius would give a probability of collision of  $7.9 \times 10^{-7}$ . Therefore the result for this particular encounter between PartnerSat 1 and Ehkspress I has a probability of collision which is nearly an order of magnitude larger. An additional case involving Telstar 401 is shown in Figure 10.

Following this same approach, the probability of collision for every encounter occurring between the entire population of active, geostationary satellites and all inactive objects capable of reaching the geosynchronous altitude can be determined. A histogram describing the resulting distribution of probability of collision may be calculated, each value of which may be multiplied by the probability of collision value for each bin to obtain the distribution shown in Figure 11. The result shows the contribution to the total probability of collision for each bin and therefore that the total probability of collision is not dominated by large outliers. Overall, the results indicate that the annual probability of collision for the entire threat source population against the entire active population is  $4.1 \times 10^{-5}$ . As a sanity check, note that the total number of encounters corresponding to this result is 4364 which, when multiplied by the probability of collision corresponding to a uniform distribution ( $7.9 \times 10^{-7}$ ), gives an annual probability of collision equal to  $3.4 \times 10^{-3}$ .

## Conclusions

The probability of collision between the population of active, geostationary satellites and inactive, geosynchronous objects has been reliably characterized. A new approach based on active satellite east-west station keeping performance has been presented and compared with previously published approaches based on volume density or orbital covariances. The approaches have been shown to be conceptually consistent and provide order of magnitude quantitative agreement. The new results indicate that, today, the annual probability of collision is more than one in one thousand, a result significantly larger than a previous, less detailed, volume density based estimate.

The probability of collision in the geostationary orbit, small but not negligible, inevitably results from the technological development and historical operation of geostationary satellite communications. Although unfortunate, the failure of Telstar 401 has provided the motivation and resources, through the cooperative agreement between MIT Lincoln Laboratory and commercial satellite operators, to understand and begin responding to this orbital situation. Lincoln Laboratory now posses a validated concept of operations for providing encounter support, procedures for routinely calibrating transponder ranging data and approaches for maximizing orbital precision while minimizing sensor time requirements. Under a continuing cooperative agreement, Lincoln Laboratory will use these results to develop a system for monitoring encounters between all cataloged threatening resident space objects and partner satellites to provide the technology to confidently and efficiently address the geosynchronous encounter situation now and in the future.

## References

- [1] Private communication.
- [2] Private communication.

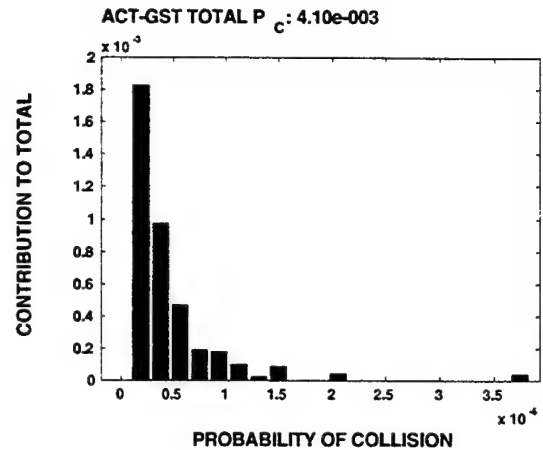


Figure 11. Probability of Collision Contributions

- [3] R. I. Abbot and J. Sharma, "Determination of Accurate Orbits for Close Encounters between Geosynchronous Satellites," Proceedings of the 1999 Space Control Conference, Lexington, Massachusetts, 13-15 April 1999, MIT Project Report STK-254, 71-85.
- [4] Private communication.
- [5] M. Hechler and J.C. Van der Ha, "Probability of Collisions in the Geostationary Ring," *J. Spacecraft*, 18(4), 361-366, July-August 1981.
- [6] D.J. Kessler, "Derivation of the Collision Probability between Orbiting Objects: The Lifetimes of Jupiter's Outer Moons," *Icarus* 48, 39-48, 1981.
- [7] K. T. Alfriend, M. R. Akella, D-J. Lee, J. Frisbee and J. L. Foster, "Probability of Collision Error Analysis," Proceedings of the 1998 AIAA/AAS Astrodynamics Specialist Conference, Boston, Massachusetts, 10-12 August 1998.
- [8] K. Chan, "Collision Probability Analyses for Earth Orbiting Satellites," *Advances in the Astronautical Sciences* 96, 1033-1048, 1997.
- [9] L.J. Friesen, A.A. Jackson, IV, H.A. Zook and D.J. Kessler, "Analysis of Orbital Perturbations Acting on Objects in Orbits Near Geosynchronous Earth Orbit," *J. of Geophysical Research*, 97(E3), 3845-3863, 25 March 1992.

\* This work was performed under a Cooperative Research and Development Agreement between MIT LL and PanAmSat. Opinions, interpretations, conclusions and recommendations are those of the author or authors and do not necessarily represent the view of the US Government.

# Orbital Debris Size Estimation from Radar Cross Section Measurements

R. Lambour, T. Morgan, and N. Rajan  
MIT Lincoln Laboratory, 244 Wood St. Lexington, MA 02420-9185

## Abstract

MIT Lincoln Laboratory has conducted a measurement program for man-made orbital debris since 1991 in response to NASA's need to characterize the orbital debris population and facilitate manned spaceflight activities. The primary sensors used in that effort are the Haystack and HAX radars located at the Lincoln Space Surveillance Complex (LSSC) in Westford, Massachusetts. This paper will describe the initial results from a new effort being conducted at LSSC, the objective of which is to assess the procedure for the determination of debris size from RCS data. NASA has selected a set of 43 resident space objects to serve as a test set. Data are being collected at multiple frequencies by simultaneously tracking each object with Millstone/Haystack and Millstone/HAX. Each object will be tracked at 3 different elevations with each radar pair, resulting in a total of six tracks per object. All three radars are collecting narrowband RCS data that will be used to produce size estimates using the NASA Size Estimation Model, but Haystack and HAX are also collecting wideband data to facilitate independent size estimation when needed. This paper will discuss the data collection, data reduction, and size estimation techniques employed as well as present results from the first year of the effort.

## Introduction

The number of orbital debris fragments in the size range of 1-30 cm has been estimated at over 100,000. This is a fairly large number and raises concerns regarding the safety of satellites in orbit and their ability to withstand impacts from orbital debris. NASA is particularly interested in the safety of the International Space Station and of the astronauts who will conduct extra-vehicular activities during the construction of the station. In addition, the debris fragments represent potential radar and optical clutter for ground-based and space-based surveillance systems.

In order to quantify the risk posed to satellites by the orbital debris population, NASA has undertaken a statistical characterization of the orbital debris environment. MIT Lincoln Laboratory has participated in this effort since 1991 with the Haystack and Haystack Auxiliary (HAX) radars located at the Lincoln Space Surveillance Complex (LSSC) in Westford, Massachusetts. These radars have been utilized in a staring mode to collect data on the near-Earth orbital debris population<sup>1</sup>. In addition, the FPS-85 space surveillance radar located at Eglin AFB, Florida, has also contributed a significant amount of data on near-Earth orbital debris obtained during its normal operation.

These data sources have allowed NASA to characterize the population of orbital debris. The number of debris fragments and their distribution as a function of altitude and inclination has been estimated and has allowed the development of orbital debris environment models which are used to specify the environment for objects such as the International Space Station. Also of importance is knowledge of the size distribution of the debris fragments. When discussing size, we refer to an equivalent sphere diameter (ESD), which is the inferred diameter of an object calculated under the assumption that it is spherically shaped. If the size of an object is known, an estimate of its mass, and thus impact energy, can be made. Knowledge of impact energy facilitates determination of satellite vulnerability. In addition, the effects of atmospheric drag on the object can be estimated and, thus, its orbital lifetime. This allows introduction of a time-dependent component into the modeling of the orbital debris environment.

The size of the object must usually be estimated from radar cross-section (RCS) data. NASA has developed of an RCS-to-ESD mapping function, which is referred to as the Size Estimation Model (SEM)<sup>2,3</sup>. This model was derived from multi-frequency radar range data collected on ~40 simulated orbital debris fragments produced by a hypervelocity collision. The pieces were observed at a number of different frequencies and orientations and RCS probability density functions were derived to characterize the RCS as a function of frequency and object size. The end result is presented in Figure 1, which shows a

\*This work sponsored by NASA under Air Force Contract No. F19628-95-C-0002. Opinions, interpretations, conclusions and recommendations are those of the author and are not necessarily endorsed by the United States Air Force.

graph of RCS normalized to the square of the wavelength as a function of ESD normalized to wavelength. The data from the ~40 fragments are shown as points and the mapping function is shown as a solid line overlaying the data. The ESD of debris objects is routinely estimated by using this RCS-to-ESD mapping function with the FPS-85 data; this has produced a catalog of size estimates for debris objects.

NASA has begun using the Liquid Mirror Telescope located in Cloudcroft, New Mexico, to acquire additional debris observations. This is a zenith-staring, 3-m aperture telescope that was built to characterize the optical orbital debris environment in the 1-10 cm size range<sup>4</sup>. Diameters for debris objects can be derived from the optical data once an optical phase function and albedo are either determined or assumed for the objects. NASA recently compared these optical diameters and the radar diameters from the FPS-85 data and noted some discrepancies. Those discrepancies have led to the study described in this paper, which is an effort to characterize a number of debris objects and gain insight on the RCS-to-size estimation procedure. This study is separate from the ongoing debris observation program at LSSC using the Haystack and HAX radars. This paper will provide an overview of our objectives and our techniques and provide some results from the first year of the effort.

### Objectives and Approach

The objective of the current study is to gain insight on the procedure for the determination of size from RCS. NASA has selected a set of 43 Resident Space Objects (RSO) for characterization (cf., Table 1). MIT Lincoln Laboratory is collecting RCS measurements on these objects using the three radars at the LSSC. The radars are summarized in Figure 2. As of December 1999, data collection had been completed on 15 of the 43 objects. Those 15 objects are highlighted in Table 1.

Each RSO was tracked jointly by the Millstone and Haystack radars and also by the Millstone and HAX radars. Each RSO was tracked at three different elevation angles in order to provide a random set of aspect angles. Every attempt was made to duplicate the pass geometries for each pair of radars, but this proved difficult in practice. The end result is 6 joint tracks for each object. The data for RCS and size characterization were collected using narrowband waveforms with the Millstone, Haystack and HAX radars. For each track, Haystack and HAX also collected wideband data, which can be used to provide an independent size estimate, if necessary. In addition, radar calibration spheres were tracked whenever possible during the debris tracking sessions in order to provide data on the radar calibration.

All three radars recorded RCS vs. time in the principal polarization (PP) and orthogonal polarization (OP) channels. Those channels represent left-circular polarization, and right-circular polarization, respectively. The RCS data were integrated non-coherently over a time span of approximately 200 msec. For Haystack, this integrated measurement is equivalent to the type of data collected by the radar when it is operating in its stare mode for debris data collection. These integrated RCS measurements are sent through the NASA SEM in order to derive the equivalent sphere diameter (ESD) at ~200 msec intervals. Figure 3 presents a flowchart that describes the size estimation procedure. The RCS data are integrated as described earlier. Then the PP and OP returns are summed (PP+OP). The summed measurements are normalized by the square of the wavelength and the corresponding value of  $d/\lambda$  is interpolated from the NASA SEM curve. For any given track, this procedure produces a time series of ESDs.

These size estimates are then examined statistically in order to derive a representative size for the object. The statistical quantities calculated for each track of an object are listed in Table 2. The mean size represents an average size for the object over the course of the track. We also generate histograms of the PP and OP RCS, the PP/OP ratio, and the ESD estimates.

Examination of the ESD histograms shows that multiple peaks often characterize the size distribution for an object. An example of this behavior is shown in Figure 4. Peaks are evident in the size distribution at ~6, ~11, and ~20 cm. This presence of multiple peaks in the size distribution suggests that the radar observed more than one characteristic dimension for the object. These observations have led us to attempt to break up the observations and derive two representative sizes for each object. These sizes are intended to represent a long and a short dimension for the object. We have termed this analysis a *clustered* statistical analysis.

For each object, a cumulative distribution function (CDF) and a probability density function (PDF) are calculated using all of the data collected<sup>5</sup>. This calculation is done separately for each radar. The size corresponding to the 50% point is selected as the threshold size at which to separate the size

distribution into two. The PDF is examined to ensure that this 50% size is a reasonable point at which to separate the data. Then, a mean, standard deviation, and median size is calculated from the two separated size distributions. These statistics represent two characteristic sizes for the object, a short and long dimension.

In addition, the narrowband RCS signature sometimes allows us to perform an independent assessment of the size of the object using theoretical arguments. An example of this type of analysis will be presented in the next section.

As a last step, an object folder is generated for each object. The object folder summarizes the track histories, RCS data and size estimates as well as their associated statistics, cluster analysis, and narrowband signature analysis. The object folder is summarized in Figure 5 and represents the final product of the analysis.

## Results

We now present examples of the data collected and the results of the statistical analysis. We first consider Object 4719, which is debris from the breakup of an Agena D upper stage that took place in 1970. Since the object is a piece of debris, we have no *a priori* knowledge of the size of the object other than the size estimate generated from the FPS-85 radar. That size estimate is 0.86 meters and represents an ESD.

The Millstone Hill radar (MHR) data on this object show a repeatable specular lobing pattern in the PP return for all tracks collected. An example is shown in Figure 6. This pattern facilitates size estimation from the narrowband signature. The peak-to-peak period in the PP data is ~20-25 seconds. The right hand side of Figure 6 presents an expanded view of several of the specular peaks. Each peak is narrow and exhibits some fine-scale structure (lobing). In between the large-amplitude peaks, there are sometimes smaller-amplitude, wider peaks. The OP return follows the same general pattern as the PP return with the exception that there are no large-amplitude specular peaks. These features suggest that we are looking at an object that has one dimension significantly longer than the other, like a thin cylinder or dipole-shaped object<sup>6</sup>. The specular returns in the PP channel are then the reflection from the cylinder when it is viewed broadside, and the lower-amplitude, wider returns in the same channel would be the reflection from the smaller ends of the object. We have assumed that the object is tumbling in such a manner that this end-over-end motion is what was observed by the radar.

Using the end-over-end motion assumption and assuming that the object is shaped like a cylinder, we can estimate the dimensions of the object using the specular peaks. The tumble rate is  $2\pi$  in ~50 sec or 0.126 rad/sec. The null-to-null width of the main lobes of the specular reflections is ~1 sec. Using  $\theta = \lambda/L$ , this suggests a long dimension of ~1.84 m. Then, the amplitude of the specular (~8 dBsm) can be used to estimate the second dimension from  $RCS = kaL^2$  (Ref. 7). The second dimension,  $a$ , is about 7 cm. Repeating this analysis with a number of different specular peaks suggests that the object is long and thin, with a short dimension of ~10-20 cm and a long dimension of 1.5-2.5 m.

Figure 6 presents the mean and median size estimates for Object 4719 derived from the data collected at LSSC. There is fairly good agreement in the mean and median sizes derived by the three radars from track to track. However, the mean and median size estimates fall well below the FPS-85 size estimate and the standard deviations are high. The high deviations are due to the observation of specular reflections during the tracks. For the same reason, the means tend to be well above the median values for all of the tracks. These estimates suggest that the object has a mean size of 0.53 – 1.22 m and a median size of 0.28 – 0.70 m. These means and medians have a wide range of values, and are not in good agreement with the size estimates derived from the narrowband signature.

The narrowband signature data and the spread in mean and median sizes strongly suggests that the radars observed an object which is not well characterized by one size estimate. Therefore, we performed a clustered statistical analysis for Object 4719. The 50% point in the CDF corresponds to a size of 0.4206 m for the MHR data, and a size of 0.4275 m for the combined Haystack/HAX data sets. The size distribution for each track was split at the appropriate threshold value and statistics were calculated on the data above and below these points. The results for the MHR data are shown in Figure 8. The mean and median values for the short axis are very consistent from track-to-track and range from 0.16 – 0.21 m. The mean and median values for the long axis are more variable. Mean values range from 1.34 – 2.91 m and median values range from 0.76 – 1.31 m. We note that these results from MHR are consistent with the narrowband signature analysis results described earlier.

The cluster analysis results for the Haystack and HAX data are shown in Figure 9. The results lack the same consistency as the MHR results, they are more variable from track to track, but are roughly consistent with the MHR results. The mean sizes for the short dimension of the object are 0.24-0.6 m and the median values for the short dimension range from 0.23-0.59 m. For the long dimension, the mean sizes are 1.4-2.9 m and the median sizes are 0.8-2.03 m.

The conclusions that can be drawn about Object 4719 are that it is a long, thin, roughly cylindrical shaped object with a short dimension of ~10-30 cm and a long dimension of ~1.4 – 3.0 m. The slight discrepancies in estimated sizes for the three radars suggest that Object 4719 is more complex than a simple cylinder.

As a second example, we consider an object for which we have been able to find information on its true size. Object 20 is an inactive scientific payload called Vanguard 3 that was launched in 1959 to study the atmosphere and Van Allen radiation belts. It is a 0.508-m diameter magnesium sphere equipped with an external boom that is 0.66 m in length. A single diagram shows that there are 4 long, thin, equally spaced antennae extending from the sphere<sup>8</sup>. The lengths of the antennae are unknown. The FPS-85 size for this object is 0.85 m.

Figure 10 presents two examples of the MHR RCS data collected on this object. The data are complex, but show a periodic modulation which is present in all of the MHR tracks. The peak-to-peak period for the modulation is ~60 sec. The PP RCS trace alternates between periods of rapid, relatively large amplitude variations and less rapid, smaller amplitude variations. These RCS features suggest that this payload was in a complex tumble alternately presenting features of relatively long and short scale lengths to the radar.

Occasionally, specular flashes were observed (cf., Fig. 10). As was done with Object 4719, the narrowband signature can be analyzed to estimate the object dimensions. The key point for this analysis is estimating the tumble period. The average length of time between the specular flashes in Figure 10 is 129.8 seconds. Between each pair of flashes, a period of rapid PP and OP RCS variation is seen, followed by a brief period of less rapid variation in the PP channel and a significant drop in the OP channel, which is then followed by rapid PP and OP variations again. This suggests that the radar is detecting returns from a long dimension, then a direct return from a shorter dimension, followed by returns from a longer dimension again. Thus, a tumble rate  $2\pi$  in 129.8 seconds was adopted for MHR narrowband signature analysis. The largest specular peak has an amplitude of 6.64 dBsm and a null to null width of ~10.4 seconds. We assume that the object is cylindrical in shape and tumbling end-over-end. Using  $\theta = \lambda/L$ , this suggests a length of ~0.46 m. Then, the peak amplitude of the specular (~6.64 dBsm) can be used to estimate the second dimension from  $RCS = kaL^2$  (Ref. 7). The second dimension,  $a$ , is about 0.81 m. Repeating this analysis with a number of different specular peaks suggests that the short dimension lies between of ~0.41-0.54 m and the long dimension is between ~0.25-0.96 m. These results are in rough agreement with the known size of the object, but are systematically low. This is may be a result of the cylindrical shape assumption, which is a poor assumption for this object.

Figure 11 presents the mean and median size estimates for Object 20 derived from the various LSSC data. The MHR sizes are consistent from track to track, and the HAX sizes initially agree with the MHR sizes fairly well. In later tracks, the HAX and Haystack sizes are significantly larger than the MHR sizes. The MHR data suggest that the object has a mean size ranging from 0.54 ~ 0.71 m and a median size ranging from 0.5 ~ 0.67 m, all of which are well below the FPS-85 size estimate. The HAX results suggest a mean size of 0.48-1.39 m and a median size of 0.45 – 1.25 m. The Haystack results suggest a mean size of 1.24 – 1.27 m and a median size of 1.15 – 1.21 m. These estimates are all within the range of known dimensions for the object (cf., Fig. 10), but are not in good agreement with the FPS-85 size estimate.

Because Object 20 is a complex object we performed a clustered statistical analysis on the data under the assumption that a single size estimate would not adequately characterize this object. The 50% point in the CDF corresponded to a size of 0.57 m for the MHR data set, and a size of 0.992 mm for the combined HAX/Haystack data sets. The size distribution for each track was split at the appropriate threshold value and statistics were calculated on the data above and below these points. The results for the MHR data are shown in Figure 12. The mean and median values for the short axis are consistent from track to track and vary from 0.33-0.39 m. The mean and median values for the long axis are more variable and range from 0.77-0.93 m. The results are consistent with the narrowband signature analysis described earlier, but they are not in good agreement with the known short and long dimensions for the object.

The cluster analysis results from the Haystack and HAX data are presented in Figure 13. The size estimates are significantly higher and more variable than those derived from the MHR data. The mean

sizes for the short dimension vary from 0.46-1.05 m and the median sizes for the short axis vary from 0.45-1.08 m. For the long axis, the mean sizes vary from 1.84-2.13 m and the median sizes vary from 1.74-2.06 m. The results are not in good agreement with the known dimensions of the object. However, the lengths of the 4 antennae are not known and may be responsible for the discrepancy in the results. The data on this object are still under investigation.

### Summary and Current Status

Multi-frequency RCS data have been collected on 15 out of 43 objects selected by NASA for characterization. Those 15 objects are listed in bold type in Table 1. Each object was tracked jointly by MHR/Haystack and MHR/HAX over three different elevation angles for a total of six tracks per object. Radar calibration sphere data were also obtained to evaluate the calibration of the radars. The data from each track was analyzed and statistics were generated for the PP and OP RCS, the PP/OP ratio, and the ESD estimates. In addition, a clustered data analysis has been performed on the size estimates for those objects that appear to have more than one characteristic size. The results of these analyses have been collected in object folders. We plan to complete preliminary characterization of all 15 objects by mid-January, 2000.

The goal of the analysis is to investigate the RCS-to-size mapping function and determine a representative size (or sizes) for each object. The results for Object 4719 and Object 20 were presented in the previous section. Preliminary results for several of the other 14 objects are presented in Table 3. The table presents the object number, FPS-85 size, and a range of sizes for short and long dimensions derived from each radar. LRIR refers to Haystack. The sizes are in meters. The size estimates appear to agree fairly well with one another in most cases, although there are some objects for which the sizes derived from the different radars are not in good agreement. In most cases, the FPS-85 size and the LSSC sizes are not in good agreement. The FPS-85 size estimates result from a single observation as the object penetrated the radar beam at a single orientation. In addition, the FPS-85 observations are at UHF frequencies (440-442 MHz) which may account for some of the discrepancies. The analysis is in progress.

### References

- 1.) Setteceri, T. J., *et al.*, Haystack Radar Measurements of the Orbital Debris Environment; 1994-1996, JSC-27842, NASA Johnson Spaceflight Center, Houston, TX, May 1997.
- 2.) Bohannon, G. E., Comparisons of Orbital Debris Size Estimation Methods Based on Radar Data, Report No. 920123-BE-2048, XonTech, Inc., Los Angeles, CA, May 1992.
- 3.) Bohannon, G. E., and N. Young, Debris Size Estimation Using Average RCS Measurements, Report No. 930781-BE-2247, XonTech, Inc., Los Angeles, CA, September 1993.
- 4.) Africano, J. L., *et al.*, NASA/JSC Optical Orbital Debris Program: Results from the Liquid Mirror Telescope (LMT) and the CCD Debris Telescope (CDT), in *Proceedings of the 1999 Space Control Conference*, Project Report STK-254, MIT Lincoln Laboratory, Lexington, MA, April 1999.
- 5.) Meyer, S. L., *Data Analysis for Scientists and Engineers*, Peer Management Consultants, Ltd., Evanston, IL, 1975.
- 6.) Andrews, S. E., private communication, 1999.
- 7.) Barton, D. K., *Modern Radar System Analysis*, Artech House, Boston, MA, 1988.
- 8.) Caprara, G., *The Complete Encyclopedia of Space Satellites*, Portland House, New York, NY, 1986.

**Table 1: List of Objects Selected for Characterization**

Object	FPS-85 Size	Notes
20	0.85	Vanguard 3
82	1.1	Scout X-1 upper stage
85	0.19	Explorer 9 debris
155	0.23	<b>Debris from Able-Star upper stage breakup</b>
324	0.16	Debris from Able-Star upper stage breakup
341	0.71	<b>Delta upper stage</b>
462	0.21	Debris from Able-Star upper stage breakup
2121	0.83	OV1-4
4712	0.15	Soviet ASAT debris
4719	0.86	<b>Debris from Agena D breakup</b>
5187	0.31	Soviet ASAT debris
6350	1.67	<b>Cosmos 546</b>
7042	0.31	Debris from breakup of Delta second stage
7050	0.26	Debris from breakup of Delta second stage
7185	0.2	Debris from breakup of Delta second stage
8614	0.97	<b>Cosmos 798</b>
9982	0.26	Tansei-03 debris
10841	0.16	Debris from breakup of Delta second stage
12542	0.43	<b>Debris from breakup of Delta second stage</b>
13377	0.96	<b>Cosmos 1390</b>
13511	0.13	Debris from Able-Star upper stage breakup
14357	0.2	<b>Debris from Cosmos 1275 breakup</b>
14569	0.31	ETS-3 debris
15005	0.97	<b>Cosmos 1566</b>
16268	0.34	Debris from Cosmos 1691 breakup
17023	0.17	Debris from breakup of Delta second stage
17478	0.11	Debris from Ariane upper stage breakup
17805	0.14	<b>Debris from Cosmos 1375 breakup</b>
18361	1.92	<b>Transit 19</b>
18530	0.18	Oscar 27 debris
18599	0.3	Debris from breakup of Delta second stage
21101	0.99	<b>Cosmos 2126</b>
21114	1.32	SL-12 auxilliary motor
21386	0.14	Debris from breakup of Delta-1 upper stage
21523	0.16	Debris from breakup of Delta-1 upper stage
21835	1.05	<b>Magion 3</b>
22415	0.39	Debris from breakup of SL-16 upper stage
22443	0.15	Debris from breakup of SL-16 upper stage
23297	0.25	Cosmos 1710 debris
23486	0.17	Debris from breakup of SL-19 upper stage
23952	0.18	Ops 0856 debris
24124	0.21	Debris from Pegasus HAPS breakup

**Table 2: Statistical Quantities Tabulated during Object Characterization**

Minimum and Maximum PP and OP RCS values
Mean and Standard Deviation of PP and OP RCS, PP/OP ratio, and ESD estimates
Median of PP and OP RCS, PP/OP ratio, and ESD estimates
Mean Absolute Deviation of PP and OP RCS, PP/OP ratio, and ESD estimates
5% and 95% values for PP and OP RCS, PP/OP ratio, and ESD estimates

**Table 3: Estimated Sizes for Debris Objects**

Object	FPS-85 Size	MHR Short	MHR Long	LRIR Short	LRIR Long	HAX Short	HAX Long
20	0.85	0.46-0.55	1.08-1.23	0.99-1.06	1.84-2.00	0.46-1.08	1.86-2.13
82	1.1	0.28-0.49	0.54-1.22	0.56-0.63	1.11-3.10	0.60-0.70	1.20-2.23
155	0.23	0.05-0.07	0.13-0.16	0.11	0.14-0.17	0.11-0.13	0.15-0.16
12542	0.43	0.05-0.06	0.16-0.30	0.08-0.12	0.26-0.63	0.21-0.60	0.47-0.84
17805	0.14	0.06-0.07	0.15-0.20	0.09-0.11	0.30-0.38	0.12-0.19	0.47-0.62

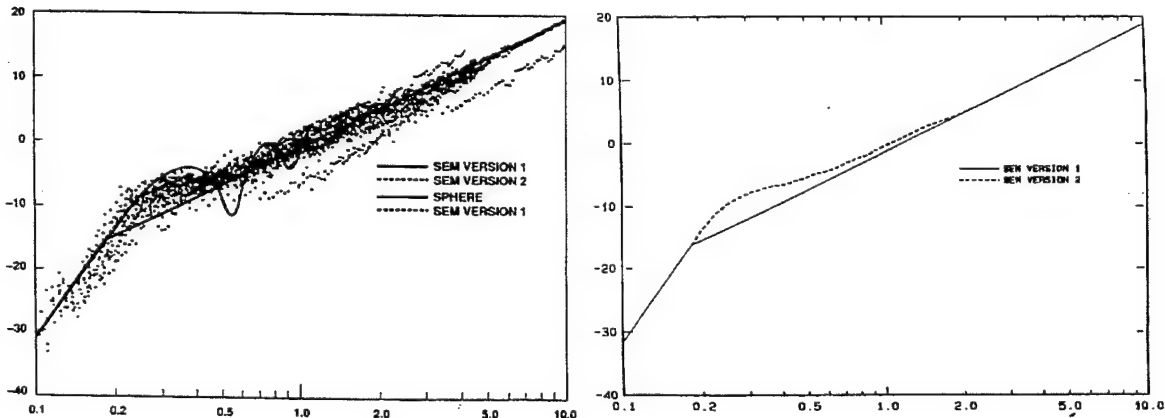


**Figure 1:** (Left) The RCS data used to derive the NASA SEM Version 2. The overlaid curve represents the RCS of a sphere. The x-axis for both plots is diameter/ $\lambda$  and the y-axis is RCS/ $\lambda^2$ ; (Right) The NASA SEM curve derived from the RCS measurements. The dashed curve labeled version 2 is the mapping function used in this paper.



Figure 2: Radars located at Lincoln Space Surveillance Complex in Westford, Massachusetts.

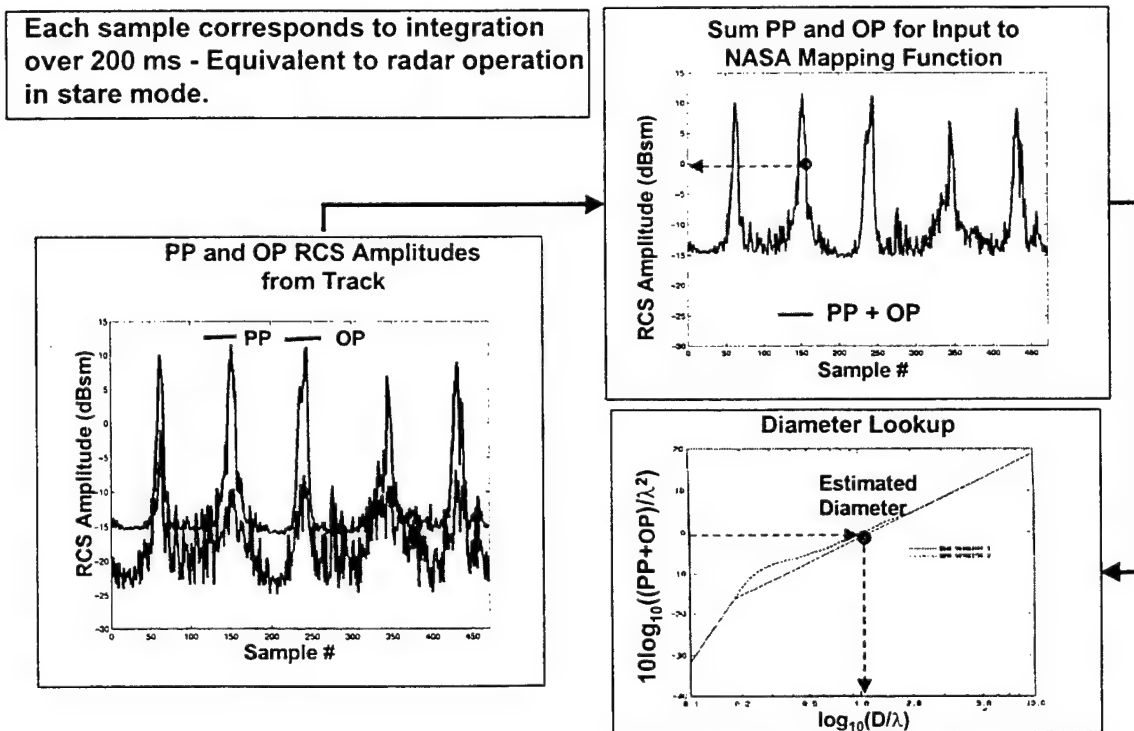
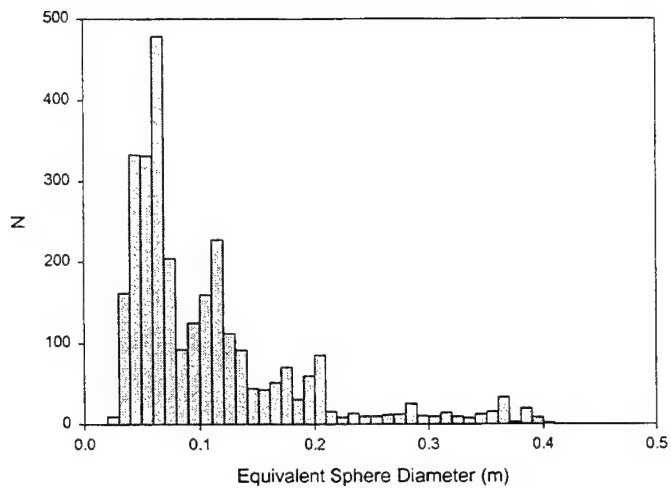
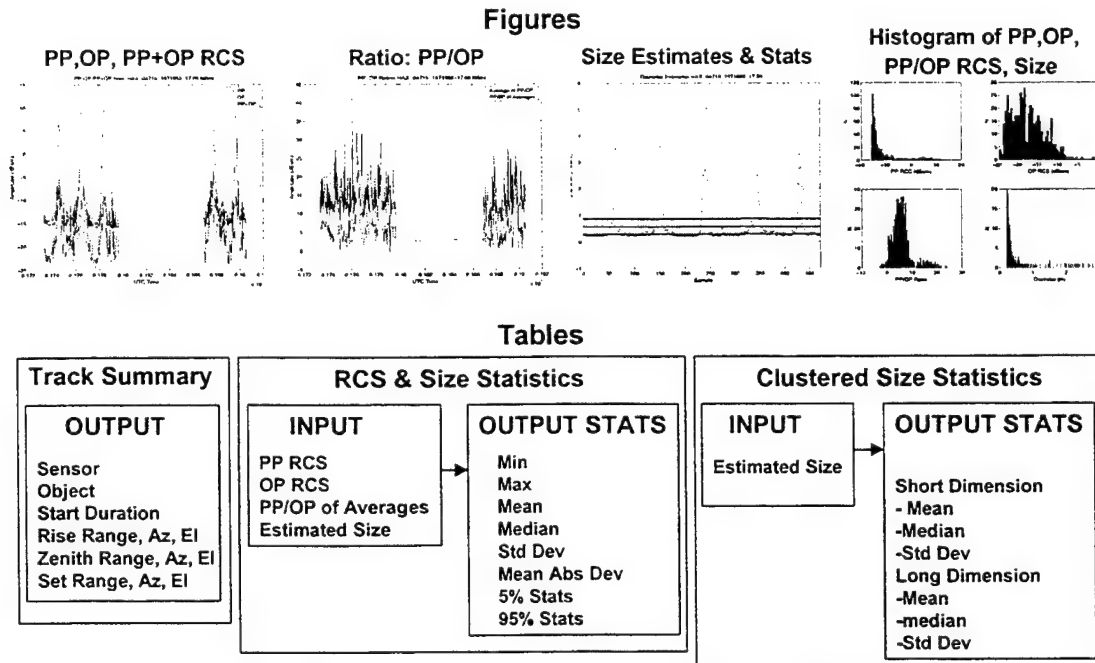


Figure 3: Flowchart describing the size estimation procedure.



**Figure 4:** Distribution of ESD estimates for object 14357. The data used to produce the size estimates were collected on day 216 of 1999 with the Millstone Hill Radar.



**Figure 5:** Summary of the contents of an object folder. The folder contains the listed figures and statistical analysis generated from data collected by all three radars.

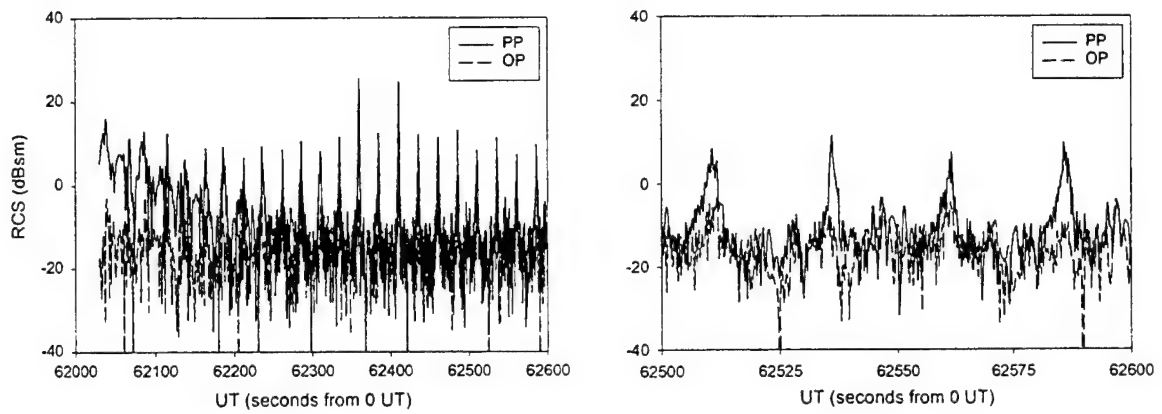


**Figure 6:** (Left) PP and OP RCS data on Object 4719 obtained at MHR on day 146 of 1999; (Right) The same data set expanded to show detail.

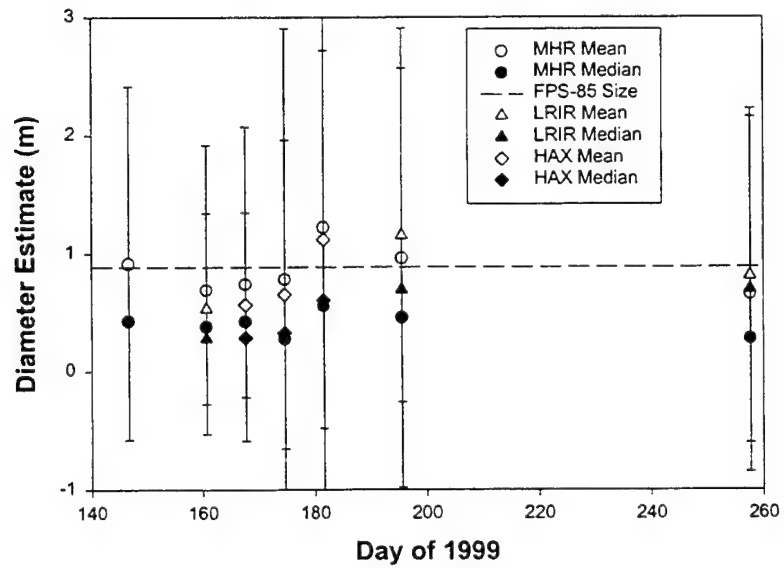


**Figure 7:** Mean and Median size estimates for Object 4719 from Millstone (MHR), Haystack (LRIR), and HAX. The FPS-85 derived size estimate is plotted as a dashed line for reference.

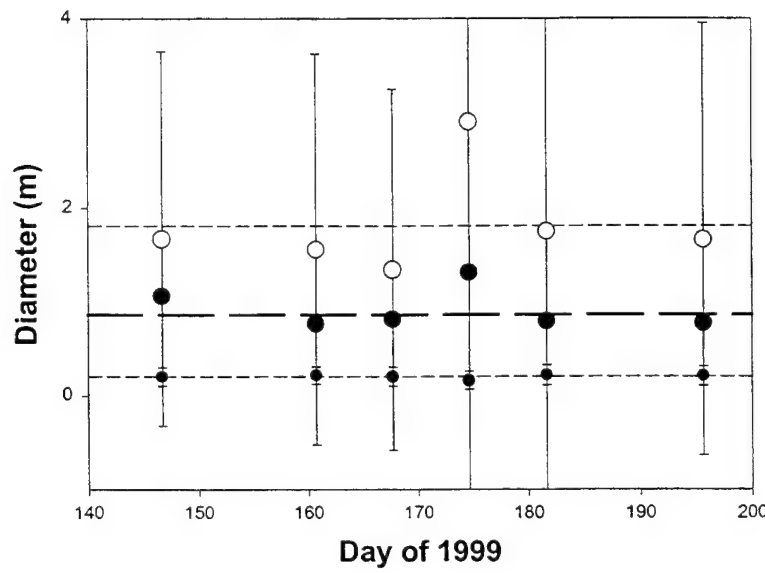


Figure 8: Mean and median size estimates from MHR data for the short (small circles) and long (large circles) dimensions of Object 4719. Mean values are shown as open circles, Median values are shown as filled circles. The FPS-85 size estimate (0.86 m) is the long-dashed line.

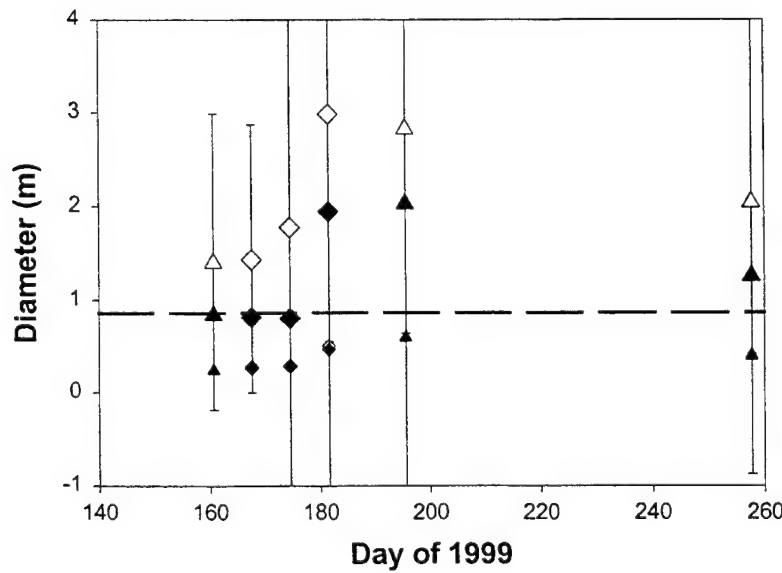
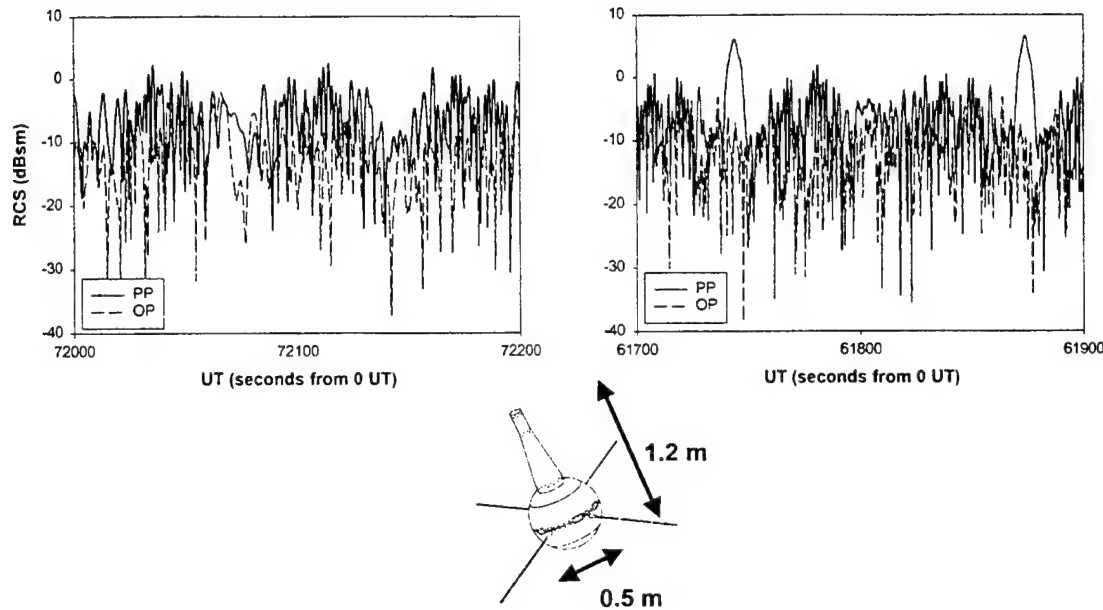
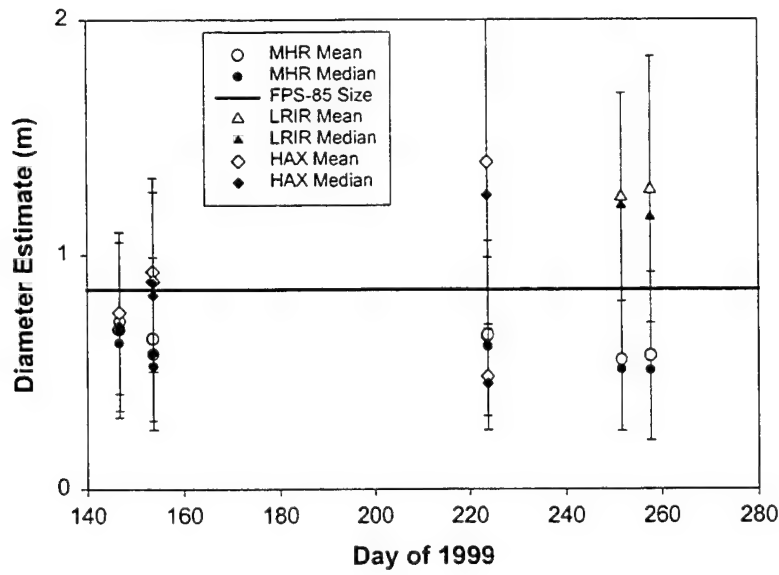


Figure 9: Mean and median size estimates from Haystack (triangles) and HAX (diamonds) data for the short (small symbols) and long (large symbols) dimensions of Object 4719. Mean values are shown as open symbols and median values are shown as filled symbols. The FPS-85 size estimate is the long-dashed line.



**Figure 10:** (Left) RCS data collected on Object 20 by the MHR on day 153 of 1999. (Right) Data collected on Object 20 by the MHR on day 257 of 1999. At the bottom of the figure is a diagram of Object 20.



**Figure 11:** Mean and median size estimates derived for Object 20 from Millstone (MHR), Haystack (LRIR), and HAX. The FPS-85 size is presented as a solid line for reference.

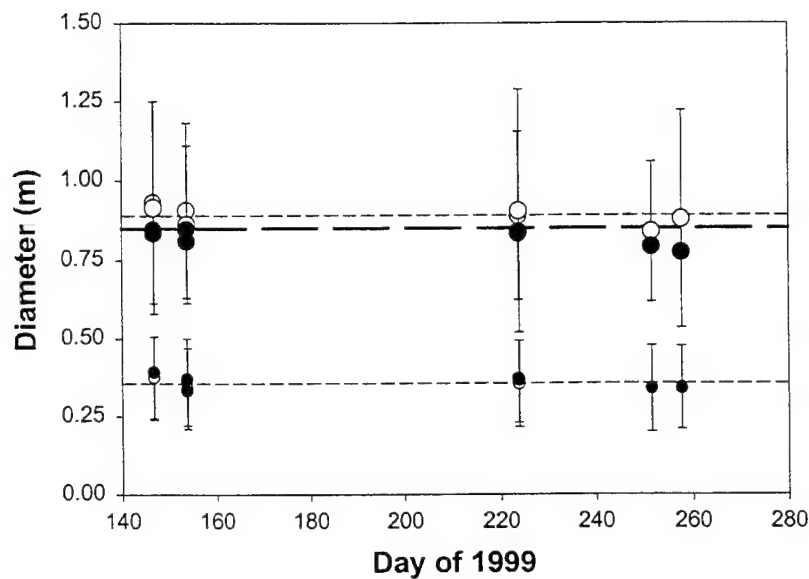


**Figure 12:** Mean and median size estimates from MHR data for the short (small circles) and long (large circles) dimensions of Object 20. Mean values are shown as open circles and median values are shown as filled circles. The FPS-85 size estimate is the long-dashed line.

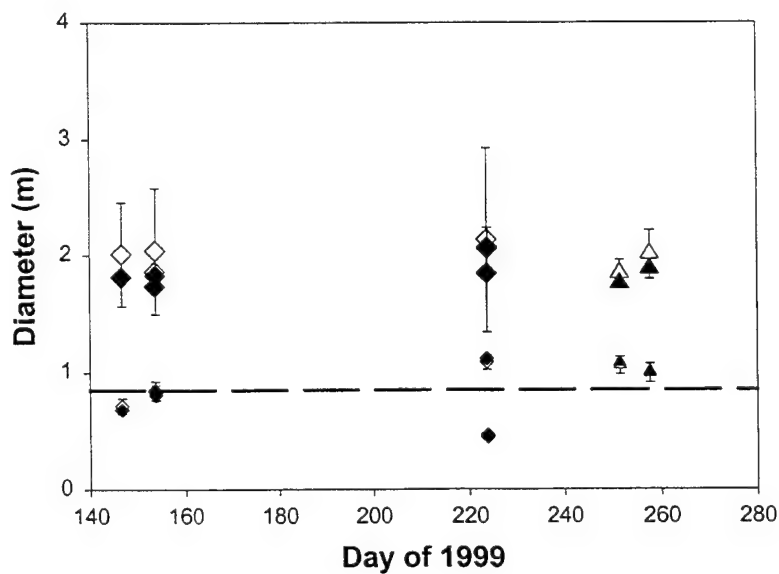


**Figure 13:** Mean and median size estimates from Haystack (triangles) and HAX (diamonds) data for the short (small symbols) and long (large symbols) dimensions of Object 20. Mean values are shown as open symbols and median values are shown as filled symbols. The FPS-85 size estimate is the long-dashed line.

# **PROGRESS REPORT FOR THE CANADIAN AUTOMATED SMALL TELESCOPE FOR ORBITAL RESEARCH (CASTOR) SATELLITE TRACKING FACILITY**

Mr. Michael A. Earl and Dr. Thomas J. Racey: The Space Surveillance Research and Analysis Laboratory  
Department of Physics, Royal Military College of Canada, Kingston, Ontario, Canada

## **Abstract**

Planning and constructing an optical satellite tracking facility is a difficult task, especially when considering the various hardware and software packages that are available. Once the initial construction has been completed, the different components of that facility have to be tested for accuracy. This paper will describe the progress of the planning and testing of the CASTOR satellite tracking facility located in Kingston, Ontario, Canada.

## **Introduction**

The CASTOR satellite tracking facility has been manually operational since January 29, 2000. Testing of the CASTOR facility involves four specific concerns. The first of these concerns is the scheduling of those satellites that will be accessible to CASTOR at any given time of night. The second is the tracking and the image acquisition of the aforementioned satellites. The third is the analysis of the acquired images. Lastly, the final orbit determined from the data extracted from the images has to be addressed.

Completion of the CASTOR system is expected by the summer of 2000. At that time it is hoped that it will be routinely tracking Molniya and other high eccentricity satellites on a regular basis. Once the entire system is operational, it will provide a blueprint for future CASTOR sites across the country.

The Space Surveillance Research and Analysis Laboratory (SSRAL) are using the CASTOR facility to track and study Molniya payload satellites. The Molniya payload satellite will therefore be used as the example throughout this paper.

## **CASTOR Hardware and Software**

The SSRAL had to address both accuracy and expenditure concerns when choosing the hardware and software that would comprise the CASTOR apparatus. Table 1 describes the hardware that CASTOR is comprised of and Table 2 describes the software that controls it.

Celestron Model CG-14 14 Inch Aperture Schmidt-Cassegrain Reflecting Telescope	This telescope is the optical tube assembly (OTA) of CASTOR.
Software Bisque Paramount Model GT-1100 Robotic Telescope Mount	This telescope mount is boasted to be one of the most accurate robotic telescope mounts for amateur astronomy. It is a German Equatorial design.
Apogee Model AP-7 Charge-Coupled Device (CCD) Camera	This CCD camera has a quantum efficiency of 85% over a wide range of visible wavelengths and has a back-illuminated design.
Datum Inc. Model bc620AT Global Positioning System (GPS) Receiver	The GPS receiver will provide a millisecond accuracy time base for satellite streak end-point determination.
Ash Manufacturing Model REA 10 Foot 6 Inch Diameter Observatory Dome	This observatory dome contains the CASTOR hardware mentioned above. A Lanphier shutter window provides a weather-tight environment for the hardware contained within.
Merlin Controls Dome Control Hardware for Ash Dome	This hardware will enable the dome to automatically line up its Lanphier shutter window to the telescope's pointing position.

Table 1: The hardware used by the CASTOR satellite tracking facility.

<b>Software Bisque's TheSky Astronomical Software Level IV Version 5</b>	This software is the main astronomical software for CASTOR. Satellite two-line element sets (TLEs) can be loaded so that the user can see the current satellite position superimposed onto the simulated sky for his/her location.
<b>Software Bisque's CCDSoft CCD Camera Software</b>	This software can accommodate a wide variety of CCD camera makes and models. It is also a fine image processing and astrometry tool.
<b>Software Bisque's T-Point Telescope Pointing Software</b>	This software is used to correct for any predictable pointing error, such as inaccurate polar alignment.
<b>Software Bisque's Orchestrate Telescope and Camera Automation Software</b>	This software allows the user to write a script containing specific targets (such as satellites) and exposure times for the CCD camera that will be run by TheSky. This allows automation of the satellite tracking process
<b>Analytical Graphics' Satellite Tool Kit (STK)</b>	This software is the main satellite analysis tool for CASTOR. It allows the user to see any satellite's ground track and actual orbit and provides access data for any user-defined facility.
<b>Analytical Graphics' STK/Connect Module</b>	This module of STK allows user interfacing with STK from any other PC or UNIX terminal. This module will be used mainly for satellite scheduling.
<b>Analytical Graphics' Precision Orbit Determination Software (PODS) Module</b>	WSPOD is the main orbit determination software used by CASTOR.
<b>NetCreations PinPoint Astrometry Software</b>	This software is freely available from the Internet and can be used for accurate astrometry of any image of any scale or rotation.
<b>JavaScript Streak Detection Algorithm</b>	This software has been developed by Mr. Phil Somers of the Defense Research Establishment Ottawa (DREO)
<b>Software Bisque's Automadome Dome Automation Software</b>	This software will be the main interface between TheSky and the Merlin Controls dome automation hardware.

Table 2: The software used by the CASTOR satellite tracking facility.

The Merlin Controls dome hardware and the Software Bisque Automadome software will not be installed until the summer of 2000. In the meantime, the other hardware and software components will be thoroughly tested so that a smooth transition between manual and automatic mode can be attained. Figure 1 demonstrates how the various hardware and software components will be used when CASTOR is fully automated.

### Scheduling

When performing any satellite tracking routine, one must know which satellites will be available to track for that facility's location and viewing constraints. The Satellite Tool Kit (STK) from Analytical Graphics can be used to do a preliminary assessment of those Molniya payloads that are accessible from SSRAL at any time. STK is run on a Unix platform, while TheSky and Orchestrate is run from a PC. It is obvious that a user could simply run STK and determine the accessibility of a satellite, generate tables, manually transfer the data files over to the PC and create an Orchestrate script from that. This would be a time consuming effort, since many satellites will be accessible to the facility in question. The solution would be to use an interface tool between the STK (Unix) software and TheSky (PC) software. This tool is the STK/Connect module. It enables the user to run STK from a PC as well as interface to download and upload information. A scripting utility can be used in order to automate the process of starting up STK, loading in the satellite element sets (elsets) desired, generating accessibility text files, and uploading these files to the PC. The files are then automatically analyzed and the Molniya elsets pertaining to those accessible Molniya payloads are extracted and saved in TheSky's local satellite elset directory. An Orchestrate script is automatically created as this is occurring. This script will contain the accessible Molniya satellites and the correct integration times

for the CCD camera pertaining to each of the respective ranges. Therefore it will be possible for CASTOR to determine which Molniya payloads it will track for any specific night.

Scheduling must also involve the preliminary determination of the facility's constraints. Factors such as the lowest tolerable elevation of the satellite, the satellite's observed angular velocity (dependent on the range), and the satellite's phase angle are critical. The scheduling software can determine these quantities while it writes the Orchestrate script. As a result those satellites that are at a high elevation at the beginning of a session will appear in the Orchestrate script until such time as the satellite drops below the threshold elevation defined by the user.

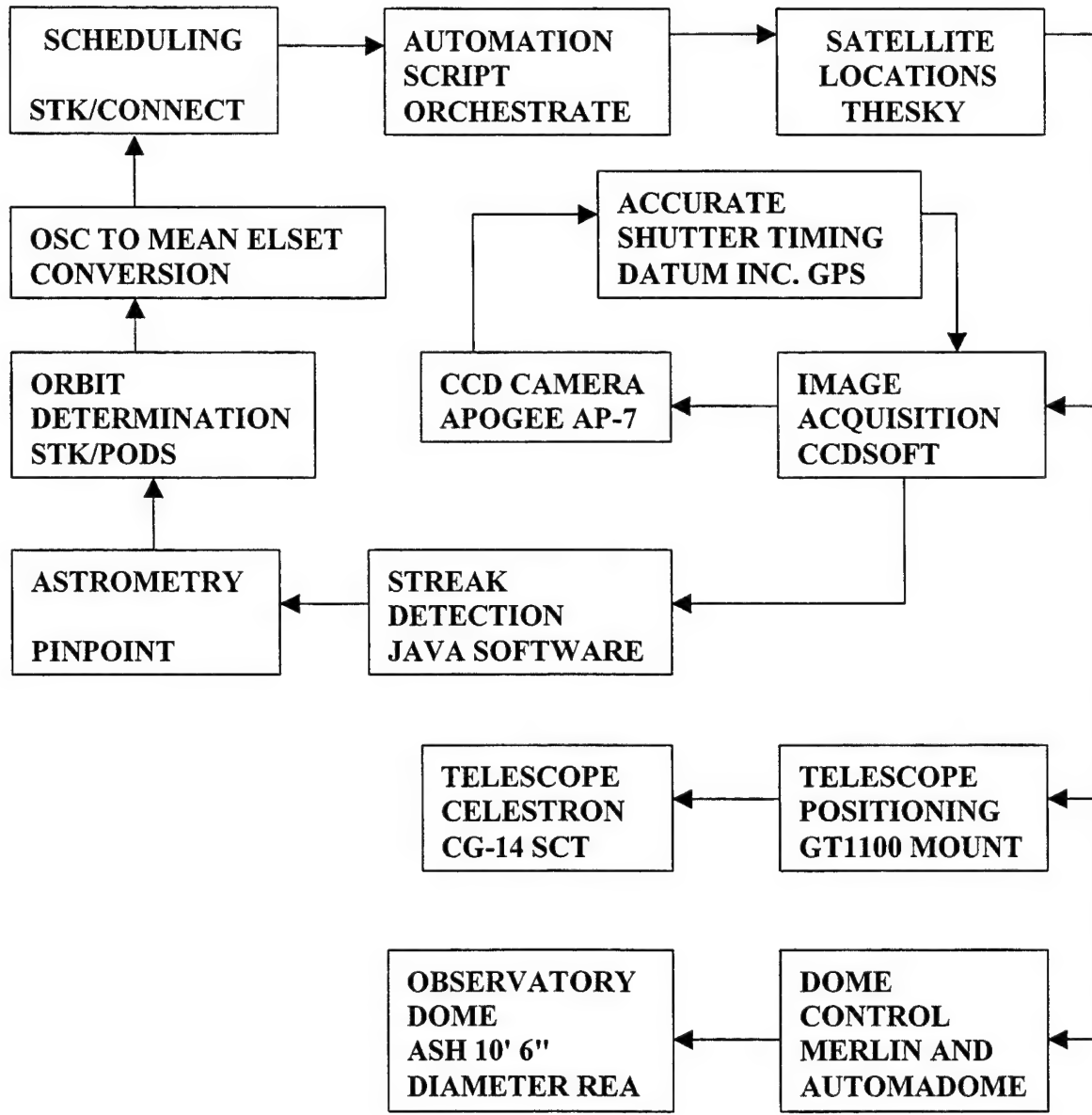


Figure 1: The integration of the CASTOR hardware and software.

### Satellite Tracking and Image Acquisition

Once the Orchestrate script is written TheSky will access the elsets that pertain to those objects in the Orchestrate script. The Orchestrate script can then be run to perform the satellite tracking for that night. This portion of the CASTOR facility is operational with the exception of the automatic dome control. The robotic mount (GT-1100) will slew the Celestron telescope to point to the satellite that pertains to the Orchestrate script. The CCD camera will then take an image for the specified exposure time. The CCD camera and the GPS receiver are connected in the sense that when the shutter of the camera opens/closes the time (accurate to a millisecond) of both events are stamped on to the FITS header of the image file. Thus, the precise times pertaining to the endpoints of the satellite streaks are known. The image will then be downloaded and automatically saved. The CCD camera also has a shutter strobe capability whereby the camera can be turned on and off for specified lengths of time within the main exposure time. This is used to determine the direction of the satellite's travel in the image and provides a larger set of data points to analyze per image. This may improve the accuracy of the final orbit determination. Figure 2 is an actual image taken with CASTOR that demonstrates this shutter strobe feature.

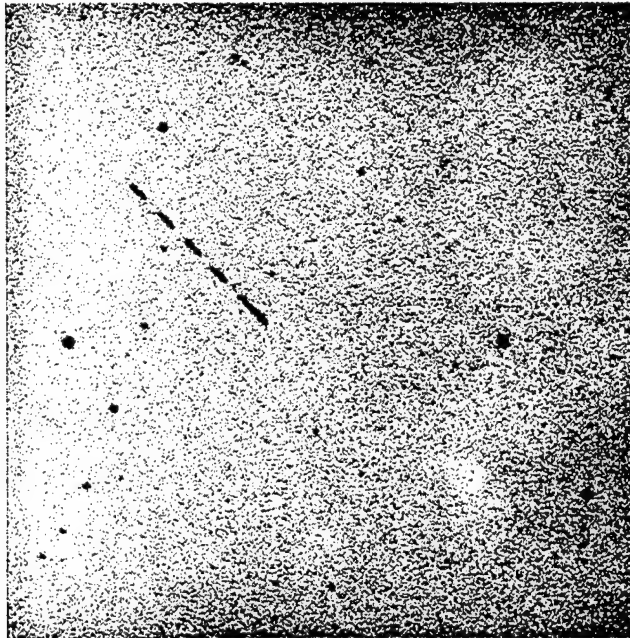


Figure 2: An image of the Molniya 1-77 payload satellite (SSC 20583) taken by CASTOR. The shutter strobe option has been engaged and has been set for a larger exposure time at the beginning of the main exposure (the longest streak) and for smaller off-on exposures afterward. This was a 30-second exposure in which the first exposure was six seconds, followed by an off-on strobe of three seconds each. The satellite is therefore travelling right to left in the image. The satellite was 35000 km in range from the CASTOR facility at the time of imaging.

The shutter strobe option is also useful for those circumstances where the satellite either exits or enters the CCD camera's field of view while the camera shutter is still open. This is often the case when decaying satellites are being tracked. If the strobe were not employed in this situation, only one data point pertaining to the only endpoint in the image would be recorded. It would be necessary however to define standard strobe times for specific main exposure times. Since the exposure times would be dependent on the range (or apparent angular velocity) of the satellite, this can be done in a reasonable time by trial and error. During one such tracking session of Molniya payloads such a list was created. Table 3 lists the results. To describe the table, the first row will be used as an example. If the Molniya payloads were 5000 to 10000 km in range from the CASTOR facility the main exposure time would be one second. This would be the exposure time in which the entire satellite streak could be kept within the field of view of the

camera. During the main exposure time (of 1 second) the camera shutter would first stay open for 0.2 seconds. The camera shutter would then close for 0.1 seconds and then open again for 0.1 seconds, etc. until the main exposure time has elapsed. This would produce a long streak, followed by four streaks of equal length that would be half the length of the first streak. If the satellite does exit the field of view during this exposure, it is possible to recover the times of each endpoint that can be seen in the image using the strobe times. Those Molniya payloads whose ground tracks are over North America generally reach ranges of 40,000 km at apogee. Those Molniya payloads whose ground tracks are over central Russia can still be seen by CASTOR but at lower elevations and ranges that typically reach 43,000 km at apogee. This is what range of 40000 + km is referring to in Table 3.

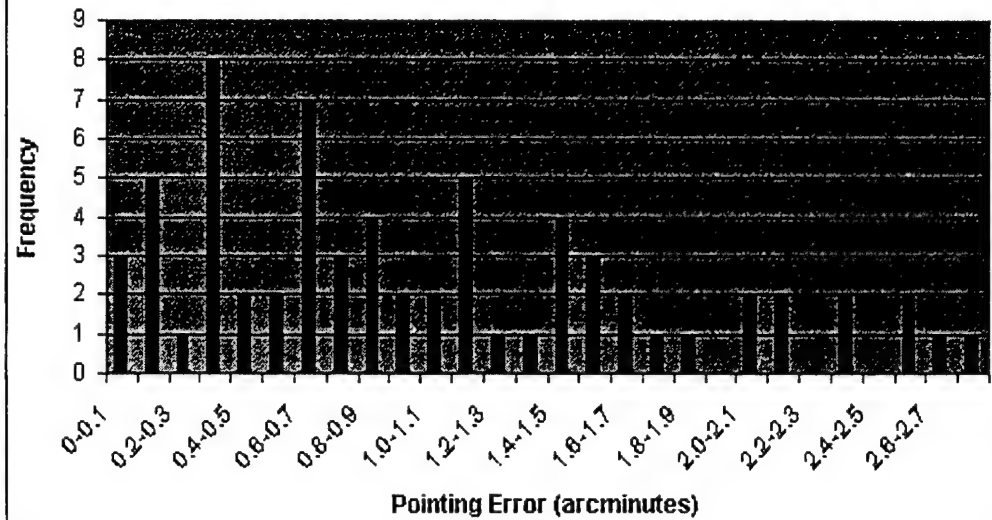
Range (km)	Main Exposure (sec)	Strobe Times (sec)
5000 to 10000	1	0.2, 0.1, 0.1
10000 to 15000	2	0.4, 0.2, 0.2
15000 to 20000	5	1.0, 0.5, 0.5
20000 to 25000	10	2.0, 1.0, 1.0
25000 to 30000	20	4.0, 2.0, 2.0
30000 to 40000 +	30	6.0, 3.0, 3.0

Table 3: CASTOR exposure and shutter strobe times for different Molniya payload ranges.

The field of view (FOV) of the CASTOR system has been determined to be 11.5 by 11.5 arc-minutes. This means that a very small area (about 1/132 of a square degree) is being imaged per exposure. In order to ensure that the satellite is within the FOV during the entire CCD exposure the telescope mount must have accurate pointing over the entire visible celestial hemisphere. Since the GT-1100 is a German Equatorial mount, precise polar axis alignment is necessary to ensure that the pointing accuracy is at or under 1 arc-minute. Polar alignment of the mount was done through a high power eyepiece. The polar axis of the scope was first found by disengaging the right ascension (R.A.) gear so that the R.A. axis moved freely. The star field was viewed through the eyepiece while the R.A. assembly was rotated. The scope was then carefully slewed in declination until the star field would not move out of the FOV while the R.A. assembly was rotated. Once the polar axis had been found, it was aligned to the epoch 2000 North Celestial Pole (NCP). Once the mount was polar aligned, it was necessary to determine the pointing accuracy over a wide range of slew angles and declinations. Since Molniya payloads were being used as an example, the pointing accuracy was determined by slewing the scope within the northern part of the equatorial sphere. This area is where the Molniya payloads (as well as the SL-6 rocket bodies that placed these payloads in their orbits) are most likely to be found. A total of 100 slews were performed in this region of the sky at declinations ranging from 0 degrees to +80 degrees. The results were both surprising and encouraging. The majority of the pointing errors were between 0.1 and 1.9 arc-minutes. A closer inspection of the results revealed that the smaller pointing errors were encountered with small slew angles, which was expected, and that the larger pointing errors resulted from large slews and/or high declination slews, which is again not surprising. What was surprising was that although the polar alignment was done totally by eye (no CCD cameras involved) the pointing error did not exceed 3 arc-minutes over the entire (northern) sky for all declinations between 0 and +80 degrees. Figure 3 briefly illustrates the pointing errors encountered. The pointing error was determined by calculating the angular separation between the destination coordinates (contained in the FITS header of the image) and the true coordinates of the center of the image. The pointing error in Figure 3 is therefore the radial pointing error. Closer inspection of the pointing errors of the individual axes (R.A. and Declination) will be performed shortly.

The pointing accuracy of the robotic mount may be improved by using the T-Point telescope pointing software. T-Point can compensate for any naturally occurring source of pointing error (such as an inaccurate polar alignment). A T-Point model for CASTOR will be performed shortly. Judging by the encouraging results so far, a T-Point model may not significantly improve the pointing accuracy of the mount since the mount is rated as having an average radial pointing error of 2 arc-minutes. The decision whether or not to use a T-Point model would also depend on whether or not the pointing error encountered thus far is accumulative, i.e. the pointing error grows larger with each consecutive slew performed.

**Figure 3: CASTOR pointing accuracy without T-Point**



Looking at Figure 3, the lower pointing errors encountered (those from 0.1 to 0.5 arc-minutes) were those for slew angles of less than 10 degrees and for declinations between 0 and +60 degrees. The pointing errors of 0.6 to 2.0 arc-minutes were experienced for slew angles of between 10 and 30 degrees and for declinations of between 0 and +60 degrees. The higher pointing errors of 2.0 to 2.9 arc-minutes were experienced for slew angles of 10 to 20 degrees at declinations between +60 and +80 degrees. It may be necessary to use a specific T-Point model for the higher declinations in order to ensure optimum pointing accuracy in all parts of the observable celestial hemisphere.

While the robotic mount is pointing the telescope to the satellites' positions the shutter opening of the observatory dome must remain in sync with the telescope aperture. In order to have a totally automated tracking facility the dome must also automatically slew its shutter in azimuth and elevation. The Automadome dome control software and the Merlin Controls automatic dome hardware will provide this automation process. This component of the CASTOR facility will not be in place until the summer of 2000. In the meantime a manual dome control hardware system has been developed at SSRAL in order to make the facility functional manually. A wide-field video camera is installed on top of the telescope. This camera is connected to a monitor that is placed within the lab. This system provides real-time monitoring of the CASTOR hardware as it is being used. When the telescope is being slewed, the dome shutter opening can be manually lined up with the telescope aperture. When the facility becomes fully automated this system will remain in place as the manual override system.

Another concern to be addressed is the satellite acquisition rate. Both the R.A. and Declination axes of the robotic mount have maximum slew speeds of 1.5 degrees per second. The satellite acquisition rate can be maximized through careful scheduling. An automatic scheduler can be made to search for that satellite on the main schedule list that is the closest to the one last chosen i.e. search for that satellite that requires the smallest slew angle. This will ensure that the slew angles will be kept to a minimum and therefore keep the pointing errors small (with or without a T-Point model in place). The results of this planning would be automatically entered into the Orchestrate script. One major drawback in using a German Equatorial mount is that when the telescope has to slew to an area of the sky that lies on the opposite side of the celestial meridian from its last known position, it has to slew through the NCP to get there. If it doesn't do this it will slew the scope into the mount base causing damage. An automatic scheduler would have to take this into account in order to avoid a higher pointing error and a longer slew time that could decrease the satellite acquisition rate considerably.

### Image Analysis

Once the images have been acquired, streak detection and astrometry on the detected streak end-points must be performed in order to extract the tracking data needed for the orbit determination process. At the present time the satellite streaks contained within the image are detected manually by eye. A JavaScript automatic streak detection software is currently being developed by Mr. Phil Somers of Defense Research Establishment Ottawa (DREO). This streak detection software will be used with auto-astrometry software called PinPoint. This auto-astrometry software uses the World Coordinate System (WCS) and the Hubble Guide Star Catalog (GSC) to perform astrometry that should be accurate within 1 arc-second provided that the streak detection software properly centroids the streak end-points and the GSC stars within the image. Testing of this software will begin shortly.

### Orbit Determination

SSRAL currently uses the Precision Orbit Determination Software (PODS) for performing orbit determination. This software is a module of the Satellite Tool Kit (STK) therefore STK/Connect may be used to perform the orbital determination task automatically. PODS will use the tracking data files generated by the PinPoint astrometry software to update the osculating orbital elements of the satellite. To be able to use these orbital elements to track the satellite at a later time an osculating to mean element set conversion must take place. SSRAL has obtained a software package that can perform this conversion. Once the mean element set has been created, the scheduler can use it and the other determined elsets in STK to begin the tracking process once again. Once CASTOR is fully automated, an investigation into the most accurate technique of orbit determination will be undertaken. This will involve a study into which part(s) of the Molniya orbit to analyze in order to maximize the accuracy of the orbit determination. It will also involve different techniques of image acquisition and timing that will simplify the image analysis and increase the accuracy of both the streak detection and the astrometry process.

### Present and Future Plans for CASTOR

At the present time, CASTOR is still in its planning and testing stages, but it can be used for high eccentricity orbit satellite tracking (such as Molniya payloads) and geo-stationary payload and rocket body tracking. At this time scheduling and image analysis is still time consuming but steps will be taken to automate both processes. At present only a small amount of satellites can be tracked at a time in order to prevent a data glut from occurring.

CASTOR will be one of a trio of automated closed-loop satellite tracking facilities located across Canada. The first CASTOR facility is in Kingston, Ontario, Canada. The second will be located somewhere in western Canada and the third will be located somewhere in eastern Canada. This trio of optical sensors will be used to provide an optical deep sky satellite tracking net in Canada.

The CASTOR facility will have to be approved by the U.S. Air Force Space Command (AFSPC) in order for it to be a contributing sensor for Cheyenne Mountain. There are a number of standards that CASTOR will have to meet in order to be a viable candidate. The first is an acceptable metric accuracy. The accuracy for each R.A. and Declination quantity for the optical sensor will have to be within 10 arc-seconds. The shutter open/close times will have to accurate to within 1 millisecond. This is a concern as far as the shutter strobe option is concerned. Only the first shutter opening and last shutter closing times are stamped onto the FITS header of the image. The timing accuracy of the other end-points depends on the shutter accuracy. The ground site location must be known to at least 0.0001 degrees in latitude and longitude and to within a few meters in altitude.

The prototype CASTOR system known as CASTOR B will still be used for low priority satellite tracking and geo-stationary belt surveys. It is theoretically possible to automate this system as well but it will be prone to the weather conditions because CASTOR B has no observatory dome to protect it.

### Summary

The CASTOR satellite tracking facility is currently in its planning and testing stages. By the summer of 2000 it is expected that CASTOR will be fully automated and accurate enough to be accepted as an AFSPC sensor.

Full automation of the CASTOR facility will involve the creation of a carefully planned scheduling routine that will automatically select those satellites that fall within the acceptable constraints of the facility. These constraints include the range of the satellite, the satellite phase angle, the lowest acceptable elevation, and especially the determination of the highest satellite acquisition rate. A major problem with the planning of this automated scheduler is that it will have to integrate with the other three branches of interest (tracking and imaging, image analysis and orbit determination). The STK/Connect software should facilitate the scheduling process.

The tracking and imaging stage of the project is completed with the exception of the automated dome component. That piece of the project will be installed by the summer of 2000. It is presently possible to do satellite tracking with the system but both scheduling and image analysis are time consuming so that the number of images are kept to a minimum to prevent data glut.

The image analysis stage has been the most difficult and time-consuming one to this point. New streak detection and astrometry software are being developed in order to automate this process and to provide more accurate end-point determinations and metric data.

The STK/Connect module should be able to automate the orbit determination process. Once CASTOR is fully automated steps will be taken to determine the best scheduling, tracking, image acquisition, image analysis and orbit determination methods in order to ensure that the CASTOR facility is the most practical and accurate it can be.

# **SPACE SURVEILLANCE WITH THE SPACE-BASED VISIBLE SENSOR\***

**Jayant Sharma**

## **Abstract**

The Midcourse Space Experiment satellite was launched in 1996. A principal sensor on board the satellite is the Space-Based Visible (SBV) sensor, a visible-band electro-optical camera designed at Lincoln Laboratory to perform the first technical and functional demonstration of space-based space surveillance. The principal task of the SBV sensor is to gather metric observations on a variety of resident space objects. In 1997, after the successful technology-demonstration phase of the mission, the SBV sensor was transitioned to a Contributing Sensor in the Space-Surveillance Network. The Space-Based Space-Surveillance Operations is now providing the Space-Surveillance Network with the first operational space-based space-surveillance sensor. With its orbital location, wide field of view, and high metric accuracy, the SBV sensor has made significant contributions to the Space-Surveillance Network. The performance of the SBV sensor and application of its observations to satellite tracking will be demonstrated. There has been an ongoing effort to increase the productivity. This paper will also describe these modifications.

## **Introduction**

After completing a successful demonstration of space-based space surveillance, the SBV sensor began contributing sensor operations in April 1998. The SBV Processing and Operations Control Center (SPOCC) receives daily tasking from Space Command. The spacecraft is operated 8 hours per day, 7 days per week performing space

---

\*This work sponsored by the Dept. of the Air Force under Air Force Contract No. F19628-95-C-0002. Opinions, interpretations, conclusions and recommendations are those of the author and are not necessarily endorsed by the United States Air Force.

surveillance. The description of the data processing was provided in a previous paper.<sup>1</sup> Sensor characteristics relevant to routine space surveillance are summarized in Table 1.

Table 1. SBV Sensor Characteristics

Spectral Range	0.3 - 0.9 $\mu\text{m}$
Spatial Resolution	12.1 arcsec/pixel
Field of View per CCD	1.4 x 1.4 Deg
Aperture, f/no	15 cm, f/3
Number of Frames per Frameset	4 – 16 frames
Frame Integration Times	0.4, 0.625, 1, 1.6 sec
Frame Sizes	420x420 pixels

Surveillance data is collected in a sidereal track mode, where the stars appear as point sources and the RSOs appear as streaks. Routine surveillance data is then processed through the onboard signal processor to extract the star and streak information as illustrated in Figure 1.

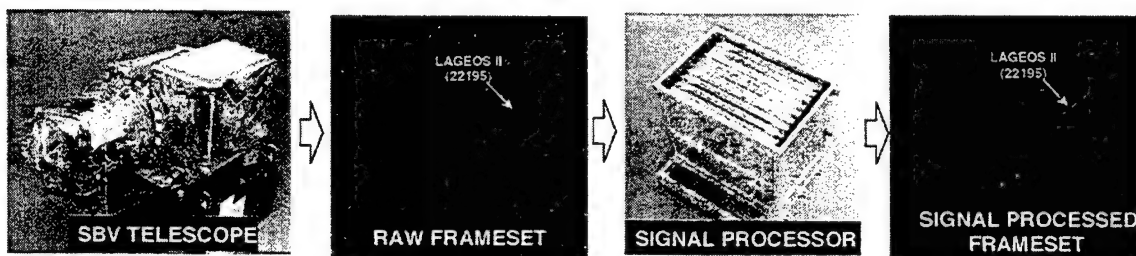


Figure 1. Routine Surveillance Data

### Space-Based Surveillance Operations

SBV operations exploit the unique properties of SBV. The orbital location provides SBV with a global coverage of the GEO belt. The wide field of permits the simultaneous detections of multiple objects.<sup>2,3,4</sup> SBV operations is performed in two modes. In the

first mode SBV is commanded to collect data on a set of tasked objects for six hours per day. Tasked operations is carried by generating an optimal schedule that maximizes the number of objects in the field of view and minimizes the number maneuvers required. The second operations mode, call GEO belt search, involves scanning regions of the GEO belt with the array of four CCD sensors as shown in Figure 2. By aligning the array along GEO belt, up to 50 degrees of longitude can be searched per hour. Current search operations focus on the GEO belt region between 0 – 90 degree E Longitude.

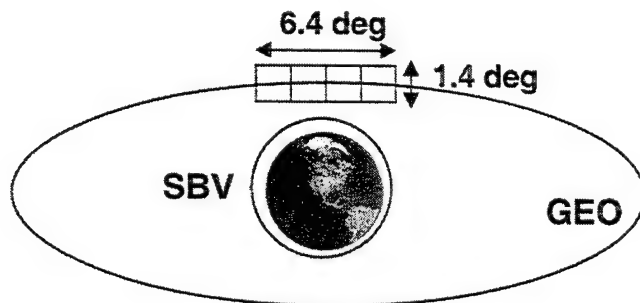


Figure 2. GEO Belt Search Geometry

Access to entire GEO belt is a key advantage of a space based sensor and is illustrated in Figure 3. Figure 3a shows the location of actively station kept satellites in the GEO belt. These satellites maintain a fixed position relative to the earth and require at least three ground-based sensors to provide complete access. Figure 3b shows the SBV detections of these satellites with both tasking and search operations, and shows that SBV has access to the entire GEO belt.

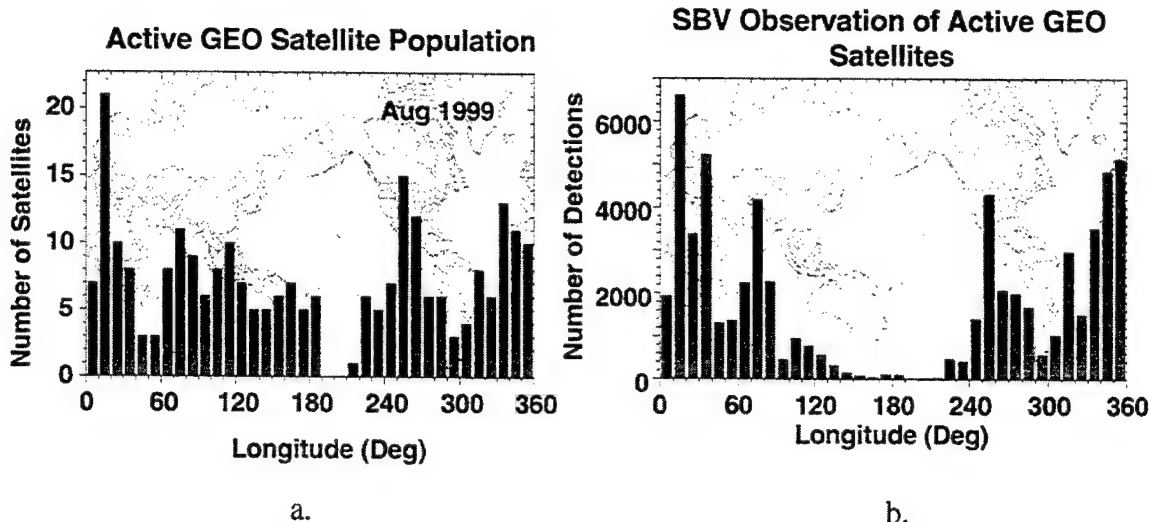


Figure 3. Global Coverage of the GEO Belt

SBV is primarily operated to observe objects with periods greater than 225 minutes (deep space objects). The current and historical productivity of the SBV sensor is illustrated in Figure 4a. This plot shows the daily number of deep space tracks collected by SBV. The productivity of SBV has been increased from 50 tracks/day to 200 tracks/day by utilizing SBVs wide field of view to capture multiple objects per frameset as shown in Figure 4b. Objects are also allowed to drift across the field of view when collecting multiple observations instead of spending time to maneuver the spacecraft.

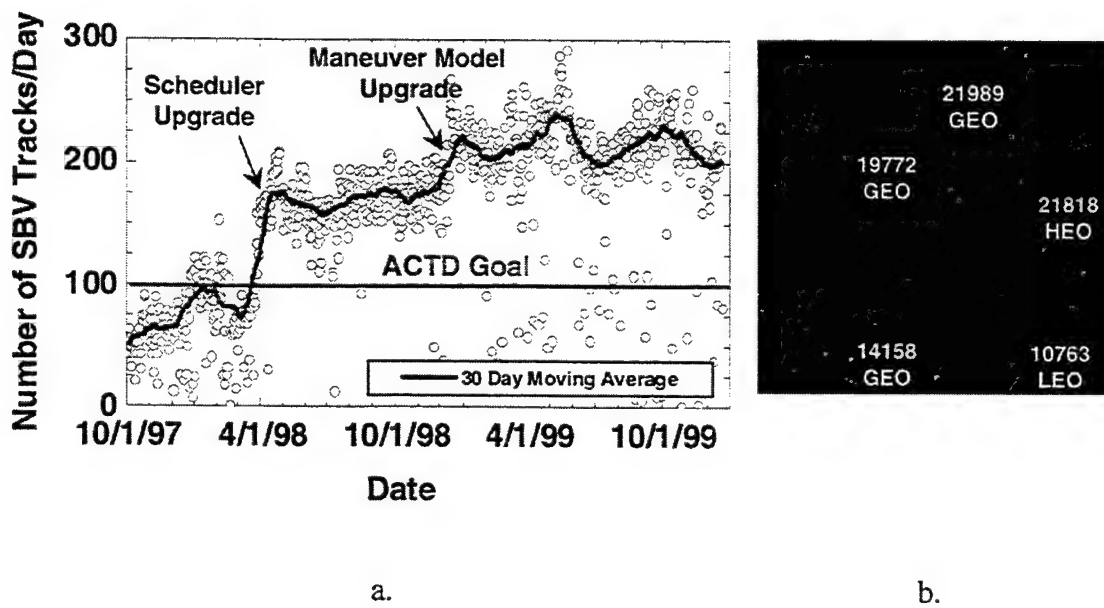


Figure 4. Current and Historical SBV Productivity

This section describes the tracking performance of the SBV sensor. Figure 5 shows that SBV is primarily commanded to collect data on geosynchronous (GEO) objects, but twenty-five percent of SBV observations are on non-GEO objects. Geosynchronous objects are those objects that have a circular orbit with approximately a 24 hour period. This plot also compares SBV's performance to the other optical sensors in the Space Surveillance Network, and shows that the SBV is the most productive optical sensor.

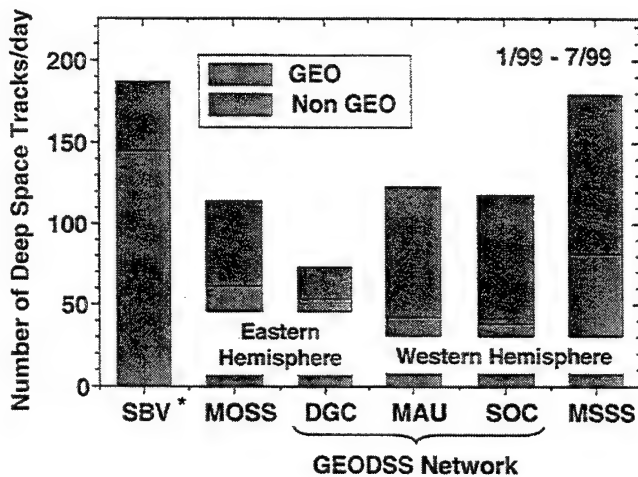


Figure 5. Comparison of Tracking Performance

(Data: Courtesy of Air Force Space Command)

\*Includes Maintenance Days)

MOSS - Moron Optical Surveillance Site

MSSS - Maui Space Surveillance System

Ground-based Electro-Optical Deep Space Surveillance system (GEODSS) Sites

MAU - Maui

SOC - Socorro

DGC - Diego Garcia

### Contributions to Space Surveillance

SBVs unique vantage point, wide field of view, and accurate observations has permitted it to make valuable contributions to space surveillance. The orbital location of SBV not only provides global coverage, but it also provides an immunity from weather outages. This combination has resulted in a high acquisition of high priority objects with global coverage. Figure 6 shows the distribution of detections of high priority objects from Space Command. SBV has been providing these detections at a ninety percent acquisition rate, and in regions without deep space radar coverage. The locations of deep space radars are denoted with triangles.

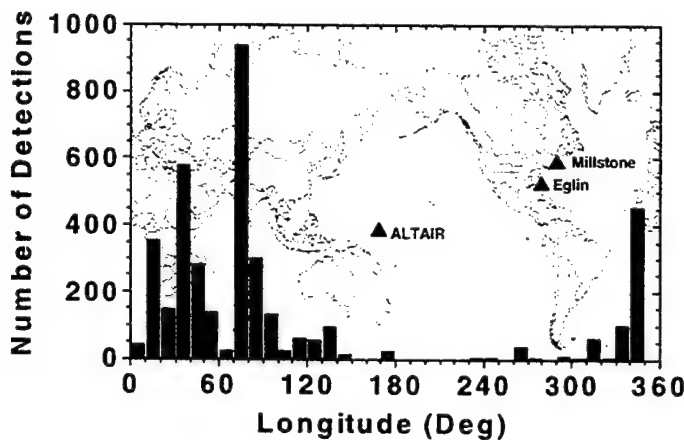


Figure 6. Distribution of High Priority Objects

SBVs wide field of view is not only aids in detecting objects whose element sets are known, but also permits the detection of objects that do not have an accurate element set. These objects are called uncorrelated targets (UCTs). The wide field of view of the SBV sensor has been instrumental in the detection of many UCTs. Most UCTs are readily identified by a careful comparison with a database of element sets.<sup>5</sup> For observations that are not readily identified, multiple detections must be linked together to generate an initial orbit solution. This was the case for the example shown in Figure 7. This figure shows the detection of three UCTs which were eventually identified as two Russian Yamal payloads and the associated upper stage.

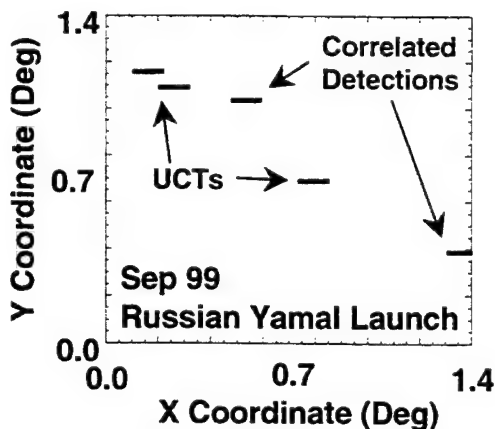


Figure 7. Detection of Three GEO UCTs

The processing of linking together detections is relatively easy for GEO objects where multiple detections are collected by repeatedly looking at the same region of the GEO belt. Initial orbit determination requires a minimum of three observations that sample a small fraction of the orbit either over single or multiple orbit revolutions. Once an element set is generated, further observations are collected and the orbit is improved. An example of this process is shown in Figure 8. In this case about five percent of the orbit is sampled by the discovery observations. The errors in the orbit rapidly decrease as additional observations are collected.

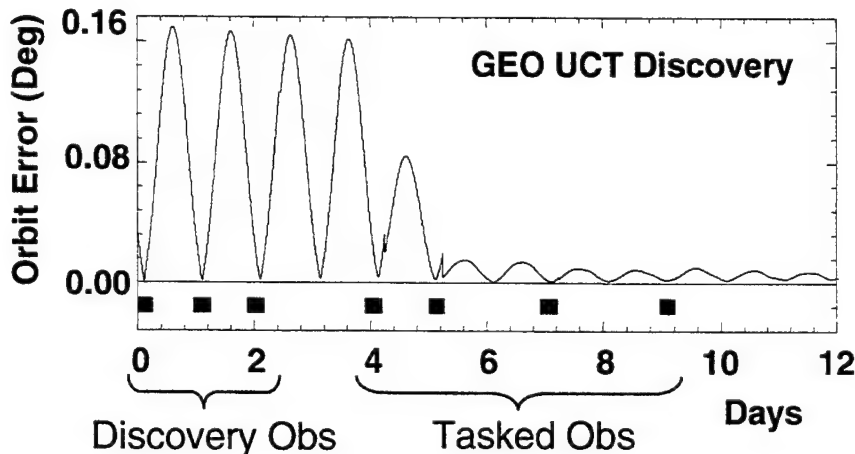


Figure 8. UCT Discovery Process

Since October 1997 SBV observations have led to the recovery/discovery of 92 UCTs in this manner. Figure 9 illustrates the location of these discoveries around the globe, and shows that the majority of the discoveries occur in the eastern hemisphere. Most of these discoveries have occurred with GEO belt search operations. By repeatedly looking at the same regions of the GEO belt, search operations are 2.6 times more effective in generating UCT discoveries than tasking operations.

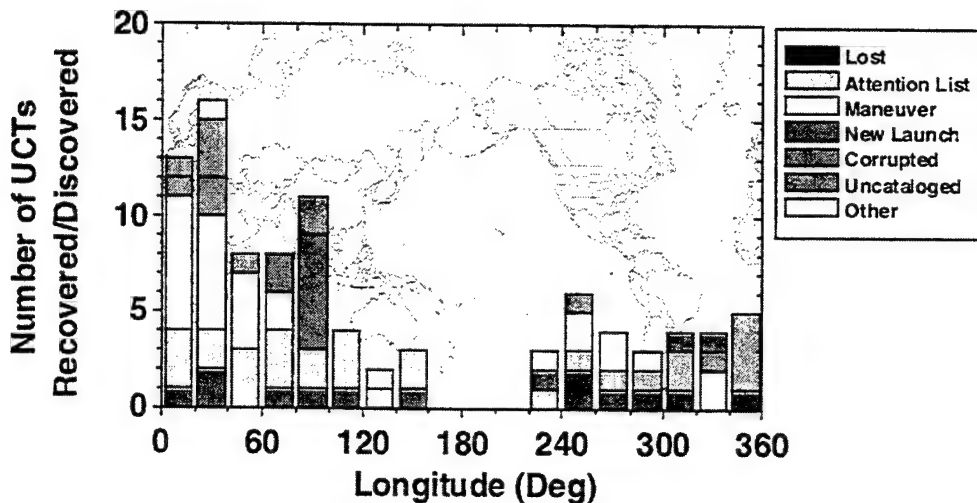


Figure 9. UCT Recoveries and Discoveries

SBV is demonstrating the impact of accurate observations in orbit determination.<sup>6</sup> The accuracy of SBV observations is assessed by collecting observations of Global Positioning System (GPS) satellites and then comparing those observations with an independently determined precise ephemeris. The distribution of the GPS residuals is shown in Figure 10, which shows that the SBV goal of one mdeg is being reached by the 68 % of the observations.

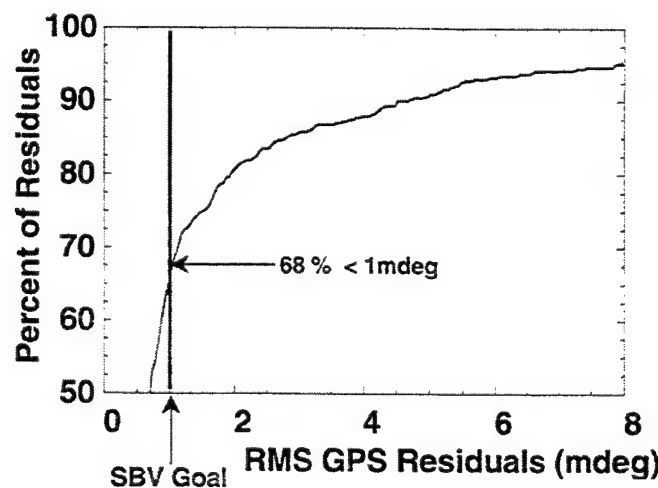


Figure 10. SBV Metric Accuracy

Utility of accurate SBV observations for orbit determination of geosynchronous satellites is illustrated in Figure 11. The results are based on tracking of the TDRS-4 communication satellite. The accuracy of the Lincoln Laboratory orbits was assessed by comparing them with a more accurate reference orbit.<sup>7</sup> The amount of data used for this example is shown in Table 2.

Table 2. Tracking Data for TDRS-4 Orbit Determination

	Tracking
Sparse SBV Tracking	6 Tracks / 14 days
Sparse MHR Tracking	3 Tracks / 14 days
Dense SBV Tracking	21 Tracks / 30 days

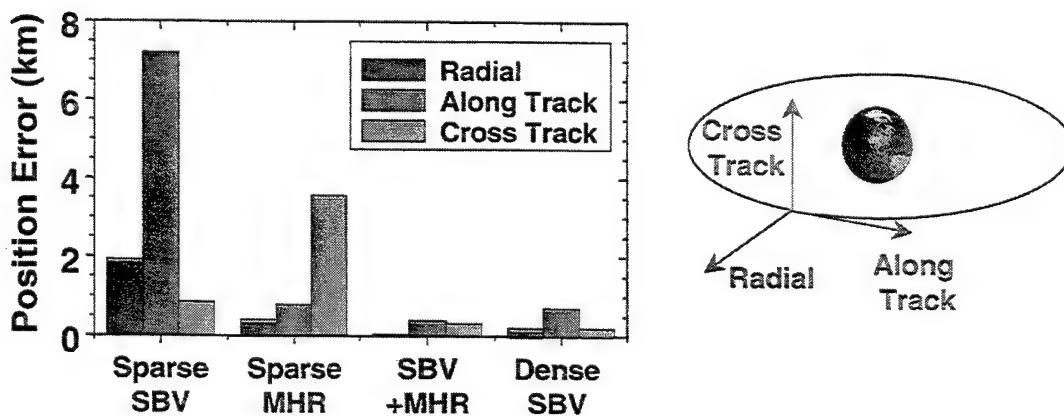


Figure 11. Orbit Determination of Geosynchronous Satellite

Figure 11 shows that combining Millstone Hill Radar (MHR) data and SBV data exploit the strength of each data set to produce a much better orbit solution. The accurate SBV angles data produces an accurate knowledge of the orbit inclination, resulting in small cross track errors. The accurate range and range rate data from the Millstone radar produces an accurate knowledge of the semimajor axis and eccentricity, resulting in small radial and along track errors. It is also possible to generate an accurate orbit with only SBV data given increased tracking.

## Conclusion

SBV is demonstrating the advantages of space surveillance from space. SBV is providing global coverage with a single sensor. Using sensitive Lincoln Lab CCDs, SBV is demonstrating the ability of a small sensor to be highly productive deep space sensor. SBV is also providing Space Command with observations of high priority objects and helping to maintain an accurate catalog with the detection and processing of UCT observations. Finally, SBV is showing the benefits of search operations by showing its effectiveness in generating UCT discoveries.

## References

1. Sharma, J., C. von Braun, E.M. Gaposchkin, *Space-Based Visible Metric Data Reduction*, Journal of Guidance, Control, and Dynamics, Vol. 23, No. 1, 2000, pp. 170-174.
2. Sharma, J., *Space-Based Visible Space Surveillance Performance*, Journal of Guidance, Control, and Dynamics, Vol. 23, No. 1, 2000, pp. 153-158.
3. G. H. Stokes, C. von Braun, R. Sridharan, D. Harrison, and J. Sharma, *The Space-Based Visible Program*, Massachusetts Institute of Technology Lincoln Laboratory Journal, Vol. 11, No. 2, 1999, pp.205-238.
4. Viggh, H.E.M., Blaufuss, D., Morton, F., Wiseman, A., R. Sridharan, *SPOCC Mission Planning System Performance*, Proceedings of the 1997 Space Control Conference, STK-249 Vol. II, MIT Lincoln Laboratory, Lexington, Massachusetts, March 25-27, pp. 25-35.
5. G.R. Zollinger, J. Sharma, and M. J. Lewis, *SBV Uncorrelated Target (UCT) Processing*, Proceedings of the 1999 Space Control Conference, STK-254, MIT Lincoln Laboratory, Lexington Massachusetts, April 13-15, pp. 175-188.
6. C. von Braun, J. Sharma, and E. M. Gaposchkin, *Space-Based Visible Metric Accuracy*, Journal of Guidance, Control, and Dynamics, Vol. 23, No. 1, 2000, pp. 176-182.
7. Abbot, R., and J. Sharma, *Determination of Accurate Orbits for Close Encounters between Geosynchronous Satellites*, Proceedings of the 1999 Space Control Conference, STK-254, MIT Lincoln Laboratory, Lexington Massachusetts, April 13-15, pp. 71-83.

## **Determination of Photometric Filters for Satellite Observations Using SILC Data**

T. Payne (Schafer Corp.), S. Gregory (UNM/AFRL), D. Payne (Schafer Corp.), L. Kann (AFRL), D. Sanchez (Schafer Corp.), D. Werling (AFRL), C. Davis, L. Finkner (Boeing)

### **Abstract**

Air Force Research Laboratory has had a collaborative effort between three branches of the Directed Energy Directorate involved in the collection and analysis of spectral data gathered under the SOI (Space Object Identification) In Living Color (SILC) Space Battlelab initiative. These data will be presented. Post-processing of the data will be discussed and objective search techniques for filter determination will be introduced. These techniques were designed to maximize the differences in brightness between satellites at the same solar phase angle. The final recommended filter set will be presented along with predictions of their expected SOI performance.

### **Introduction**

This paper presents the data analyses performed by the AFRL/DEBS team that included Schafer, Boeing, and the University of New Mexico along with DEBS. First, preparations that were necessary for processing the SILC spectra are reviewed. Then, how well the spectral data is distributed in solar phase angle, red vs. blue wavelength regimes, and solstice vs. equinox for each satellite is presented. A summary of the character of the satellites as a function of solar phase angle is then presented. Next, the transformation of the spectral data into filter data, the evaluation of which best filters discriminate the satellites, and identification of the satellites using the chosen filters (resulting SILC filters) are summarized. Finally, it is demonstrated how photometry with SILC filters could address the issue of cross-tagging.

### **SILC Spectral Data**

The spectral data were examined for anomalies after a box car smoothing function had been applied with a width of 10 pixels. The intensity values were all multiplied by  $10^{14}$  ergs/cm<sup>2</sup>/s/ Å to avoid processing in double precision and for convenience of display. So, all the intensities reported in this paper need to be divided by  $10^{14}$  in order to get the actual ergs/cm<sup>2</sup>/s/ Å values .

The processing and analysis of the SILC data for filter determination was limited to 10 satellites. Table 1 lists the satellites, their bus structure type (class number), and their known status.

**Table 1. Satellites Used for Filter Determination**

Satellites Used for Filter Determination				
Class Number	SCC Number	Satellite Name	Bus Type	Status
1	23467	UFO	Hughes 601	Active
1	23313	Sol 2	Hughes 601	Active
1	23175	Pas 2	Hughes 601	Active
2	21222	Anik E2	GE Satcom 5000	Active
2	22117	Satcom C3	GE Satcom 5000	Active
3	21639	TDRS 3	TDRS	Active
4	25331	Echostar 4	GE 7000	Active
5	23016	Galaxy IR	Hughes 376	Active
6	21641	IUS Rocket Body	IUS Upper Stage	-----
7	24786	GOES 10	Loral	Active

Spectral data was taken in two wavelength regimes: blue (3299 Å to 6689 Å) and red (6102 Å to 9529 Å). A total of 717 blue spectra and a total of 580 red spectra taken from May through July and in September 1999 were used in this analysis.

## Phase Angle Analysis

One factor in non-imaging techniques of satellite photometric signature analysis is the satellite's behavior with solar phase angle. For an initial analysis, the intensity across each wavelength regime (blue and red separately) was summed to produce a "white light" or integrated intensity. The solar phase angle is defined as the angle between the sun and the observer at the satellite. A typical satellite curve, integrated intensity vs. solar phase angle, is shown in Figure 1.

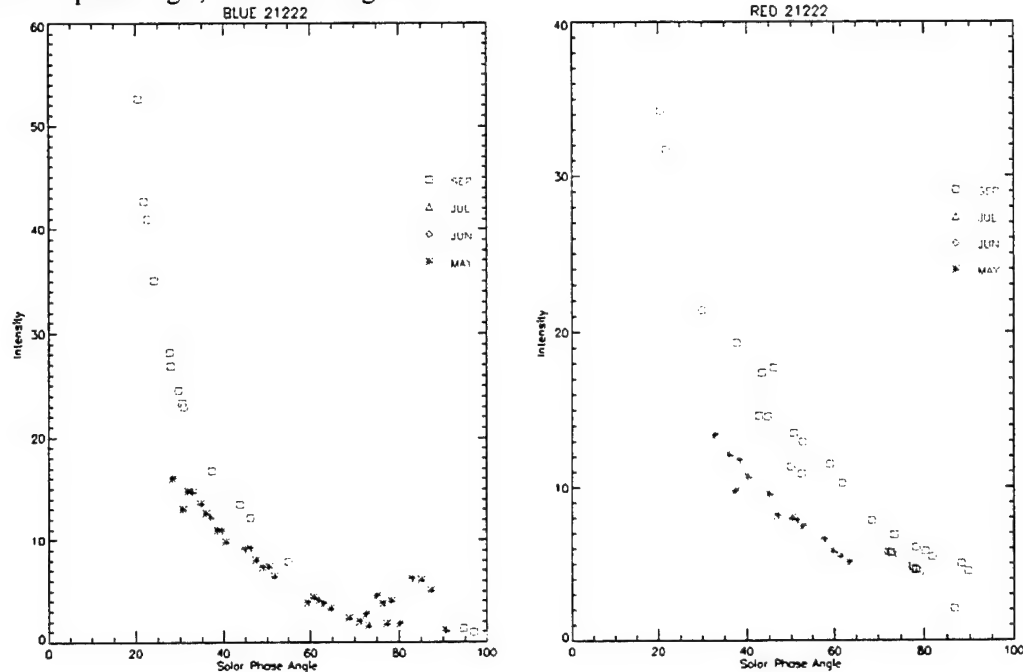


Figure 1. Integrated Intensities vs. Solar Phase Angle for 21222

The intensities are grouped by month. For satellite 21222, data was collected in May and again in September. As can be seen in Figure 1, the September (Equinox) data is much brighter than the May data. So, a glinting behavior for 3-axis stabilized satellites is observed during the Equinoxes. This effect has been identified by Beavers for 2-axis stabilized satellites and was shown to be repeatable from year to year during each Equinox (March and September). (Ref. 1)

Most of the other 10 satellites exhibit the same consistent phase angle behavior as in Figure 1: brighter at smaller phase angles, dimmer at larger ones with a concave light curve and brighter during Equinox at all solar phase angles. However, satellite 25331 shows inconsistent behavior. Figure 2 shows that 25331 behaves, in both the blue and red cases, vastly differently in June than in July. Also, the September data is more consistent with the July data. The analysis of Figure 2 leads to two conclusions: either this satellite was cross-tagged some time between the observing dates in June and the observing dates in July, or this satellite's status/orientation/operation changed during this time period. In an operational system where calibrated photometric data was collected, this type of inconsistent behavior could be automatically tagged to notify an analyst that further steps should be taken to evaluate the condition of this satellite. Therefore, these data, examined in this way, can be a viable tool for an operational system.

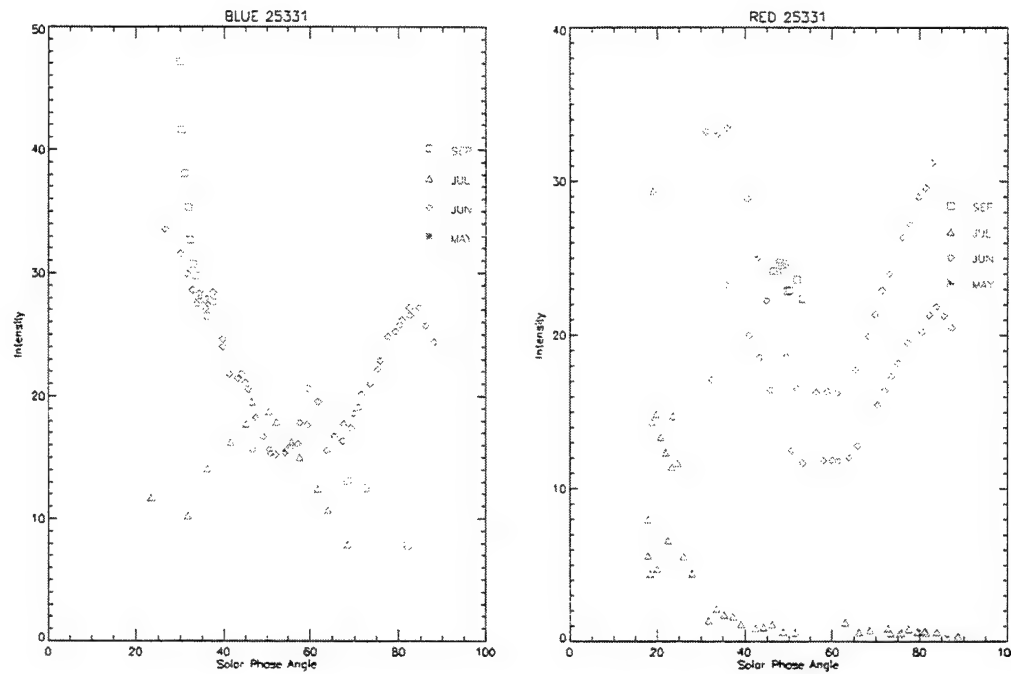


Figure 2. Integrated Intensities vs. Solar Phase Angle for 25331

#### Production of Synthetic Filter Data

To simulate actual filters, Gaussian functions were numerically generated with a full width at half maximum equaling 100, 200, and 800 Angstroms ( $\text{\AA}$ ). The filter centers were spaced 50  $\text{\AA}$  apart across the entirety of each spectrum of the red regime and of each spectrum of the blue regime. See Figure 3 for a representation of this process. The magnitudes of the individual filters were determined by multiplying the generated filter function (central peak value = 1) by each observed spectrum. Many of the synthetic filters had non-negligible values at the edge of the observed spectra. To normalize the filter magnitudes, thus removing skewing due to this “edge effect”, the integrated magnitude was then divided by the area that was actually used under the Gaussian curve.

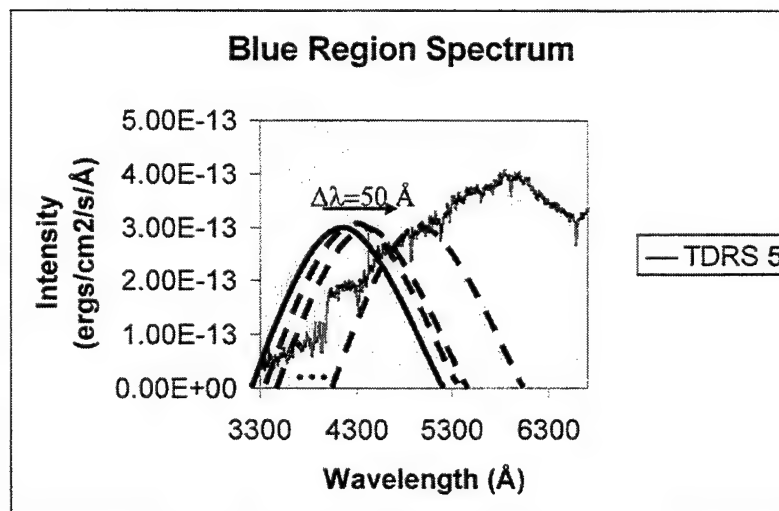


Figure 3. Synthetic Filter Generation Process

## **Quantitative Evaluation To Determine SILC Filters**

The goal of this analysis was to identify filter combinations and their central wavelength positions and widths that would maximize the probability of uniquely identifying one satellite from another. Two major parameters complicate this analysis: solar phase angle and the glinting season, i.e. much brighter September data than the May through July data. The first parameter, solar phase angle, was managed by dividing the observations into 10 degree phase angle bins and performing the analysis separately for each phase angle bin. The second parameter, equinox brightening, was managed by dividing the data into two groups. The first group contains only May through July data. The second group contains all the SILC spectra from May through the end of September. Initially, the analyses were performed on the summer data with the result that candidate filters were selected. Then the filter candidates were examined using the entire data set to verify that the candidate filters would work on the Equinox data too. Finally, the filter selection was constrained by the fact that there are six filter slots in the GEODSS filter wheel. Therefore, the six best filters were identified.

Since the solar phase angle of the blue and red observations of the same satellite were not identical, the blue and red data were necessarily analyzed separately. This also means that testing of a photometric color (the ratio of the integrated intensities through two different filters) constructed from a blue regime filter and a red regime filter was not possible. In the following presentation of the filter determination process, the blue regime will be examined first, then the red regime.

A goal for identifying new filters would be that, statistically, the integrated intensity through a filter for a satellite should be as different from all the other satellites as possible. Since there is not one value, but many values of the integrated intensity for a satellite through a filter, an average of these samples of the integrated intensities must be used. Then the wavelengths where the differences of these averages are a maximum are prime candidate wavelengths for the location of a filter. One statistical average that represents the population of intensities is the median. The median of a population is defined as that value for which half the observations will be less than the median and half will be greater. (Ref. 2) The median was used instead of the mean because the mean can easily be dominated by an extreme value in intensity.

A single filter can be identified in a straightforward manner using this technique. However, the best combinations of filters that will produce colors that will contribute to SOI also need to be identified. In order to identify these, cross-correlations were made between the synthetic filters. The cross-correlations identify at what two wavelengths the difference of the medians are both maximum. Thus, identifying a photometric color index that will maximize the differences in the integrated intensities from different satellites. These data are displayed as contour maps and black and white image maps, where the maximum of the differences of the medians are peaks and lighter or whiter areas, respectively.

Three possible filter widths were chosen as candidate widths. The possible widths were based on the widths of astronomical filter sets that have been in use for decades and the authors' experience. The three possible widths were: 100 Å, 200 Å, and 800 Å. 200 Å were used first because it was known from previous analyses that the 800 Å filters were too wide in most cases and the 200 Å filters have twice the throughput as the 100 Å filters.

First consider the blue regime. The differences of the medians for the May through July data for a filter width of 200 Å are presented in Figure 4. It shows that there is a maximum at 4150 Å for solar phase angles of 30, 70 and 80 degrees. 4150 Å is also good for all other phase angles as there is a local maximum or plateau. 4750 Å is also a candidate central filter position for though it is not a maximum for any phase angle, it catches the red end of a maxima for high phase angles and a plateau for low phase angles. Finally, 5900 Å is just redward of a plateau for 70 and 80 degrees and a local maximum for all other phase angles, which makes it an excellent candidate. The results for the 100 Å filters are consistent with these results. The same analysis of the 800 Å filters show a great deal of information is lost from integrating over such a large wavelength span.

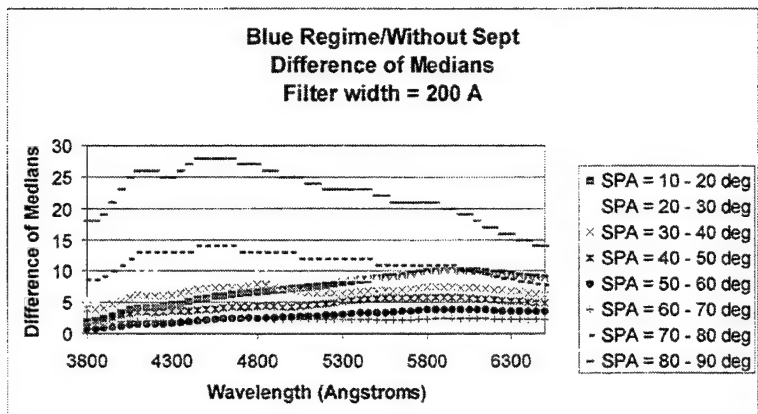


Figure 4. Difference of Medians for Blue Regime Without September Data and Filter Width of 200 Å.

There are three candidate filters at 4150 Å, 4750 Å, and 5900 Å with widths of 200 Å. With this in mind, analysis of the cross-correlation plots for the 200 Å width will provide information on whether these single filters will combine to provide useful photometric colors or whether there exists more filter combinations that will produce good photometric colors for satellites. Starting with the 0 – 10 degree solar phase angle bin, all the contour and image plots were examined. The 10 – 20 degree phase angle data show that 5900 Å filter is excellent since it corresponds to a peak in the cross-correlation as can be seen in Figure 5. Other such plots show that 4150 Å, 6300 Å, 3900 Å, and 4750 Å are good central wavelengths for filters. 3900 Å was good when 4150 Å was also good, so 4150 Å was chosen since it is not as far into the Ultraviolet where telescope throughput is lower.

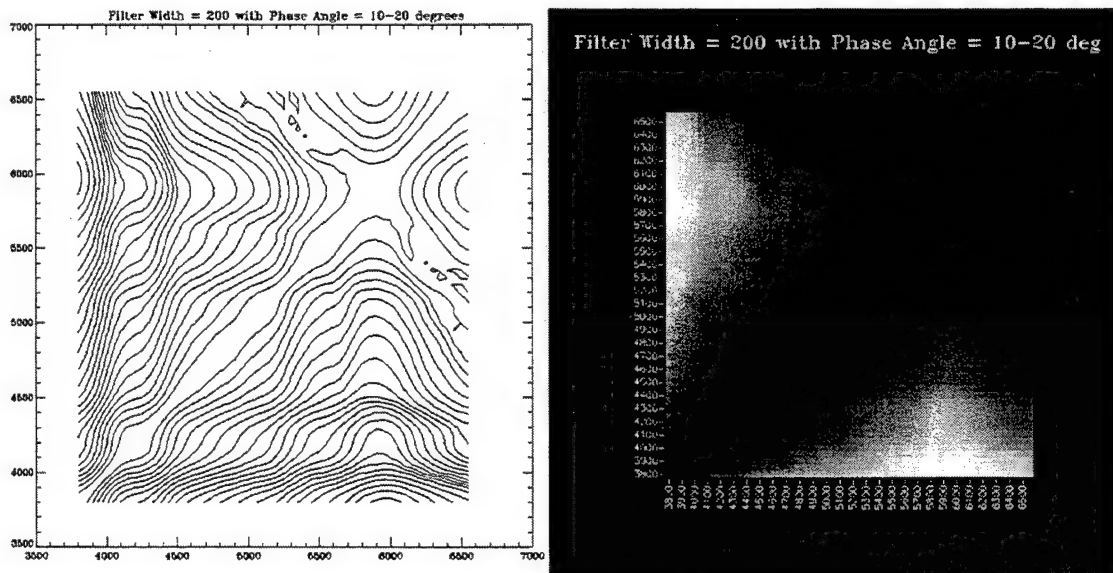


Figure 5. Contour and image maps of Blue Regime Without September Data with Filter Width of 200 Å at 10 – 20 degrees Solar Phase Angle.

The other filter widths (100 Å and 800 Å) were also examined. The 800 Å cross-correlation data show similar results to the difference of medians data for 800 Å – only two features in all the plots around 4600 Å and 6300 Å. Again, the filter width is so broad as to average over many useful, spectrally more narrow, features and thus yields less information. In the case of the 100 Å filter results, narrower, but perhaps extremely useful, features might be missed in the 200 Å data, so these were examined for additional information. The results were consistent with the 200 Å case.

This concludes the summary of the analysis of the blue regime data. The preliminary conclusions at this stage are that there should be three filters that are 200 Å wide at 4150 Å, 4750 Å, and 5900 Å. These are clearly the best central wavelengths where 200 Å is chosen over 100 Å simply because of the increased signal through 200 Å filters. Finally, there is a broad region at 6300 Å where the cross-correlation remained high at many phase angles. Therefore, there should be a fourth filter at 6300 Å with a width of 800 Å. This filter would probably be most useful for very faint satellites since it is very wide.

Now consider the data taken in the red regime. Again, analyzing the 200 Å filter width difference of medians results first. In Figure 6, there is a feature around 7600 Å that is a result of an atmospheric water vapor absorption line. This line is extremely variable from observation to observation and therefore astronomers have left it out of the spectroscopic standard stars. So it remains in the all the red data. This feature needs to be ignored by the reader. The maximum at 6300 Å is real, however and shows that 6300 Å is an excellent filter position. This verifies the results in the blue. Since this is such a broad feature and there are no other features near it, the 800 Å width for the filter will not contribute to any loss of information from the spectrum. The 100 Å and 800 Å plots of the differences of the medians bear out the same results.

Now consider the data taken in the red regime. Again, analyzing the 200 Å filter width difference of medians results first. In Figure 6., there is a feature around 7600 Å that is a result of an atmospheric water vapor absorption line. This line is extremely variable from observation to observation and therefore astronomers have left it out of the spectroscopic standard stars. So it remains in the all the red data. This feature needs to be ignored by the reader. The maximum at 6300 Å is real, however and shows that 6300 Å is an excellent filter position. This verifies the results in the blue. Since this is such a broad feature and there are no other features near it, the 800 Å width for the filter will not contribute to any loss of information from the spectrum. The 100 Å and 800 Å plots of the differences of the medians bear out the same results.

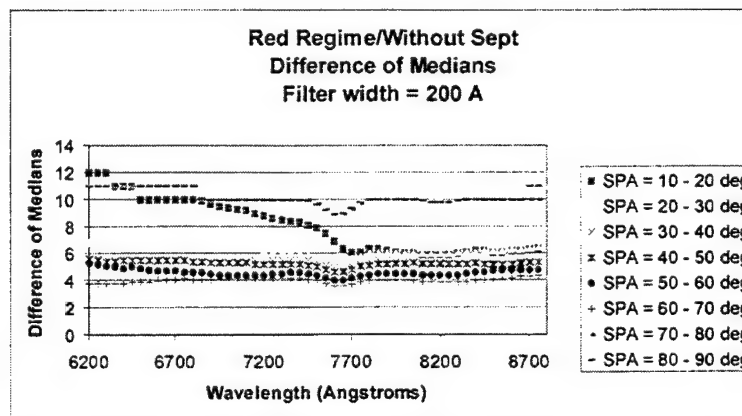


Figure 6. Difference of Medians for Red Regime Without September Data and Filter Width of 200 Å

In the cross-correlation plots, the red regime data also show that not only is a 6300 Å filter good but a 6300 Å – 8200 color is excellent and valid for all phase angles. The filter positions in the 800 Å filter width cross-correlation plots (from 6800 Å to 8400 Å) are influenced by the water vapor line. Therefore, these results were not used to determine filters. However, these plots show an increasing discrimination toward the longest wavelengths( past 8400 Å). This suggests a long pass filter with a short wavelength cutoff at 8500 Å. Finally, the 100 Å filter width cross-correlation plots yield consistent results with the 200 Å plots and no additional features. Thus the preliminary conclusions for the red regime are that an 800 Å wide filter at 6300 Å with a 200 Å wide filter at 8200 Å ought to be a very good color discriminator and a long pass filter with a short wavelength cutoff at 8500 Å should be a good filter.

The same analyses performed on the data including September (Equinox/Glint) data yield the same results. 4150 Å, 4750 Å, and 5900 Å still look like good filter locations for the 200 Å filter width. An 800 Å filter

at 6300 Å still yields maxima. High cross-correlations between a 200 Å filter at 8200 Å and the 6300 Å filter still occur. And a long pass at 8500 Å also appears to be a good discriminator.

In past years, 1000 Å wide Johnson filters were shown to be effective at SOI. The SILC initiative was to answer the question – can we find better filters? These analyses show that a combination of 4 narrow filters with one wide filter and one long pass filter should offer significantly increased SOI. To summarize the results of these analyses for determination of the SILC filters, the recommended filters are listed in Table 2.

Table 2. Recommended SILC Filters

Number	Central Wavelength (Å)	Full Width Half Max (Å)
1	4150	200
2	4750	200
3	5900	200
4	6300	800
5	8200	200
6	8500 (cutoff)	long pass

### Identification of Satellites Using SILC Filters

Using the SILC filters recommended in Table 2., integrated intensities were calculated for all the SILC observations for the ten satellites under consideration. These integrated intensities were not converted to magnitudes and so remain in a linear scale for simplicity and can be considered as simulated or mock photometric data. The data was analyzed as photometric data, in order to ascertain 1) how uniquely the SILC photometric data separates the individual satellites in feature space<sup>1</sup> over all phase angles and seasons; 2) how does SILC photometric data compare to standard broadband Johnson photometric data in identifying satellites, i.e. have better satellite filters indeed been identified; and 3) what combination of filters provides the most optimum results for SOI.

In order to address these issues, the results of the simulated SILC photometric data will be presented in a series of steps. First, examples of intensity – color plots of the data for different combinations of filters will be presented. Then a short description of the pattern recognition algorithms that were used to create a SOI software to identify the individual satellites or the bus type and produces a quantitative score on how well the satellite/bus type was identified will be presented. Third, the results from this SOI software for the SILC observations from May through July were analyzed. Finally, the same results for all the SILC observations (May through September) were analyzed. These analyses were performed on the blue regime data only. The result of this limitation is that the SOI scores for the percentage correctly identified might possibly be made higher if the red information were available to the software.

Figure 7. shows how the simulated SILC photometric data is distributed in a 2-dimensional cut through the feature space for the SILC solstice observations (May through July). The plots with the Equinox data included are consistent with Figure 7., but contain data much brighter and thus creates separate clusters for the same satellite. This plot shows that the satellites group into clusters, but some clusters are overlapping.

---

<sup>1</sup> In general feature space is a n-dimensional space that is defined by the properties that describe the population of interest. These features describe the data in terms that are of interest for a specific problem. In this case, magnitudes (integrated intensities), colors (ratios of integrated intensities), and solar phase angle create the feature space.

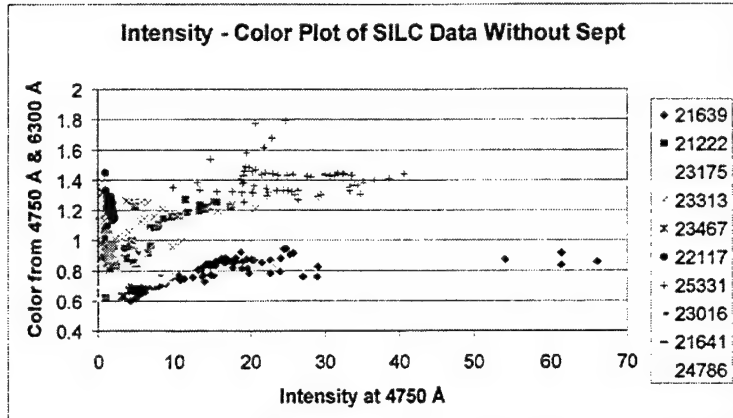


Figure 7. 4750 Å Intensity vs. 4750 Å/6300 Å Color For SILC Observations Without September.

It is worth examining the satellites that fall between intensities 0 and 10 to see if these satellite clusters actually overlap. Figure 8. enhances this region to examine more closely the satellites that lie therein. As can be seen at this larger scale, even these fainter satellites group into distinguishable clusters, although some overlap does exist. The existence of overlap indicates that the identification will probably be less than 100% correct.

At this stage, it is important to point out the clustering of the satellites that have the same bus type. Bus Type 1 contains satellites 23467, 23313 and 23175. It can be seen in Figure 7. that all these satellites fall in the same general area of both plots, but that other satellites with different bus types lie in between them: 21222 and 24786, for instance. For very faint observations, 21641 and even 22117 interfere (Figure 8.). This indicates that identifying by bus type may not be advantageous over identifying individual satellites.

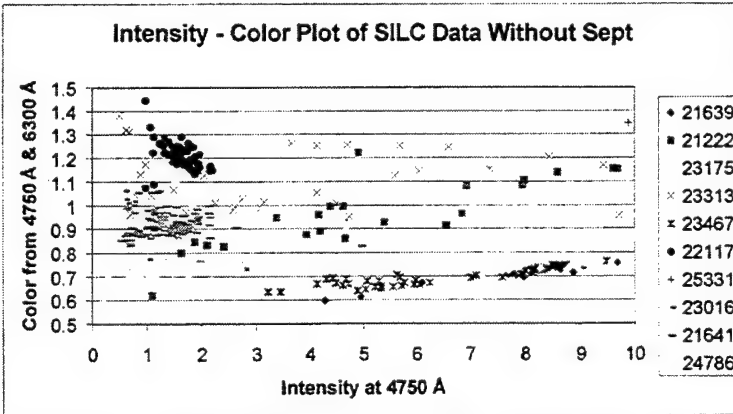


Figure 8. 4750 Å Intensity vs. 4750 Å/6300 Å Color For SILC Observations Without September On A Different Scale.

Now that an initial examination of the results show that the recommended SILC filters appear to be useful, a closer and more quantitative evaluation of these simulated SILC photometric data is appropriate. The analysis of these photometric data is in actuality, analysis of "known" data. These data are observations for which the satellite number or bus type are already known. To quantify how well or how poorly these data are clustered, the "leave-one-out" technique has been applied. The simulated SILC photometry data along with its satellite number, bus type number, and solar phase angle is input and the satellite or bus type clusters are determined. Then each single datum is removed from the clusters one at a time and tested independently with the remaining data without using the satellite identifier information (number and bus type). It is determined where each individual datum would lie with respect to all the other data clusters and identified using a Gaussian determinate of the unknown datum position in feature space and the locations of the cluster means and standard deviations in feature space. Then this result, the determination of the

satellite's number or bus type, is compared with the input identifier information. The percentage that were correctly identified is called the score and these will be presented in the following discussion. Specifically, the score is the number of observations in which the satellite was correctly identified divided by the total number of observations of that satellite. More information on the Gaussian classifier used has been presented in detail previously. (Ref. 3) Tests of the SOI software and preliminary SILC filters against truly unknown satellites were performed successfully in October 1999 during a demonstration for the Air Force Space Battlelab and U. S. Space Command.

Results for the blue regime SILC observations taken between May and July (Solstice) will be presented using the simulated photometry. First, it is instructive to examine how Johnson photometric data would appear using the identical observations. The Johnson filters B (4400 Å) and V (5500 Å) have been somewhat idealized because they were constructed with a Gaussian profile. The actual filters' profiles are very similar and the differences, for these purposes, should be negligible. Johnson B and V were the only filters constructed because of the wavelength locations of the blue cutoff on the spectra precluded Johnson U (3650 Å).

The scores for SOI using these Johnson B and V filters with solar phase angle are shown in Table 3. for individual satellite number. Refer to Table 1. for satellite and bus type information.

Table 3. SOI Score for Simulated Johnson BV Data Without September by Satellite With Solar Phase Angle.

Satellite	Score
21639	95.7
21222	97.0
23175	61.9
23313	35.7
22117	95.1
23467	97.9
25331	95.2
23016	88.8
21641	95.9
24786	90.2
Average	85.3

Now consider the results with the four SILC filters that are in the blue regime (4150 Å, 4750 Å, 5900 Å and 6300 Å) with the solar phase angle information for individual satellites (Table 4.). Comparing Table 3. and Table 4., the SILC filters increase the percentage of individual satellites identified correctly by 5%.

Now consider all the SILC data including the Equinox data from September. Overall the scores are lower. This is, in general, due to the fact that the algorithm creates one cluster per bus type or satellite number. When the September data, which is for the most part orders of magnitude brighter than the Solstice data, is introduced, the cluster region then necessarily has to expand or elongate to include these data. Future work should examine the possibility of creating multi-clusters or the addition of another feature that takes the difference in these data into account. One such possibility is to divide the solar phase angle into solar longitude and solar latitude. Then the seasonal Equinox data would be represented by the solar latitude feature. This additional feature might improve the scores. The simulated SILC filter scores with solar phase angle averaged 85.0% correctly identifying the individual satellite.

The conclusions that can be drawn from the analyses presented in this section are 1) the SILC filters provide more discriminating information on satellites than the Johnson filters; 2) the SILC filters will probably provide better SOI than is illustrated here with the inclusion of the red regime filters; 3) there is future work that needs to done on the behavior of the photometric data with solar phase angle, including study of other angles or more sophisticated clustering algorithms.

## Cross-Tagging in Clusters

The SILC initiative was to show that color photometry could help alleviate cross-tagging in clusters. Since the SILC data were not collected on cluster GEOs due to the possibility of cross-tagging, a cluster was simulated using the SILC data collected on individual satellites. A cluster was simulated by searching the blue regime data for observations that were taken within .5 degrees of the same solar phase angle. This search yielded a set of 8 observations on 6 different satellites. These included bus type 2: 22117 and 21222. Figure 9. shows the intensity-color plot using SILC filters 4750 Å and 6300 Å. It can be seen that 22117 and 21222 are very different. Also, all other satellites are distinguishable from one another. Thus, using SILC photometric data on a cluster could resolve cross-tagging. Further study needs to be done on actual clusters.

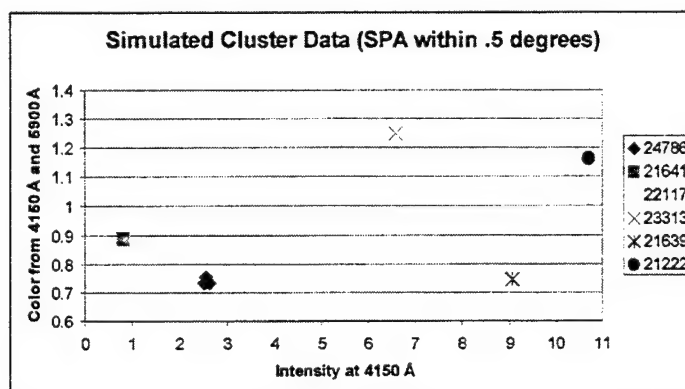


Figure 9. Intensity at 4750 Å vs. Color from 4750 Å and 6300 Å for Simulated Cluster Data.

## Conclusions

The SILC data were of high quality and enabled the selection of filters for SOI. A set of six filters are recommended. It was shown that these filters provide identification by satellite in and around the ninetieth percentile on average on the satellites observed. The results show that future work is necessary to fully develop and understand the photometric behavior of satellites in order to optimize an operational system.

A future study should be performed to explore the behavior of the photometric data with solar phase angle and the dependence of individual satellite's reflected brightness and color with solar phase angle. Future work should include further development of the pattern recognition algorithms. This should take the form of examining the possibility of creating multi-clusters or the addition of another feature that differentiates between solar latitude and solar longitude. These studies should include the study of other angles or more sophisticated clustering algorithms. A future study should be the collection of SILC photometric data. SILC filter data needs to be collected before a solid recommendation on operational shortcuts with regard to subsets (pairs and triplets) of the SILC filters can be made and an examination of blue regime and red regime data can occur. Finally, this study or another one should collect SILC filter data on GEOs in a cluster in order to provide direct evidence that this technique can help resolve cross-tagging.

## References

1. Beavers, W. I., et. al, "Cylindrical Satellite Specular Season Photometry", *Proceedings of the 1993 Space Surveillance Workshop*, Vol. II, MIT Lincoln Laboratory, 1993.
2. Bevington, P. R., *Data Reduction and Error Analysis for the Physical Sciences*, McGraw-Hill, New York, 1969.
3. Payne, T. E., et. al, "Color Photometry of GEO Satellites", *Proceedings of the 1999 Space Control Conference*, Vol. I., MIT Lincoln Laboratory, 1999.

## Space Object Identification (SOI) Using the Raven Telescopes

J.V. Lambert, P. Sydney, V. Soo Hoo, J. Africano (Boeing)  
P.W. Kervin (Air Force Research Laboratory)

### **ABSTRACT**

The Air Force Research Laboratory has been developing small-aperture telescope systems under its Raven Program for potential augmentation of the Space Surveillance Network. To date, the emphasis has been on autonomous measurement of high accuracy metric positions for deep space satellites. This capability has been successfully demonstrated both at the Air Force Maui Optical Station (AMOS) and in the Space Surveillance Network Optical Augmentation (SOA) and Small Aperture Telescope Augmentation (SATA) field tests at Edwards AFB, CA. High precession metric positions are obtained through astronomical stellar astrometry or "in-frame metrics" using background stars as the positional reference. Automated processing of the Raven images employing recent high-density, high-accuracy Naval Observatory catalogs is providing satellite positions accurate to a fraction of an arc-second. In addition to the metric positions, the automated processing also provides the brightnesses of the observed satellites. These brightnesses are referenced to the same background stars and are currently accurate to within a few tenths of a magnitude. The time average of these short observations can be compared to a spacecraft's expected brightness for the same viewing and illumination geometries determined from previous observations. Previous studies using observations from the MSSS, GEODSS, and other sources has shown that this technique could be used to supplement the current operational monitoring of spacecraft status based on the analysis of temporal variations in five to ten minute optical signatures. The accuracy and utility of the Raven brightness measurements can be further improved by restricting the background stars used in the reduction to solar-like spectral types and by using the uncertainty in the star brightness determination to weight the determined satellite brightness.

### **INTRODUCTION**

Satellite positional (metrics) and space object identification (SOI) measurements compete for the observing time available from the Air Force's Space Surveillance Network (SSN) optical sensors. The SOI data, used to monitor the operational status of spacecraft, currently consist of five to ten minute optical "signatures", temporal variations in the spacecraft's brightness, which can provide information on the object's stability. Collection of SOI data including photometric calibration is a time consuming process compared to metric data collections that require less than two minutes per target. As a result, SOI measurements are presently restricted to a small set of high interest spacecraft.

Under its Raven program, the Air Force Research Laboratory (AFRL) has been engaged in the development of small, highly automated telescopes based on commercial hardware and software as a potential supplement to the SSN Groundbased Electro-Optical Deep Space Surveillance (GEODSS) network. The Raven sensors have undergone extensive testing both in Hawaii at the Maui Space Surveillance System (MSSS) facilities and at the Optical Command, Control, and Communication Facility (OC3F) at Edwards AFB, CA, to characterize their operational performance. Rather than using the telescope mount encoders to measure the positions of tracked satellites, the Raven sensors image the satellites against the background star fields and determine the satellite positions relative to known star positions using astronomical astrometric techniques. Because the astrometric satellite positions are directly referenced to the background stars, the Raven sensors can potentially provide metric accuracies on the order of one arc-second, an order of magnitude better than the current SSN sensors.

As part of the astrometric processing of the metric data, the Raven sensors also determine the brightness of the observed satellite relative to the imaged background stars. These brightness measurements provide the average brightness of the satellite over the ten-second exposure time. By employing a "phase angle—magnitude" analysis technique, these brightness measurements can provide an alternative source of information on the operational status of spacecraft to augment and complement the current SOI measurements. Because the brightness measurements are

automatically obtained on every object observed for metric data, the Raven observations can extend SOI coverage to lower priority objects and obtain more frequent coverage of the high interest objects. The astrometric positional and photometric techniques can also be incorporated on the GEODSS sensors when the CCD upgrades are completed.

## BRIGHTNESS MEASUREMENTS

The Raven data processing for both metric positions and photometric brightness is based on standard astronomical algorithms. Data reduction routines incorporating these algorithms are available in the IRAF software developed and maintained by the National Science Foundation. The Raven data reduction programs work directly from the CCD images containing the target satellite and background stars (Fig. 1). Using the commanded telescope pointing angles as a starting point, the routines first identify the background stars by aligning the detected stars to those contained in the reference star catalog using pattern matching techniques. For the metric reduction, the offsets in the detected star positions as a function of position in the image are analyzed to obtain a "plate solution" which is then used to calculate the true position of the target satellite. For the photometric brightness determination, the cataloged visual V-band magnitudes are compared to the integrated CCD signal from the detected stars.

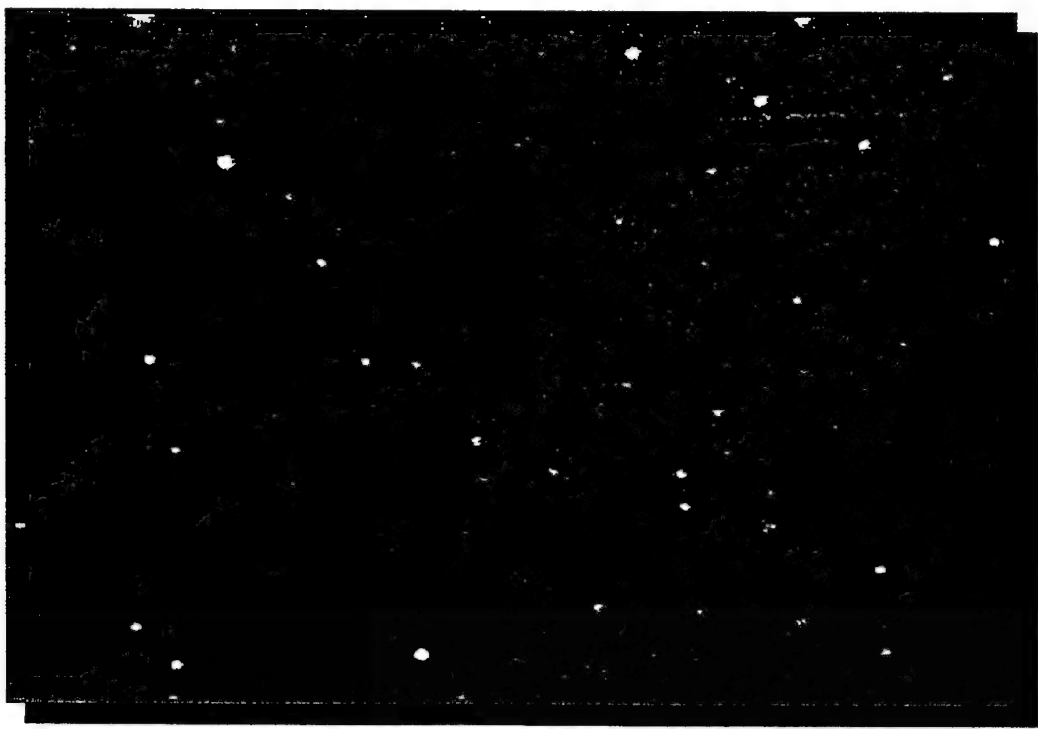


Fig. 1. Example of Raven Starfield Image with Satellite at Upper Right.

The standard equation used in astronomy for photometric reductions is:

$$V = m_o - k'M - k''CM + \epsilon C + \zeta$$

where  $V$  is the reduced exo-atmospheric target magnitude,  $m_o$  is the observed instrumental magnitude,  $M$  is the air mass through which the star is observed,  $C$  is the color (i.e., B-V) of the target star. The parameters  $k'$  (extinction),  $k''$  (color extinction),  $\epsilon$  (transformation coefficient) and  $\zeta$  (zero point) are constants determined through a least squares analysis of the reference stars. Astronomical photometric accuracies on the order of a few hundredths of a magnitude are typical using these procedures. Currently, the Raven measurements do not include observations in multiple passbands to determine target satellite color, so the color terms are dropped. Also, because the field-of-view of the Raven sensors are small (thirty arc-minutes), the atmospheric extinction is nearly uniform over the field and

the terms involving the air mass,  $M$ , can be neglected. The photometric reduction equation for Raven thus reduces to:

$$V = m_o + \zeta$$

i.e., a solution for a constant zero point off-set between the instrumental and catalog magnitudes. It must be noted that this Raven zero point is unique to each image as it contains the residual effects of extinction and reference star color variations. In a rigorous astronomical photometric measurement program, multi-passband measurements of the reference stars are made over a range of elevation angles to determine the color and extinction coefficients. The zero point resulting from these rigorous reductions is a constant of the sensor that changes slowly with sensor temperature and age.

In astronomical photometry, the instrumental spectral responses are matched as closely as possible to the standard responses for the photometric system employed. The transformation coefficient,  $\alpha$ , can then provide the correction from the instrumental system to the standard system based on the color of the target object. Because the primary objective of the Raven system is to provide metric positions, the CCD sensor is operated in a broadband mode without spectral filters to maximize the detection sensitivity, while the standard cataloged Johnson V or R band magnitude of the reference stars is used in the reduction. The relative spectral responses of the Johnson-system passbands (U, B, V, and R) are compared to a typical CCD spectral response in Fig. 2. The CCD passband is considerably wider than the standard system spectral bands and the measurements can be affected by features in the spectra of the reference stars that lie outside of the standard system responses upon which the reference star magnitudes were defined.

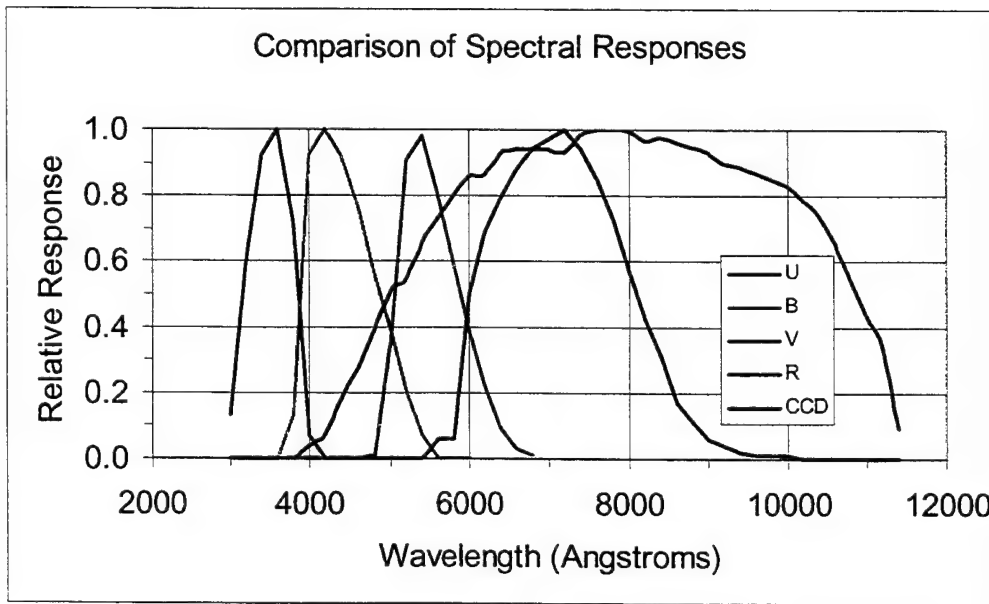


Fig. 2. Comparison of Standard Astronomical Filters and CCE Spectral Responses.

These differences between the Raven photometric reduction process and a more rigorous astronomical reduction do result in an increased uncertainty in the satellite brightnesses being obtained in the field demonstrations. The distribution of the standard deviations in the computed zero points for one night, shown in Fig. 3, can be used as an indication of the uncertainties in the spacecraft brightnesses. The median standard deviation is 0.35 magnitude and ninety percent of the standard deviations are less than half a magnitude. Approaches to improving the photometric accuracy of the Raven measurements will be discussed below. The Raven system has, however, demonstrated the capability to provide calibrated brightness data simultaneously with metric observations on many times the number of objects than can be observed for SOI with the current SSN operational sensors. During the recent eighteen week SATA demonstration at Edwards AFB, Raven obtained over one hundred and forty-six thousand brightness measurements on 1,350 objects. The system maintained an average of over one hundred and twenty brightness measurements per hour of operation, with a peak of 1,540 magnitudes for 485 unique objects on the best night. Overall, brightnesses were obtained for eighty percent of the objects attempted for metric observations.

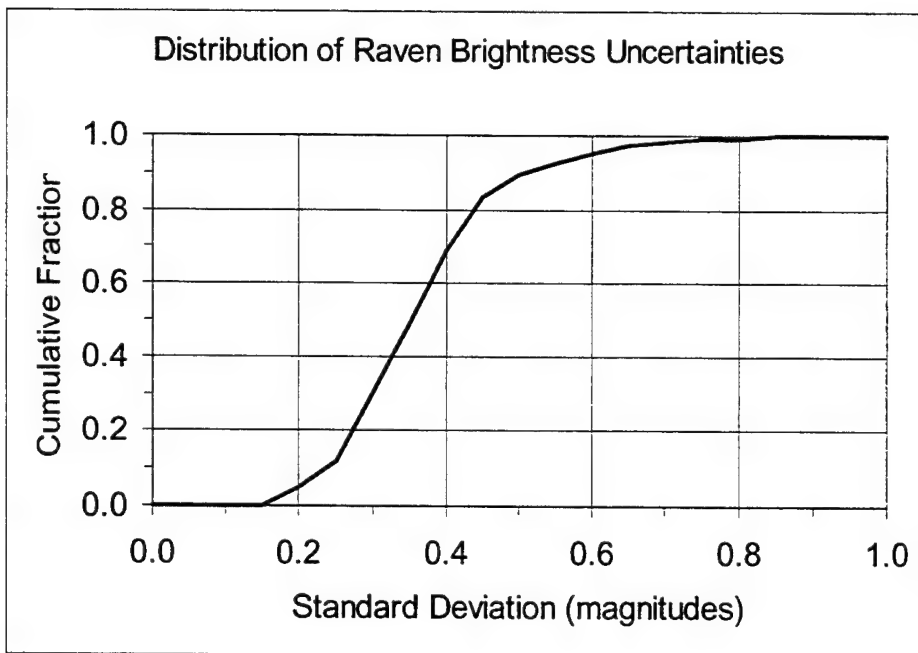


Fig. 3. Zero Point Standard Deviation Distribution, SATA Demonstration, 1 Nov 99.

#### PHASE ANGLE—MAGNITUDE ANALYSIS

To be operationally useful, a different SOI analysis approach is required for the Raven single point magnitudes. In 1989, Dr. Willet Beavers of MIT Lincoln Laboratory proposed using the phase angle versus brightness relationship as an alternative or supplemental photometric analysis technique. His theory was that under identical illumination and observing conditions an operational spacecraft will always have the same observed brightness. This condition would result because the spacecraft would be in the same orientation with solar panels, etc. in the same configuration and would be observed with the same aspect and illumination geometry. A non-operational satellite, on the other hand, should be at some non-standard orientation and/or have a different solar panel configuration (since the panels would not be tracking the Sun) resulting in a different observed brightness. Once an empirical (or modeled) brightness versus phase angle relationship is established for a class of satellites, any significant departures from the normal brightness can be interpreted as an indicator of abnormal behavior. Small brightness variations resulting from, for example, loose tolerances in spacecraft attitude control or solar panel tracking algorithms or measurement uncertainties should be expected. This approach would have the additional advantage that the total SOI observing time is reduced. The photometric measurement interval only has to be long enough to establish a mean brightness (one minute or less) rather than requiring collection of an extended signature to reveal periodic brightness variations (about ten minutes). The time required to acquire and boresight the satellite, however, remains the same.

In practice, however, the problem is more complicated. Spacecraft are generally complex three-dimensional objects. Even small variations in the illumination or viewing geometry can result in significant changes in the observed brightness. The phase angle only measures one component of this multi-dimensional geometry; other significant parameters are the solar declination and the observer's viewing aspect angles. As the solar declination changes during the year, for example, a satellite will cycle between being bottom-illuminated and top-illuminated. The observed brightness can, therefore, display systematic seasonal variations for the same phase angle. Similar variations in the illumination geometry can also result from a spacecraft's north-south motion due to its orbital inclination. The observed brightness can also be sensitive to the observer's viewing aspect. For example, viewing the right side of a spacecraft could result in a different observed brightness than viewing the left side or the bottom.

Different phase angle versus brightness relationships could thus be expected if a spacecraft is repositioned relative to the observing site or if two identical spacecraft at different geosynchronous locations are observed. One approach to overcoming these complications is to use the observational data to develop computer models of the spacecraft types of interest, then use these models as an interpolation tool to predict the observed brightnesses at viewing or illumination geometries not originally observed. As new observational data becomes available, the models can be refined to improve the brightness predictions.

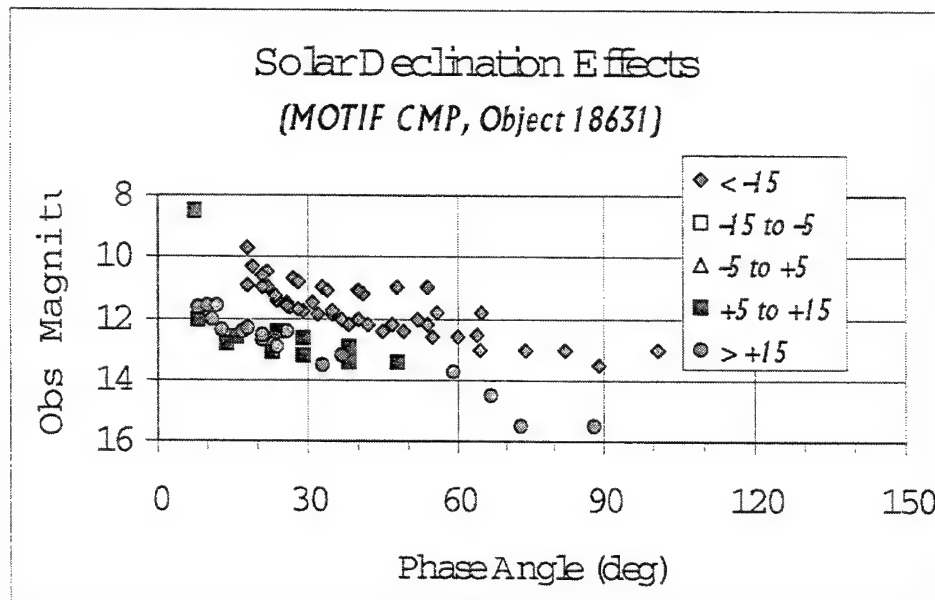


Fig. 4. Example of Observed Satellite Phase Function with Solar Declination Effects.

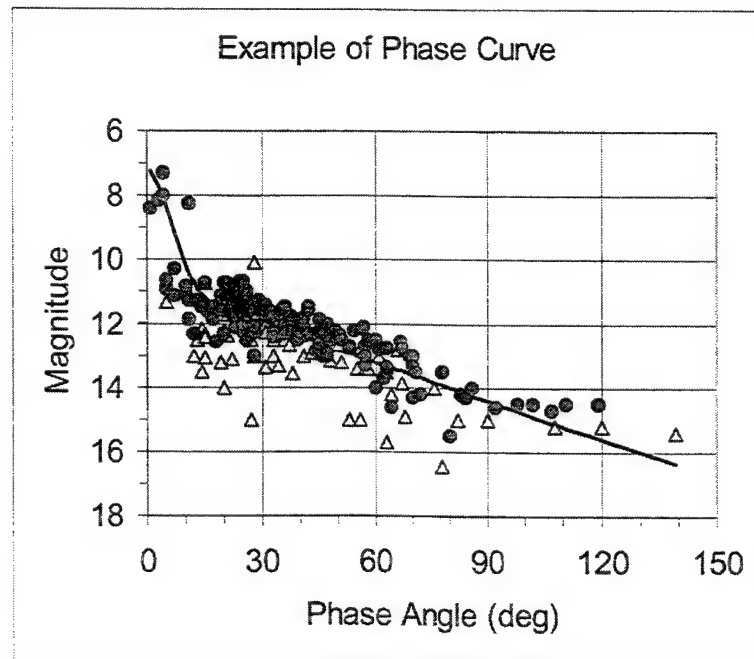


Fig. 5. Empirical Fit to Phase Functions for Two Similar Spacecraft.

Several special studies for Space Command (Refs. 1, 2, 3, and 4) have addressed the operational analysis of phase angle-magnitude relationships and have examined actual observational data for several classes of spacecraft in detail. Figs. 4 and 5 show the observed brightnesses from a single type of spacecraft. In Fig. 4, the observed brightness for an individual spacecraft are shown as a function of phase angle for various solar declinations (i.e., times of the year). The brightening at low phase angles results from specular glints off of the solar panels and Earth-pointing portions of the body. The systematic variations in the brightness with solar declination are apparent. In Fig. 5, the observed brightnesses for two of the same type of spacecraft at similar solar declinations are plotted; the solid line indicates an empirical fit to the observations.

A simple computer simulation has reproduced the major observed features of this phase angle-magnitude relation. The spacecraft was modeled using a nadir pointing diffuse cylinder with specular ends for the body with two specular flat plates for the solar panels. The solar panels rotate about an axis aligned with the Earth's axis once per day to track the Sun. A computed phase angle-brightness curve is shown in Fig. 6. One of the interesting features was the "hysteresis" effect in the curve showing that the modeled spacecraft brightness was not equal at the same phase angle before and after minimum phase. This effect was noticed in the observational data and initially attributed to scatter in the measurements. Additional modeling of the phase curves for the spacecraft of interest using more sophisticated and detailed models needs to be performed to access the relative contributions of components on the spacecraft and to identify those features and illumination geometries that can be used to distinguish satellite classes.

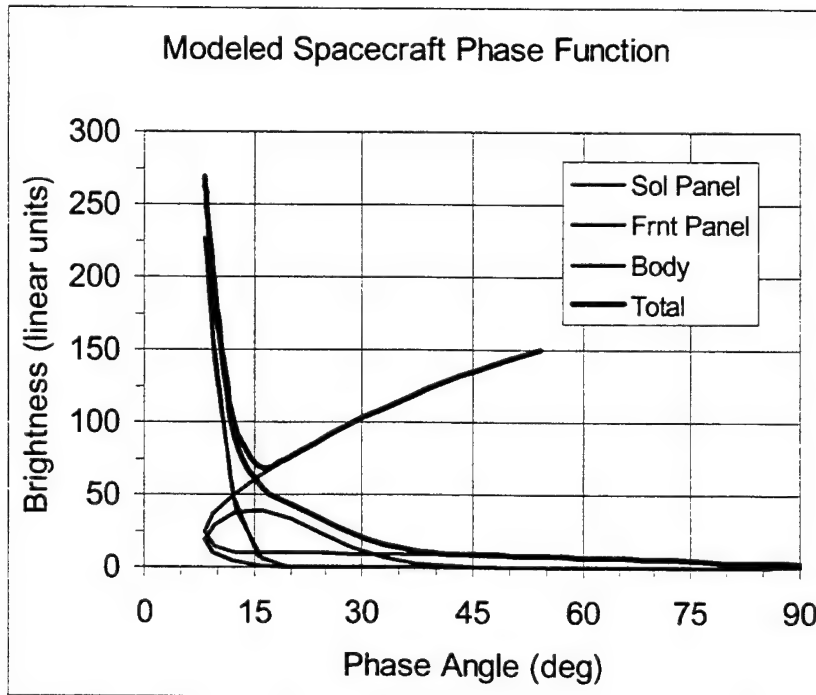


Fig. 6. Modeled Spacecraft Phase Function.

#### PHOTOMETRIC ACCURACY IMPROVEMENTS

Improvements in the photometric accuracy of the Raven single point brightness measurements can increase their operational utility by making the analyses more reliable and by permitting smaller changes to be detected. Three possible improvements are: 1) use of a better photometric star catalog, 2) application of basic CCD photometric calibrations, and 3) restriction of the reference star spectral types. The Raven data reduction software currently uses the Hubble Guide Star Catalog (GSC) as the source for both astrometric and photometric data on the background reference stars. The GSC, like most astrometric catalogs, was not intended as a photometric database. The photometric uncertainties in GSC 1.0 are typically on the order of 0.15 to 0.3 magnitudes (one sigma) with about ten percent of the errors being over half a magnitude. The magnitudes have generally been derived from two color (B

and V) photographic plates and tend to suffer from a number of limitations including image saturation for stars brighter than about twelfth magnitude. More recent star catalogs, such as the Naval Observatory A2.0 Catalog, are attempting to improve the accuracy of the assigned magnitudes by incorporating the results of new photometric surveys and more detailed calculations, but the errors continue to remain on the order of a few tenths of a magnitude. While catalogs with better magnitudes are in the works, Raven's best prospect for improving photometric accuracy in the near future is to use the best catalogs currently available and to possibly filter the stars used for the photometric reductions based on expected error sources.

The primary emphasis for the Raven telescopes to date has been for the collection of metric data and the collection of the brightness data has been a secondary consideration. In order to achieve the full photometric accuracy inherent in a CCD sensor, minor modifications to the observing procedures involving the collection of dark and flat-field image frames are required to calibrate the sensor. The dark and flat-field frames allow the pixel-by-pixel dark signal and gain variations over the CCD chip to be measured and corrected before performing the photometric reductions. These calibration frames can be collected just prior to the start of operations before opening the dome. The dark frame is collected with the camera shutter closed and the flat field can be obtained by imaging a uniformly illuminated area of the inside of the dome.

The colors or spectra of both the reference stars and the satellites also affect the photometric accuracy of the Raven brightness measurements. Fig. 7 compares the distribution of nearly two thousand measured colors for geosynchronous payloads (Ref. 5) to the Sun's color. Because the measurements are being made with the full spectral response of the CCD and compared to the narrower standard V and R band magnitudes, spectral features outside of the range of the standard bands, such as different spectral distributions and absorption lines, can significantly impact the observed intensities. For example, two stars, a very blue A0 spectral type and a very red M spectral type, could have the same apparent V-band magnitudes, but the total fluxes integrated over the CCD response would be dramatically different. While the Raven sensor could make multiple measurements of the target spacecraft using standard astronomical filter bands to determine its color and improve the photometric accuracy of the brightness determinations, there would be a significant impact on the system's operational performance by reducing the sensor sensitivity and the observing rate.

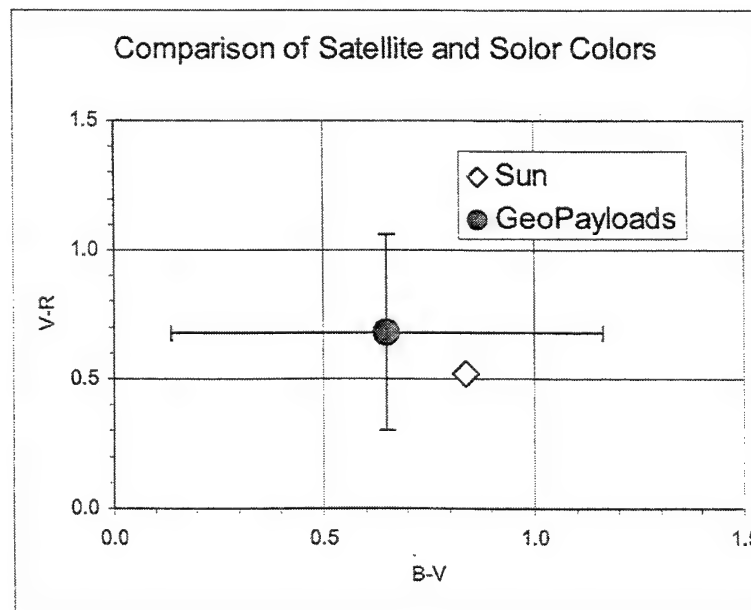


Fig. 7. Comparison of Geosynchronous Payload and Solar Colors.

An alternate approach to reducing the impact of the color effects on photometric accuracy is to restrict the spectral types of the reference stars used in the photometric reduction to near-solar types, i.e., spectral types F through K. This approach, which in essence assumes that satellites have solar color ( $B-V = +0.65$ ,  $V-R = +0.52$ ), would improve the consistency of the photometric calibrations by making the reduction less sensitive to the distribution of spectral types of the background stars in the individual frames. This approach would also better define the quantity being measured as spacecraft brightness as: "the integrated target flux relative to integrated flux of near-Solar type stars (approximating the illumination source) in the CCD spectral band". The exact range of spectral types to be employed in the reductions needs to be determined on the basis of the expected number of acceptable stars in a typical Raven frame as well as the expected improvement in accuracy. Fig. 8 shows the distribution of star colors and magnitudes in a two by two-degree equatorial field extracted from the USNO ACT catalog. In general, there should be a sufficient number of stars in most frames to support this approach. With the half-degree square field-of-view used in the SATA demonstration, the total number of reference stars available frequently exceeded one hundred and the fainter stars were ignored.

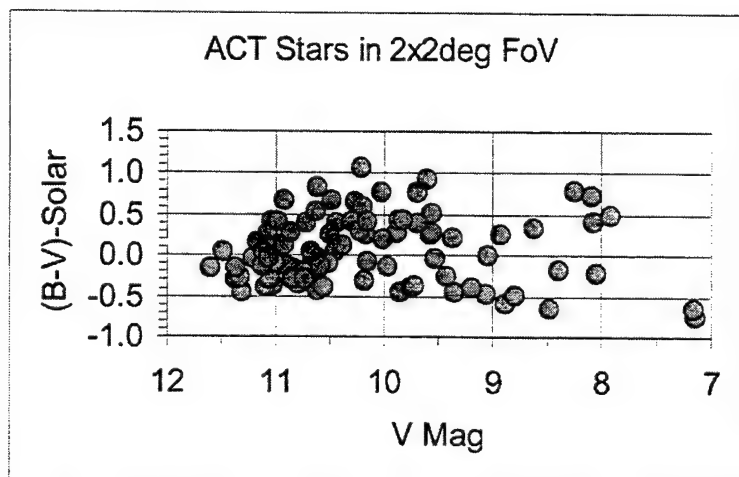


Fig. 8. Representative Distribution of Star Magnitude and Color.

Through these and other changes to the photometric techniques employed with Raven, it should be possible to achieve photometric accuracies in the range of one to two tenths of a magnitude, similar to what is currently being achieved with the existing operational SOI sensors. Near-Earth asteroid search systems such as LINEAR have similar problems in estimating the brightnesses of newly discovered asteroids and can typically achieve similar accuracies. Photometric accuracy improvements have been identified for investigation during the next phase of the Raven sensor development. A new Raven sensor is being installed on Mount Haleakala at the Maui Space Surveillance Complex for night-to-night operations. Selected areas containing well-calibrated stars will be imaged and reduced to determine the accuracy of the current processing and to evaluate new approaches.

## CONCLUSIONS

Operating autonomously, the small-aperture Raven telescopes have demonstrated their capability to provide calibrated brightness measurements simultaneously with tasked metric observations on hundreds of spacecraft each night. These brightnesses can be analyzed using SOI techniques such as "phase angle—magnitude" to provide operationally useful information on spacecraft status. The Raven observations can be used to supplement the current SSN photometric signature measurements by providing complementary information, providing more frequent observations of high interest objects, and extending SOI coverage to lower priority objects.

## REFERENCES

1. J.V. Lambert, J.L. Africano, R.K. Jessop, K.P. Moore, and W.A. Kraszewski. MOTIF Specialized Data Report: Object 18631. AFSPC Contract F05603-90-C-0010. Rockwell International Space Systems Division, Colorado Springs. 15 July 1993.

2. J.V. Lambert and W.A. Kraszewski. MOTIF Specialized Data Report: Phase Angle versus Magnitude Relationships for Two Classes of Geosynchronous Satellites. AFSPC Contract F05603-90-C-0010. Rockwell Space Operations Company, Colorado Springs. 14 April 1994.
3. J.V. Lambert. Specialized Data Report: MOTIF FY95-01, Interpretation of Geosynchronous Satellite Phase Angle versus Magnitude Relationships. AFSPC Contract F05603-90-C-0010. Rockwell Space Operations Company, Colorado Springs. 30 November 1994.
4. J.V. Lambert. Specialized Data Report: MOTIF FY95-02, Comparison of Visual Magnitude versus Phase Angle Data from Three Maui Sensors. AFSPC Contract F05603-90-C-0010. Rockwell Space Operations Company, Colorado Springs. 28 April 1995.
5. W.I. Beavers, J.Y. Cho, R.L. Irelan, P.J. Trujillo, and D.E. Olden. Project Report STK-229: Satellite Multicolor Photometry. MIT Lincoln Laboratory. Lexington. 1 December 1994.
6. Space Surveillance Network Optical Augmentation (SOA) Final Report. Air Force Research Laboratory, Maui, HI. In preparation.
7. Small Aperture Telescope Augmentation (SATA) Final Report. In preparation.

# High Precision Real Time Metric Processing for the MOSS and LINEAR Systems<sup>1</sup>

E.C. Pearce, F. Shelly, and J.A. Johnson, MIT Lincoln Laboratory

## ABSTRACT

A technique for the real time reduction of the astrometric position of a moving object detected against a background of reference stars has been developed for satellite and asteroid measurements. The technique has been implemented for the Lincoln Near Earth Asteroid Research (LINEAR) system and is currently being adapted for the space surveillance application and installed in the Moron Optical Space Surveillance (MOSS) System. The first iteration assumes a simple *a priori* focal plane model with a predetermined pixel scale with no focal plane rotation. A physical focal plane model is determined using multi-variable singular-value-decomposition (SVD) which includes linear offset, x and y scale, rotation, decentering, and a third order polynomial radial distortion characteristic of the GEODSS Main telescopes. Typically, a focal plane model can be determined with a residual error of approximately 0.5 arcsec root mean square (rms). 271648 astrometric observations reduced between June to December 1999 with the technique for the LINEAR program have produced mean systematic error of less than 0.052 arcsec and rms errors in each axis of 0.62 arcsec. Over 80% of all observations have errors of less than one arcsec. The technique is currently being adapted for use in the MOSS system, where it is expected to increase metric accuracy to near the arcsecond level and increase metric tracking throughput by eliminating the need for the system to observe a separate calibration star at the end of each track.

## 1. INTRODUCTION

The method for the precise reduction of the astrometric positions of stars and other astronomical objects on photographic plates dates back the early days of observational astronomy. In 1911, Schlesinger published a method of reduction for use with the photographic plates taken with the large 40" f/19 refractor at the University of Chicago Yerkes Observatory [1]. While Schlesinger's scientific interest was the measurement of annual parallax to derive the distances to nearby stars and predates the launch of the first artificial Earth satellite by over half a century, the fundamental techniques of astrometric reduction remain unchanged. However, numerical techniques have changed substantially over this period. While much effort went into reducing the labor required to calculate the plate constants during Schlesinger's day, today modern computers can fit complex multi-variable focal plane models using hundreds, or even thousands of reference stars per field of view.

Recently, these techniques have been adapted and refined for the demanding, real time requirements of asteroid search and space surveillance. In these applications a new challenges emerge. While

---

<sup>1</sup> The work was sponsored by the Department of the Air Force under Contract F19628-95-C-0002. Opinions, interpretations, conclusions, and recommendations are those of the author and are not necessarily endorsed by the United States Air Force.

modern astrometric reference catalogs allow the use of several hundred stars in the astrometric solution and can model complex distortions with high fidelity, these algorithms must be robust and highly automated. The algorithms must automatically recognize reference stars and reduce models reliably even with the very wide field of view telescopes in dense star fields where CCD sensors may detect tens of thousands of stars. Moreover, the algorithms must continue to perform reliably under non-ideal conditions where clouds may partially or complete obscure part of the field of view.

This report will detail the techniques developed by MIT Lincoln Laboratory for the real time reduction of astrometric measurements of satellites and asteroids. The technique has been implemented for the Lincoln Near Earth Asteroid Research (LINEAR) system and is currently being adapted for the space surveillance application and installed in the Moron Optical Space Surveillance (MOSS) System. First the different components required for high precision astrometric measurements will be introduced. Next the specific techniques of the astrometric reduction will be explored. Specific focal plane modeling results will be given for the Ground-Based Electro-Optical Space Surveillance (GEODSS) system 1.0 m f/2.15 main telescope. The effectiveness of this reduction will be demonstrated with observational results with the LINEAR asteroid search program. Finally, the modification required to adapt these techniques to the even greater real time demands of space surveillance for the MOSS system will be outlined.

## 2. COMPONENTS OF A HIGH PRECISION ASTROMETRIC SYSTEM

In order to reliable perform high precision astrometric reductions with a surveillance system, several system components must rigorously work in harmony. First, a foundation of accurate astrometric coordinate system reductions must be laid. These functions make the necessary transforms from cataloged coordinates to observed coordinate, correcting for such effects as precession, nutation, annual and diurnal aberration, proper motion, and atmospheric refraction. Next, accurate mount pointing must be insured by correcting for the physical imperfections of the telescope mount. Accurate mount pointing greatly enhances the robustness of the real time field recognition required for focal plane modeling and astrometric reduction. Finally, the astrometric reduction and creation of the focal plane model complete the triad. The focal plane model allows the precise transformation of an observed Cartesian location in the focal plane to an astrometric coordinate on the celestial sphere.

### 2.1 Astrometric Coordinate System Reductions

A special effort has been made to perform celestial coordinate reductions rigorously in both the LINEAR and MOSS systems. Rigorous treatment avoids eroding the error budget but does not add significant computational requirements. The coordinate reduction software consists of a portable family of functions written in the C programming language. It can accommodate, without modification, an order-of-magnitude increase in metric accuracy, allowing extensive software reusability. Additionally, the accuracy and speed of the coordinate reductions can be optimized easily for the particular application. Originally, these functions were developed using concepts introduced by P.T. Wallace as part of the software package for the Keck 10 m telescope and now distributed as the software library **SLALIB** [2, 3]. These functions correct for the effects of precession, nutation, annual and diurnal aberration, proper motion, and atmospheric refraction. The function library allows utilization of catalogs in either the FK4 or FK5 reference system and allow the preparation of data in either system at any specified epoch and equinox.

## **2.2 Mount Modeling**

Accurate mount pointing is required to make automated field recognition and focal plane reduction effective and robust in a real time environment. As the telescope mount blind pointing improves, the search space that must be examined to identify the stars in the field of view decreases rapidly. If the mean pointing error can be decreased to less than the mean separation of the detected stars, the field recognition becomes nearly trivial. Unfortunately, astronomical mounts are rarely perfect and must be corrected for a wide range of mechanical misalignments and flexures. Typically, these mechanical imperfections are corrected using a mathematical model of the telescope mount pointing. For both the GEODSS 1 m main telescope (LINEAR) and the 56 cm MOSS telescope, a physical mount model is derived from the observations of 50-60 reference stars covering the observable hemisphere. The mount model is reduced using very similar techniques and the same multi-variable least squares method used for the focal plane modeling. For the Contraves GEODSS mount, modeling allows blind pointing of the telescope to approximately 3.0 arcsec root mean square (rms). For the modified Nike-Ajax mount used with the MOSS System, blind pointing is typically 10-12 arcsec rms.

## **2.3 Focal Plane Modeling**

The final component of the triad is the focal plane model itself. This mathematical model allows the transformation of the measured Cartesian coordinates of targets on the focal plane to corresponding coordinates on the celestial sphere. The focal plane model is calculated by observing several hundred known reference stars in the field of view and constructing a transformation between the observed focal plane coordinates and the known coordinates of the same stars on the celestial sphere. The focal plane model corrects the focal plane coordinates of the stars for offset and scale in both axes, rotation, radial distortion, and a complex axial distortion caused by misaligned optical components (decentering). The determination of this focal plane model is the primary subject of this Report. Once the focal plane model is determined, coordinates of unknown targets (stars, asteroids, or satellites) can be quickly transformed to their counterparts on the celestial sphere.

## **2.4 Astrometric Reference Catalog**

Of course, neither the mount model nor the focal plane model could be produced without an accurate all sky astrometric reference catalog. The current astrometric reduction software used the U.S. Naval Observatory USNO-SA1.0 Catalog [4]. This astrometric reference catalog is selected from the much larger USNO-A1.0 catalog of 488,006,860 stars. The USNO-A1.0 catalog was reduced using the USNO Flagstaff Station Precision Measuring Machine (PMM). Several major photographic surveys, including the Palomar Observatory Sky Survey I (POSS-I) O and E plates, the UK Science Research Council SRC-J survey plates, and the European Southern Observatory ESO-R survey plates were used to produce the catalog. The USNO believes the typical astrometric error is about 0.25 arcsec.<sup>2</sup> The SA-1.0 catalog includes selected stars from the complete catalog with a near uniform density of approximately 1000 stars/deg<sup>2</sup> in the magnitude range 15-19 mv.

---

<sup>2</sup> MIT/LL intends to replace the USNO-SA1.0 with SA2.0 catalog. The SA2.0 is a re-reduction of the original plates using an improved reference system and algorithm.

One significant challenge for implementing real time astrometric reductions is quickly accessing the large star catalog database to retrieve the reference stars for a particular field of view. In order to minimize the time it takes to retrieve all of the cataloged reference stars in the field of view, the catalog is stored in a presorted and organized way. First, the stars are put into separate files where each file contains all of the stars for a  $1.25^\circ$  band of declination. Since the camera has a declination field of view of  $1.2^\circ$ , no more than two files are required for any one field. Next, all of the stars in a file are sorted by right ascension. A separate binary index file is maintained which gives an offset and count for each ten arc-minutes of right ascension. This allows the software to seek to and read the positions of all stars in the desired right ascension range with no more than four reads and four seeks. In general, less than one second is required to retrieve all of the catalog stars for a particular field. Once the stars have been read a final pass is made to eliminate any stars that are more than one tenth of a field of view from being visible in the image.

### 3. PHYSICAL FOCAL PLANE MODELING WITH SVD

#### 3.1 Approach

The MIT/LL control and image processing software that operates both the LINEAR and MOSS systems use the same consistent philosophy and methodology for mount calibration, photometric calibration, and focal plane modeling. Each of these tasks is treated as a model-fitting problem, with similar calibration data collection methodology and substantial software commonality. The approach can be outlined as follows. First, a linear model is defined for the system, physically describing the transformation from the measured datum to its ideal, real-world value. Second, calibration data is collected spanning the entire multi-dimension space of the independent variables evolved in the specific problem. Third, the free parameters of the model are fit using a robust linear least squares method.

For the specific case of focal plane modeling, the linear model describes the scale, rotation, and optical distortions found in the optical system of the telescope being modeled. The calibration data consists of the observed location several hundred background astrometric reference stars from an all sky catalog. Finally, the free parameters of the model, the model coefficients<sup>3</sup>, are determined by a least-squares minimization method using singular value decomposition (SVD).

#### 3.2 Formal Model Specification and Model Functions

Formally, the focal plane model can be specified using the two equations

$$\xi = \left( \sum_{j=1}^m a_j f_j(x, y) \right) + e_\xi, \quad (1)$$

$$\eta = \left( \sum_{j=1}^n b_j g_j(x, y) \right) + e_\eta. \quad (2)$$

---

<sup>3</sup> Traditionally, the model coefficients are called “plate constants”, referring to the application of the technique on photographic plates. Often, the term is retained even in when the technique is used with electro-optical sensors.

The model transforms the focal plane coordinates of an arbitrary point,  $(x, y)$ , in pixel units to the ideal standard coordinates in the sky plane,  $(\xi, \eta)$  in angular units. The functions  $f_j(x, y)$  and  $g_j(x, y)$  are the model functions used and the constants  $a_i$  and  $b_i$  are the model coefficients. The small quantities  $e_\xi$  and  $e_\eta$  represent the residual not corrected for by the model and is minimized during the model fitting process.

The model functions can be physical (representative of actual physical effects), empirical, or a combination of both. For the LINEAR and MOSS systems, only physical model functions are used. Generally, physical model functions allow a complete model to be fit using fewer functions than would be required with a suite of empirical functions. Moreover, the model coefficients correspond to actual physical attributes of the system, such as camera rotation, that can be monitored. Table 1 shows the model functions used for both the LINEAR and MOSS focal plane reductions<sup>4</sup>. The functions are expressed and fit in the Cartesian coordinate system.

**Table 1. LINEAR/MOSS Focal Plane Model Functions.**

	Function $f_0$	Function $g_0$
<b>Scale</b>	$x$	$y$
<b>Rotation</b>	$y$	$x$
<b>Offset</b>	1	1
<b>Radial Distortion (<math>r^2</math>)</b>	$x\sqrt{x^2 + y^2}$	$y\sqrt{x^2 + y^2}$
<b>Radial Distortion (<math>r^3</math>)</b>	$x^3 + xy^2$	$x^2y + y^3$
<b>Decentering (1)</b>	$3x^2 + y^2$	$2xy$
<b>Decentering (2)</b>	$2xy$	$x^2 + 3y^2$

Some notes on the specific functions are appropriate here:

- To first order, the simple linear functions for scale determine the angular pixel size of the camera. However, the numerical value is only valid at the field center. At other points in the focal plane, radial distortion will alter the pixel angular size.
- Rotation is modeled with a first order approximation. Note that in the Cartesian representation, a second, artificial degree of freedom is added as two coefficients represent this single rotation angle.
- The unity model functions fit an offset of the focal plane and are used in specific focal plane model solutions to correct simple translational error. In models that are retained for

---

<sup>4</sup> Note that MOSS does not require the decentering terms nor a complex radial distortion model due to its small field of view compared to the GEODSS main telescope. Currently, MOSS is using only four of the model functions above operationally.

use on other fields, these terms are zeroed and a new offset is determined that is appropriate for that field of view.

- The radial distortion is modeled using a third-order polynomial. Typically, wide field of view telescopes show an  $r^3$  distortion. The GEODSS 1 m f/2.15 telescope requires the additional  $r^2$  term to accurately model the distortion near the edge of the field.
- Decentering is a complex axial distortion that occurs when the optical components of the system are not precisely aligned. The distortion is second order and requires two coefficients to describe.

### 3.3 Multivariable Fitting with SVD

Model fitting consists of determining some optimal set of coefficients  $\{a_i, b_j\}$  that best satisfies Equations (1) and (2) above. The basic approach is to define a merit function that quantifies the agreement between the modeled and the collected data. The coefficients of the model are then adjusted to minimize the merit function.

The MIT/LL software determines the best-fit coefficients by a least-squares minimization method using singular value decomposition (SVD). The algorithm is described in detail by Press and is based on a routine by Forsythe *et. al.*, which itself is based on the original work of Golub and Reinsch [5, 6, 7]. The SVD method is particularly suited for model fitting applications where the data does not clearly distinguish between two or more of the basis functions being modeled. This occurs in physical focal plane model fitting because the model functions do not necessarily form a complete orthonormal set of functions. When models are fit with other least-squares methods, such as the method of normal equations, these coefficients tend to be fit as large, delicately and unstably balanced values. When the same functions are fit with SVD, these coefficients tend to approach zero. This feature is particularly well suited for applications where the same software is used with multiple systems, some of which may not require certain model functions in the final solution. Additionally, the algorithm is robust and nearly always properly converges, making it suitable for automated processing.

The mathematical details of SVD are beyond the scope of this Report. However, the method will be introduced. The SVD method first defines a design matrix,  $\mathbf{A}$ , which contains a row for each observation and a column for each model function. In this particular application, the design matrix is given by

$$\begin{aligned}\mathbf{A}_{i,j} &= f_j(x_i, y_i) \\ \mathbf{A}_{i+n,j} &= g_j(x_i, y_i)\end{aligned}\tag{3}$$

where  $x_i$  and  $y_i$  are the  $n$  unmodeled positions of the reference stars in focal plane coordinates (pixels). Each reference star supplies two data points for the coefficient fit.<sup>5</sup>

Next, a target vector  $\mathbf{T}$  is defined. The target vector contains the data we intend to model. In this case it is simply the standard coordinates of the reference stars in the field of view. Thus,

---

<sup>5</sup> In all equations, the variable  $i$  is used to iterate over the  $n$  observations and  $j$  is used to iterate over the  $m$  model functions.

$$\begin{aligned}\mathbf{T}_i &= \xi_i \\ \mathbf{T}_{i+n} &= \eta_i\end{aligned}\tag{4}$$

where  $(\xi_i, \eta_i)$  are the standard coordinates of the  $i^{\text{th}}$  reference star in the sky plane. The standard coordinates for each reference star are given by

$$\xi_i = \frac{\cos \delta_i \sin(\alpha_i - \alpha_0)}{\sin \delta_i \sin \delta_0 + \cos \delta_i \cos \delta_0 \sin(\alpha_i - \alpha_0)}, \tag{5}$$

$$\eta_i = \frac{\sin \delta_i \cos \delta_0 - \cos \delta_i \sin \delta_0 \cos(\alpha_i - \alpha_0)}{\sin \delta_i \sin \delta_0 + \cos \delta_i \cos \delta_0 \cos(\alpha_i - \alpha_0)}. \tag{6}$$

In these equations,  $\alpha_i$  and  $\delta_i$  are the observed right ascension and declination of the  $i^{\text{th}}$  reference star and  $\alpha_0$  and  $\delta_0$  are the observed right ascension and declination of the tangent point.<sup>6</sup> Now, finding the best-fit model is equivalent to finding the vector  $\mathbf{a}$  that minimizes the least-squares merit function

$$\chi^2 = |\mathbf{A} \bullet \mathbf{a} - \mathbf{T}|^2. \tag{7}$$

Because of the composition of the design matrix and target vector, and the choice of the least-squares metric, singular value decomposition may be used to find the vector of best-fit coefficients,  $\mathbf{a}$ . To perform the minimization, the SVD method decomposes the design matrix into product of three matrices,  $\mathbf{U}$ ,  $\mathbf{W}$ , and  $\mathbf{V}$ ,

$$\mathbf{A} = \mathbf{U} \bullet \mathbf{W} \bullet \mathbf{V}. \tag{8}$$

The matrices  $\mathbf{U}$ ,  $\mathbf{W}$ , and  $\mathbf{V}$  each have special properties, which characterize singular value decomposition.  $\mathbf{U}$  and  $\mathbf{V}$  are each orthogonal while  $\mathbf{W}$  is diagonal with only non-negative elements. When the design matrix is decomposed in this way, the coefficient vector may be solved easily as

$$\mathbf{a} = \sum_{i=1}^m \left( \frac{\mathbf{U}_{(i)} \bullet \mathbf{T}}{\mathbf{w}_i} \right) \mathbf{V}_{(i)}, \tag{9}$$

where  $\mathbf{U}_{(i)}$  denotes the  $i^{\text{th}}$  column of  $\mathbf{U}$ ,  $\mathbf{V}_{(i)}$  denotes the  $i^{\text{th}}$  column of  $\mathbf{V}$ , and  $m$  is the total number of model functions. The vector  $\mathbf{w}$  contains the non-negative diagonal elements of the matrix  $\mathbf{W}$  from decomposition specified in equation (8). The vector  $\mathbf{a}$  represents the model and contains the coefficients originally given in equations (1) and (2) ( $a_i = \mathbf{a}_i$  and  $b_i = \mathbf{a}_{i+n}$ ).

The standard coordinates of an unknown target are determined by applying the model given in equation (1) and (2) with the coefficients determined in equation (9). Then, the standard coordinates can be converted back into observed coordinates  $(\alpha, \delta)$  of the object using

<sup>6</sup> The sky plane is the imaginary plane tangent to the celestial sphere with the point of tangency with the sphere at the boresight of the telescope. Hence, this point is called the tangent point.

$$\alpha = \alpha_0 \tan^{-1} \left( \frac{\xi}{\cos \delta_0 - \eta \sin \delta_0} \right), \quad (10)$$

$$\delta = \tan^{-1} \left( \frac{\sin \delta_0 + \eta \cos \delta_0}{\sqrt{\xi^2 + (\cos \delta_0 - \eta \sin \delta_0)^2}} \right). \quad (11)$$

### 3.4 Field Recognition and Iterative Reduction

Once the image processor has detected and returned the centroid of all detected stars in the focal plane and the catalogued star positions have been retrieved from the database and converted appropriately to observed then standard coordinates, the actual focal plane reduction can begin. Initially, the correspondence between the detected targets in the focal plane and the reference stars must be determined. This is done with an iterative algorithm that refines the matching solution by eliminating obvious outliers until the solution converges within the expected tolerances. The outlier elimination removes bright stars that bloom on the CCD focal plane or are incorrectly matched to the corresponding catalogued object.

For the first iteration, a simple focal plane model is assumed that includes only a predetermined pixel angular size. The focal plane coordinates of the detected stars are converted to standard coordinates using the predetermined pixel scale and telescope boresight position as reported from the mount model. Each catalog star is then matched to its closest image star within a maximum offset of 60 arcsec. Once these matches are made, a initial focal plane model solution is generated giving an initial estimate of camera rotation, offsets, and radial distortion as well as a refined pixel scale. The rms error,  $\rho$ , is then calculated and the 60 arcsec maximum fit error is replaced with  $2\rho$ . The entire process is then repeated using the refined, higher fidelity focal plane model and new limits. The process then iterates until the resulting rms error is less than one half the pixel angular size (approximately 1.13 arcsec). Typically, 70% of the catalog stars are matched on the first iteration and that number is reduced to approximately 65% percent after the final iteration.<sup>7</sup>

## 4. APPLICATION

The application and observational results of these techniques will now be described in detail. First, the development of a high fidelity focal plane for the GEODSS 1 m f/2.15 telescope will be discussed. Next, the results using this focal plane model and other astrometric techniques to asteroid measurements with the LINEAR system will be summarized. Finally, plans for the adaptation of the techniques to the more demanding real time requirements of space surveillance will be discussed.

---

<sup>7</sup> One of the dangers of this process is that the outlier removal will “cut loose” the stars near the edge of the field of view, resulting in a poor coverage of the edge of the field of view and a low quality model. Examination of the post-fit residuals consistently shows uniform coverage of the entire focal plane even with the outlier removal process.

#### 4.1 Focal Plane Model for the GEODSS 1 m f/2.15 Telescope

The GEODSS 1 m f/2.15 telescope is used primary by AFSPC operationally for satellite tracking from three sites distributed around the world. The large aperture and wide field of view is ideal for space surveillance applications. The GEODSS main telescope has a clear aperture of 101.6 cm and a focal length of 218.4 cm (f/2.15). The system provides a usable focal plane of 80 mm. While both the image quality (80% illumination over a 2 arcsec circle) and illumination (10% uniformity over 80 mm) are excellent, significant geometrical distortions exist in the focal plane that must be modeled. In particular, the optical system has a strong radial distortion. At a radius of 20 mm from the focal plane center (approximately 0.52°), the distortion is approximately 4.5 arcsec. However, the distortion increases rapidly and at the field edge (40 mm radius, 1.05°) the distortion exceeds 35 arcsec. The distortion is approximately cubic in nature and if unmodeled, would impact asteroid measurement requires at a radius of only 1000 arcsec, leaving only the inner 12% of the focal plane covered the MIT/LL CCID-16 camera useful for astrometric observations. Figure 1 shows graphically the unmodeled radial distortion of the focal plane.

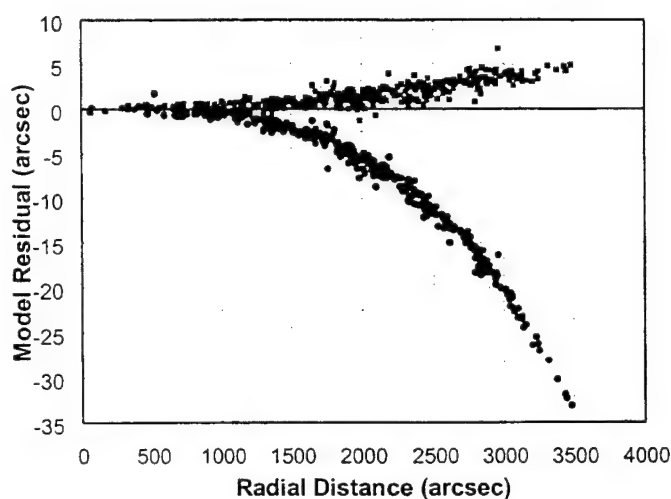


**Figure 1. Radial Distortion of the GEODSS Focal Plane.**

At a radius of 20 mm from the focal plane center (approximately 0.52°), the distortion is approximately 4.5 arcsec. However, the distortion increases rapidly and at the field edge (40 mm radius, 1.05°) the distortion exceeds 35 arcsec. The distortion is approximately cubic in nature and if unmodeled, would impact asteroid measurement requires at a radius of only 1000 arcsec, leaving only the inner 12% of the focal plane covered the MIT/LL CCID-16 camera useful for astrometric observations. Figure 1 shows graphically the unmodeled radial distortion of the focal plane. The y-axis shows the angular residual for each star while the x-axes shows the angular distance from the center of the field of view. The lower curve shows the residuals with no radial distortion modeled and reveals the approximately cubic distortion out to the field edge (3500 arcsec radius). The upper curve shows this distortion partially modeled with a pure third order polynomial. This residual distortion can be adequately modeled to sub-arcsec accuracy with the addition of a second order term.

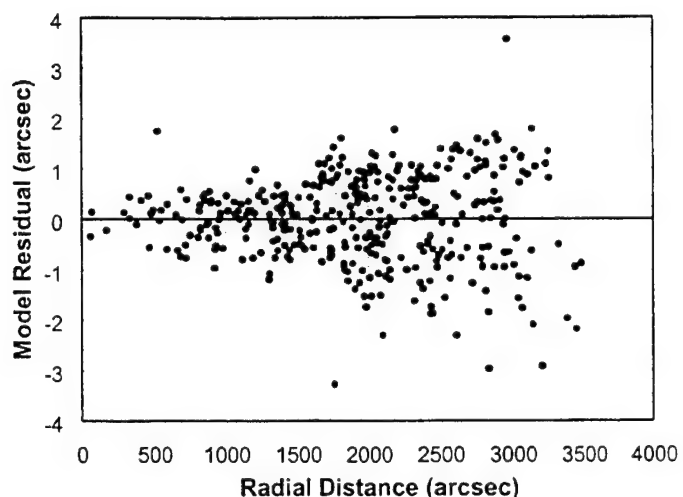
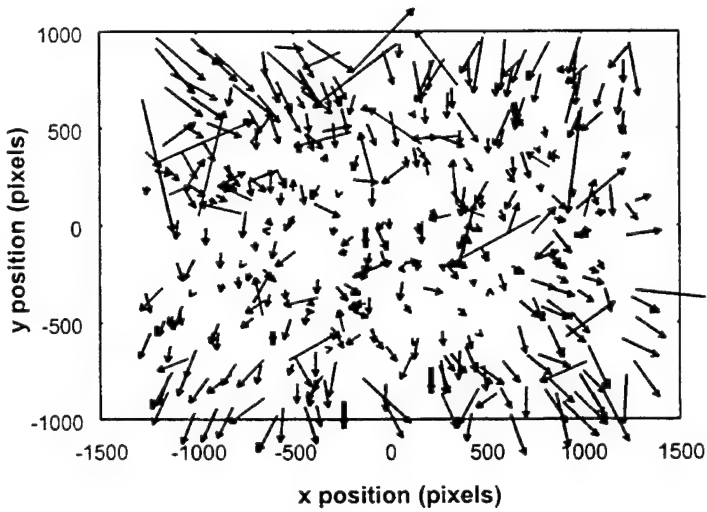


**Figure 2. Radial Distortion Modeled with Second Order Polynomial.**

particular star.

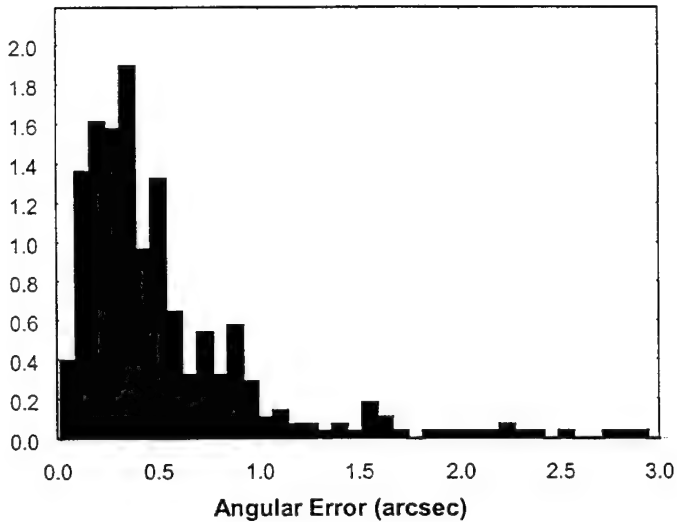
Figure 3 shows the error vector plot of this GEODSS focal plane after scale, rotation, and the third order polynomial radial distortion has been modeled. The character of the remaining unmodeled distortion is now visually obvious. Although the errors increase dramatically with radius, there is also a strong angular dependence. This distortion is called decentering and is caused by misalignment of the optical components in the telescope. With this particular GEODSS Main telescope, the distortion amounts to approximately 4 arcsec. Fortunately, the error is easily corrected with the second-order model functions given in Table 1.

Figure 2 shows the residuals once the radial distortion is completely modeled with a third order polynomial. The systematic errors in  $r$  are removed, however, the magnitude of the error clearly increases with increasing distance from the field of view center. This demonstrates the limitations of this type of two-axis presentation and analysis. A more advanced form of graphical analysis, the error-vector plot, proves helpful here. The error-vector plot shows a vector for each reference star used in the model fit. The position of each vector represents its position in the focal plane while the magnitude and direction of the vector represents the residual modeling error in the



**Figure 3. Vector Error Plot of GEODSS Decentering Error.**

After the decentering error has been removed, the focal plane model is able to reduce the error over the entire GEODSS field of view to near 0.5 arcsec rms. The histogram of the resulting residual distribution is shown in Figure 4.



**Figure 4. Error Histogram of Complete GEODSS Main Focal Plane Model.**

#### 4.2 Lincoln Near Earth Asteroid Research (LINEAR)

The techniques described in this Report have been used extensively to reduce the astrometric observations taken by the LINEAR system. Table 2 summarizes the results as computed by the Minor Planet Center [8]. The table shows the total number of observations and the mean and standard deviation angular residuals of the observations against the known asteroid orbits. Observations are broken down by month since June 1999. The columns “<x>” show the total number of observations within an x-arcsec error circle. Summary rows show the incremental and cumulative totals in each of these error circle bins.

**Table 2. Astrometric Residuals of LINEAR Observations.**

Month	Total	<1	<2	<3	<4	=4	mean RA	SD RA	mean Dec	SD Dec	mean Total	SD Total
Dec 99	32158	24891	6239	811	157	60	0.04	0.63	-0.04	0.67	0.06	0.92
Nov 99	52565	42462	8972	935	161	35	0.04	0.56	-0.02	0.58	0.04	0.81
Oct 99	81571	66211	13749	1361	180	70	0.04	0.72	-0.04	0.59	0.06	0.93
Sep 99	60810	50134	9816	741	104	15	0.04	0.54	-0.06	0.58	0.07	0.79
Aug 99	558	450	97	11	0	0	-0.04	0.57	-0.06	0.54	0.07	0.79
Jul 99	17860	14934	2685	194	38	9	0.03	0.53	-0.02	0.54	0.04	0.76
Jun 99	26126	19597	5778	646	92	13	0	0.63	-0.03	0.67	0.03	0.92
Total	271648	218679	47336	4699	732	202	0.04	0.62	-0.04	0.60	0.05	0.84
%		80.50	17.43	1.73	0.27	0.07						
Cum %		80.50	97.93	99.66	99.93	100.00						

Table 2 shows the quality of the LINEAR astrometric observations are impressive and competitive with any of the major asteroid search programs. Systematic errors are less than 0.052 arcsec and over

80% of all observations are within the 1-arcsec error circle. The standard deviation of the observations is approximately 0.84 arcsec, which is comparable to the typical residuals of the reference stars used in the focal plane model reduction. Note that the angular pixel size of the LINEAR system with the MIT/LL CCID-16 camera is 2.26 arcsec. Thus, the astrometric reduction is able to achieve sub-pixel accuracy.

#### 4.3 Space Surveillance Applications (MOSS)

In Summer 2000, the Moron Optical Space Surveillance (MOSS) System will be modified to use many of the same techniques described above for the LINEAR program. Currently, the MOSS system generates a high fidelity focal plane model as part of its calibration process. The focal plane model is generated monthly and rms error over the entire field of view is typically between 1 and 2 arcsec.<sup>8</sup> The focal plane model is used to reduce the observed satellite position, but the tangent point of the field of view is taken directly from the modeled telescope pointing, which is corrected to first order using a local, but off-focal plane, calibration star.

Due to the large processing requirements to reduce a separate focal plane model for each observation or track, the MOSS system will continue to use a pre-determined high fidelity focal plane model. However, the mount offset for each observation will be obtained by fitting a simple second-order model over the inner fraction of the focal plane. The second-order model will include only offset and rotation, and include only a small fraction of the stars near the center of the field of view. Hence, an extremely accurate pointing error can be derived with a limited investment in database and numerical processing. Additionally, metric throughput is enhanced since the observation of the off-focal plane calibration star is no longer required. Using these techniques, MIT/LL expects to more than double the metric capacity of the system while simultaneously improving data accuracy to near the 1.5 arcsec rms level.

### 5. CONCLUSION

In this Report, the techniques for high precision focal plane modeling and real time astrometric reduction for both the LINEAR and MOSS systems have been described. The techniques represent a unique blend of traditional astrometric techniques and rigor with the demanding real time requirements of space surveillance and high volume searching. The algorithms and techniques reliably produce observations of sub-pixel accuracy. Future significant improvements in astrometric accuracy with these systems are unlikely to be found without customizing the design of the optical system and focal plane sensor specifically for higher astrometric accuracy and compromising the search performance or dramatically increasing the processing requirements of the systems.

### 6. REFERENCES

1. F. Schlesinger, "Photographic Determination of Stellar Parallax Made with the Yerkes Refractor, III," *Astrophysical Journal* 33, 161 (1911).
2. P.T. Wallace, "Pointing and Tracking Algorithms for the Keck 10-Meter Telescope," in *Instrumentation for Ground Based Optical Astronomy: Present and Future*, ed. L.B. Robinson, Springer-Verlag, New York (1987).

---

<sup>8</sup> MOSS, with the MIT/LL CCID-10, camera has a angular pixel size of approximately 3.84 arcsec/pixel.

3. P.T. Wallace, "SLALIB -- Positional Astronomy Library 2.4-0 Programmer's Manual," Starlink User Note 67.45, ([http://star-www.rl.ac.uk/star/docs/sun67.htm/sun67.html#xref\\_](http://star-www.rl.ac.uk/star/docs/sun67.htm/sun67.html#xref_)), 12 October 1999.
4. D. Monet *et. al.* "USNO-A V1.0: A Catalog of Astrometric Standards," U.S. Naval Observatory Flagstaff Station.
5. W.H. Press et. al., Numerical Recipes in C, New York: Cambridge University Press (1989).
6. G.E. Forsythe, M.A. Malcolm, and C.B. Moler, Computer Methods for Mathematical Computations, Englewood Cliffs, N.J.: Prentice-Hall (1977).
7. G.H. Golub and C.F. Van Loan, Matrix Computations, Baltimore: John Hopkins University Press (1983).
8. "Residual Statistics for Observatory Codes", Minor Planet Center, World Wide Web <http://cfa-www.harvard.edu/iau/special/residuals.txt> (December 1999).

## **COBRA DANE Space Surveillance Capabilities**

P. Chorman, Riverside Research Institute

### **Executive Summary**

With construction of the International Space Station underway, increased importance is placed on systems which can track potentially hazardous space debris. The COBRA DANE phased array system in Shemya, AK offers advantages over most Space Surveillance radars for maintaining the satellite catalog (SATCAT), providing early coverage of New Foreign Launches (NFLs) and, in particular, tracking the large and increasing population of orbital debris for collision avoidance with spacecraft. Due primarily to its L-band operating frequency, COBRA DANE can acquire objects which are too small to be detected by dedicated and collateral UHF Space Surveillance sensors (between 4 - 10 cm), but are large enough to destroy the Space Station, Shuttle Orbiter, or other high-value satellites. The system is available for near continuous support of routine tasks, debris measurements and high-priority events including de-orbits, breakups and maneuvers.

Following the COBRA DANE System Modernization (1990-1993), funding shortfalls led to deactivation of its Early Warning and Space Surveillance missions. Not widely known was the fact that the site remained continuously operated and enhanced for its primary mission, collecting technical data on every missile event within its field-of-view including numerous New Foreign Launches. A recent series of demonstrations has shown that COBRA DANE is still one of the most accurate and capable sensors available for Spacetrack and is particularly well suited for cataloging debris. The system was officially reinstated in the Space Surveillance Network on 1 Oct 1999.

### **Program History**

COBRA DANE (AN/FPS-108) was fielded in 1976 by Raytheon. The radar is situated near the end of the Aleutian chain at one of the western-most points in the United States (52.74°N/174.09°W), approximately 480 nautical miles from the Kamchatka Peninsula. Throughout the majority of its service it has fulfilled three concurrent missions for the USAF: data collection on FSU/CIS strategic missile systems as a national technical means of treaty verification (its primary mission); Early Warning to CINCNORAD/CMAFS for the event of ballistic missile attack against CONUS and southern Canada (corollary mission); and Space Surveillance/Space Object Identification for maintenance of the USAF inventory of near-earth orbiting objects including early observation of New Foreign Launches (secondary mission).

In 1990 the USAF awarded Raytheon the \$60 million COBRA DANE System Modernization (CDSM) program to extend its operational life by at least 10 years while providing significantly enhanced data collection capabilities. The modernization involved replacing aging and unsupportable radar, computing and communications interface equipment including the Receiver/Waveform Generator, Digital Signal Processor, ADPE, displays and recording peripherals. The majority of transmitter, array and facility

subsystems remained intact. All operational software was rewritten and enhanced using the Ada programming language (approximately 300,000 source lines of code), marking CDSM as the first large-scale radar development effort using Ada. The modernized system contained one of the most flexible radar pulse schedulers available. System reliability was significantly improved.

In April 1994, only months after completion of the major upgrade, budget constraints forced the discontinuation of all but the primary mission. It was not well known within the Space Surveillance community that COBRA DANE remained continuously operated as the backbone of the US Technical Surveillance sensor suite. All of its original Early Warning and Space Surveillance capabilities were either retained for future need or enhanced as a result of ongoing modifications.

#### Recent Enhancements

A number of important enhancements followed CDSM. The first of these was replacement of all 96 Receiver Low-Noise Amplifiers with more reliable and lower noise-figure GaAs FET amplifiers. This further improved overall reliability and increased system sensitivity by about 25%. COBRA DANE's inherent availability,  $A_i$ , for 1999 was better than 99.9%, excluding the roughly 30 minutes of daily PM, with a MTBCF of 884 hours. The system now achieves about 13.2 dB SNR under standard reference conditions consisting of a -20 dBsm sphere at 1,852 km range (1,000 nmi) and 1 degree steered elevation along azimuth boresight using the 1 msec mediumband track waveform. The system can achieve 15 dB SNR under these same conditions with its maximum 1.5 msec pulselwidth.

A Satellite data collection capability was implemented which allows any desired PRF/waveform combinations in the waveform suite to be applied to satellites, including NFLs, under mission profile control. Prior to the enhancement all satellite data collection was limited to Space Surveillance tasking in accordance with USSPACECOM Regulation 55-12 (now UI 10-40). The modification offers new wideband imaging and space object identification capabilities, but is most frequently used for post-mission calibration of missile data by comparison with returns from known satellites.

COBRA DANE's Field-of-View was expanded by increasing the azimuth scan by +/- 8 degrees from the horizon up to 30 degrees elevation. The Extended FOV prolonged time-in-track on both satellite and missile events and opened the radar to new collection opportunities such as high-inclination New Foreign Launch folders that were never before visible.

An Automatic Transmitter Run-up capability was implemented to improve operating cost efficiency and provide back-up means of data collection in the event of communications failure. The Auto Run-Up permits continuous surveillance at a more cost efficient, lower duty factor setting of 1.5% (one-quarter average power with maximum pulselwidth), vice the full 6%, while allowing the system to respond autonomously to missile events. In this mode, targets are tracked at quarter power until the initial launch and impact point predictions are made. A non-CONUS earth-impacting trajectory triggers gradual run-up

of transmitter duty factor, spoiling excess energy through boresite. Full duty is achieved in less than 30 seconds, in time for mission profile activation so that there is no loss of data. With this strategy the same detection performance is achieved as full-power operation but over a refined surveillance region and with significantly lower cost through reduced fuel consumption at the power plant (approx. \$2.4 million/year savings in fuel alone). An additional savings was realized in reduced spares consumption. For acquisition, Auto Run-Up serves as back-up. In nearly all cases the system is manually driven to full power with appropriate surveillance fences emplaced for each event.

Most recently, an Extended Range capability became available which effectively triples the unambiguous tracking range. DANE has always had "power to spare", but was artificially range limited in its software by radar pulse scheduler constraints. Today it is primarily limited by sensitivity out to approximately 14,000 km. Software checks are still in place, however, to drop track on orbital objects with periods greater than 225 minutes as a security measure. Only minor parameter changes will entirely lift that constraint and the system will no longer need to be regarded strictly as a near-earth space tracking station.

#### SATCAT Maintenance

COBRA DANE is typically operated at the reduced duty factor of 1.5% outside periods of missile data collection opportunity as a fuel and cost savings measure. Routine surveillance fences which consume only a portion of available radar resources are maintained for no-notice or short-notice events. The unused portion of radar energy, even at the reduced duty factor level, is sufficient to generate a considerable amount of high-quality Space Surveillance data without impact to the primary mission or to overall fuel consumption, and hence operating cost.

Under special agreement between the Central MASINT Office (CMO) and USSPACECOM effective 1 Oct 1999, COBRA DANE now performs Space Surveillance when not engaged in higher-priority collections. A data link to the radar from Cheyenne Mountain was installed allowing daily automatic object tasking, data transmission back to the mountain, and catalog updates to the radar. The National Air Intelligence Center (NAIC) also refined the routine missile surveillance coverage to consume an even smaller fraction of transmitter duty when the system is "idle" (0.36%), thereby freeing more energy for Space Surveillance (1.14% d.f. total).

Under this arrangement COBRA DANE provides about 2,500 observations on an average of 500 satellites per day in support of catalog maintenance. Of these, approximately 2,000 observations are collected on 400 tasked (known) satellites. A 10-degree wide high-elevation debris fence was activated to detect uncataloged objects that are small enough to elude the rest of the SSN. This narrow debris fence results in about 500 additional metric observations per day on roughly 100 Uncorrelated Targets (UCTs).

As a result of CDSM, ample computer processing and memory reserves exist to accommodate the continuous growth in SATCAT volume. The system is currently configured to store and process up to 12,000 orbital element sets on known objects plus

1,000 on unknowns. This is easily expandable out to 15,000 objects total through simple parameter changes.

As for system accuracy, Table 1 shows typical metric and RCS accuracies from recent calibrations. The metric errors are based on a calibration track of object 22076 on 11 Jan 2000 using NASA Satellite Laser Ranging (SLR) Network derived precision ephemerides as the standard. RCS errors were measured on calibration sphere object 5389 on 10 Jan.

Metric & RCS Accuracy	Range Error (m)	Azimuth Error (deg)	Elevation Error (deg)	RCS Error (dB)
Bias term	0.29	0.001	0.003	-0.09
Fluctuation, 1 sigma	2.92	0.054	0.053	1.15

Table 1. System metric accuracy against object 22076 using NASA SLR precision data as standard. RCS accuracy is based on a track of object 5398.

In Sept 99, the Space Warfare Center (SWC) performed an independent analysis of the metric observation usefulness and accuracy, concluding in their evaluation report that "The COBRA DANE data quality is as good or better than that currently received from the most accurate SSN radar sensors, such as Eglin or Cavalier."

#### Debris Tracking Capabilities

A requirement of increasing importance to NASA and USSPACECOM is maintaining current orbital elements on all known satellites and cataloging the tens of thousands of unknown debris objects in low earth orbit which pose a threat to manned space vehicles. The SSN has a practical limitation in the size of objects which can be reliably tracked of ~10 cm for reflective targets at about 1,000 km altitude; however, objects between 1 to 10 cm in size moving at speeds in excess of 8 km/sec can destroy the Space Station or Shuttle, let alone a man in spacewalk, if evasive maneuvers cannot be directed due to SSN tracking limitations. The International Space Station will be the most heavily shielded spacecraft ever flown, but it can only stop objects up to about 1 cm. The Shuttle Orbiter is routinely hit, and fortunately all collisions to date have been with extremely small (sub-millimeter) particles which only damaged tiles and windows (over 32 windows have had to be replaced). There are an estimated 100,000 or more objects in the lethal size category that cannot currently be cataloged.

The catalog volume is steadily increasing as the injection and break-up rates greatly outpace the gradual decay process from orbit. Figure 1, taken from the NASA/JSC website, illustrates this trend. During the five years in which COBRA DANE was not exploited by Space Command, the volume grew by nearly 2,000 objects, an increase due mostly to debris. The visible jump in volume near 3 June 96, for example, was due to a single break-up event. The fourth stage of a Pegasus launch vehicle Hydrazine Auxiliary Propulsion System (HAPS) was fragmented into more than 700 pieces large enough to be tracked. In May 97, a Proton motor fragmented into more than 72 detectable objects.

During a single week in February 98, three upper stage rocket motor break-ups occurred involving Soviet, European and Japanese vehicles, creating dozens of known and countless unknown fragments still in orbit. Such events occur frequently, and the challenge of tracking every object spawned is not within reach. Figure 2 is one of the more popular images of the near-earth satellite population based on the actual catalog at a time when there were far fewer objects in orbit.

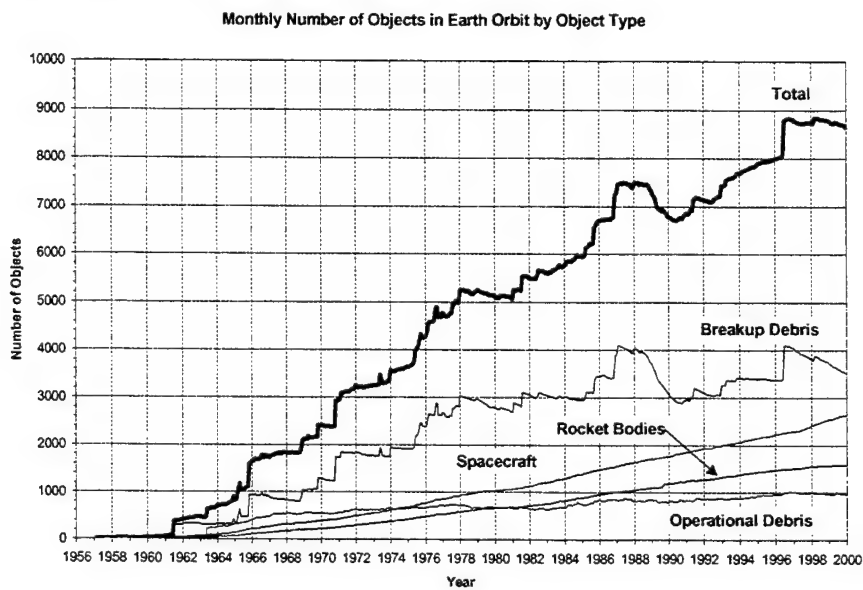


*Figure 1. Increase in satellite catalog volume over time, the largest portion of which is due to fragmentation debris. (With permission, E. Stansbery, NASA/JSC Orbital Debris website.)*

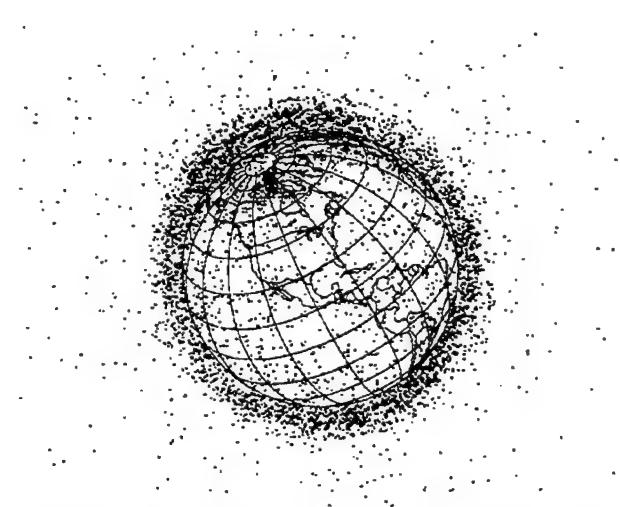


*Figure 2. Density of known objects in near-Earth orbit based on actual catalog volume. (From N. Johnson, D. McKnight, Artificial Space Debris.)*

COBRA DANE has a considerable advantage in the role of debris tracking relative to its Space Surveillance Network counterparts. The L-band radar “sees” debris objects in the hazardous but hard to detect size category better than any of the ground-based UHF

radars. Its phased array beam steering obviously enables it to search a given volume of space faster than any of the mechanically scanned dish antennas currently employed on a limited basis for debris characterization. When the dish radars are used for debris experiments they are typically operated in a "stare" or "stare and chase" mode, detecting objects which happen to fly through the narrow, fixed beams as a means of statistical sampling. Another limitation is that they are unable to track more than one object at a time, except for the event that multiple objects are in the same beam. Although some of the dish radars can detect objects much smaller than 1 cm due to their operating frequency and receiver processing (mainly pulse integration), they are relied upon more for estimating the debris population and composition rather than for cataloging new pieces and maintaining their orbital elements in the database.

As for the phased arrays, FPS-85 and PARCS have larger power aperture products than COBRA DANE, but DANE's operating frequency is a greater advantage here. Figure 3 illustrates the effect of operating wavelength on Radar Cross Section (RCS) of a conducting sphere. The L-band system with 24 cm wavelength views a 5 cm diameter sphere (-25 dB optical cross section) with a -25 dBsm RCS, whereas a UHF system with 71 cm wavelength sees this same object with a -44 dBsm RCS, seventy five times smaller. Although the figure applies to a spherical object, the conclusion is the same using NASA's empirically derived Size Estimation Model for complex debris shapes, since the object is in or near the Raleigh scattering region at either wavelength. This comparison is not complete, however, without factoring in all other system parameters which affect detection performance, including transmitted power, effective aperture area and available pulsedwidths. With all things considered, COBRA DANE still has more than a twenty-five to one single-pulse sensitivity advantage over the key Space Surveillance Sensor (FPS-85) for objects in this size category, and a larger margin of sensitivity over the NAVSPACECOM VHF system, PARCS and the remaining phased arrays.

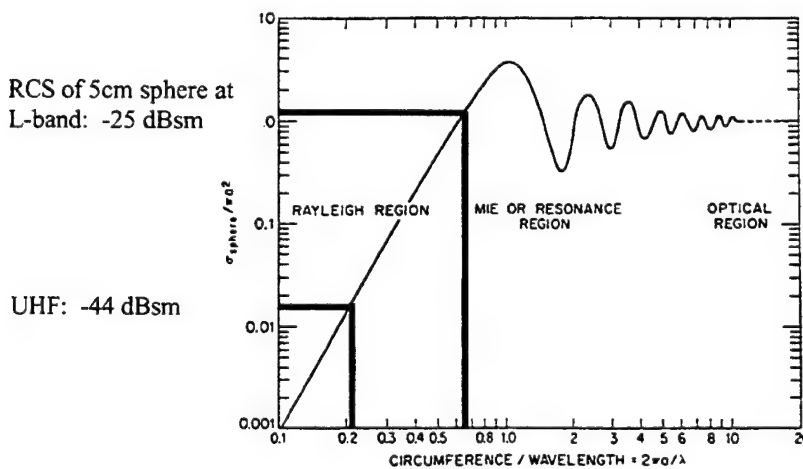


Figure 3. Radar Cross Section vs. operating wavelength of a conducting sphere. RCS values are shown for a 5 cm object as observed by L-band radar (24 cm wavelength) and UHF (71 cm). There is an 18.8 dB advantage at L-band for objects in the Rayleigh scattering region, where objects are smaller than the wavelength.

While COBRA DANE cannot completely fill the gap between the hazardous and the minimum SSN observable size objects (from 1 to 10 cm out to 600 km altitude), it can detect and track objects as small as 4 to 5 cm beyond this altitude. For example, a 5 cm sphere at 1,000 km altitude transiting a COBRA DANE fence at 50 degrees elevation will be approximately 1248 km from the radar, accounting for earth curvature, and will yield an ample 15 dB signal-to-noise ratio. This assumes maximum pulselwidth in search and accounts for scan and propagation losses. This same target condition for FPS-85 would produce little more than 1 dB SNR, making the object hardly detectable based on a single pulse<sup>1</sup>.

As a space surveillance asset through 1994, COBRA DANE provided updates on nearly 20% of the total satellite catalog. This percentage consisted mostly of known satellites tracked under specific tasking, without attempts to catalog the smaller, unknown debris objects, tens of thousands of which routinely pass through COBRA DANE's coverage. The majority of UCTs detected by DANE in the past were acquired almost inadvertently through horizontally placed missile surveillance fences. This search strategy is not efficient for an orbital debris mission since detection ranges are much longer than necessary. Where detectability is an issue, higher elevation fences are more effective up to the point where scan loss predominates. Figure 4 illustrates this for a 5cm object in a 1,000 km circular orbit passing overhead along azimuth boresite. Maximum sensitivity is achieved at about 57° elevation, the point at which scan loss outweighs the gain achieved with shorter slant range in a higher elevation fence. The conclusion is the same for any object size and altitude in a near-circular orbit. The sensitivity roll-off is (coincidentally) fairly symmetric near the peak. The scan loss which is responsible for this is plotted in Figure 5. Note that the array face tilt angle, or mechanical boresite in elevation, is 20°. The bottom line implication is that maximum detectability in a debris fence is achieved *when the average beam steer is approximately 37° above mechanical boresite*. A +/-30° horizontal fence, for example, should be oriented 50 - 51 degrees in elevation and centered in azimuth (319°). Other factors such as optimizing time-in-track and covering lower inclination orbits were considered secondary for the tests which followed.

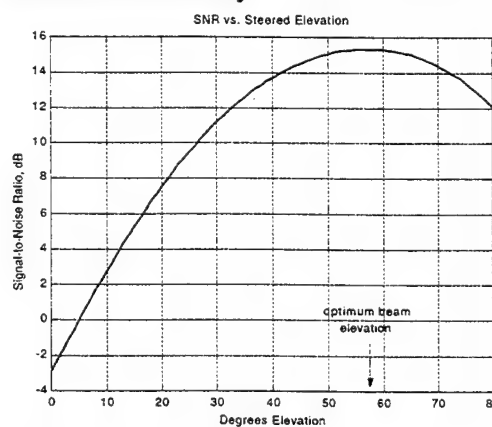
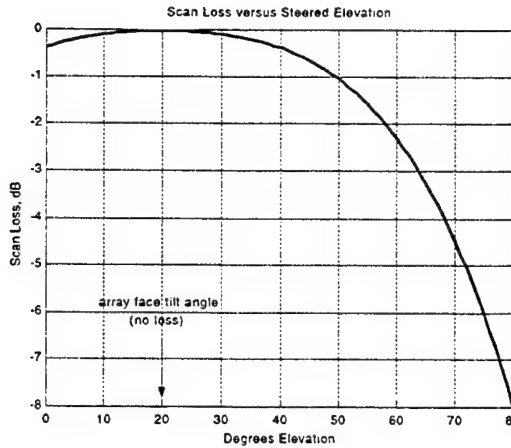


Figure 4. Sensitivity vs. Steered Elevation for a 5cm dia. object in 1,000 km circular orbit.

<sup>1</sup> Based on FPS-85 sensitivity performance : 50 db SNR on a 0 dBsm target @1,000 Km range, boresighted. Reliable detection might require more involved signal processing such as pulse integration combined with a shorter range, higher elevation search using M-out-of-N detection.



*Figure 5. Two-Way Array Scan Loss vs. Steered Elevation, defined by:*

$$L_s \equiv [1 - 0.265(u^2 + v^2) - 0.712(u^2 + v^2)^2]^2$$

With the above sensitivity tradeoff in mind, tests were conducted to determine DANE's potential in a more dedicated debris tracking role. A number of search strategies were tried, including vertically and horizontally aligned single row/single column fences and combinations of the two, to determine which orientation yielded the greatest volume of UCTs over a 24-hour period. The horizontal fence was most effective. Applying all available spacetrack radar duty (1.14%) in a single-row fence of 30° width and 50° elevation with maximum pulsedwidth resulted in between 700 and 800 UCT tracks per day on 15 and 16 Feb 99. The vast majority of these objects (over 90%) had L-band RCS values less than -10 dBsm, or 35 cm based on NASA's Size Estimation Model for complex debris shapes. This is the point where SSN coverage limitations first become evident. Over 40% had an RCS below -20dBsm, (> 7.5 cm), where SSN tracking is essentially unreliable, and about 2% had an RCS in the vicinity of -30 dBsm, or just under 5 cm. A small portion of the larger objects were mistagged as UCTs due to a combination of staleness of the catalog (received several days prior to test time) and inadequate time in track for reliable orbit determination and correlation on subsequent passes.

One of the most prominent debris experiments was a full-power test involving a 60° wide azimuth single-row search. Results were so promising that NASA/JSC requested COBRA DANE's participation in the April 99 International Debris Measurement Campaign using the identical search strategy, depicted in Figure 6. During the NASA effort more than 1200 unique uncorrelated objects were found by DANE which were not part of the known object catalog. On these, over 15,000 metric observations were provided to SWC and NASA for orbit determination. At least half of the debris pieces were estimated to be smaller than 7.5cm.

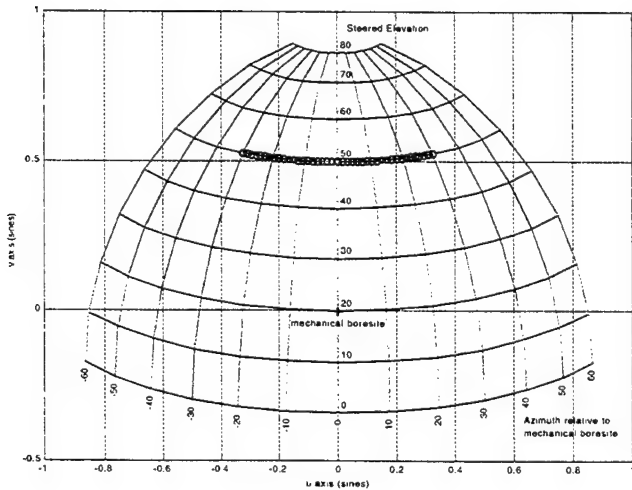
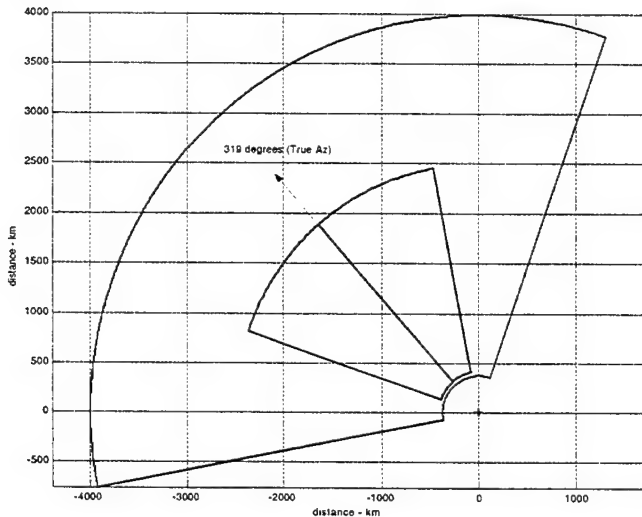


*Figure 6. Full-Power Debris Fences (sine space representation and top-down view) used in 9-10 April 99 International Debris Measurement Campaign and the subsequent NASA debris cataloging effort. Fence dimensions are: 415-2500 km Range limits, 289-319 and 319-345 deg Azim, 50-50.6 deg Elev, 0.93 Pd, -16 dBsm RCS and 0.141 deg/sec flythrough rate. Fence consumes 3% duty total. 3% "reserve" duty was left for tasking/retracking previously acquired UCTs.*

In Sept 99, NASA/JSC funded a larger-scale debris cataloging effort to run the radar at full-power 12 hours at a time for 21 days. By the close of this collection period more than 50,000 observations were generated, 561 new objects were cataloged, and 6 satellites which were previously considered lost were recovered. Highest tasking priority was placed on potential "Space Station crossers" (i.e. objects with inclinations > 51 deg and altitudes < 600 km). About 119 such objects were found. Most surprising was DANE's ability to track at least 4 suspected NaK (sodium potassium) coolant drops from the leaking defunct Russian nuclear-powered RORSAT constellation. Using elsets created from COBRA DANE, the X-band imaging Haystack radar was used to independently

assess their size and shape. The objects were confirmed to be spherical with approximately 7 cm diameter. Although smaller NaK droplets have been observed by other contributing sensors, these are the first such objects to be consistently tracked and cataloged.

Following the 21-days of collection, delays in data link reactivation with Cheyenne Mountain and the resumption of limited-duty operations resulted in the loss of many of the newly cataloged objects. Only about 200 remain in the database.

#### Summary

As of Oct 1999 COBRA DANE has resumed its historic secondary mission of Space Surveillance on a non-impacting basis with primary mission data collections. In a limited duty capacity it has already increased the volume of inventoried satellites and continues to locate new debris pieces as they are injected into orbit and spawned from break-ups and collisions. For the first time in SSN history, objects smaller than 10 cm are being tracked consistently enough to be permanently catalogued.

In its original operating mode through 1994, with a full suite of missile surveillance fences maintained close to horizon, the system was not exploited for its inherent ability to locate and track small debris. Despite this application of available radar resources, the system still managed to update nearly 20% of the entire inventory of known objects. If COBRA DANE were utilized in a more dedicated spacetrack mission then the percentage of catalogued objects tracked would exceed 20%, and the database would be considerably larger and better maintained (i.e. more current).

DANE is situated to observe the most densely populated bands of debris in low-earth orbit, with inclinations above 50 degrees. Since the site is contractor maintained and operated under NAIC direction, and is typically available between high-priority collection periods, it is considerably easier to exploit for debris measurements and spacetrack tasking than many adjunct SSN radars. An enhanced FOV in 1995 increased the data collection opportunities for both Space Surveillance and Technical data collection missions. Lower inclination orbits are now visible to the radar, depending on target altitude. An extended range tracking capability was recently made available which enables surveillance out to 14,000 km range. Even without the benefits of these modifications, COBRA DANE offers capabilities superior to many of the radars currently relied upon for debris tracking and precision orbit determination.

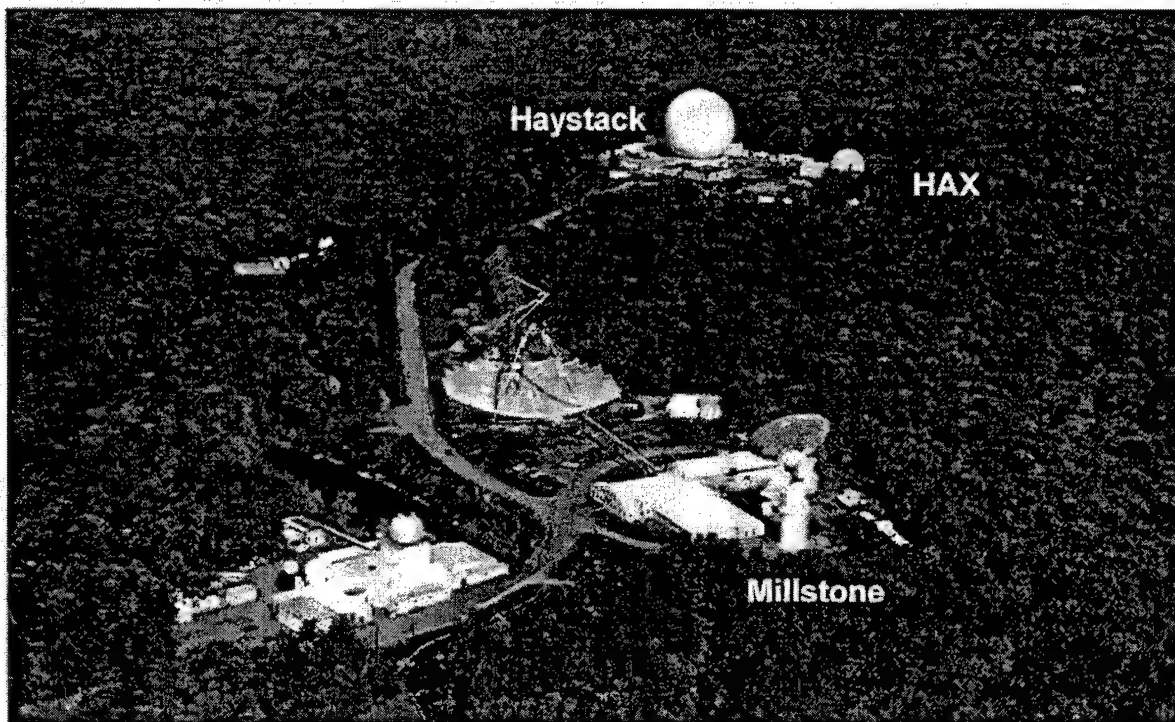
# Operations at the Lincoln Space Surveillance Complex

Fred D. Rosenberg, Ph.D.

MIT Lincoln Laboratory

## **Introduction and Overview**

Millstone Hill Radar was the first radar to operationally track geo-synchronous objects. Haystack Long Range Instrumentation Radar is the only sensor capable of imaging objects out to synchronous range. Together with the Haystack Auxiliary Radar (HAX) they comprise the Lincoln Space Surveillance Complex (LSSC).



The LSSC sensors operate as contributing sensors to the Space Surveillance Network as part of their mission to develop and transfer new hardware, software, analysis and operational techniques to the rest of the space surveillance network. The deep space tracking capabilities at ALTAIR and Eglin are based upon Millstone developed software. The imaging workstations at US Space Command CIC and other locations are exact duplicates of the workstations developed and used at MIT Lincoln Laboratory.

This past year major emphasis was started to modernize the hardware and software of the LSSC radars based upon the Radar Open Systems Architecture (ROSA) first used for the development of the Cobra Gemini radar, and currently being used to modernize all of the radars at Kwajalein. Research and operations continue to support a Cooperative Research and Development Agreement (CRDA) with a number of commercial companies to protect their geo-stationary communication satellites from collisions with dead payloads and rocket bodies in the

geosynchronous belt, to optimize their collision avoidance maneuvers when necessary, and to support their positioning of payloads in new orbital slots. A joint Millstone-Haystack/HAX data collection effort on small objects was conducted for NASA to help characterize small object signatures at different frequencies and geometries, with the goal to support NASA's modeling of the mass and size of all objects that are potential threats to all manned missions. Prototype database access and display structures for Millstone signature and network metric data have begun to be proven very valuable. These projects (except for the prototype database access) are reported elsewhere in this year's Space Control Conference.

## Operations

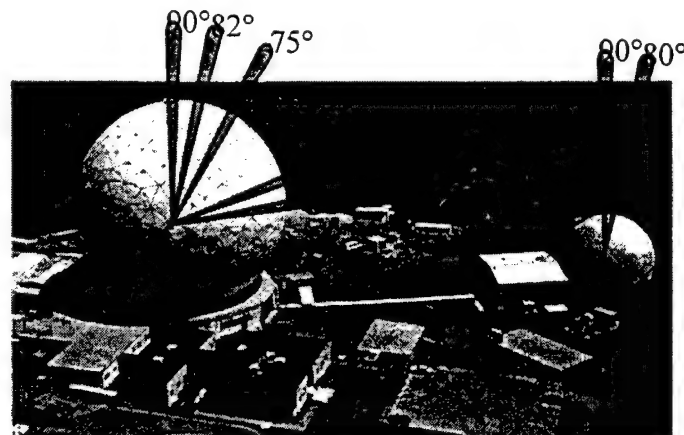
### Haystack & HAX

Haystack and HAX's primary responsibility is to provide images of near earth and deep space objects for mission identification and assessment. Haystack LRIR operates for thirteen weeks per year, in one to two week blocks, 16 hours per day, 7 days per week. (Haystack is a shared facility with the North East Radio Observatory Consortium that operates Haystack for radio astronomy research the rest of the year). Haystack LRIR can image objects out to geosynchronous range with a resolution of 25 cm. HAX is available for near earth imaging 52 weeks per year, 16 hours per day, 5 days per week, with a resolution of 12 cm. In fiscal year 1999 a total of 756 imaging tracks, producing over 14 thousand images, were performed in support of the primary imaging function. In addition 704 calibration tracks were performed to support this effort.

The two radars also cover new domestic and foreign launches for mission identification and assessment, and for payload deployment diagnostics. A total of six launches were specially covered in fiscal 1999.

Haystack Imaging & Launch Coverage						
IMAGING TRACKS	190	585	775	301	455	756
LAUNCHES	4	4	8	1	5	6
CALIBRATION TRACKS	278	454	732	371	333	704
IMAGES over COMM	2,665	5,379	8,044	4,338	9,749	14,087

Haystack and HAX's other primary function is to collect data to help characterize the low altitude space debris environment. Either radar stares at a single direction overhead (or to the south to see lower inclination orbits). Data are recorded only when an object passes through the beam. The object RCS is a measure of the objects size.



Assuming a circular orbit, the range to the object is a measure of its altitude, and the direction through the radar beam is a measure of the object's inclination. Over 600 hours per year of these data are collected at each radar, providing most of the in situ data for NASA's orbital debris models.

SPACE DEBRIS DATA COLLECTION						
Staring Hours	340	643	983	647	670	1,317

### Millstone Hill Radar

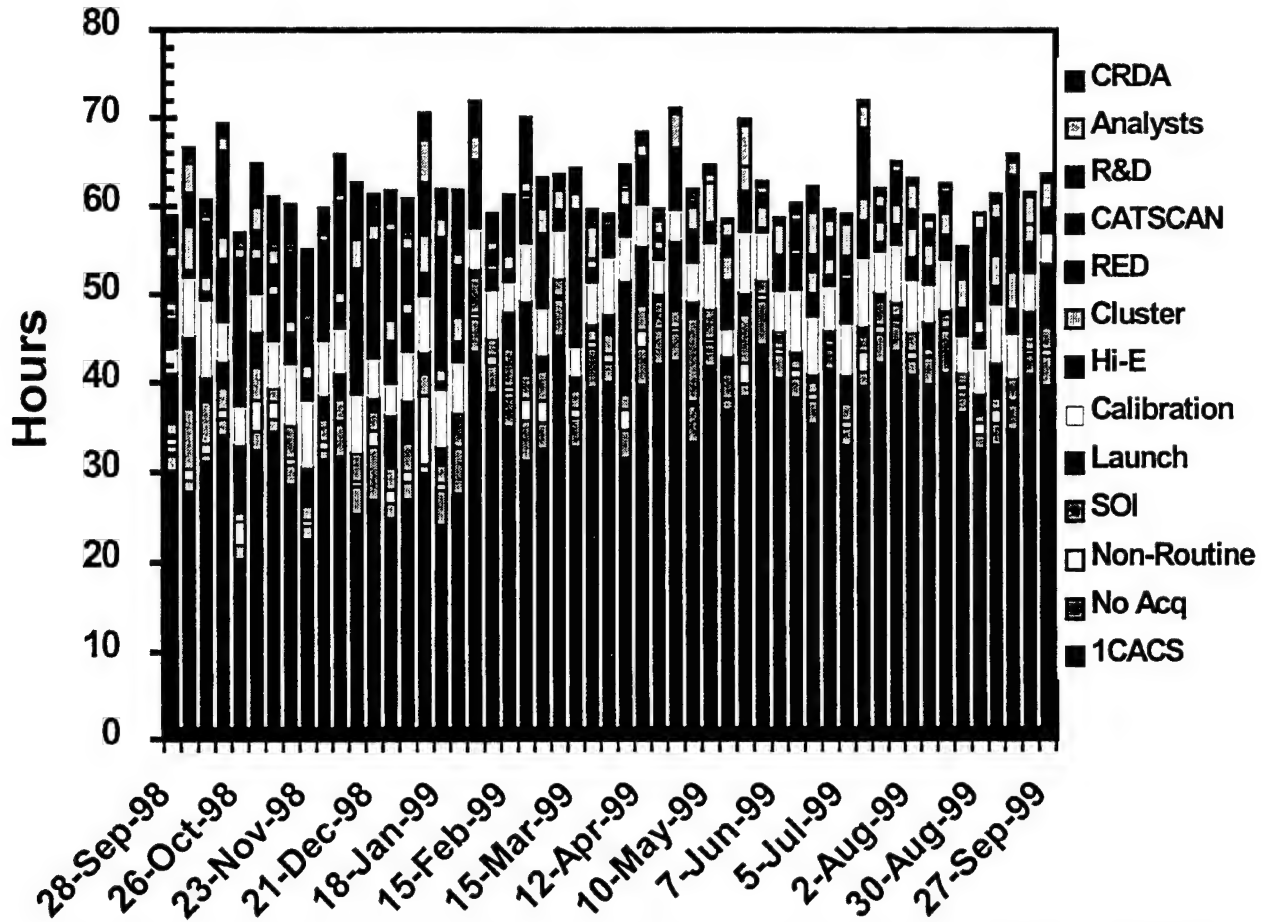
Millstone's responsibilities are to track primarily deep space objects in support of catalog maintenance, to support coverage of launches, and to provide Space Object Identification (SOI) data for payload identification and diagnostics. Sensor tasking comes from Air Force Space Command 1CACS, and U.S. Space Command SCC and CIC. Fifty-five hours per week are scheduled in support of this tasking. In FY1999 Millstone contributed 20,909 tracks comprising 234,956 metric observations to Space Command. In addition, Millstone supports internal analyst requests, some R&D, and CRDA support (reported elsewhere).

TOTAL MHR TRACKING			
# of Tracks	18,726	20,909	
# of Observations	188,447	234,956	

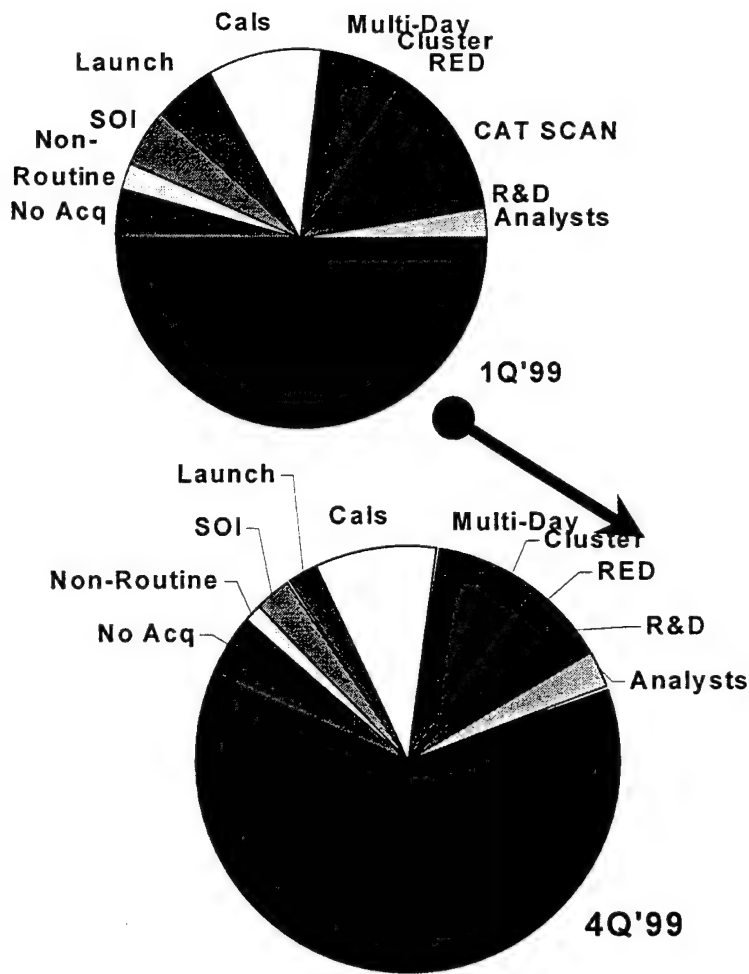


Wide week-to-week variances in time allocation are mainly due to variations

in launch coverage and non-routine tasking. This year a major effort was taken to better allocate tasking time. The effects of this effort is best seen in the pie charts. The percentage of time in direct 1CACS tasking was increased substantially by better managing the time devoted to calibrations (while still maintaining the same level of metric accuracy) and by having 1CACS increase its tasking level. In the past Millstone would frequently run out of tasking, at which it would self task (see "CATSCAN" in the 1Q'99 pie chart).



With the increased tasking level Millstone does not have to do any self-tasking now. There was also a joint effort by 1CACS and Millstone to better task cluster objects. Previously Millstone would track all objects in a cluster whenever one object was tracked in response to tasking. Now 1CACS tasks all of the objects in the cluster together. Initial improvements in Millstone's response were set back by the increased overall tasking. Further efforts are underway to address this minor concern.

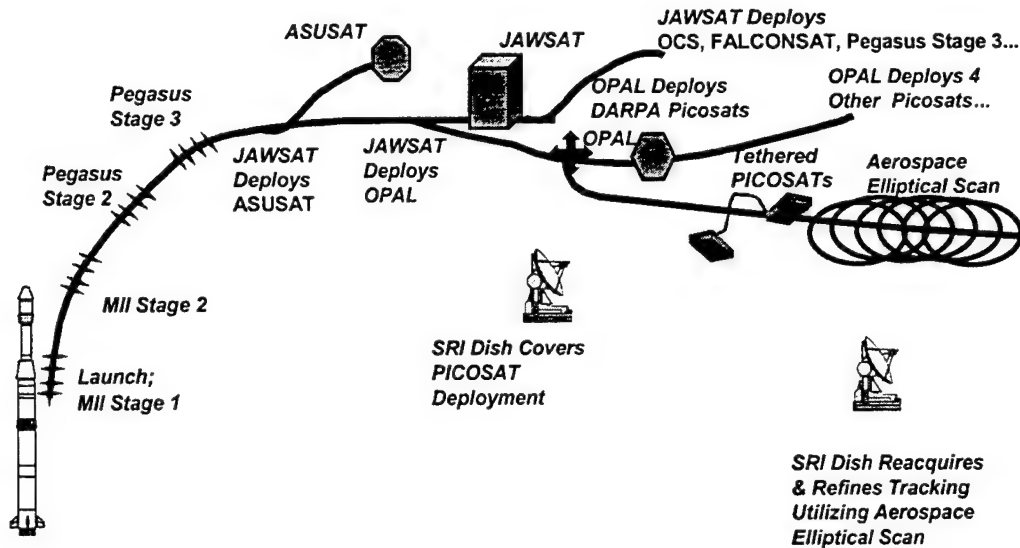


### LSSC Joint Operations and Projects

While the primary functions of the radars differ, there are operations and projects that require them to function together. New foreign launches are covered by both Millstone and either Haystack or HAX: Millstone to search, acquire, track and form a preliminary identification of all objects in the launch complex; Haystack or HAX, via a handover from Millstone, to image and perform a detailed object identification and mission assessment. The relatively large beam-width and range search capability of Millstone, and the high resolution of Haystack and HAX form a natural complement to each other's strengths and weaknesses.

This past year's non-historic NFLs highlighted the critically important contributions of the LSSC radars and analysts. The domestic Minotaur launch of five mini-satellites, and six daughter pico-satellites is illustrative of the LSSC coverage of some low altitude launches. LSSC sensors were unique in being able to correctly acquire, track and identify the tight complex of small payloads. Rapid acquisition and hand-off from Millstone to HAX, and rapid image processing and analysis

by HAX, were new operational challenges to LSSC personnel. We plan to better integrate these launch coverage lessons into future operations with the SCC and other SSN sensors.



Non-historic geo-synchronous launches were challenges to LSSC analysts. Apogee burns outside of Millstone and ALTAIR coverage required a combination of intelligent radar searches, SBV searches and Eglin UCT analysis to find the payloads, and to reconstruct the deployment scenarios. LSSC analysis and data were also critical in diagnosing the problems associated with the failed launches of DSP and Milstar satellites. Motion solutions, and piece counts were important to the accident investigation teams.

This year the LSSC radars also conducted a study for NASA on the RCS signatures of a number of small (10 cm to 1 m) objects. The different operating frequencies of the three radars-- 1.295 GHz, 10 GHz, and 16.7 GHz-- and the 25 cm and 12 cm range resolution of Haystack and HAX, provide the best available RCS vs. size capability of any sensor site.

LSSC is also modernizing all three radars based upon the Radar Open Systems Architecture (ROSA) first used for the development of the Cobra Gemini radar, and currently being used to modernize all of the radars at Kwajalein. Future hardware and software improvements to any of these radars will be able to first be operationally tested at one of the LSSC radars. The modernization will also allow any of the LSSC radars to be operated from any location on the secure network. This should provide more effective joint operations, particularly for identifying objects soon after a new launch.

## Summary

Millstone, Haystack and HAX continue their primary tracking and imaging support, as well as collecting data to characterize the debris environment. In addition, particularly in response to an increase in non-historic NFLs, they provide unique joint tracking and identification support. Modernization efforts will enable the sensors to work together more efficiently, and provide operating test-beds for future modifications of any ROSA radar.

## Lincoln Space Surveillance Complex (LSSC) Modernization

T.L. Sangiolo  
MIT Lincoln Laboratory

**This work is sponsored by the Air Force under A/F contract #F19628-95-C-0002.  
Opinions recommendations and conclusions are those of the author and are not  
necessarily endorsed by the United States Air Force**

### **1. Introduction**

Recently, Lincoln Laboratory designed and built the Dual Band Radar utilizing legacy systems, including the Process and Control System (PACS) of the LRIR and HAX. In the course of developing the Dual Band Radar, these legacy systems were implemented utilizing state of the art technology. Upon completion of the Dual Band Radar system, Lincoln Laboratory embarked upon a project to modernize the four Radar Systems (ALCOR, MMW, TRADEX and ALTAIR) on Kwajalein utilizing the technology of the Dual Band Radar. This program is called KMR Modernization and Remoting (KMAR). At the same time, independently, another group at Lincoln Laboratory was exploring ways to modernize the three LSSC radar systems (HAY, HAX, and Millstone (MHR) with Dual Band Radar technology. Since the two efforts were similar, it became apparent that sharing knowledge and resources would be beneficial to both. It was further recognized that making these systems to be as closely identical as possible would result in more benefits for Lincoln Laboratory and the government.

This approach reduces duplication of efforts, maximizes the efficiency of using human resources across all areas of radar development, and provides a way to use LSSC Radars as a radar test-bed, in close proximity of Lexington, where new designs could be implemented and tested prior to shipping them to Kwajalein. This has turned out to be a perfect example of transferring technology from multiple Radar Systems to the development of a new radar system, Dual Band Radar, and then feed back the knowledge gained to the two new radar development efforts KMAR and LSSC modernization. The paper describes the use of improved common hardware architecture and common core software system to implement a broad modernization project that will eventually cover seven radars. This commonality will be followed in the future to streamline the maintenance of these radars. The hardware architecture for the modernization has been identified as Radar Open Systems Architecture (ROSA). Open Systems and Commercial-Off-The-Shelf (COTS) have been defined by their respective source by the following for all to have a consistent interpretation of their use in this document.

- **Open Systems (DOD/SEI)**

**“ An open system is a collection of interacting software, hardware and human components, designed to satisfy stated needs, with the interface specification of components fully defined and available to the public, maintained according to group consensus and in which the implementation of components are conformant to the specification. ”**

- **COTS (summary from Federal Acquisition Regulations)**

- Customarily used for nongovernmental purpose and has been sold, leased or licensed to the general public
- Exists a priori (in a catalogue or price list)

## Radar Open System Architecture (ROSA)

Radar Modernization with ROSA encompasses an entire Radar system with the exception of the Antenna and its associated Motor Drive electronics, the Transmitter electronics, and the RF portion of the receiver. A simplified block diagram of the KMAR ROSA Architecture is illustrated in Figure 1 and depicts what has been modernized by color. Figure 2 illustrates how ROSA is configured as a distributed processing system as was the legacy HAY/HAX PACS system. Having a distributed processing system has many advantages among which are the following:

1. Reduced development time and O&M cost
2. Decomposition provides efficient use of engineering resources.
  - Allows many small development teams (distributed locations)
  - Allows for concurrent integration, test and evaluation
3. Components easily added, shared and modified
4. Migration to new technology can be done at the unit level
5. New developments can begin with working components
6. Better acquisition model, reduced NRE
7. Subsystems encapsulate specific radar function
8. Underlying hardware and software is hidden
9. Subsystem components completely define their functionality and interfaces to the outside world

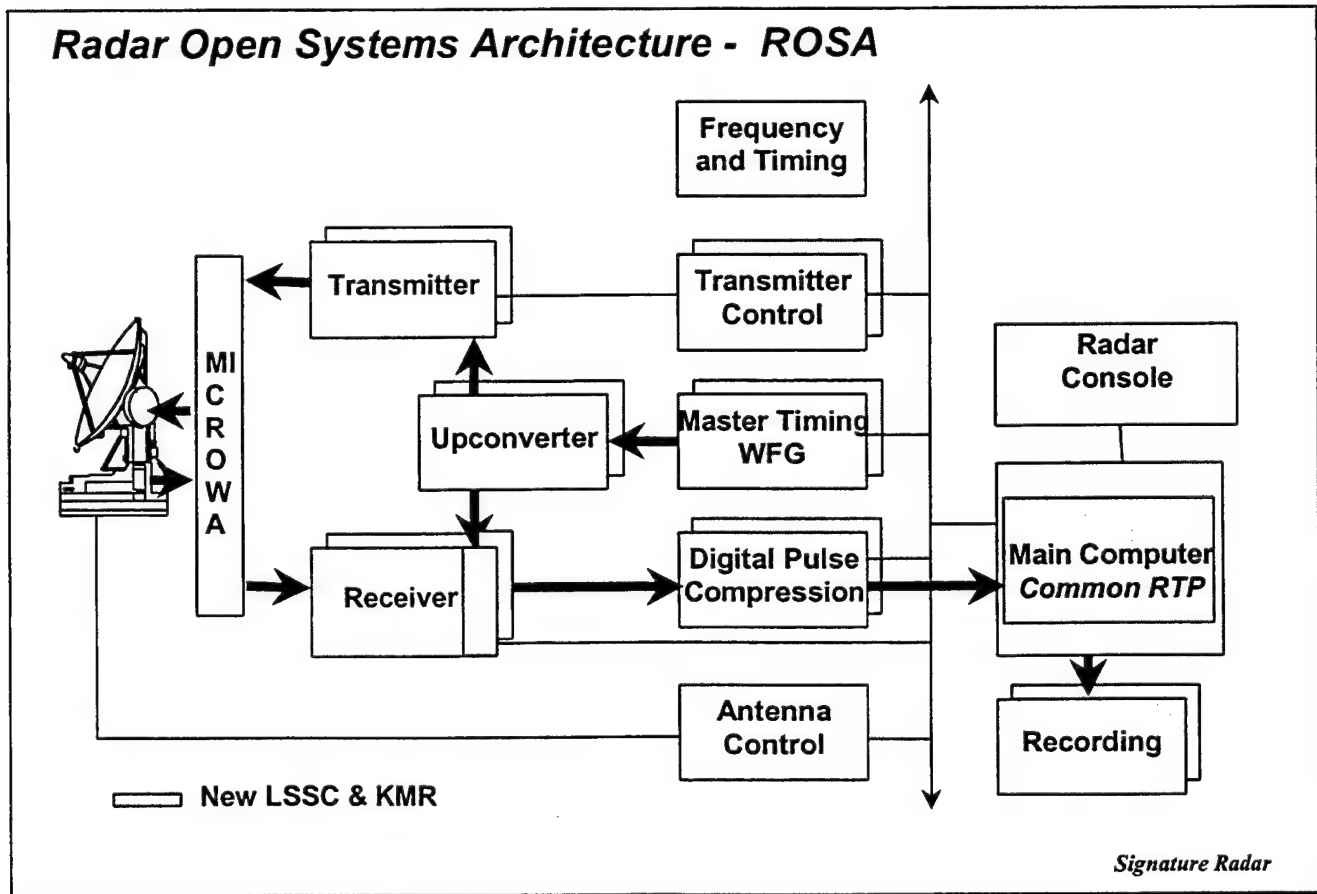


Figure 1 – Simplified Block Diagram of ROSA

What makes ROSA unique is that its primary architecture composition consists of all Commercial-Off-The-Shelf (COTS) interfaces and components. Each ROSA subsystem is comprised of an identical four board COTS set. These are the following:

1. Motorola 604– Power PC Single Board Computer (SBC)
2. Systran - Reflective Memory Interface (PMC connection to Motorola 604)
3. True Time - Time of Day Clock
4. SBS Greensprings Board for Power Supply monitoring

The communication between all of the subsystems is accomplished by the use of the COTS Systran Reflective Memory. This allows the control parameter distribution of tasks throughout subsystems and the main Radar Computer. This facilitates program development by decomposing the system.

The other major characteristic of the KMAR ROSA system is that it utilizes a common core real-time program (RTP) for all of its radars. Each sensor having unique configuration files that contain sensor specific characteristics accomplishes this. For the LSSC modernization two major software modules had to be incorporated into the “Core RTP (Debris for HAY and HAX and deep space tracking for Millstone).

The ROSA architecture lends itself to adding additional subsystems readily. For example if there are additional range windows to process then an additional Receiver subsystem and Digital Sampling system could be added. If the additional range window has independent control then an additional Timing System could also be added. The system is very flexible as the following figures 2-4 illustrate.

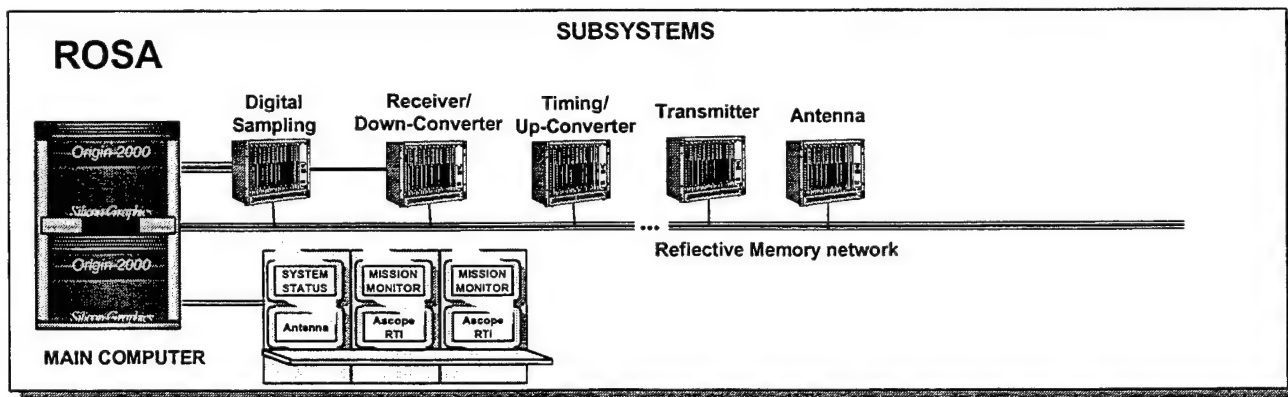


Figure 2 - KMAR ROSA Architecture

The HAY/HAX Radar Process and Control System Architecture with ROSA is illustrated in Figure 3. This System has independent Antenna and Transmitter Subsystems. Currently this system operates either of the Radars, but not simultaneously. This architecture lends itself to dual Radar operation easily with the addition of independent Upconverters, Downconverters, MTS and Digital Sampling subsystems and for complete independence with its own Origin 2000 Radar Computer.

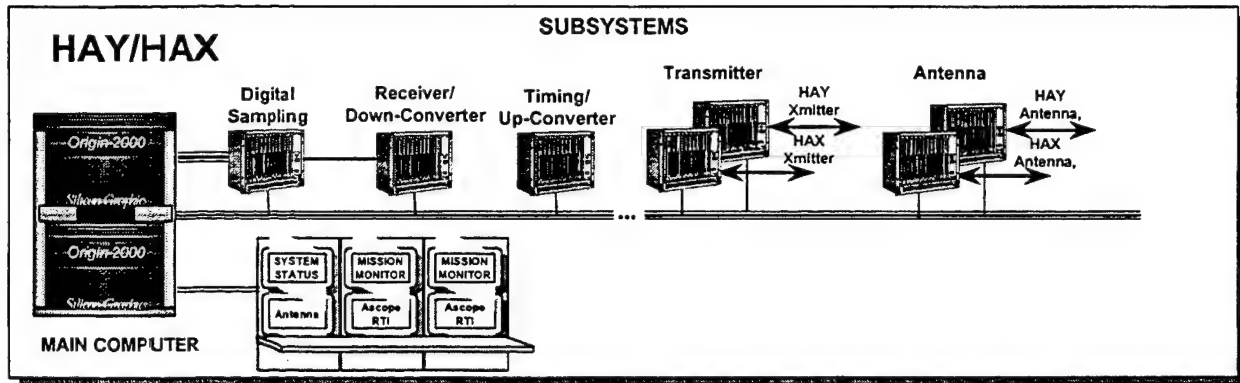


Figure 3 - HAY/HAX Radar ROSA Architecture

The Millstone ROSA implementation is illustrated in Figure 4. This system has a combined Timing and Transmitter subsystem.

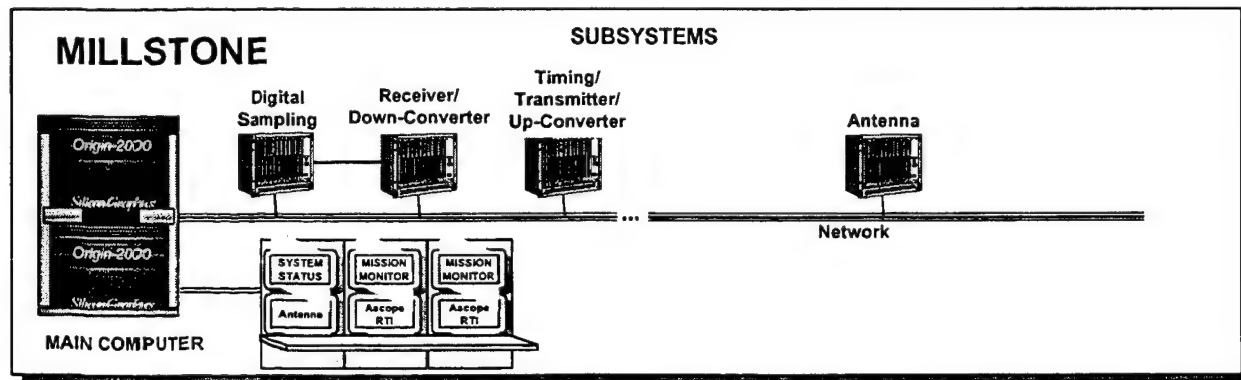


Figure 4 – Millstone Hill Radar ROSA Architecture

### **3. Waveform Generation an example of modernization**

Currently the HAX and LRIR radars use wide bandwidth (2 GHz and 1 GHz respectively) linear FM pulse waveforms for data collection. There are two Waveform Generators utilized in the existing system a Narrowband and a Wideband Generator. The Narrowband Generator is utilized in Pulsed Continuous Wave and Narrow bandwidths of up to 10MHz. It is also used in Wideband waveforms to correct for doppler during receive time due to the fixed waveform generated by the Wideband generator. The wide bandwidth linear FM waveforms are generated using a voltage controlled oscillator that is phase locked to the system reference frequency. This technology dates back to the original ALCOR 500MHz-bandwidth waveform generator developed in 1967. This system with both ramp generators and associated equipment is contained in four 19inch racks.

The Wideband linear FM pulse is generated for a fixed pulse duration of 256:s. This is restrictive in that it limits the Pulse Repetition Frequency (PRF) of the Radar because of their duty cycle limitations. In the case of Hay and Hax these are 35% and 30% which translates to a PRF of 1367 and 975 respectively. Parameters of the current waveform and clock pulse generators are the following:

- **Digital Narrow Band Waveform generator**
  - Supports CW, NB and WB Modes
  - $F_0$  10MHz, Bandwidth  $\pm 1.25\text{MHz}$
- **Analog Wide Band Waveform generator**
  - WB Mode Only
  - Fixed 256 $\mu\text{sec}$  Pulse Width
  - $F_0$  6GHz, Bandwidth  $\pm 512\text{MHz}$

The replacement waveform generators used in the ROSA System are Commercial Off The Shelf (COTS) Direct Digital Synthesizers (DDS). These units are located in the Master Timing Subsystem (MTS) and develop linear FM chirps over parameter controlled pulse-widths that are used in all modes of operation. There is a separate waveform generator for transmit and receive. Having independent generators allows dynamic test target capability utilizing the transmit waveform generator as a correlation source at receive time driven from an independent test target file.

Control parameters (Starting Frequency, Slope, Starting Phase and pulse-width) are received from the MTS control computer via the Versa Module European (VME) bus. As with its predecessor, the output of the digital waveform generator is frequency translated and multiplied to the appropriate transmit and receive frequencies. Characteristics of the Waveform Generator are the following:

- **Raytheon (Hughes) COTS VME Digital Waveform Generator**
  - Supports all waveforms CW, NB and WB modes
  - 960 MHz Clock Frequency
  - 128 MHz Bandwidth
  - Variable Pulse Duration
  - Waveform list generation

### **4. Master Timing System**

The PACS legacy Master Timing System is also a VME based system utilizing SSI Integrated circuits. Utilizing this technology required the Custom LL designed VME boards to be in a 9U-280 wire-wrap form factor. The KMAR MTS technology was designed with very large Field Programmable Gate Array's

(FPGA's) and fabricated with Printed Circuit boards. This reduced the packaging to a 6U-160 form factor and occupied fewer board slots, which allowed the Waveform Frequency Generators into the MTS.

Figure 5 is the block diagram of the KMAR MTS VME architecture. This reduced volume architecture will replace the current MTS as well as adding new functionality to the MTS such as the Wide Band Ramp Generator (WBRG), and Clock Pulse Generator.

The Master Timing System generates all of the precise timing signals necessary to control all of the Radar Subsystems at a Pulse Repetition Interval (PRI) rate. The MTS is comprised of the standard subsystem four board COTS set and in addition two Raytheon COTS Waveform generators and three Lincoln Laboratory designed boards.

The three Lincoln Laboratory designed boards are the following:

1. TG - Timing Generator board
  2. CPG - 40MHz Variable Clock Pulse Generator board
  3. WBRGI - Hughes Wideband Ramp Generator Interface board
- The Master Timing System Timing Generator (TG) Board - This board generates the precise PRI, Transmit and Receive strobes for its respective system. It provides the Fine Range control for the Clock Pulse Generator and generates timing strobes for Transmit and Receive time.
  - The Clock Pulse Generator (CPG) Board - This board's function is to provide the Variable Phase 40 MHz clock that is utilized for A/D clocks. The phase resolution of the CPG is 11.25 Pico seconds.
  - The Wideband Generator Interface (WBRGI) Board - This board generates the precise "Start" and "Stop" triggers to the Hughes DWRBG board. It synchronizes the TG .1usec triggers to its appropriate 960 MHz clock to ensure the precise start of the Hughes DWBRG.

## ROSA MASTER TIMING SYSTEM

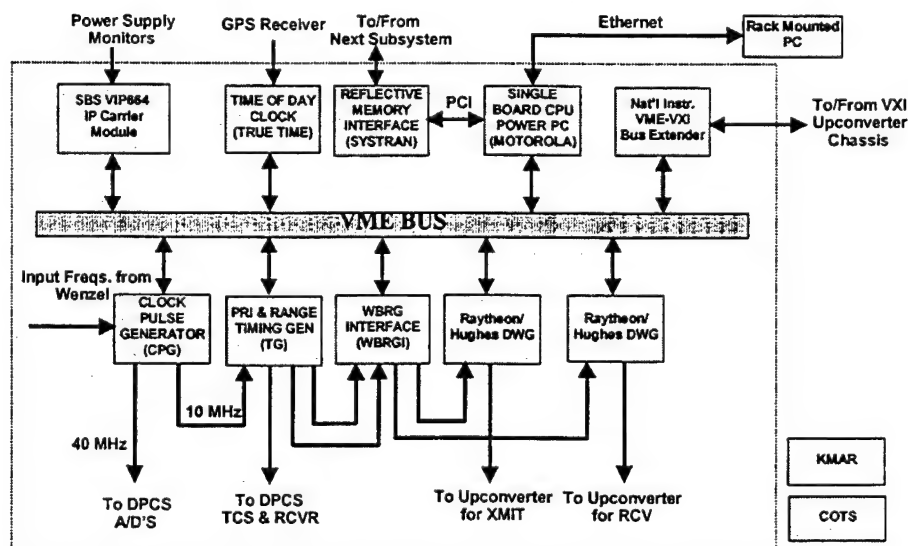


Figure 5 – ROSA Master Timing System Block Diagram

## 5. Summary

A major modernization is underway for the three LSSC radar's HAY/HAX and the MHR utilizing the KMAR ROSA architecture. This includes new computer architecture, replacing the Master Timing System (MTS) and Digital Sampling System and radar Consoles with newer technology and replacing the analog waveform generation hardware with state of the art, direct digital synthesis hardware for waveform generation. In addition, the Downconverters and Upconverters are implemented with VXI technology that lends itself to vastly superior system control and analysis.

The ROSA modernization will provide many new features for the HAY/HAX radars, which include variable wideband pulse-widths for higher PRF's and extended wideband range capability. In addition, the capability of having mixed waveform modes to enhance tracking. The modernization of the MHR will improve its Low Earth Orbit tracking capability as well as having multi-target tracking capability.

With KMAR ROSA technology implemented at LSSC, the three Radars could serve as a potential test-bed for future algorithmic and hardware upgrades. ROSA also provides a common hardware and software base for LSSC personnel as well as Kwajalein personnel. Figure 6 illustrates all of the seven Lincoln Laboratory Radars that are being modernized with ROSA. Looking at the frequencies and various applications that these radars perform illustrates the flexibility of ROSA both in hardware and software.

The ROSA hardware was recently evaluated to modernize the Eglin FPS-85 Radar. Because of its flexible architecture it lends itself very well for that modernization too. This architecture with its current implementation for the Kwajalein and LSSC Radars spans frequencies of VHF to W Band (95 GHz).

## Lincoln Laboratory Modernization Radars *Frequency Bands*

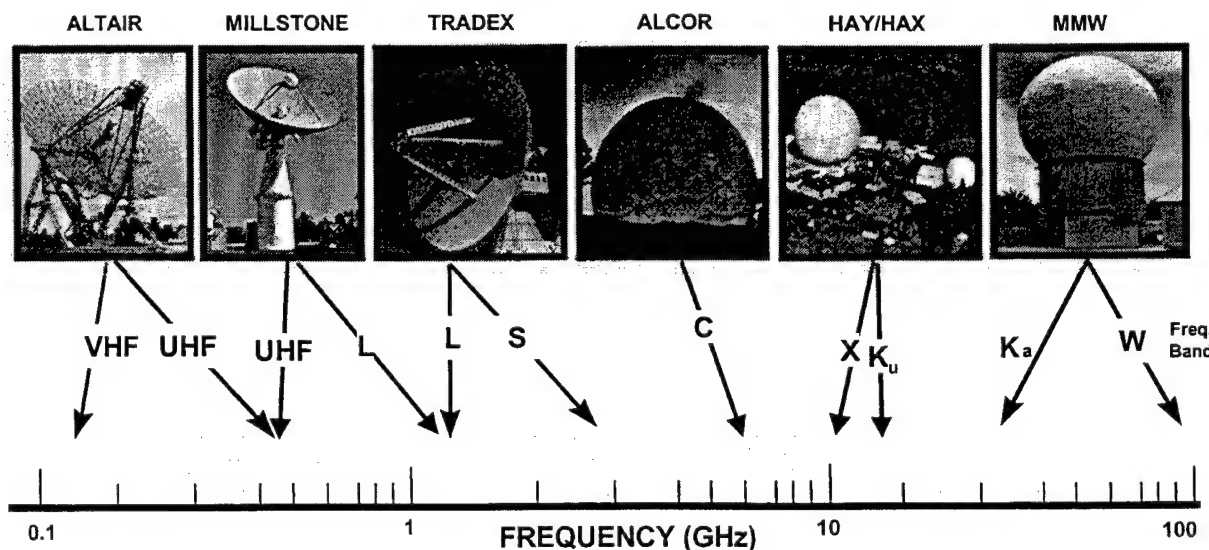


Figure 6 Lincoln Lab ROSA Modernization Radars

## Configuration Trades for a Space Object Surveillance Fence

J. K. Beard (Raytheon Electronic Systems)

**ABSTRACT.** We examine the mission and requirements of space surveillance as currently met by the existing NAVSPACECOM VHF surveillance fence. Upcoming replacement cost considerations provide a cost offset for a new radar. A technology date of about 2002 provides a basis for a trade space that leads to a new configuration.

A summary requirement is to maintain the orbital object catalog of objects 30 cm and larger. An increasingly important but currently unfunded requirement is to provide alerting of collisions between debris and operational spacecraft, particularly high value, high risk space vehicles such as the International Space Station (ISS) and the Space Shuttle. Orbital objects as small as 1 cm are a threat to the ISS, the Space Shuttle, and other spacecraft.

The existence of a well thought out VHF fence supports development of scaled CW fence concepts, but sufficient investment in development of pulsed concepts is warranted to explore operational advantages. A 1 cm debris size and antenna cost considerations drive toward wavelengths of 6 cm or shorter, but an allocation in the 3 GHz region is underway. The bottom line is that we should reexamine the mission and requirements of space surveillance and reevaluate multiple solutions.

**REQUIREMENTS.** The space surveillance mission, simply summarized, is to support the catalog of orbital objects [1, 2, 3, 4, 5, 6, 7]. Currently, this catalog is about 9,000 objects [8]. Due to uncertainty in orbital elements of each object, maneuvers, breakups, and collisions, maintenance of this catalog is best met by a surveillance fence that sees most objects often. Derivative requirements such as Chambered Round are also stated, and met by such a fence [7].

Protection of the ISS and Space Shuttle from collisions with space debris is a known threat that is getting increasing emphasis [9, 10, 11]. Building in tolerance of debris sizes to about 1 cm in the ISS and Space Shuttle is deemed practical [9 p. 46], but the main protection against debris of larger sizes is tracking this debris and taking appropriate measures to prevent collisions. Since 1 cm debris will stay in 300 km to 450 km orbit from about a month to about a year before decaying, depending on the solar cycle [9, p. 31], debris in this size range must be detected reliably to 600 km altitude to provide data on a time scale appropriate to spacecraft mission planning and execution.

The number of space objects has increased linearly since about 1960 [6, page 20]. Due to international agreements on explosions and debris generating mechanisms such as explosive bolts, in place since about 1995 with most countries with launch capabilities, increase of space debris densities is now less rapid than in the past. Projected flux of debris objects is expected to remain at about  $4 \times 10^{-5}$  objects per square meter per year in the important orbital regime of 900 km altitude for another decade or two [6, page 171] but will inevitably increase after that time due to collisions between existing debris particles and resulting debris breakups.

**WAYS AND MEANS TO MEET THE MISSION.** Candidate sensors for space surveillance must include space based sensors as well as ground based sensors.

Candidate ground based sensor options, with feasibility issues, are

- Upgrade Existing VHF Surveillance Fence: The high altitude (high gain) receiver sites at Elephant Butte, NM and Hawkinsville, GA are key to the ability of the radar to achieve its best sensitivity. These antennas are large arrays of exposed dipoles. These antennas are scheduled for replacement in about 2002 due to the end of their useful life. This is a very

expensive proposition and provides significant cost offset supporting a microwave upgrade concept. Similar issues with the O&M costs of the transmitter solid state modules and other issues will need to be addressed to keep significant capabilities. Bottom line: expensive life cycle replacements and similar issues require large expenditures in the 2002 time frame. A significant investment might reveal less expensive alternatives to keep part or all of this capability. But, the long wavelengths used mean that this radar will never be useful in detecting 1 cm debris at 600 km altitude.

- New Active RF: Several studies [12, 13, others] that open up the trade space for a new radar have shown that a microwave system can meet the mission with much smaller transmit antennas and simpler antenna concepts. This will be a new start development program. A wavelength of 6 cm or shorter must be used to maintain sensitivity for debris sizes down to 1 cm.
- EO/IR: Ground based EO/IR sensors have been used successfully to detect and track individual orbital objects for some time. However, the solid angle searched by an individual sensor is small, and an practical architecture for a search fence that does not allow fly-through is not obvious. An investment may reveal such a viable concept, but this sensor would necessarily not be all weather. Its best use seems to be as an auxiliary sensor with cueing from another sensor.
- Laser Radar: Lasers have been used to track individual objects to very high accuracies for some time. These sensors have the same problems in maintaining a high probability of intercept search fence as explained above for EO/IR sensors, both space and ground based.

Candidate space based sensor types, with feasibility issues, are

- Space Based Active RF: Average power limitations of solar powered satellites prevents full time long range detection. High probability of detection would require a large and thus very expensive constellation. Such a constellation would survey a limited altitude regime because of detection range limitations. An overall configuration that does not allow fly-through is not obvious.
- Space Based Passive EO/IR: For the purposes of orbital object surveillance, this type of sensor has a trade of sensitivity versus field of view for a given aperture size. An architecture that provides a fixed fan beam search fence is not Reasonable aperture sizes do not provide a viable search volume for a small constellation, particularly with uncooled focal planes. Again, we have a large, expensive constellation that would survey a limited altitude regime.
- Space Based Laser Radar: The Active RF discussion applies, with the added issue of beam size and object fly-through. Best use of laser radar is raster scan or windshield wiper scan, which would not provide high probability of detection for objects subtending small angles and having high angle rates at the sensor due to orbital object fly-through. A practical laser radar fan beam concept is not obvious.

Of these alternatives, three combinations survive the tests of viability in meeting the mission, affordable in cost, and low risk:

1. New Active RF. Economical pulsed concepts similar to a scaled version of the BMEWS AESA upgrade have difficulty with sensitivity and debris fly-through because of the small beamwidths necessary to keep sensitivity high and the high angle rates of LEO objects. Use of beam occupancy to perform verification and track to estimate six orbital elements exacerbates the fly-through problem, and an economical concept that does not involve more than one transmitter is not obvious. As a result, this sensor would seem to be a CW fan beam at microwave frequencies, and could be considered a scaling of the VHF surveillance fence. Sufficient investment should be made in pulsed concepts to determine if a competitive concept is available that will measure six orbital elements from a single site.

2. Retain Existing VHF Surveillance Radar. This option requires new technologies to solve existing O&M issues, particularly to reduce life cycle costs of the antennas.
3. Retain Some Existing VHF Capability, Add Microwave Fence. This approach would leverage some or all of the existing VHF fence to mitigate any schedule risk of the microwave fence and possibly reduce its development and life cycle costs. It might also supplement it by providing verification and track data for newly detected orbital objects. The microwave fence would still have to see 1 cm debris up to 600 km altitude to meet the requirement of protection of the ISS and Space Shuttle, and supporting cost offsets from standing down the VHF capability would be reduced.

REQUIREMENTS FLOWDOWN. The new capability must, in general, match or exceed the capabilities of the existing VHF surveillance fence and reduce costs. The fan beam must extend over 22.5 degrees of longitude arc at altitudes where high probability of intercept is required to prevent fly-through as the fence rotates with the Earth through an object's 90 minute orbit. Since the fan beam will cross the orbit every 12 hours as the Earth rotates, the radar will "see" objects at least twice a day. The product of the radar average power, transmitter antenna gain, and receiver antenna area must be on the same order as that for the detection channel of the existing VHF system to maintain the same sensitivity. Other configuration trades, such as fan beam thickness and dwell time, are also important.

The VHF fence was designed and configured in a time when minimum object sizes of 1 foot were the accepted requirement. This defined an absolute minimum frequency of 75 MHz and a center frequency of 150 MHz to keep 1 foot objects at the limit of the Airy region. This fence was begun at 108 MHz and later changed to 216.98 MHz. The absolute minimum center frequency for keeping any viable radar equation sensitivity for 1 cm objects is 2.4 GHz, and the Airy region limit for 1 cm objects is a center frequency of 4.8 GHz.

SMALLER ORBITAL OBJECTS POSE SPECIAL PROBLEMS. Small objects, from 1 cm to 10 cm in size, are of special interest in protection of space vehicles because objects of this size will penetrate or otherwise damage spacecraft on impact [9, p. 46]. Smaller objects are more common than larger objects.

Smaller objects are more subject to drag, and objects on the order of 1 cm in size at altitudes of 600 km and lower are subject to significant change in orbital elements over a single orbital period. Therefore, tracking them all may be impractical because ambiguities in association of detections 12 hours apart might not be correctly resolved to a high confidence level. In addition, a 1 cm object will decay from 600 km altitude to 400 km altitude (where it will be a hazard to the ISS and Space Shuttle) in a year during the low point in the solar cycle, and a few weeks at the peak of the solar cycle. These particles will decay from 400 km to reentry in about 10 days at the peak of the solar cycle and a few months at the minimum of the solar cycle [6 p. 29, 9 p. 31]. In a year, 80% of orbital objects in this size range at altitudes from 200 km to 600 km will decay to reentry and be replaced by orbital objects decaying from higher altitudes. Therefore, sensing 1 cm objects at 600 km is appropriate to maintaining an awareness of orbital objects in this size range. A multiple hypothesis tracker (MHT) or similar technology will be required to track most of them, and maintaining track of individual objects without special attention will become more difficult as its orbital altitude decays.

PRODUCING ORBITAL ELEMENTS ON FIRST PASS IS DIFFICULT. This requirement is difficult to meet with a single sensor while maintaining an unmodulated CW fan beam search fence, even with triangulation. This is because, even though the position can be obtained in three dimensions through two axis monopulse in two receivers, only two bistatic range rates are measured with an unmodulated CW waveform. Receivers in the plane of the fan beam can obtain velocity in this plane, but not velocity across the plane. This is 5 numbers, not the 6 that is

required to define all the orbital elements of an object. Because high probability of intercept without allowing fly-through is deemed the more important requirement, the existing VHF fence was designed to produce 5 numbers. Since we can meet the mission with the VHF fence by using other sensors or waiting for a second detection by the VHF fence, the same relaxation of this requirement for the microwave fence may be allowable.

Because range rate resolution is better at higher frequencies at the same dwell, chirp rate of radar returns caused by the  $v^2/R$  relative acceleration allows a measurement of velocity across the plane of the search fence. The quantity  $v$  here is the crossrange component of relative velocity and the quantity  $R$  is the range to the target; minor complication accrues to bistatic configurations. This will be very helpful in the use of a microwave search fence but will not provide high accuracies because of the short dwell times from the thin fan beams necessary to keep transmitter antenna gain high.

Velocity normal to the fence plane can be sensed by a receiver site out of the plane of the fence. Such a site would have multiple preformed receiver beams in two dimensions to cover detections at different altitudes but would be otherwise similar to receiver sites in the fence plane.

The conflict in functional allocation between the detection and tracking requirements is a classical sensor problem and is sometimes met by the use of separate modes or even additional sensors. For example, the original 1960s BMEWS radars used separate horizon search and track radars, and the active electrically steered array (AESA) upgrades use separate modes. The BMEWS design prevents fly-through by controlling the revisit interval at each horizon search beam position while allocating sufficient beam occupancy to the track modes to meet its limited track objectives. This option is not available to the microwave RF sensor because the fan beam must be very thin to keep antenna gains high and orbital objects often exhibit high angle rates, and fly-through is unavoidable if the fence is reallocated for even one dwell.

The option of using multiple FM sine waves or other modulation on the waveform to measure range will produce all 6 orbital elements in a single pass, and this option deserves more study. Significant disadvantages of this approach include complications in the signal processing and additional difficulties in ambiguity resolution when a large number of objects is detected in a single dwell. These difficulties may be mitigated by advances in digital signal processing hardware over the life cycle of the new microwave sensor.

Use of a separate sensor is the best option. Often the object has been detected prior to its crossing the fence by another sensor and the data provided by the VHF fence completes the orbital parameter set at that time. When the VHF fence provides the first detection of an orbital object, the surveillance fence alerts the Space Track community and another sensor provides data that completes the orbital set of the new object, or the surveillance fence itself provides the second detection 90 minutes or even 12 hours later.

An additional pencil beam RF sensor could provide the verification and tracking function. Such an additional sensor could be a major cost driver. An X band cued, pencil beam ESA with a pulsed waveform would be an excellent choice for this sensor from the functional point of view.

An additional passive EO/IR sensor, co-located with the receiver sites, could provide a verification and track capability. Although not all-weather, a 1 meter aperture, cued to a line of sight by new detections, could serve this function at a very moderate cost. This sensor would be available for other uses when not required by the surveillance fence.

**PRINCIPAL COST TRADE ISSUES ARE DRIVEN BY ANTENNA CONSIDERATIONS.** In terms of fabrication cost, the most expensive items, by far, are the arrays and transmitter. Antenna life cycle costs dominate the overall cost picture of the existing VHF fence because of the large

antenna sizes necessary and because these large antennas are made up of dipoles exposed to the elements. A microwave system will have smaller antennas. The necessity that the receive antenna effective area approximate that of the VHF system, to achieve comparable sensitivity, is achieved by the fact that the VHF system uses only one 1200 foot array for detection in the low altitude sites and two 2400 foot arrays for detection in the high altitude sites. Thus, the necessary receive antenna area of two 2400 foot VHF arrays is daunting but achievable. A microwave system will use all antennas at a given site in multiple preformed beams for detection to meet sensitivity requirements. Thus, the natural scaling of receiver antenna length normal to the fence plane while multiplying the number of antennas along the fence plane, both in proportion to wavelength, preserves sensitivity if all of the receive antennas are used to form multiple preformed beams for detection. Thus, the effective antenna area for a microwave receiver site is that of only the detection antennas at the VHF sites, not the area of all the antennas at a VHF receiver site, and very significant gains in antenna size are achieved. The smaller microwave antennas will be protected from the elements and will have entirely different O&M and life cycle support schemes.

Transmitter cost is also a significant cost issue, though far less so than antenna cost. The existing VHF main transmitter radiates about 750 kW, and a similar average power will be required of a microwave site to maintain the sensitivity of the existing VHF capability.

The cost of prime power for the transmitter is a significant O&M cost. The state of the art of DC to RF efficiency is 20% to 30%, and this range is seen in all sizes, including solid state transmitters, and shows no major variation with frequency.

Phase matching of the antenna elements can be considered a feasibility or risk issue. For microwave antennas, the use of multiple line antennas makes phase matching in a given line antenna a design issue, but phase matching at the receiver sites for multiple parallel antennas determines their ability to perform accurate direction finding in the plane of the fence. This phasing problem scales with frequency and there is no strong effect versus frequency.

Digital signal processing effects do vary quite significantly with frequency. As a rule of thumb, the processing load is proportional to the bandwidth processed, which in turn is proportional to frequency for a CW surveillance fence of a given fan beam thickness. The use of multiple preformed beams in a digital approach requires that separate receivers be used at each receiver antenna, multiplying the requirements for data acquisition and digital signal processing, again in proportion to center frequency. Signal chirp is neglected in the current VHF fence but cannot be ignored at higher frequencies, again multiplying digital signal processing in proportion to frequency. The number of objects "seen" by the radar also increases with frequency, this effect having a law that exceeds linear multiplication in proportion to center frequency. In spite of this daunting case for large processing requirements, processing is distributed among receiver antennas and is thus inherently parallel to some degree, and current COTS processing capability is well up to processing the bandwidth from each antenna at any center frequency under consideration.

Data processing is another factor that increases with frequency due to the increase in the number of objects. Currently, data processing is done in Dahlgren, not at the sites, which raises data flow architecture issues because of the effect of increased data generated at the sites. These overall architecture issues are unresolved.

**BANDWIDTH REQUIREMENTS ARE NOT A MAJOR DRIVER.** Bandwidth is a very real cost. Although bandwidth cost is not part of the POM or dollar amount allocated to development or design, this cost is part of the system cost and is taken into account to provide a balanced system engineering design with true cost accounting in the measures of merit used to evaluate center frequency trades. Orbital objects can exhibit both opening and closing velocities approaching

escape velocity, 11.18 kilometers per second. This means that the Doppler bandwidth requirement is about  $1.49 \cdot 10^4$  times the center frequency. This is about 32 kHz for the 216.98 MHz VHF fence, 447 kHz at 3 GHz, 716 kHz at 4.8 GHz, and 1.5 MHz at 10 GHz. Clear bands of this size do not exist except for the current NAVSPACECOM allocation for the VHF fence, and making way for a new microwave fence will necessarily impact existing allocations. The cost of this impact increases with the bandwidth cleared for the new system. However, a bandwidth of 1.5 MHz for a radar of this importance should not be prohibitive.

One possibility to reduce bandwidth requirements for a new microwave capability might be to use part or all of the existing VHF fence to provide surveillance of high range rate objects to reduce bandwidth requirements of a new microwave capability. This is attractive because high Doppler objects are in orbits with very high eccentricity. A disadvantage may be that small debris in such orbits decays more slowly than small debris in near circular orbits and would not be seen reliably with a narrowband microwave fence, but such objects have a combination of low radar cross section (RCS) and high altitude over a high percentage of the time, and, as such, have a low probability of detection with any sensor. A narrowband microwave sensor will still see these objects when they pass through its fence plane near perigee.

**DRAFT CONCEPTS.** Pulsed fan and pencil beam concepts have not been sufficiently explored to prove out the attractive option of detecting and measuring six orbital elements in a search fence. A pulsed concept will meet the mission and requirements if

- A fan beam is used for search (scanning pencil beams would allow fly-through)
- Receive while transmit is done to prevent fly-through
- The fence is not perturbed by the use of RF assets to perform verification and track.

A CW fan beam fence will meet the mission and requirements if

- An unmodulated CW waveform is used
- The fence is maintained continuously
- The sensitivity is similar to that of the existing VHF fence
- At least two receiver sites are used, and
- An auxiliary sensor or other sensors are used to complete the orbital parameter set for newly detected objects.

Orbital debris down to 1 cm at altitudes of 600 km and below will be reliably detected if the center frequency is above about 4.5 GHz, depending on other radar sensitivity drivers such as average power and antenna sizes.

A single receiver site can perform detection but will only compute two direction cosines and a bistatic range rate, so two receiver sites are necessary to compute a position by triangulation. The two bistatic range rates computed allow computation of object velocity in the plane determined by the object position at the time of detections and the receiver phase centers (the fence plane, if both receivers are in the fence plane), but velocity normal to this plane is estimated only by the chirp rate of the signal (a sign ambiguity remains in this computation), which is less accurate than the bistatic range rate measurements. A third receiver site out of the fence plane will allow computation of all 6 orbital parameters if all three have good signal to noise ratio (SNR); this receiver will require additional complexity in signal processing over that of receiver sites on the fence plane because this site must form beams directed to different orbital altitudes.

The full orbital set will be obtained on the first pass by the use of separate sensors. As an example, the AN/FPS-85 Space Track Radar at Eglin AFB, one of the PAVE PAWS sites, or one of the Phillips Laboratories CONUS EO/IR sites could be used as a verification and track sensor for the existing UHF fence. Figure 1 at right shows the radar field of view (FOV) of all active Space Track sensors for orbital objects at 500 km altitude, and Figure 2 shows the EO/IR field of view. The data from these sensors could come before or after the first detection by the CW fence. Waiting for the next detection by the CW fence is an attractive option when quick response is not imperative and is often done with the existing VHF fence. The next detection usually comes on the next orbit, typically in about 90 minutes, but will nearly always come within 12 hours when the Earth's rotation moves the fence across the object's orbit again.

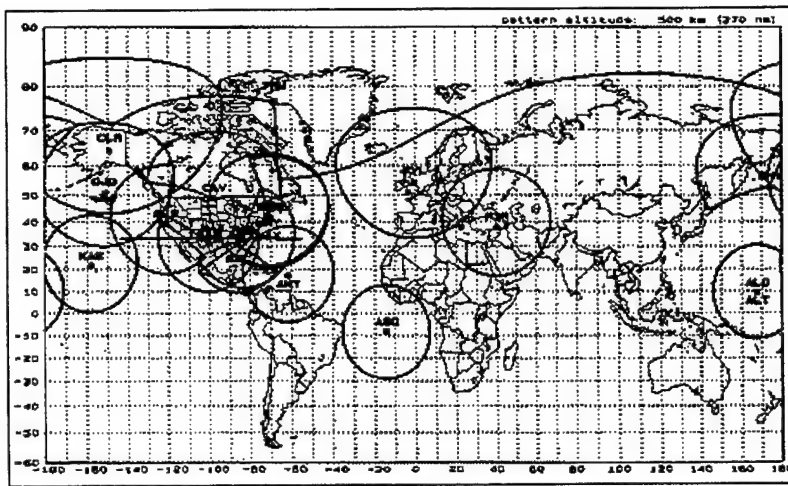


**Figure 1. Space Track Radar Field of View at 500 km Altitude (From <http://www.fas.org/spp/military/program/track/overview.htm>)**

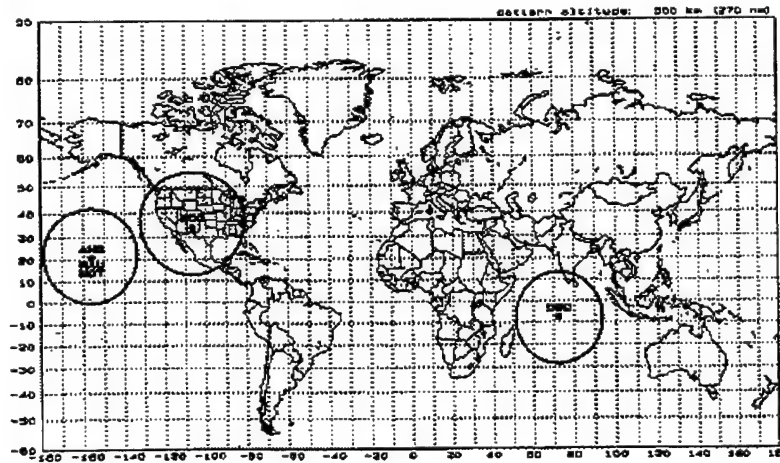


**Figure 2. Space Track EO/IR Field of View at 500 km Altitude (From <http://www.fas.org/spp/military/program/track/overview.htm>)**

An auxiliary EO/IR sensor could provide verification and track of new detections. A 1 meter reflector sited at one of the receiver sites would be cued to a line of sight and reacquired and track for a few seconds to provide a complete orbital set. Cost of this type of sensor is moderate relative to other system costs.

The bandwidth allocation of the new microwave fence can be reduced if part or all of the existing VHF fence is used to detect objects in highly eccentric orbits. Small debris in highly eccentric orbits would be seen by the microwave fence when it crosses its fence plane near perigee.

A pulsed RF sensor can be used for verification and track. Most current work [12, 13, others] has focused on CW sensors, and a reexamination of pulsed RF concepts with a 2002 technology date may result in a practical design concept that meets overall requirements.

**STRENGTHS OF THE DRAFT CONCEPTS.** The main strengths of the draft microwave CW fence concept include low risk and moderate initial cost. Relative to the current VHF surveillance

fence, the draft microwave CW fence has improved orbital element accuracy and improved life cycle cost. The microwave concept meets the mission in much the same way as the current CW fence, since it is essentially the same concept but scaled for frequency. The smaller antennas convey major simplifications in cost and siting considerations. The higher frequency allows some estimation of a 6th orbital element when detections are made from two or more sites placed in the fence plane, and a third site out of the fence plane would allow estimation of all 6 orbital elements on the first detection. A center frequency above 5 GHz and sensitivity at least equal to the current VHF fence will allow monitoring of 1 cm debris at 600 km altitude, so that density and orbital elements of debris at 400 km (typical ISS or Space Shuttle mission altitude) can be accurately predicted over time scales appropriate to planning and execution of missions.

**ISSUES OF THE DRAFT CONCEPTS.** Unless the center frequency is at least 5 GHz, utility in protection of the ISS and Space Shuttle from 1 cm debris is in question. Frequency allocation for a band at 3 GHz is underway, but the bandwidth currently obtained is sufficient for an initial capability but not wide enough to observe the same range rates as the current VHF capability. Frequency allocation at 5 GHz or above are deemed more difficult than at 3 GHz and are not underway at this time.

Operation of a receiver site co-located with the transmitter site is an attractive option since sufficient isolations are obtainable at microwave frequencies, and CW air defense systems using co-located receivers have been deployed. However, in heavy rain, scattered transmitter energy may cause severe spurs in the receiver due to dynamic range limitations. In cases of high object density, this may cause resolution of ambiguities to fail. This makes co-location of one receiver site with the transmitter a less attractive option.

Maintaining sensitivity as frequency changes requires that the effective receiver antenna area not change significantly with frequency. For antennas with fixed steering, cost per element does not follow a smooth curve with frequency because antenna concepts change. Receiver antenna cost does, in general, decrease with increasing frequency, but antenna cost must be carefully examined for any given concept.

The wider bandwidth requirement, and the fact that the new system will "see" about an order of magnitude more objects than the current VHF fence, raise issues of processing and data communications architecture. The simplest solution is full time high data rate links to Dahlgren and Cheyenne Mountain, which may become a cost issue.

The new sensor can obtain 6 orbital elements on the first pass when detections from two or more receivers is obtained with good SNR and signal chirp data is used. A North-South sign ambiguity remains, and accuracy of the sixth parameter is not as good as the others because of the short dwell times. A third receiver site out of the fence plane can obtain the sixth parameter with good accuracy, but with significant system complexity impact for that receiver site. The best option, at least for the near term, appears to be the use of other Space Track sensors of opportunity to perform verification and track of new detections, as is now done with the VHF fence.

The requirement to obtain 22.5 degrees of latitude coverage to prevent fly-through by objects with a 90 minute orbit determines the width of the fan beam. To obtain 22.5 degrees of coverage at 400 km altitude requires a fan beam width of about 140 degrees for a transmitter at a latitude of 33 degrees. Coverage at 600 km altitude requires about 125 degrees.

Most work to date has been on the trades associated with microwave concepts scaled from the existing VHF fence. Broader investigations that include pulsed or modulated CW waveforms and other differences and innovations can only strengthen the system concept development process.

WHAT ABOUT KEEPING SOME EXISTING VHF CAPABILITY? The VHF fence is in place with its frequency allocation, infrastructure, and data transfer architecture. Less visible capabilities such as off-line analysis of detection anomalies are part of the existing capability. Continuing the VHF capability for at least a few years allows overlap with the new microwave capability, mitigating any schedule gap risk in meeting the mission. After examination of experience and the capabilities of both sensors and reformulation of the concept of operations (CONOPS) of the use of the sensors, a decision could be made to keep a portion of the VHF capability.

The disadvantage to keeping the VHF capability is that its best use is with the high altitude receiver sites in Elephant Butte, NM and Hawkinsville, GA. The antenna life cycle replacement due at these sites in 2002 represents a major part of the cost offset for the new microwave fence, and without these sites the argument for keeping the VHF capability is less compelling. Even at its best, the VHF site is less capable than a microwave fence in obtaining 6 orbital elements on the first pass.

Complementary usage of the VHF and microwave sites is an option. This option would be to use the microwave fence at a slightly different latitude than the VHF fence so that detections would occur closely spaced in time from the two fences. Each sensor would use the other to obtain the 6 orbital elements on a single orbital pass. This would relax the requirements on the FPS-85 and allow downing this system for technology retrofit.

Keeping the VHF capability, in part or in whole, requires that its life cycle and O&M cost issues be successfully addressed. This will require some investment. For example, a new receiver antenna concept that is both less expensive, and does not have a total replacement design end of life, is required to mitigate operating costs. The VHF antenna modules, in spite of their design being part of the very successful and reliable family of solid state AESA modules used in PAVE PAWS, BMEWS AESA upgrades, and ROTHR, have a unique environmental problem in that they are unprotected from the elements and temperature cycle over a wide range; resulting related O&M issues should be solved. Antiquated power supply capabilities need to be replaced with new designs, and other technology retrofits need to be applied.

CONCLUSIONS. In the light of the fact that a frequency allocation at 3 GHz is underway, a reasonable plan is to field a single microwave transmitter using this 3 GHz frequency allocation, a single receiver co-located at this site, and to use one of the sites currently used as a VHF fence receiver site to take advantage of existing data communication capabilities. An auxiliary EO/IR sensor at this site would complete facilities required to take full advantage of initial microwave fence capability and develop the experience necessary to maximize returns on investment on maturing this capability. This would be a first capability, and the concept would be reviewed before proceeding. The VHF capability will be fully maintained until the new microwave site is in place, allowing the planning for transition to the new capability to adjust to information gained in use of this initial capability. Baseline concept changes, resiting, center frequency changes, and other improvements will then be implemented as appropriate.

Phillips Laboratories, NRL and NAVSPACECOM have recently completed top down studies. Although the results of the Government studies are not public and thus did not contribute to this report, it is likely that many of the recommendations of these studies do agree with many of the points made here, and with those of the NAVSPACECOM studies [12, 13]. At this point, it seems advisable to consider these steps:

- Reexamine the mission, requirements and CONOPS using the results of the funded studies and other recent data, particularly the (at present unfunded) NASA requirement for detecting 1 cm debris,
- Consider mixes of sensors over the next 5, 10, and 20 year periods,

- Open up the concept to include pulsed concepts, modulated waveforms, and innovative new concepts,
- Develop detailed architectures to be made available at specific times in the near term, and
- Follow results of timely properly funded planning exercises with a definition of a specific concept for implementation.

REFERENCES.

1. "Space Systems Threat Environment Description (TED) (U)," DST-2660F-722-93, 29 October 1993 (USSPACECOM Document)
2. "Mission and Functions of the Naval Space Surveillance System," OPNAV Instruction 5450.206, Department of the Navy, CNO, OP-943, 22 June 1981
3. "Satellite Detection and Reconnaissance Defense (U)," Operational Requirement No. AD-01503, CNO OP-761 or Ser 0014P76, 31 December 1959
4. "Space Surveillance Requirements (U)," Headquarters US. Space Command, Peterson AFB, CO, 30 August 1995
5. "Operational Requirements Document for the Naval Space Command Surveillance System (U), (DRAFT)" NAVSPACECOM, 21 November 1995
6. "Orbital Debris, A Technical Assessment," National Research Council, ISBN 0-309-05125-8, National Academy Press (1995), available in HTML at <http://books.nap.edu/books/0309051258/html/index.html>
7. Naval Space Command Information Booklet, available in HTML at <http://www.peterson.a.mil/usspace/fbnavspa.htm>
8. Naval Space Command Unclassified Catalog, available from the Goddard Space Flight Center Bulletin Board at <http://oigsysop.atsc.allied.com/scripts/foxweb.dll/app01?>
9. "Protecting the Space Shuttle from Meteoroids and Orbital Debris," National Research Council, ISBN 0-309-05988-7, National Academy Press (1997), available in HTML at <http://www.nap.edu/books/0309059887/html/index.html>
10. "Orbital Debris May Pose Significant Risk to the Space Shuttle," National Academy of Sciences Press Release, 16 December 1999, available in HTML at [http://www4.nationalacademies.org/news.nsf/\(ByDocID\)/88F6A953F8830CEB8525677400635511?OpenDocument](http://www4.nationalacademies.org/news.nsf/(ByDocID)/88F6A953F8830CEB8525677400635511?OpenDocument)
11. "Protecting the Space Shuttle from Meteoroids and Orbital Debris," National Research Council, ISBN 0-309-05988-7, National Academy Press (1997), available in HTML at <http://books.nap.edu/books/0309059887/html/index.html>
12. "Next Generation NAVSPACECOM Space Surveillance Concept," Final Report, NAVSPACECOM Contract N00612-94-D-8401, 07 March 1996.
13. "Microwave Space Surveillance System Design Study," Final Report, NAVSPACECOM contract to Eagan, McAllister Associates, Inc, performed by Syracuse Research Corporation under subcontract 7903-001, 9 November 1999.

SPACE CONTROL CONFERENCE 2000

DISTRIBUTED TRACKING

Alan Collinson<sup>1</sup>, Michael A. Bailey<sup>2</sup>, Stephen J. Goodenough<sup>3</sup> and Edward Goodchild<sup>4</sup>

ACKNOWLEDGEMENTS

1. The work described in this paper was carried out under the sponsorship of the Joint UK/US Scientific Cooperative Research Exchange (SCORE). Many agencies were involved in this project. At times we believed that the complex technical issues that we had to deal with were trivial compared with the mechanics of making the programme happen. The fact that it did happen, and was an outstanding success, was due to the hard work of many people and we must thank the following people whose contributions were way above that which duty required. To Maj John P Beauchemin, Ken Blutt, Norm Davis, Johnny Fleeman, Steve Lewis, Sqn Ldr Al Mellor Jones, Maj Trish Ratteree, Stephen Rhodes, Dr Bob Rohlfs, Dr Brian Shand, Cathy Smith, Bernadette Van-Buskirk and Dan White we extend our thanks. However, perhaps our greatest thanks should go to Sqn Ldr Clive Harrison who had the day to day responsibility for the most difficult programmatic issues.

INTRODUCTION

2. The long range sensors which provide early warning of ballistic missile attack and act as collateral spacetrack sensors perform their missions working, in many respects, independently. The sensors are integrated into their respective networks in a "command" sense but there is only limited system-level integration of the detection and tracking functions. There are two reasons why this has been so. The "first generation" sensors had limited resolution and their early warning functions were based on a statistical assessment of the number of targets present to be detected. Automatic correlation of the targets seen by multiple sensors from this generation was not possible. However, there was also an important philosophical issue. If two sensors or sensor chains reported threats independently, the chance of a false alarm was significantly reduced and this provided greater confidence in the warning to the National Command Authorities.

3. Even when the first generation sensors were upgraded there was little scope for addressing multiple sensor integration. To meet the challenges of the Cold War threat, maximum possible track accuracy had to be sacrificed in favour of being able track, with acceptable accuracy, possibly many hundreds of objects and generate warning launch and predicted impact messages in very short spaces of time.

4. However, the radar systems are very capable and possess a considerable latent capability which, in a different threat environment can be investigated and, hopefully, exploited. Indeed, this capability is an aspiration of USSPACECOMMAND which aims in the future to achieve "Integrated Focussed Surveillance"<sup>5</sup>.

---

<sup>1</sup> Collinson Systems Limited, 25 Thornton Road, Pickering North Yorkshire, YO18 7HZ

<sup>2</sup> UK Ministry of Defence, Northumberland House, Northumberland Avenue, London, WC2N 5 BP

<sup>3</sup> Defence Evaluation and Research Agency Malvern, St Andrew's Road, Malvern, Worcs, WR14 3PS

<sup>4</sup> ASA, North Block, Bentley Hall, Blacknest, Alton, Hants GU34 4PU,

<sup>5</sup> "The Long Range Plan", USSPACECOMMAND.

5. In 1999, an experiment was conducted to investigate if this latent potential was sufficient to allow fusion of data from two of these sensors and build composite tracks which were of greater accuracy than the tracks made by either sensor independently. This paper describes the infrastructure which had to be installed at the radar sites to be able to conduct the experiment, the nature of the experiment and some of the more important results.

#### DEVELOPMENT OF THE INFRASTRUCTURE

6. Before discussing the experiment in more detail, the underlying concept of the infrastructure which had to be built must be described. The current processes of detection and tracking carried out by the radars may be summarised as follows. New surveillance detections are submitted to a track initiation process which verifies the presence of an object and initialises a track file on the object. Periodically, the tracker requests updates on the object until a predetermined accuracy or fixed time limit expires. On completion of the initial tracking requirement, the track is submitted to threat processing and, depending on the assessment, further tracking may or may not be required. For example; if the object is classified as a satellite, tracking consistent with the satellite tasking category and suffix will be carried out; if the object is a missile, tracking may cease and a launch and predicted impact message will be generated and transmitted rearwards. There are a number of "nodes" in this functional process where data can be recorded on magnetic tapes for post mission analysis but, for all practical purposes, there is very little scope for gaining access in real time to this closed loop process.

7. In order to attempt fusion in real-time it was decided that an external tracker would be most appropriate. The Target Oriented Tracking System (TOTS) tracker produced under joint US/UK sponsorship and manufactured in the UK by ASA Limited was the tracker of choice. The mission computer systems, which in both cases were Cyber computers, receive radar returns from the front end of their radars via a radar control (RCL) computer. The radar data at this interface is uncorrected for bias, calibration and the effects of ionospheric correction. It was noted that there were significant differences between the algorithms used by the two radar sites to correct radar returns before providing them to the native trackers. It was decided to "intercept" returns at the RCL-Cyber interface. Access to the radar return data from this interface provided the opportunity to investigate the pre-processing calibration algorithms and also to insure that the "plots" sent to TOTS were as accurate as possible.

8. The implementation of the interface was carried out by ASA Limited and General Dynamics Systems Inc (GDIS) of Colorado Springs working to specifications created by the UK Defence Evaluation and Research Agency. The interface was only at the RCL-Cyber Interface in a logical sense. It was not possible to interfere with the direct connections made between the RCL and the Cyber and achieve the desired result because of the corruption this would have caused to the signal timings. Thus it was decided that the best way to implement the interface wold be to connect the TOTS equipment to the "Cyber Channel" interface which is the same interface point used by the RCL. This interface was capable of operating in real-time and dealing with the full bandwidth demanded by the radar return data. Thus, in principle, radar returns from the RCL were captured by Cyber software and redirected out to the new interface. In practice, GDIS implemented a far more flexible software interface capable of directing a much wider

variety of Cyber data to the interface with the TOTS System which would normally be capable of being recorded to the mission history tapes.

9. ASA developed a specific-to-purpose PCI-based computer interface to communicate with the Cyber Channel. Cyber data was provided to external systems via a 100Base-T Local Area Network (LAN). The ASA PCI interface provided data to the LAN in such a way that the messages from the different radar sites were as similar as possible. All data passing on the LAN were recorded using a specially designed Historical Recording Facility (HRF).

10. Having gained access to the radar returns, it was then necessary to replicate the Cyber pre-processing algorithms to condition the radar data prior to passing the data to the TOTS tracker. The corrections required were as follows;

- Creation of absolute range from coarse and fine range components.
- Creation of absolute azimuth and elevation angles from a pointing angle and monopulse measurements.
- Conversion of amplitude measurements into radar cross section measurements.
- Correction of elevation angle measures for the effects of ionospheric refraction.
- Correction of range measurements for the effects of ionospheric refraction.
- As required, the matching of returns from different polarity slope linear frequency modulation (LFM) pulses to eliminate the effects of range doppler coupling.

11. The corrections described were implemented in a software module called the Data Conditioning Interface (DCI). The DCI output which comprised position and size measurements and the time of the measurement are known as plot data. A key design factor was the fact that the plot data was as similar in form as possible irrespective of the sensor network from which it was derived. The plot data is then provided to the TOTS tracker.

12. TOTS uses the plot data to attempt to update any existing local tracks. If the data cannot be associated with existing tracks, new tracks are initiated. TOTS is a very aggressive track initiator and a new track can be started with a single report. A benefit of this approach is that it enables objects to be tracked very close to the system noise floors where detection is only sporadic. Thus, using the TOTS tracker it may be possible to detect objects which would otherwise be significantly below the noise threshold.

13. An important feature of TOTS is that each report may be used as often as required, i.e. when a plot has been used it does not preclude it being used again if it can usefully update another track. Inevitably the track initiation strategy leads to a large number of tracks which are found to be non-viable and subsequently are pruned out but TOTS has been designed to be scalable and can maintain track of very large numbers of objects without overall system degradation.

14. Plots are accumulated into tracks using a Kalman filtering process. TOTS has a suite of Kalman filter tracking models which handle all plausible types of object motion, for example, boosting flight, post boost acceleration, ballistic flight, etc. In general, when a new report is received, it will update any track which can use the plot and a single plot may be used by several exiting tracks. Tracks can be formed by any of the active models. After filtering, the viability of each track is tested and tracks which fail are pruned out.

15. Viable smoothed tracks, or the plots which were used to create them, could be transmitted to the data fusion centre using standard Air Force Space Command Digital Information Network (SDIN). The communications links were operated by Freeway 1100 system: a commercial off-the-shelf piece of equipment. The equipment configuration which was installed at the radar sites for the experiment is illustrated in Figure 1.

16. At the data fusion centre a third TOTS system was used to attempt data fusion using either the plot or track data from the radar sites.

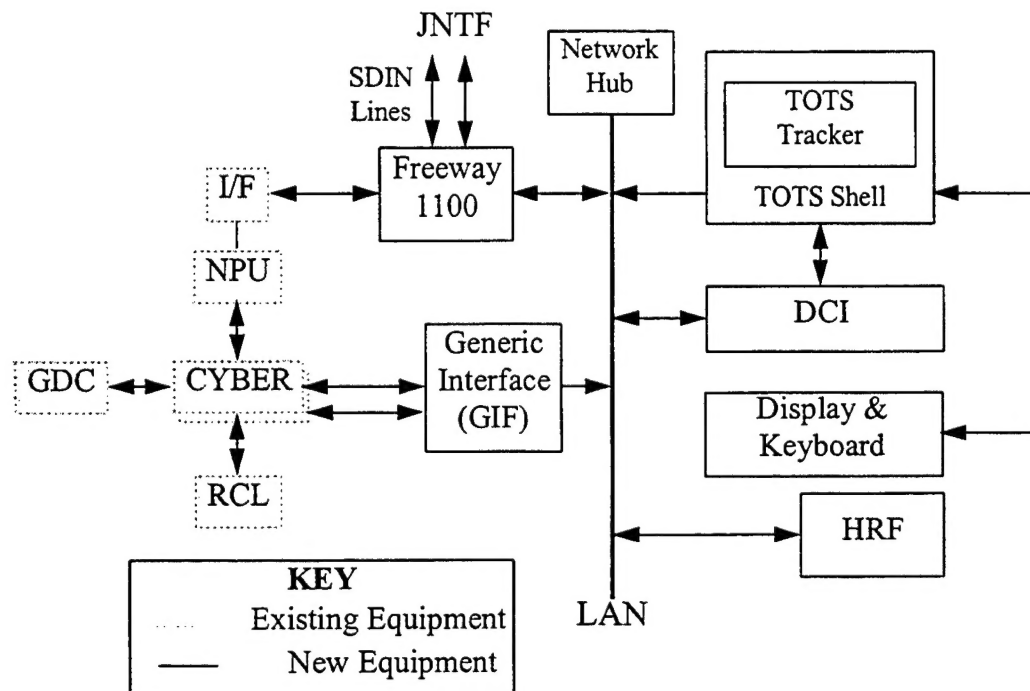


Figure 1 Distributed Tracking

#### THE EXPERIMENT

17. The experiment was conducted over a period of two weeks during which nine periods were allocated to tracking. Experiments were conducted using the sensors to track low earth orbit (LEO) satellites at long ranges, whenever possible when the satellites were in coverage of both radars. A number of different criteria were adopted for planning suitable candidates for tracking.

18. The most important tracking candidates were a group of satellites for which accurate optical track data was available which could provide a source of "truth data". The aim of tracking these objects was to establish the accuracy of the composite tracking. Various calibration spheres and objects with precise ephemeris were also chosen to observe the effects of observation in different parts of the sky with a view to determining if there were any observable ionospheric effects.

19. Further objects were selected to determine if it was possible to correlate the observations from different sensors and reconcile the Space Object Identification features.

#### THE RESULTS

20. Data Fusion Architecture Some problems were identified with the equipment installed at the radar sites but these were minor and it may be concluded that the equipment was capable of fusing data from two widely separated, but similar, radars. In some cases the radars were observing targets in a challenging environment at extreme ranges. Further, although a number of iterations of testing will be necessary to achieve optimal tracking, even at this first attempt the benefits of processing gain were demonstrated.

21. Plot Fusion Within the constraints of its architecture, in particular the throughput capacity of the computer systems used for the tracking it was demonstrated that plot fusion is a viable mechanism for fusing a limited operational picture. A maximum of 17 objects concurrently in track by the two radars was observed during DTE. This fusion was achieved using minimal bandwidth, 2 x 9.6 Kbaud SDIN lines between the radars and the fusion centre.

22. Maintenance of combat ID It was demonstrated that the TOTS tracker was capable of maintaining track, and thereby combat ID, on tracks which were broken due to gaps in radar coverage.

23. Prototype Auto Cross Cueing The ability to provide plot data to a forward-based radar was demonstrated. The plot data was used to create a local track. The local track was then used to create a radar cue. Having acquired the object, locally generated plots were then fused into the composite track which was reported to the fusion centre. The architecture required manual intervention to inject the cue at the radar site under direction from the fusion centre.

24. Ionospheric Phenomenon Examples were observed during the experiment of highly individual 'signatures' on certain tracks which were created at a time when ionospheric sensors were indicating the presence of a disturbance in the atmosphere. TOTS was able to create tracks during this event which were apparently no less accurate than any other tracks. Further investigation should be undertaken to determine if there is a potential mechanism for using the radars to recognise the ionospheric disturbance automatically without use of additional ionospheric sensor support.

25. Corruption of Radar Cross Section in Plots Preliminary analysis of radar cross section (RCS) data showed that the data was inconsistent. The problem may be as a result of the analysis method used or the computation of RCS in the DTE equipment. Further investigation of this phenomenon should be undertaken because in its present form it would not be possible to undertake discrimination.

26. Inconsistency between radar sites Plot data observed showed inconsistencies between the two radar sites. Initial investigation was inconclusive and further investigation is required to determine if the effect is caused by an error or malfunction in the DCI or whether the effect is an attribute of the radar.

27. Track Accuracy and Uncertainty During the experiment a complete evaluation of track data against high accuracy truth data was not possible. Further work should be undertaken to determine the accuracy of the track data. Initial evaluation of the track data indicated that the uncertainty associated with tracks was too high, typically by an order of magnitude. Further work is necessary to optimise the tracking to assess correctly the track uncertainty. The analysis carried out to date indicated that an increase in track accuracy of approximately an order of magnitude is possible using data fusion.

#### RECOMMENDATIONS

28. The use of track fusion should be considered for routine use by Air Force Spacecommand for tracking of satellites and missiles to improve accuracy of tracking and accuracy of raid size assessment.

29. The improved track sensitivity offered by composite tracking should be investigated further for use in debris investigations and the tracking of smaller satellites than would otherwise be possible with single sensors.

30. Further analysis work needs to be completed on the implications of this work for discrimination and SOI.

31. Further work should be undertaken to investigate the effects of ionospheric disturbances on these radar systems.

REPORT DOCUMENTATION PAGE			Form Approved OMB No. 0704-0188
<p>Public reporting burden for this collection of information is estimated to average 1 hour per response, including the time for reviewing instructions, searching existing data sources, gathering and maintaining the data needed, and completing and reviewing the collection of information. Send comments regarding this burden estimate or any other aspect of this collection of information, including suggestions for reducing this burden, to Washington Headquarters Services, Directorate for Information Operations and Reports, 1215 Jefferson Davis Highway, Suite 1204, Arlington, VA 22202-4302, and to the Office of Management and Budget, Paperwork Reduction Project (0704-0188), Washington, DC 20503.</p>			
1. AGENCY USE ONLY (Leave blank)	2. REPORT DATE 11-13 April 2000	3. REPORT TYPE AND DATES COVERED Project Report	
4. TITLE AND SUBTITLE  Proceedings of the 2000 Space Control Conference		5. FUNDING NUMBERS  F19628-95-C-0002	
6. AUTHOR(S)  S.E. Andrews (Editor)			
7. PERFORMING ORGANIZATION NAME(S) AND ADDRESS(ES)  MIT Lincoln Laboratory 244 Wood Street Lexington, MA 02420-9108		8. PERFORMING ORGANIZATION REPORT NUMBER  STK-255	
9. SPONSORING/MONITORING AGENCY NAME(S) AND ADDRESS(ES)  AFSPC/DOY ESC Hanscom Air Force Base Bedford, MA 01730 150 Vandenberg St. Suite 1105 Peterson AFB, CO 80914		10. SPONSORING/MONITORING AGENCY REPORT NUMBER  ESC-TR-99-063	
11. SUPPLEMENTARY NOTES  This report is based on studies performed at Lincoln Laboratory, a center for research operated by Massachusetts Institute of Technology. The work was sponsored by the Department of the Air Force, AFSPC/DOY, under contract F-19628-95-C-0002. Papers appearing in this Proceedings were sponsored by multiple sources.			
12a. DISTRIBUTION/AVAILABILITY STATEMENT  Approved for public release; distribution is unlimited.		12b. DISTRIBUTION CODE	
13. ABSTRACT (Maximum 200 words)  <p>The eighteenth Annual Space Control Conference was held on 11, 12, and 13 April 2000. ESC acts as administrative sponsor of the event which is held at the Lincoln Laboratory facility on Hanscom AFB, and the program is coordinated with Air Force Space Command and the Air Force Research Laboratory. The purpose of this series of conferences is to provide a forum for the presentation and discussion of space control issues.</p> <p>This <i>Proceedings</i> documents those presentations from this conference that were received in time for pre-conference publication. The papers contained were reproduced directly from copies supplied by their authors (with minor mechanical changes where necessary). It is hoped that this publication will enhance the utility of the conference.</p>			
14. SUBJECT TERMS			15. NUMBER OF PAGES 206
			16. PRICE CODE
17. SECURITY CLASSIFICATION OF REPORT Unclassified	18. SECURITY CLASSIFICATION OF THIS PAGE Unclassified	19. SECURITY CLASSIFICATION OF ABSTRACT Unclassified	20. LIMITATION OF ABSTRACT Same as report